# Quantum Well Structures for Plasma Instability-based Terahertz Radiation Sources

Author: Justin John Butler

---

Boston College Electronic Thesis or Dissertation, 2012

Boston College

The Graduate School of Arts and Sciences

Department of Physics

# QUANTUM WELL STRUCTURES FOR PLASMA INSTABILITY-BASED TERAHERTZ RADIATION SOURCES

a dissertation

by

JUSTIN JOHN BUTLER

submitted in partial fulfillment of the requirements

for the degree of

Doctor of Philosophy

December 2012

# QUANTUM WELL STRUCTURES FOR PLASMA INSTABILITY-BASED TERAHERTZ RADIATION SOURCES

Justin John Butler

Advisor: Professor Pradip Bakshi

## ABSTRACT

This thesis is a theoretical study of the electron transport and response properties of epitaxially-grown, low-dimensional semiconductor quantum well heterostructures, under steady-state, current-driven (nonequilibrium) conditions. These structures operate in the Terahertz (THz) frequency and submillimeter wavelength range, and are the leading candidates for compact, coherent sources of THz radiation. This work is divided into two parts: Part I consists of an analytical study of the individual quantum well units, and the tunneling transmission characteristics, for which reasonably accurate algebraic expressions are obtained. An underlying philosophy of this work is the desire to describe each of the key components involved, independently, through these simple analytical expressions. In Part II the numerical study of the transport and radiation response of the quantum well structures specially designed to generate THz radiation based on the plasma instability concept is presented. Several models are proposed which describe the overall electron transport and which determine the underlying nonequilibrium steady state. In particular, the key features of the experimental current-voltage (IV) curves for such structures are explained, and the corresponding response properties are determined. The modeling and simulation of these potential optoelectronic devices is a crucial tool for elucidating the precise mechanisms and interplay of the many microscopic processes which give rise to the observed behavior. Key features of the radiation response arise from the intersubband plasma instability which occurs due to the resonant interaction of an emission and an absorption mode, and these features are compared with the experimental observations.

# Table of Contents

# Acknowledgments

I would like to thank Professor Pradip Bakshi for the opportunity to conduct this research and for providing the financial support that made it possible. I am grateful for his confidence in my ability to handle this project, and his suggestions and advice as this work was taking shape. I would also like to thank him for the patience he has shown when things were not proceeding so smoothly. I would like to thank Professor Kris Kempa for his helpful insight in many areas. Professor Naughton has also been extremely accomodating and always had useful advice, not only as a commitee member, but also as Chairman of the Physics Department.

I am grateful to the Department of Physics for the financial support I was given, and to the staff: Nancy Chevry, Gisele Byda, and Jane Carter. They continue to provide invaluable assistance and to help things run smoothly in the department.

I wish to thank my parents John and Darlene for their support and constant encouragement. You are both an inspiration, and many things would not have been possible if it weren't for your care and guidance. I want to thank my siblings as well, Nathan, Kerry, and Brian for their support and encouragement over the past several years. Although it's not said often, I love you all very much!

I would like to thank my close friend Dave Cray for his unique outlook in life and providing a much needed distraction from research throughout the years.

Finally and most importantly a very special thanks goes to my fiance Danielle for her continuing love and her belief in me. I could not have done this without you.

## Chapter 1

# Introduction and Overview

---

## 1.1 Semiconductor Quantum Well Heterostructures and Devices

---

Quantum well (QW) heterostructures are the building blocks of many of the most advanced semiconductor devices due to their wide range of applications. There has long been an interest in the electronic and optical properties of heterostructure QW-based and superlattice-based devices because they provide a novel environment in which to study particle dynamics in low-dimensional systems, in contrast to bulk materials. They are essential elements of the highest performance optical sources and detectors, such as the mid-infrared QW heterostructure lasers [1, 2], high-efficiency QW heterostructure LEDs [3], and QW solar cells [4]. QW's are continually employed in high-speed and high-frequency digital and analog devices [5], and can also be used as part of electronic devices such as heterojunction-based bipolar transistors [2, 6], modulation-doped field effect transistor (MODFET), resonant tunneling devices, and as an optical component in waveguides, microresonators, and mirrors [7]. However, reliable and efficient sources operating in the *terahertz* (THz) region, between lower frequency microwaves and the higher frequency far-infrared, are still lacking. In this thesis we study novel QW structures as possible candidates for sources of THz radiation.

A *heterostructure* is a semiconductor material with a position-dependent chemical composition. The layers that make up a heterostructure can be made exceedingly thin, with thicknesses on the order of a single atomic layer. This is possible because of the advancement of precise growth techniques, such as Molecular Beam Epitaxy (MBE) [8]. The ability to form such thin layers make heterostructures one of mans significant engineering conquests. Just as Nature's atom puts electrons into discrete energy states, mans quantum-confined heterostructure forces electrons into discrete energy states as they pass through a heterostructure device. By exploiting this ability, we can influence when, where, and how electrons interact with their surroundings. The energy levels of a heterostructure can be tailored so that transitions between levels correspond to photons in a particular region of the electromagnetic spectrum, for instance, the THz region. Additionally, there is the ability to 'tune' the energy levels and their relative placement by applying a voltage bias, creating novel device scenarios. Depending on the number of heterojunctions formed, complex structures can be built up from simple QW systems such as the single symmetric and asymmetric QW's, and the triangular QW, for example. The success in the growth of QW structures makes a study of introductory quantum physics realizable in these man-made semiconductor materials. To this end, *one of the main goals of this thesis is to obtain reasonably accurate analytical closed-form algebraic expressions for the energy levels and wavefunctions of these simple QW units.* Although the calculation of the energies and states of composite structures typically requires involved numerical procedures, the insight gained from analytical approximations (for the simple constituent units) can be an invaluable asset in the study of QW-based heterostructures.

In the seminal work that first recognized this possibility of quantum confinement in heterostructures, Esaki and Tsu in 1970 theorized that a particular heterostructure implementation could result in negative resistance at certain applied biases [9]. The following year, Kazarinov and Suris proposed that the man-made energy states of quantum-confined heterostructures could be used for the basic optical transition for a new type of laser [10]. An important characteristic of *intersubband* transitions (transitions *within* the conduction band), the dipole moment, was first experimentally observed in 1985 [11, 12] by an absorption measurement. The first intersubband emission was observed by Helm et al. in the far-infrared (FIR) frequency range in a voltage-biased superlattice structure under resonant tunneling conditions [13, 14]. Quantum well infrared detection based on intersubband absorption has also been well developed, resulting in the quantum well infrared photodetector (QWIP) working at wavelengths of 4 $\mu m$ and 10 $\mu m$ [15, 16]. The development of intersubband-based *sources* operating in the THz region has been relatively slow however, due to the fact that in thermal equilibrium, most of the carriers are in the ground state, whereas for emission, a population inversion between two subbands must be maintained for radiative transitions. This requires an appropriate device set-up, either with an applied bias, or a pumping scheme which creates occupation of higher subbands.

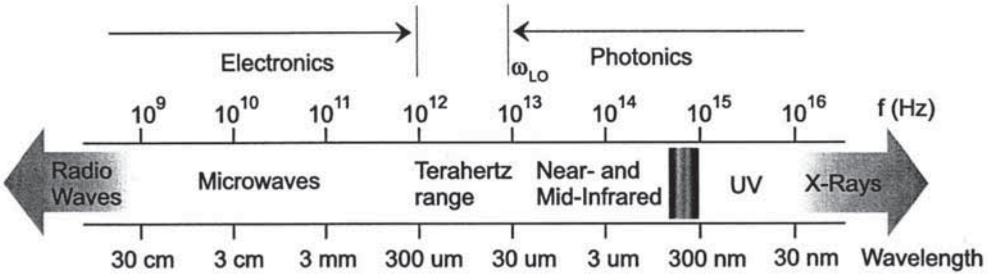

Figure 1.1: The electromagnetic spectrum, showing the THz gap between conventional electronics and photonics.

The desire for compact, coherent and tunable sources of THz radiation has driven many intense research efforts. The spectral properties and capabilities of electromagnetic waves in the THz frequency and submillimeter wavelength range are important for practical purposes, such as industrial, medical and defense applications [17, 18]. This is so, because many molecules have their characteristic vibration and/or rotational frequency within the THz region, and consequently, the radiation has many potential applications in areas such as genetic research, drug development, environmental monitoring, medical imaging, and security screening, etc [19]. Loosely defined, the THz spectral region lies between 30 and 300 $\mu m$ wavelength and $10^{12}$ to $10^{13}$ Hz in frequency. As illustrated in Figure 1.1, these boundaries mark convenient divisions between the capabilities of two broadly different technologies: conventional electronics and photonics. Referring to Fig. 1.1, from radio waves to microwaves, up to the THz frequency range, electronics have dominated due to their ease of use and functionality. The limitation of electronics in covering the Thz range is due to an impedance limitation, which is based on macro charge oscillations [20]. From the high-frequency end of the spectrum, while photonics has been successfully implemented in the form of modulators, detectors, amplifiers, and used in optical communications and data transmission, access to the THz region is still limited. The push to close the so-called *THz gap* has resulted in the development of the quantum cascade lasers (QCL's) [21], based on significant modifications of the mid-IR QCL's [22].

## 1.2 Plasma Instability-based Emission

Quantum well structures specially designed to generate THz radiation based on the plasma instability (PI) concept are studied in this thesis. In a plasma there exist collective oscillations through which wave-particle interactions may transfer free energy in the system into a collective mode. An instability develops if the amplitude of collective oscillations can grow (at the expense of free energy). The source of free energy in a system can arise in various ways, such as through a change in the distribution function from its equilibrium state. For example, if the distribution function develops a (velocity) gap, then by the Penrose criterion an instability can occur [23]. This situation can arise when a beam of particles (i.e. a current) is injected into a plasma, and this is called a current-driven plasma instability.

The phenomena of plasma oscillations and instabilities is well known in the study of gaseous plasmas [23-26]. Early attempts in 1961 by Pines and Schrieffer [27] to investigate if such processes could occur in solid state systems were unsuccessful due to the low mobilities of the carriers. In a bulk solid state plasma for the transfer of energy from the current into the plasma oscillations to happen (the threshold for instability), the carrier drift velocities must be very high, on the order of the Fermi velocity. Accelerating carriers to reach this threshold could induce strong plasma heating, thus preventing coherent plasma wave generation. Thus such a current-driven plasma instability (CDPI) could not exist in such low-mobility systems. Several theoretical attempts were made in the mid-1980's to investigate the possibility of CDPI in layered solid state plasmas [28-30]. The studies at this time were simplified "cold beam" approaches which did not account for scattering and carrier heating effects.

In 1987 at Boston College a systematic investigation was initiated by Bakshi and Kempa for determining the feasibility of CDPI in solid state systems, resulting in a series of papers. This included the study of the threshold conditions for an instability in type I and type II semiconductor superlattices [31, 32], superconductors [33], and an investigation of the effect of a velocity gap in the carrier distribution, with the implications for novel device applications [34]. The possibility of CDPI in quantum wires and quantum wire superlattices were also studied [35], as well as the spontaneous generation of plasmons [36] induced by a beam of ballistic electrons in modulation doped heterojunctions. The amplification of plasma modes in semiconductor heterostructures [37] were assessed for their potential use. The growth rates of current-driven plasma waves in layered systems [38] were studied, providing guidelines for selecting the best systems for possible device applications. In contrast to the uniform systems mentioned above, a periodic density modulation in a quantum wire [39] results in a significantly lower driving electric field required for achieving the onset of instability, making this system a possible candidate for experimental verification of this phenomena.

A coupling arrangement such as a grating would be required to convert the energy of the growing plasma waves into radiation [40]. Electromagnetic radiation arises at the frequency of the plasma wave when the grating period corresponds to the plasmon wave number. Furthermore, for optimal efficiency, the plasmon wave number for the most unstable mode must be matched to the grating period. The grating-coupling efficiency for layered systems was then established [41]. Experimental evidence of the (radiative) decay of optically excited coherent plasmons in a two-dimensional electron gas (2DEG) was shown by Vossebuerger et al [42].

Even though the feasibility for CDPI was established for several 2DEG systems [31-41], their experimental realization required specially designed very high mobility samples. In contrast, *bounded* systems could offer many advantages [43] and these were investigated next. In the studies previously mentioned, the external electric field was applied along the 'unbounded' dimension with the resulting growing plasma waves propagating along this direction as well. In a bounded plasma however, reflection of the waves in the direction of restricted motion can occur, offering several distinct advantages. Bounded plasmas, which have several eigenmodes [43] make it possible to pump energy from the current into the plasma under a variety of conditions. The effects of collisions can be reduced by reducing the size of the active region. Additionally, a coupling mechanism is not necessary, as the plasma oscillations of a bounded plasma couple directly to electromagnetic radiation. A theoretical study was carried out [44] for a steady-state nonequilibrium 1D finite length plasma model establishing the feasibility of achieving a strong instability with a growth rate exceeding the typical dissipative collision rates. These ideas could be extended to other geometries, including quantum well structures with proper injection and extraction schemes to maintain the appropriate nonequilibrium steady state.

A basic paper [45] in 1997 established the essential conditions for obtaining an intersubband plasma instability in quantum well structures: it is the *resonant interaction of an emission mode and an absorption mode.* A three level scenario, with upper and lower levels occupied, but the middle level kept empty by extraction generates such an instability. A collaboration was initiated with the Technical University of Vienna (TUV) for the design, growth and characterization of several QW structures intended to generate THz radiation. A summary of subsequent work [46-52] is given in Part II. This thesis is a continuation of the ongoing study devoted to plasma instability based emission from quantum well heterostructures.

## 1.3 Transport and Response Modeling

---

The electronic transport properties provide an important diagnostic tool for studying and developing functional and reliable nanostructures and optoelectronic devices. Diagnostic methods such as photoreflectance, electroreflectance, electroluminesence, and characteristic IV curves reveal the underlying physics and the functional bounds of such devices. In particular, the structure's IV-curve shows how the structure/device responds under a changing bias, and in general is a very commonly and widely used diagnostic tool in semiconductor device physics. Accurate transport models are useful for understanding and predicting the behavior of the devices and reveal the internal processes responsible for the observed behavior, thereby providing a comprehensive picture of the microscopic physics.

Central to the transport modeling is establishing the *non-equilibrium steady state* (NESS) as a function of the applied bias. There are two conservation conditions: Since there is no source or sink of carriers in the active region, the outgoing current equals the incoming current, and the system is in a steady state. Also, the energy conservation demands that the entering energy flux is greater than or equal to the outgoing energy flux, and the reduction, if any, implies an energy loss process in the active region. These conditions place bounds on the possible NESS's a structure will obtain under a certain bias. Once the NESS is determined, the radiation response can be calculated. We are particularly interested in the response characteristics when the conditions for plasma instabilities (Sec. 1.2) are realized.

An important feature in the study of these structures is the coexistence of a continuum distribution with the quantized, bound state distribution. When the system is bounded by thin barriers the outside continuum levels penetrate into the structure. This is especially important at low biases, for both forward and reverse bias. However as the bias is increased the continuum population depletes, and the system is primarily characterized by quantized levels.

## 1.4 Thesis Overview

---

This thesis is broadly a study of quantum well heterostructures intended for potential use as sources of THz radiation. After the Introduction (Chapter 1), Chapter 2 consists of the requisite solid-state physics background.

Part I of the thesis, which consists of Chapters 3-6, focuses on describing, in an *analytical* fashion, each of the basic units (quantum wells and barriers) that make up more complicated, real heterostructure devices. Chapter 3 details the work done for simple quantum wells (QW): the single finite symmetric QW, the single finite asymmetric QW, the finite triangular, or wedge well, and the finite symmetric double QW. Simple analytical expressions are obtained for the energy levels which are reasonably accurate and globally valid. Chapter 4 introduces the tunneling transmission probability for the rectangular barrier and the triangular barrier. A mapping is established connecting the two results. Chapter 5 deals with the finite width double barrier, in which a new complex transcendental equation for the energy eigenvalues is derived. The imaginary parts of the complex energy roots represent the leakage rates through the barriers. Finally in chapter 6, the situation of compounding the basic units is addressed. The underlying philosophy to the first part of the thesis is to obtain analytical descriptions of the energies and wavefunctions of the basic units and of the resulting composite system, which can then be used to analytically calculate the response of the system.

Part II focuses on establishing the transport models that are consistent with the observed current-voltage (IV) characteristics. In particular, the essential physics behind the notable features in the IV's is determined for both forward and reverse bias directions. The NESS is determined at each bias, and the resulting radiation lineshapes are then studied.

# Bibliography

[1] M. Keever, "Measurements of hot-electron conduction and real-space transfer in GaAs-AlxGa1-xAs heterojunction layers," Appl. Phys. Lett., vol. 38, p. 36, (1981).

[2] Z. S. Gribnikov, K. Hess, and G. A. Kosinovsky, "Nonlocal and nonlinear transport in semiconductors: Real-space transfer effects," J. Appl. Phys., vol. 77, p. 1337, (1995).

[3] Z. I. Alferov, "The double heterostructure concept and its applications in physics, electronics, and technology," Rev.Mod. Phys. 73, 767 (2001).

[4] Z. I. Alferov, V. M. Andreev, and V. D. Rumyantsev, "III-V Solar Cells and Concentrator Arrays," in High-Efficient Low-Cost Photovoltaics, vol. 140, V. Petrova-Koch, R. Hezel, and A. Goetzberger, Eds. Berlin, Heidelberg: Springer Berlin Heidelberg, pp. 101-141.

[5] Frensley, W.R. *Heterostructures and Quanutm Well Physics, from heterostructures and Quantum Devices* VLSI Electronics: Microstructure Science, Academic Press, San Diego, (1994).

[6] B. R. Nag, *Electron transport in compound semiconductors*, (Springer Series in Solid-State Sciences) vol. 11. (Berlin: Springer-Verlag, 1980).

[7] D. Miller, "Optical Physics of Quantum Wells," 2011.

[8] Singh, J. *Semiconductor Devices: An Introduction* (McGraw-Hill, 1993).

[9] Esaki, L., Tsu, R. "Superlattice and negative differential conductivity in semiconductors" IBM J. Res. Dev., **14** p. 61, 1970.

[10] Kazarinov, R.F., Suris, R.A. "Possibility of the amplification of electromagnetic waves in a semiconductor with a superlattice" Soviet Physics: Semiconductors, **5** pp 707-709, 1971.

[11] West, L.C. and Eglash, S.J. "First observation of an extremely large-dipole infrared transition within the conduction band of GaAs quantum well" Appl. Phys. Lett., **46** pp 1156-1158, 1985.

[12] Mii, Y.J., Wang, K.L., Karunasiri, R.P.G. and Yuh, P.F. "Observation of large oscillator strengths for both 1 → 2 and 1 → 3 intersubband transitions of step quantum wells" Appl. Phys. Lett., **56** pp 1046-1048, 1990.

[13] Helm, M., Colas, E., England, P., DeRosa, F., and Allen, S.J. Jr "Observation of grating-induced intersubband emission from GaAs/AlGaAs superlattice" Appl. Phys. Lett., **53** pp 1714-1716, 1988.

[14] Helm, M., England, P., Colas, E., DeRosa, F., and Allen, S.J. Jr "Intersubband emission from semiconductor superlattices excited by sequential resonant tunneling". Phys. Rev. Lett., **63** p. 74-77, 1989.

[15] Rosencher, E., Vinter, B., and Levine, B., editors. *Intersubband Transitions in Quantum Wells* NATO ASI Series. Plenum Publishing, 1992.

[16] Levine, B.F. "Quantum well infrared photodetectors" J. Appl. Phys., **74** pp. R1-R81, 1993.

[17] A.G. Davies, E.H. Linfield, M. Pepper, *The terahertz gap : the generation of far-infrared radiation and its applications : papers of a discussion meeting held at The Royal Society on 4 and 5 June 2003* Phil. Trans. R. Soc. Lond. A, 362(1815), 2004. Special issue with a compilation of 16 papers.

[18] M. Tonouchi, "Cutting edge terahertz technolgy," Nature Photonics, 1, p.97, 2007.

[19] P.H. Siegel, "Terahertz technolgy in biology and medicine," IEEE Trans. of Micro. Theory and Tech., 52 (10), p.2438, 2004.

[20] K. Kempa, P. Bakshi, C. G. Du, G. Feng, A. Scorupsky, G. Strasser, C. Rauch, K. Unterrainer, and E. Gornik, "Towards stimulated generation of coherent plasmons in nanostructures", J. of Appl. Phys., 85(7) pp. 3708-3712, 1999.

[21] B. S. Williams, "Terahertz quantum-cascade lasers," Nature Photonics 1, 517 (2007).

[22] J. Faist, F. Capasso, D.L. Sivco, C. Sirtori, A.L. Hutchinson, and A.Y. Cho, "Quantum cascade laser," Science **264**, 553 (1994).

[23] N. Krall and A. Trivelpiece, *Principles of Plasma Physics*, McGraw-Hill, New York (1973).

[24] S. Ichimaru, *Basic Principles of Plasma Physics-A Statistical Approach* W.A. Benjamin Inc. Massachusetts (1973).

[25] A.B. Mikhailovskii, *Theory of Plasma Instabilities*, Vol.1 Consultants Bureau, New York (1974).

[26] L. Chen, *Waves and Instabilities in Plasma* Edited by F. Cap, World Scientific, Singapore (1987).

[27] D. Pines and J. R. Schrieffer, "Collective behavior in solid-state plasmas". Phys. Rev., 124, p. 1387-1400, (1961).

[28] B. G. Martin, J. J. Quinn, and R. F. Wallis, "Theory of the effect of a dc current on surface polaritons in n-type silicon", Surf. Sci. **105**, 145 (1981).

[29] B.G. Martin and R.F. Wallis, "Theory of dispersion instabilities associated with surface electromagnetic waves in layered semiconductor media", Phys. Rev. B **32**, 3824 (1985).

[30] P. Hawrylak and J.J. Quinn, "Amplification of bulk and surface plasmons in semiconductor superlattices", Appl. Phys. Lett., 49, 280 (1986).

[31] P. Bakshi, J. Cen, and K. Kempa, "Amplification of surface modes in type II semiconductor superlattices", J. Appl. Phys. **64** (4), 2243 (1988).

[32] J. Cen, K. Kempa, and P. Bakshi, "Amplification of a new surface mode in the type-I semiconductor superlattice", Phys. Rev. B **38**, 10051 (1988).

[33] K. Kempa, J. Cen, and P. Bakshi "Current-driven plasma instabilities in superconductors", Phys. Rev. B **39**, 2852 (1989).

[34] P. Bakshi and K. Kempa, "Possible mechanism for plasma instabilities in solid state devices", Phys. Rev. B **40**, 3433 (1989).

[35] P. Bakshi, J. Cen, and K. Kempa, "Current driven instability in quantum wires", Solid State Comm. **76**, pp. 835-837 (1990).

[36] K. Kempa, P. Bakshi, J. Cen, and H. Xie, “Spontaneous generation of plasmons by ballistic electrons”, Phys. Rev. B **43**, 9273 (1991).

[37] J. Cen, K. Kempa, and P. Bakshi, “Amplification of plasma modes in semiconductor heterostructures”, Solid State Comm. **78**, pp. 433-437 (1991).

[38] H. Xie, K. Kempa, and P. Bakshi, “Growth rates of current-excited plasma waves in semiconductor layered systems”, J. Appl. Phys. **72**, 4767 (1992).

[39] K. Kempa, P. Bakshi, and H. Xie, “Current-driven plasma instabilities in modulated lower-dimensional semiconductor systems”, Phys. Rev. B **48**, 9158 (1993).

[40] D.C. Tsui, E. Gornik, and R.A. Logan, “Far infrared emission from plasma oscillations of Si inversion layers”, Solid State Comm. **35**, 875 (1980).

[41] K. Kempa, P. Bakshi, H. Xie, and W.L. Schaich, “Current-driven plasma instabilities in solid-state layered systems with a grating”, Phys. Rev. B **47**, 4532 (1993).

[42] M. Vossebuerger, H. G. Roskos, F. Wolter, C. Waschke, H. Kurz, K. Hirakawa, I. Wilke, and K. Yamanaka, “Radiative decay of optically excited coherent plasmons in a two-dimensional electron gas”, J. Opt. Soc. Am. B 13, 1045 (1996).

[43] P. Bakshi and K. Kempa, “Current-driven plasma instabilities in lower dimensional systems”, Superlattices and Microstructures 17, 363 (1995).

[44] K. Kempa, P. Bakshi, and E. Gornik, “Plasma instabilities in a steady-state nonequilibrium one-dimensional solid-state plasma of finite length”, Phys. Rev. B **54**, 8231 (1996).

[45] P. Bakshi and K. Kempa “Mathematical Signatures of Plasma Instabilities in Low- Dimensional Solid State Systems” in *Condensed Matter Theories*, J. Clark and P. Panat (eds.), NOVA Science Publishers, Vol. 12, 399 (1997)

[46] P. Bakshi, K. Kempa, C. G. Du, G. Feng, A. Scorupsky, G. Strasser, C. Rauch, K. Unterrainer, and E. Gornik, “Toward stimulated generation of coherent plasmons in nanostrucures”, J. Appl. Phys. 85, 3708 (1999).

[47] P. Bakshi, K. Kempa, A. Scorupsky, C. G. Du, G. Feng, R.Zobl, G. Strasser, C. Rauch, Ch. Pacher, K. Unterrainer, and E. Gornik, “Plasmon-based terahertz emission from quantum well structures”, Appl. Phys. Lett. 75, 1685 (1999).

[48] P. Bakshi, K. Kempa, “Inter-subband plasmon-emission-based THz lasers”, Physica E 7, pp. 63-68 (2000)

[49] G. Feng, “Transport and Response Properties of Non-Equilibrium Steady State Semiconductor Quantum Well Structures”, PhD dissertation (Boston College, 2002).

[50] P. Bakshi, K. Kempa, *Plasma Instabilities in Quantum Well Structures, in Condensed Matter Theories, Vol. 20*, Edited by J.W. Clark, R.M. Panoff, and H. Li, pp. 45-53 (2006)

[51] M. Coquelin, R. Zobl, G. Strasser, E. Gornik, V. Umansky, and M. Heiblum, “THz emission based on intersubband plasmon resonances,” AIP Conf. Proc., vol. CP 1199, pp. 145-146, (2010).

[52] M. Coquelin, G. Strasser, E. Gornik, P. Bakshi, and M. Ciftan, “Controlled generation of resonant electron-electron scattering induced current in quantum well structures” Appl. Phys. Letters **95** 172108, (2009).

## Chapter 2

# Semiconductor Physics

---

To understand the physics and operational characteristics of semiconductor devices, the fundamental principles must be first examined. This chapter reviews the fundamental semiconductor and solid state physics background necessary for understanding the work done in this thesis. While most of the concepts are quite general, the focus will be on the GaAs/$\mathrm{Al}_x\mathrm{Ga}_{1-x}\mathrm{As}$ and $\mathrm{In}_{1-x}\mathrm{Ga}_x\mathrm{As}$ material systems. Due to precision growth techniques, restriction in the motion of charge carriers occurs, which has a profound effect on the energy level structure and transport. As the relevant processes responsible for THz-related phenomena originate between *subbands* within the conduction band, the complexity of the valence band is ignored. One of the key ideas presented here is that many common heterostructures and devices in use are composed of simpler units such as quantum wells and potential barriers. In this chapter the motivation is presented for individually studying some of these basic building blocks. In later chapters (3-6) the full analytical work is laid out detailing how the approximate analytical expressions for the energies, wavefunctions, and tunneling transmission characteristics of these units are determined. Details on the formal topics discussed in this chapter can be found in Ashcroft and Mermin [1], Davies [2] and Kelly [3], for example, while the topic of QW's and associated physics can be found in Morrison [4], Gilmore [5], and Singh [6].

This chapter is broadly divided between the formal theoretical description of heterostructures and the description of the basics of quantum well heterostructures. The chapter is organized as follows: In Subsection 2.1 the atomic properties of the GaAs, AlGaAs and the InGaAs system are reviewed, including discussion of the lattice constant and the energy gap. Subsection 2.2 discusses the density of states, followed in subsection 2.3 with the Fermi-Dirac distribution. In Subsection 2.4 the important Fermi-Dirac integrals $\mathcal{F}_n$ are introduced, along with a new reasonably accurate two-part approximation to the $\mathcal{F}_{1/2}$ integral.

The next half of the chapter involves the description of subband formation, the two-dimensional electron gas (2DEG), and the Schrodinger-Poisson system which is encountered in the study of low-dimensional QW heterostructures.

## 2.1 **Heterostructure Formalism**

### 2.1.1 Bulk III-V Semiconductors

The properties of semiconductor materials in general, are unique in that they permit one to locally modify the energy-band structure of a given semiconductor compound, thereby controlling the motion of the charge through the structure. In order to understand how such local modification of band structure can affect this motion, an understanding of the energy bands of bulk semiconductors [3, 1, 7] is needed. As the heterostructures studied in this thesis are based on the III-V semiconductors a brief statement will be made concerning their properties. In binary III-V compounds, such as GaAs, InAs, AlAs, AlSb, and the ternary compound $\mathrm{Al}_x\mathrm{Ga}_{1-x}\mathrm{As}$, there are 8 outer electrons (3 from Ga and 5 from As) which contribute to the electronic properties. The most commonly occurring (compound) crystal structure based on these materials is the zinc-blende structure, shown in Figure 2.1.1. This is a face-centered cubic (fcc) lattice with a basis consisting of one atom of the third main group, and one of the fifth main group, attached to each lattice point. For instance, in the binary GaAs, each Ga atom is surrounded by four As atoms, and each As atom is surrounded by four Ga atoms in a tetrahedral geometry.

An important characteristic in the formation of semiconductor compounds is the *lattice constant*. The lattice constant is defined as the distance between the next-neighbor lattice points (not the actual distance between the atoms), and is in general dependent on pressure and temperature. This will determine the appropriate material to be grown on a given substrate. For a compound $A_xB_{1-x}$,

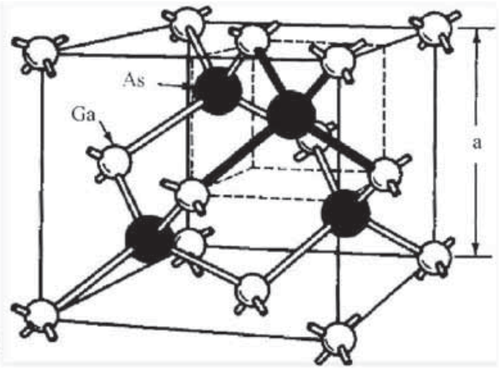

Figure 2.1: The zinc-blende crystal structure for GaAs, which consists of a face-centered structure with a 2-atom basis in a tetrahedral form. The constituent Ga and As atoms are labeled.

an effective lattice constant can be found from the expression, known as Vegard's Law [6, 8]

$$a^{alloy} = xa_A + (1-x)a_B \tag{2.1}$$

The lattice constant for GaAs [12] is $a = 5.65325$ Å (T=300 K) and for AlAs [9], $a = 5.66$ Å (T=300 K). For InAs [10] with an Indium concentration of 5% ($In_{0.05}Ga_{0.95}As$), the following expression can be used (units in Å)

$$a = 6.0583 - 0.4050x \tag{2.2}$$

and has the value $a = 6.0583$ Å (T=298.15 K). Figure 2.2 shows various binary compounds plotted as a function of the lattice constant $a$ and energy gap $E_{gap}$. This diagram is useful for determining which materials will provide high-quality crystal growth. The lattice-matching between AlAs and GaAs is evident from the nearly vertical line in Fig. 2.2 in the first shaded column, and indicates that the $Al_xGa_{1-x}As$ alloys would be relatively easy to prepare (evaporating AlAs onto a GaAs substrate) without strain energy build-up. The formation of hetero-interfaces between semiconductors with different lattice constants results in the appearance of a built-in strain which can be used as another controlling parameter for the band engineering. Such is the case of InAs grown on GaAs (resulting in InGaAs) in which the lattice constant is strongly dependent on the Indium concentration, Eq. (2.2), and so even appreciable amounts of Indium can result in the formation of large domains or clumps or

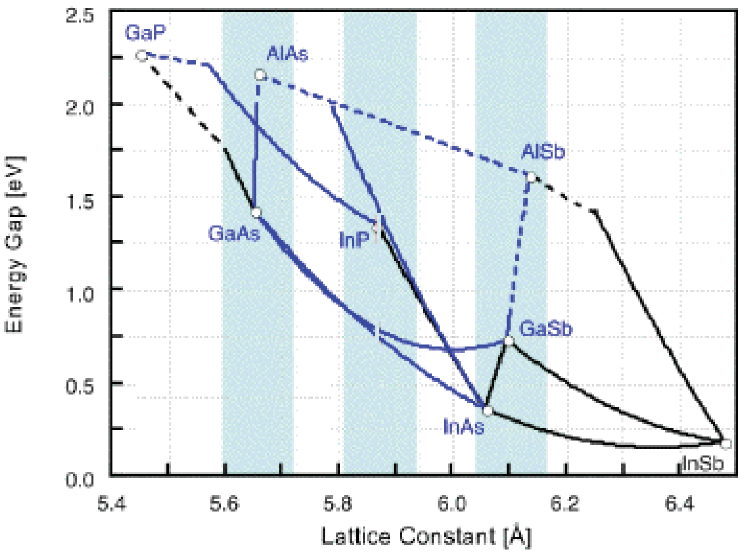

Figure 2.2: The lattice constant $a$ and energy gap of various semiconductors. Full lines indicate a direct-gap semiconductor and broken lines indicate an indirect-gap semiconductor. The (first) shaded column indicates by the vertical line that GaAs and AlAs are nearly lattice-matched.

material because of the lattice-mismatch. One rather extreme scenario is the formation of quantum dots which have atomic-like properties and are active area of research in itself [11]. However, the structures studied in this work have only a 5% Indium concentration with a minimal resulting lattice mismatch (7% between GaAs and InAs). Even so, the introduction of 5% Indium into the GaAs system essentially creates a 'pocket', or rather deep quantum well relative to the neighboring GaAs, drastically altering the potential profile and internal electrostatics of the device. The InGaAs system itself has proven to be an important material for high-frequency device applications due to high electron mobility and large intervalley separation in the conduction band [12].

The energy gap $E_{gap}$ is defined as the difference between the valence band $E_v$ (the highest occupied band) and the conduction band $E_c$ (the lowest empty energy band). Figure 2.4 illustrates that the conduction band edge for GaAs is found at either at the $\Gamma$ (0,0,0), L (1,1,1)$\pi/a$, or X (2,0,0)$\pi/a$ point, where $a$ is the lattice constant. However, the smallest energy difference is at the point $k = 0$, known as the $\Gamma$-point, and also as the Brillouin zone center, and therefore GaAs is characterized as a direct-gap material. This property has allowed GaAs to be used extensively in LED's and laser diodes for example. In contrast, the compound AlAs is an indirect-gap material, as shown in Figure 2.5, and therefore requires a momentum transfer for relaxation from the conduction band-edge to the valence band-edge.

The vertical axis in Fig. 2.2 shows the energy gap $E_g$ indicating that AlAs has a larger band gap than GaAs, a property crucial to the formation of quantum wells (discussed below), and has a temperature dependence given as [13]

$$E_g(eV) = 1.519 - 5.405x10^{-4}\frac{T^2}{T+204}, \qquad \text{for GaAs} \tag{2.3}$$

$$E_g(eV) = 2.239 - 6.04x10^{-4}\frac{T^2}{T+408}, \qquad \text{for AlAs} \tag{2.4}$$

The ternary alloy system $\mathrm{Al}_x\mathrm{Ga}_{1-x}\mathrm{As}$, with $0 \leq x \leq 1$, plays an important role in many state-of-the-art semiconductor devices. Alternating semiconductor layers of very high quality can be created easily with varying concentration $x$, with the most exploited characteristic being the bandstructure. Figure 2.3 summarizes the most important aspects of the alloy [3] for room temperature. At $x = 0$, GaAs has a room temperature bandgap of 1.42 eV. With increasing substitution of Ga with Al, the bandgap of the alloy rises. At $x = 1$, AlAs is an indirect-gap semiconductor with a minimum energy separation at the $X$ point. A crossover occurs from direct to indirect around $x = 0.45$, as seen in the figure. For the InGaAs alloy, the bandgap variation is from 0.39 eV to 1.5 eV [14, 10]. Fundamental materials parameters such as the band offset and energy gap for example, can be conveniently reported in tabular form for binary semiconductors, as in the review by Vurgaftman et al. [15]. Ternary alloys, however, have a degree of freedom in material composition, making tabular recording prohibitive. For any ternary material $\mathrm{A}_x\mathrm{B}_{1-x}\mathrm{C}$, composed proportionally of the two constituent binaries $(\mathrm{AC})_x$ and $(\mathrm{BC})_{1-x}$ , a range of values exists over the mole fraction $x$ for any generic material parameter $P$.

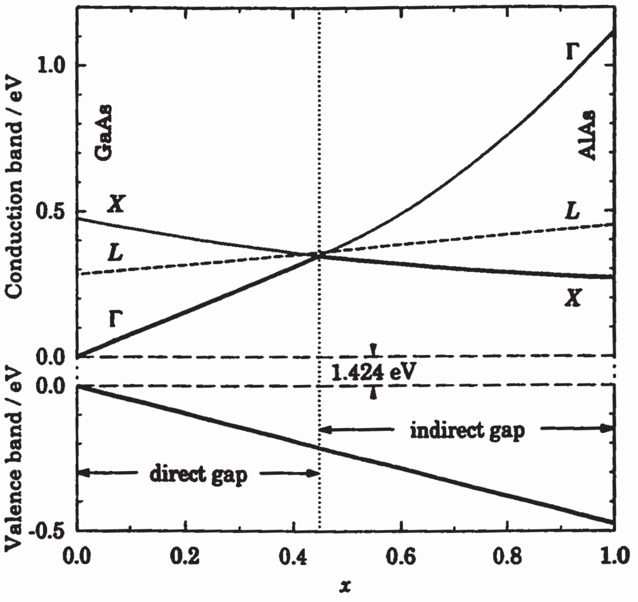

Figure 2.3: Energies of the three lowest conduction bands for the ternary compound $\mathrm{Al}_x\mathrm{Ga}_{1-x}\mathrm{As}$, as a function the mole concentration $x$. The labels $\Gamma$, $X$ and $L$ refer to the points of symmetry. The vertical dotted line marks the point $x = 0.45$ at which the compound transitions from direct-gap to indirect-gap.

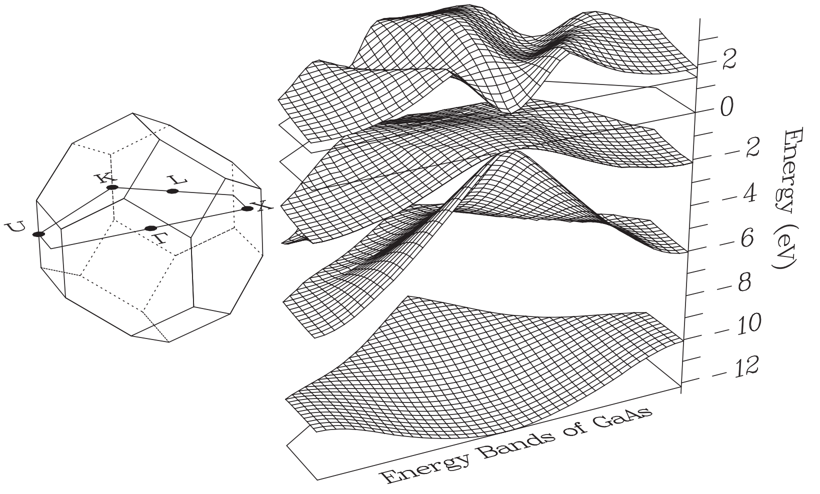

Figure 2.4: The energy band structure of GaAs. Also shown are the symmetry points.

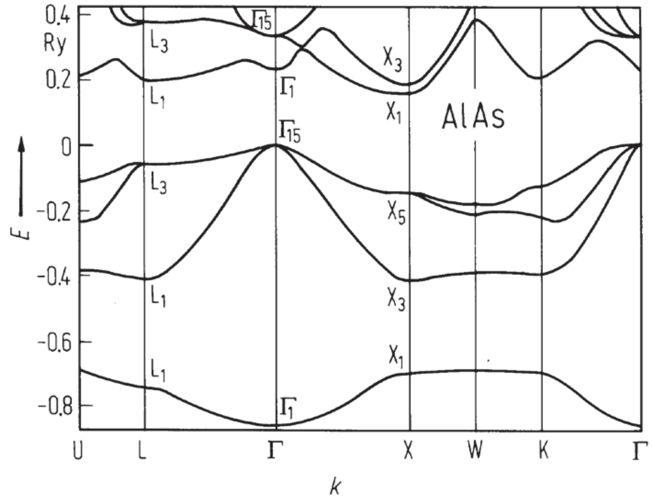

Figure 2.5: The energy band structure of AlAs, illustrating the smallest energy difference lies (indirectly) between the points $X_1$ and $\Gamma_{15}$.

### 2.1.1.1 Effective Mass

From the view of electrostatics, the crystal is made up of spherically symmetric ionic core potentials making it a much different and complex scenario than that of the vacuum. Therefore there are forces on the electrons complicating the motion. However, one can still use elements of the 'free-electron' gas model [1] to determine the effect on the electron. First, it can be shown that the group velocity $\mathbf{v}_g$ of the wavepacket associated with the electron is indeed equivalent to the (classical) velocity $\mathbf{v}_{classical}$ of the electron, as

$$\mathbf{v}_g = \frac{\partial \omega}{\partial k} = \frac{1}{\hbar}\frac{\partial E}{\partial k} = \frac{\hbar \mathbf{k}}{m} = \frac{\mathbf{p}}{m} = \mathbf{v}_{classical} \tag{2.5}$$

where the result from the free-electron model, $E(k) = E_c + (\hbar^2 k^2)/2m$, has been used. This parabolic dispersion relation between $E$ and $k$ is an important one, and is explained in more detail below in the following sections. Now for the moment considering an external force $F$ acting on the electron, given by

$$F = m\frac{d\mathbf{v}_g}{dt} = m\frac{1}{\hbar}\frac{\partial}{\partial t}\frac{\partial E}{\partial k} = m\frac{1}{\hbar}\frac{\partial^2 E}{\partial k^2}\frac{\partial k}{\partial t} \tag{2.6}$$

and the corresponding increase in momentum given as

$$F = \hbar\frac{\partial k}{\partial t} \tag{2.7}$$

Equating Eq. (2.6) and (2.7), gives

$$m\frac{1}{\hbar}\frac{\partial^2 E}{\partial k^2}\frac{\partial k}{\partial t} = \hbar\frac{\partial k}{\partial t} \qquad \Longrightarrow \qquad m \equiv m^* = \hbar^2\left(\frac{\partial^2 E}{\partial k^2}\right)^{-1} \tag{2.8}$$

That is, within the crystal structure the electron behaves as if it has a mass given by the above formula, and is referred to as the *effective mass*, denoted $m^*$. The effective mass does not represent the real mass of the electron, but takes into account the effect of the background potential due to the atoms in the crystal and is represented by the curvature of the dispersion (through the second derivative term). As long as the assumption of a parabolic dispersion $E(k)$ relation is valid, the effective mass will be a good approximation. In general $m^*$ depends on the direction of the resulting motion as the applied force $F$ and acceleration $a$ do not point in the same direction and is a tensor quantity. However for the present purposes it is assumed independent of a particular direction.

For the commonly used semiconductor GaAs, the effective mass is relatively small, with a value $m^* = 0.067m_e$, where $m_e$ is the free electron mass [16]. For $\text{In}_{0.05}\text{Ga}_{0.95}\text{As}$, with a 0.05% concentration, the effective mass is given by $m^* = 0.0648m_e$ [14].

### 2.1.2 The Density of States

---

The density of states (DOS) is a fundamental concept of condensed matter physics, and its role is also of importance in understanding the density of particles in a QW heterostructure, the transition probabilities, dielectric functions, and the absorption and emission characteristics, for example. Similarly, in a Fermi system, many properties are determined by the number of electrons which lie within a small energy interval of the Fermi surface. This in turn is determined by the density of states at the Fermi energy. Low-dimensional systems are thus preferred for use as optoelectronic devices because their DOS is larger at the bottom of the band [2], i.e., where the states are more densely packed.

In any realistic system there are an uncountable number of particles, energies, and corresponding states. It would be impossible to obtain complete information for a given system by solving the Schrodinger equation for each particle. It is more sensible to ask for any given energy, what the number of *available* states are. For this reason the counting of states must be made, so that the number of available states at each energy can be determined, allowing then the DOS to be established. This is basically a function that when multiplied by an interval of energy, provides the total concentration of available states in that energy range. The 'finiteness' of the density of states comes from the Pauli principle, which states that only two electrons of opposite spin can occupy one

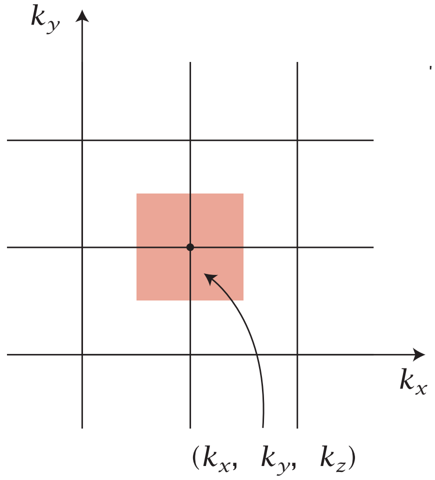

Figure 2.6: Volume (shaded) associated with a given state in k-space: a top view onto the $(k_x, k_y)$ plane

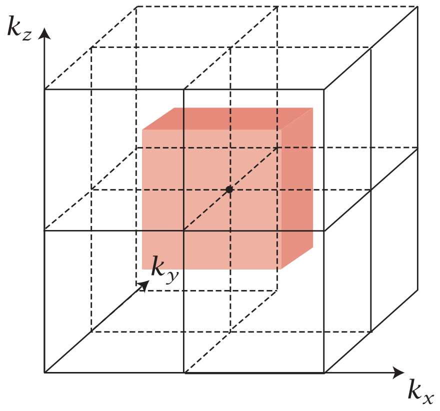

Figure 2.7: Volume (shaded) associated with a given state in k-space: three-dimensional side view.

volume element of *phase space*, which is defined as a six-dimensional space made up of real space and momentum space, such that the positions and momenta are distinguishable. Accordingly, the position-momentum uncertainty relation states

$$\Delta x \Delta y \Delta z \Delta p_x \Delta p_y \Delta p_z = (2\pi\hbar)^3, \tag{2.9}$$

which upon using the de Broglie relation, $p = \hbar k$, becomes

$$\Delta x \Delta y \Delta z \Delta k_x \Delta k_y \Delta k_z = (2\pi)^3 \quad \Longrightarrow \quad \Delta k_x \Delta k_y \Delta k_z = (2\pi)^3/V \tag{2.10}$$

where $V = \Delta x \Delta y \Delta z$ is the volume element in real space. The volume of **k**-space per allowed value of **k**-vector is $\Delta \mathbf{k} = (2\pi)^3/V$. Equivalently, one can consider the quantized wave vector components within a cube of side length $L$ (Fig. 2.7),

$$\Delta k_x = \frac{2\pi}{L}, \qquad \Delta k_y = \frac{2\pi}{L}, \qquad \Delta k_z = \frac{2\pi}{L}. \tag{2.11}$$

To find the contribution to the number of states per volume, sum over all possible **k**-states,

$$\frac{1}{V}\sum_{\mathbf{k}} \quad \Longrightarrow \quad \frac{2}{(2\pi)^3}\int d\mathbf{k} \quad \Longrightarrow \quad \frac{2}{(2\pi)^3}\int_{-\infty}^{\infty}\int_{-\infty}^{\infty}\int_{-\infty}^{\infty} dk_x dk_y dk_z, \tag{2.12}$$

where the limits $\Delta\mathbf{k} \rightarrow 0$ and $V \rightarrow \infty$ were taken, and the factor of 2 accounts for spin. For quasi-two dimensional problems such as QW heterostructures in which motion is restricted in two dimensions, the integral above is expressed as

$$\frac{2}{(2\pi)^2}\int_0^\infty\int_0^\infty dk_x dk_y \quad \Longrightarrow \quad \frac{2}{(2\pi)^2}\int_{disk} d\mathbf{k}, \tag{2.13}$$

which is an integration over the $k_x$- and $k_y$-directions. The integral over a disk in $\mathbf{k}$-space is simply $\pi k^2$. Therefore

$$\frac{2}{(2\pi)^2}\int_{disk} d\mathbf{k} \quad \Longrightarrow \quad \frac{2}{(2\pi)^2}(\pi k^2) \quad \Longrightarrow \quad \frac{m^* E}{\pi\hbar^2} \tag{2.14}$$

The energy $E$ is related to $k$ by the expression $k^2 = 2m^*E/\hbar^2$, and the 2D DOS $\mathcal{D}_{2D}$ is expressed as

$$\mathcal{D}_{2D} = \frac{m^*}{\pi\hbar^2} \tag{2.15}$$

Note that this is independent of the energy $E$, and forms a series of plateaus, or steps, as shown in Fig. 2.9.

It should be noted that for the above expression $\mathcal{D}(E)$ to be valid, the wave number range d$k$ should be small. However, d$k$ should still be large enough that there enough states in the range d$k$; otherwise $\mathcal{D}(E)$ cannot be approximated by a simple continuous function. If the spacing d$k$ truly becomes zero, $\mathcal{D}(E)$ turns into a distribution of infinite spikes. The $\mathcal{D}(E)$ will determine the total number of states per unit volume in an energy band between $E$ and $E + dE$, with the total number given by

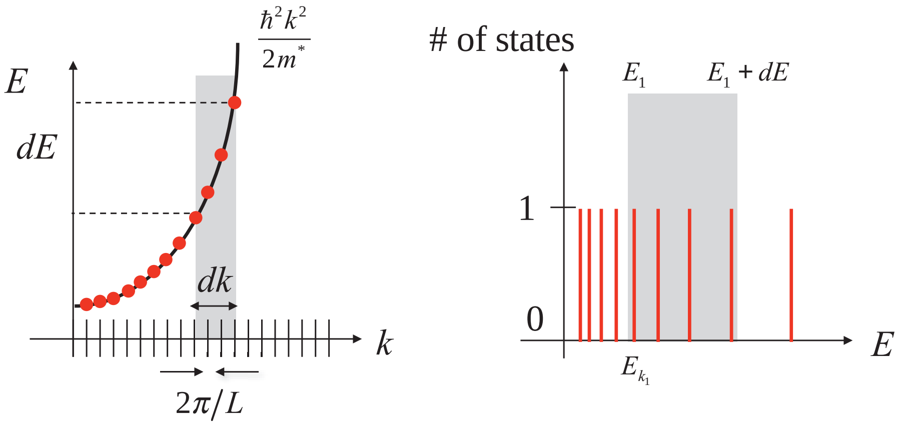

Figure 2.8: The parabolic energy dispersion, illustrating the density of states $\mathcal{D}(E)$, and how more closely packed the states are at the bottom of the band.

$$N = \int_{E}^{E+dE} \mathcal{D}(E)dE. \tag{2.16}$$

For a (1D) parabolic dispersion $E = E(k_z)$, the $k$-space length associated with an energy interval $dE$ is found from the slope of the curve, or $dE/dk_z$. As we can't view a purely 3D dispersion relation, we use surfaces of constant energy in $k$-space, and the idea of the separation of these surfaces is directly related to the $\Delta k$ and $\Delta E$ (see Fig. 2.9). Additionally, it is common to derive the DOS for 1D, 2D, and 3D, for the free electron, in which there are spherical constant energy surfaces, but in reality this is no longer the case, and so these surfaces become ellipsoids. Figure 2.8 shows the $\mathcal{D}(E)$ for different dimensions.

### 2.1.3 The Fermi-Dirac Distribution

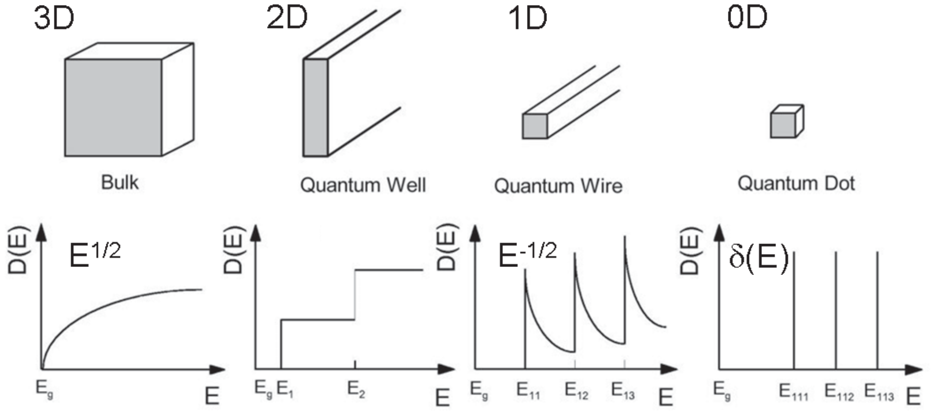

Figure 2.9: The density of states $\mathcal{D}(E)$ as a function of energy for different dimensions.

The DOS gives information regarding the energy levels of a system. The next step is to determine *how* the levels are filled. In contrast to classical Boltzmann statistics, the quantum mechanical characteristics of an electron gas are taken into account in Fermi-Dirac statistics. The quantum properties which are explicitly taken into account are the wave nature of electrons, and the Pauli exclusion principle. The statistical mechanics of ideal Fermi-Dirac systems is developed in terms of special functions defined by integrating the mean occupation number against powers of the single-particle energy. The average occupation (the probability of occupancy of energy levels) for electron states is determined by the Fermi-Dirac distribution function $f_{FD}(E, \mu, T)$. Fermions are half-integer spin particles, which obey the Pauli exclusion principle which postulates that only one fermion can occupy a single quantum state. As this restricts the number of particles which occupy a state to be either one or zero, $f_{FD}(E, \mu, T)$ may be interpreted as a probability of the state being occupied. The mean occupancy for a single-particle state with energy $E$ is

$$f_{FD}(E, \mu, T) = \frac{1}{1 + e^{-\beta(\mu - E)}}, \qquad \beta = 1/k_B T, \tag{2.17}$$

where the chemical potential $\mu$ is a function of density and temperature. Note that the above expression does indeed have the minimum and maximum values of zero and one, respectively: at $T = 0$, the argument of the exponential is $-\infty$ when $\epsilon < \mu$ or $+\infty$ when $\epsilon > \mu$ hence, the occupancy is unity for all states with $\epsilon$ below $\mu$ and is zero for all states with $\epsilon$ above $\mu$. Therefore, at absolute zero a Fermi gas is described as *completely degenerate* and is characterized by a frozen distribution in which all orbitals with $\epsilon < \epsilon_F$ are occupied and all orbitals with $\epsilon > \epsilon_F$ are vacant. In the limit of zero temperature,

$$f_{FD}(E, \mu, T = 0) = \Theta(\mu - E), \tag{2.18}$$

where the Heaviside step-function $\Theta(x) = 0$ if $x < 0$, and 1 if $x > 0$. For energies far above $\mu$, implying $(E - \mu) >> k_B T$, the exponential factor is large, and Eq. (2.17) becomes

$$f_{FD}(E, \mu, T) \approx exp\left(-\frac{E - \mu}{k_B T}\right), \tag{2.19}$$

which is known as the *Boltzmann distribution.*

### 2.1.4 The Fermi-Dirac Integrals $\mathcal{F}_n$

---

The equilibrium electron density $n_{3D}$ in a three-dimensional semiconductor with a parabolic conduction band can be found as follows. Starting with the **k**-space integration,

$$N = 2\sum_{\mathbf{k}} f(E_{\mathbf{k}}) = \frac{2L^3}{(2\pi)^3}\int d\mathbf{k} f(E_{\mathbf{k}}), \tag{2.20}$$

where the factor of 2 in front of the summation accounts for spin, and $f(E_{\mathbf{k}})$ is the Fermi-Dirac distribution function given by eq. (2.17). The number density is

$$n_{3D} = \frac{N}{L^3} = \frac{2L^3}{(2\pi)^3}\int d\mathbf{k} f(E_{\mathbf{k}}) \tag{2.21}$$

Changing the variables from $k$ to $E$, with $k^2 = 2m^* E/\hbar^2$ and $dk = \sqrt{2m^*/\hbar^2} dE/2\sqrt{E}$. The above expression for $n_{3D}$ becomes

$$n_{3D} = \frac{2}{(2\pi)^3}\int 4\pi k^2 dk f(E),$$

$$= \frac{8\pi}{(2\pi)^3} \int \left(\frac{2m}{\hbar^2}\right) E \left(\frac{2m}{\hbar^2}\right)^{1/2} \frac{dE}{2\sqrt{E}} f(E),$$

or

$$n_{3D} = \frac{(2m^*)^{3/2}}{2\pi^2\hbar^3} \int_0^\infty \frac{E^{1/2} dE}{1 + e^{\beta(E-\mu)}} \tag{2.22}$$

Letting $x = \beta E$, and $\rho = \beta\mu$, the above expression can be rewritten in terms of the Fermi-Dirac integral

$$\mathcal{F}_{1/2}(\rho) = \int_0^\infty \frac{x^{1/2} dx}{1 + e^{-\rho} e^x} \tag{2.23}$$

as

$$n_{3D} = \frac{(2m^* k_B T)^{3/2}}{2\pi^2\hbar^3} \mathcal{F}_{1/2}(\rho) \tag{2.24}$$

In general, the Fermi-Dirac integral of order $n$ is defined as [17, 18]

$$\mathcal{F}_n(\rho) = \int_0^\infty \frac{x^n dx}{1 + e^{-\rho} e^x}, \qquad 0 \leq \rho < \infty \tag{2.25}$$

and these functions appear in the study of Fermi systems, and consequently in semiconductor physics. The nomenclature was introduced in the 1920's by Pauli [19] and Sommerfeld [20] in the study of the degenerate electron gas in a metal, and the most useful orders are $\mathcal{F}_{1/2}$ for the number density, and $\mathcal{F}_{3/2}$ for the energy density. In general these integrals cannot be analytically expressed in terms of simpler functions (with the exception of $\mathcal{F}_0$ for the 2DEG). The well-known Sommerfeld expansion was developed to study electrons in metals, in which $\mu >> k_B T$ [1]. For the present purposes evaluation of the $n_{3D}$ for all $\mu$ and $T$ is needed, and therefore the Sommerfeld expansion will fail. For the case of $T = 0$ however, the expression in Eq. (2.22) becomes, (with $f_{FD} = 1$ up to $E = E_F^0$ and 0 thereafter)

$$n_{3D}(T=0) = \frac{(2m^*)^{3/2}}{2\pi^2\hbar^3}\int_0^{E_F^0} E^{1/2}dE = \frac{(2m^*)^{3/2}}{2\pi^2\hbar^3}\frac{2}{3}E^{3/2}$$

and

$$n_{3D}(T=0) = \frac{1}{3\pi^2}\left(\frac{2m^*E_F^0}{\hbar^2}\right)^{3/2} \tag{2.26}$$

where $\mu = E_F^0$ is the Fermi energy at $T = 0$. In the section below a *new analytical approximation* is developed for the integral expression $\mathcal{F}_{1/2}$, Eq. (2.23).

#### 2.1.4.1 Analytical Approximation of the Fermi-Dirac Integral $\mathcal{F}_{1/2}$

The $\mathcal{F}_{1/2}$ integral cannot be simplified any further, and therefore it is desirable to have a reasonably accurate analytical approximation valid for all $\mu$ and $k_BT$. There have been earlier approximations made for these integrals [17, 21], but the formulas are rather complicated. A simple two-part approximation is outlined here for the $\mathcal{F}_{1/2}$ integral, Eq. (2.23). Recognizing that for large $\rho$, the integral will grow as $\rho^{3/2}$, since it attains the value $(2/3)\rho^{3/2}$ given by Eq. (2.26) when $\rho \to \infty$, we obtain two different approximations for $\rho < 1$ and $\rho > 1$. This integral was evaluated numerically for many values of $\rho$, and very good numerical fits were found for the domains $\rho < 1$ ($\mu < k_BT$) and $\rho > 1$ ($\mu > k_BT$). For the domain in which $k_BT$ dominates, a quadratic fit to $\mathcal{F}_{1/2}$ vs. $\rho$ is given as

$$\mathcal{F}_{1/2}^{approx}(\rho < 1) = P_2(\rho) \equiv [0.67804 + 0.52785\rho + 0.19031\rho^2] \tag{2.27}$$

For the domain in which $\mu$ is dominant, apart from the energy scaling factor $\rho^{3/2}$, a cubic fit to $\mathcal{F}_{1/2}$ in the variable $1/\rho$ is given by

$$\mathcal{F}_{1/2}^{approx}(\rho > 1) = \rho^{3/2} P_3(1/\rho) \equiv \rho^{3/2}[0.66723 - 0.03322(1/\rho) + 1.1034(1/\rho)^2 - 0.34264(1/\rho)^3] \quad (2.28)$$

The 3D density $n_{3D}$ is now written from Eq. (2.24) as

$$n_{3D} = \frac{(2m^* k_B T)^{3/2}}{2\pi^2 \hbar^3} \mathcal{F}_{1/2}^{approx}(\rho) \quad (2.29)$$

where

$$\mathcal{F}_{1/2}^{approx}(\rho) = \begin{cases} \rho^{3/2} P_3(1/\rho), & \rho > 1 \\ P_2(\rho), & \rho < 1 \end{cases} \quad (2.30)$$

Plots of $P_2(\rho)$ and $P_3(1/rho)$ are compared with their exact numerical values obtained from $\mathcal{F}_{1/2}$, as shown in Figure 2.10 (a) and (b). Fig. 2.11 gives the percentage error for (a) $P_2(\rho)$, and (b) $P_3(1/rho)$. The maximum error incurred for $P_2(\rho)$ is 0.15%, and the maximum percent error for $P_3(1/rho)$ is about 1.7%. These approximations will be used to calculate the continnum density population for the structures studied in this thesis.

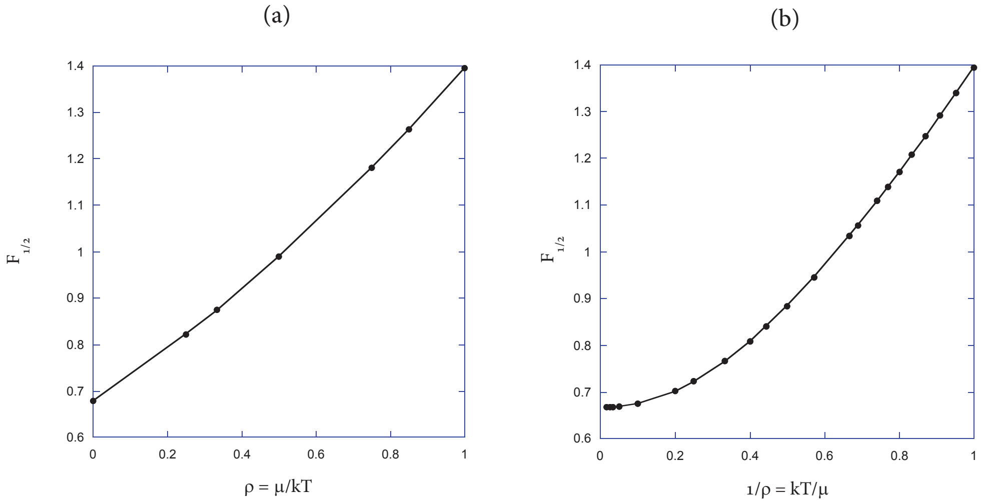

Figure 2.10: Comparison of the two-part approximation of $\mathcal{F}_{1/2}$ (solid lines) and its numerical evaluation (solid circles). (a) In terms of $\rho = \mu/kT$ (a) a quadratic fit as a function of $\rho$ for the $k_B T$-dominated range, $\rho < 1$ and (b) a cubic fit vs. $1/\rho$ for the domain in which $\mu$ dominates, $\rho > 1$.

### 2.1.5 2DEG Charge Density

---

The charge density $n_{2D}$ for the 2DEG is given by

$$n_{2D} = \frac{m^*}{\pi\hbar^2}\int_{E_i}^{\infty}\frac{dE}{1+e^{-\beta(\mu-E)}} \tag{2.31}$$

where $E_i$ is the $i$-th subband energy. At zero temperature ($T = 0K$), the Fermi distribution is a step potential at $\mu = E_F^0$, and

$$n_{2D} = \frac{m^*}{\pi\hbar^2}(E_F^0 - E_i)\Theta(E_F^0 - E_i) \tag{2.32}$$

For non-zero temperature ($T \neq 0$), the full integration over $f_{FD}$ remains, with $f_{FD}(E, \mu, T)$ given by Eq. (2.17). That is,

$$n_{2D} = \frac{m^*}{\pi\hbar^2}\int_{E_i}^{\infty}\frac{dE}{1+e^{-\beta(\mu-E)}}. \tag{2.33}$$

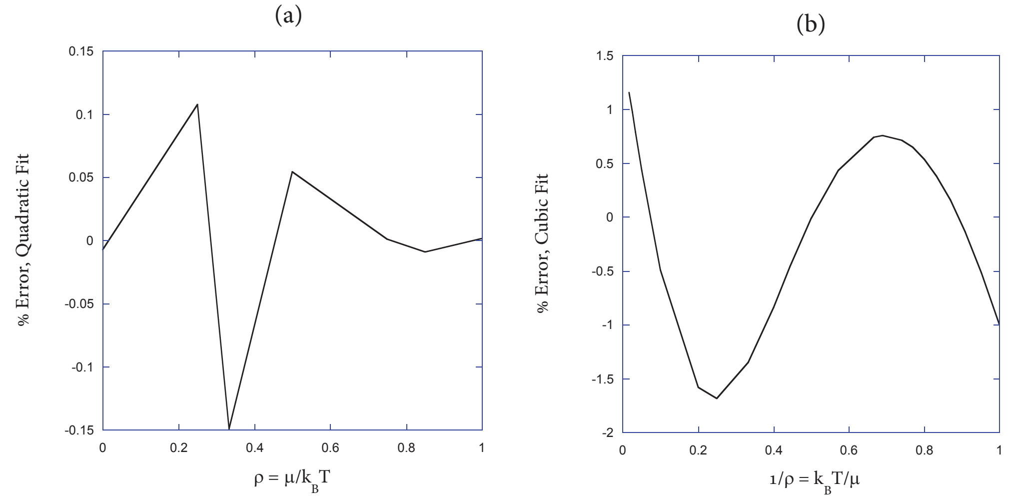

Figure 2.11: (a) Plot of the percent error for the quadratic fit to $\mathcal{F}_{1/2}$ for $\rho < 1$, and (b) the cubic fit to $\mathcal{F}_{1/2}$ for $\rho > 1$. Solid lines are exact values, and the points indicate the polynomial fit values.

This integral is evaluated analytically by noting it is of the form

$$\int \frac{dx}{1+e^{x}} = -\ln(1+e^{-x}) + C, \quad x \equiv -\beta(\mu - E) \tag{2.34}$$

where $C$ is an integration constant. Upon substitution the integral becomes

$$n_{2D} = \frac{m^*}{\pi\hbar^2\beta}\int_{-\beta(\mu-E_i)}^{\infty}\frac{dx}{1+e^{x}}$$

which leads to

$$n_{2D} = \frac{m^*}{\pi\hbar^2}kT\ln\left(1+e^{\beta(\mu-E_i)}\right). \tag{2.35}$$

This is the expression for the charge density in the 2DEG for finite $T$.

## 2.2 **Quantum Well Heterostructures**

The following four subsections group together the description of heterostructure and quantum well theory, including subband formation, the 2DEG, and the solution of the Schrodinger-Poisson system. The last section of this chapter outlines the motivation for the analytical study of various 1D quantum wells commonly occurring in semiconductor heterostructures and devices, and comprises Chapters 3 to 6 (of Part I).

### 2.2.1 Subbands

Heterostructures are created by growing alternating layers of different band gap semiconductors, such as GaAs and AlGaAs (the focus of this work), creating a stack-like structure (Fig. 2.13). Bandstructure modification and tailoring is accomplished through epitaxial techniques, in which atoms are deposited (in vapor phase) onto a substrate, and metal organic chemical vapor deposition (MOCVD), for example. The Molecular-Beam-Epitaxial (MBE) technique [13, 2, 22], which was used to grow the samples studied in this thesis, can produce discontinuities in the potential profile on the order of a monolayer ($\sim 3$ Å), allowing for a high level of control in creating barriers and wells, in which charge carriers will experience *confinement.* Since the bandgap of GaAs is smaller than that of $\mathrm{Al}_x\mathrm{Ga}_{l-x}\mathrm{As}$, the ensuing band gap profile of the new ternary compound gives rise to effective potential wells and potential barriers for the charge carriers. There are three main types of heterostructures that form, depending on the relative location of the band offset for each material, and are presented in Figure 2.12. The most widely used type of heterostructures is type I in which a narrow-gap material (GaAs) is grown between two larger-gap materials (AlGaAs) (see Figure 2.12(a).

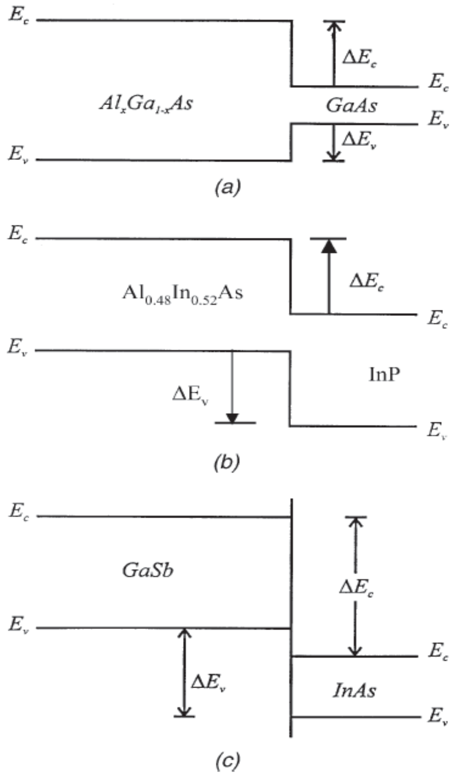

Figure 2.12: The main types of heterostructures: (a)- type I; (b)- type II; (c)- type III, for typical semiconductor materials. The conduction and valence band are given by $E_c$ and $E_v$ respectively.

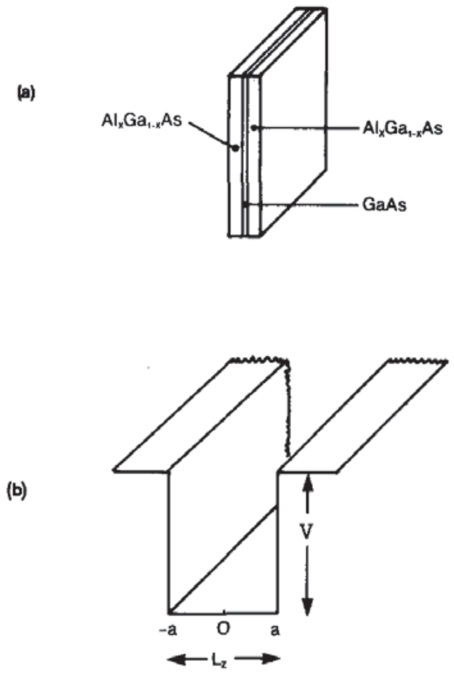

Figure 2.13: Schematic illustration of an $\mathrm{Al}_x\mathrm{Ga}_{1-x}$As-GaAs-$\mathrm{Al}_x\mathrm{Ga}_{1-x}$As quantum well heterostructure, in which a narrow-band-gap active GaAs layer is sandwiched between two thick wider-gap $\mathrm{Al}_x\mathrm{Ga}_{1-x}$As layers.

It should be noted that for the case of a single heterointerface, confinement may also occur due to the formation of a wedge-type potential profile, as shown in Fig. 2.14. This is known as the *two-dimensional electron gas* (2DEG), and is the basis for many of the early heterostructure device designs [3, 23]. In the case of two or more interfaces (heterojunctions) the potential profile is generally referred to as a heterostructure, and roughly speaking, if the middle layer is sufficiently thin for *quantum properties* to be exhibited, then such a band alignment is termed a *quantum well* (QW). The potential barrier height of the QW is determined by the Aluminum alloy concentration $x$ of the surrounding material (in this case $\mathrm{Al}_x\mathrm{Ga}_{l-x}\mathrm{As}$). These quantum wells perturb the crystal periodicity in the growth direction, here taken as the $z$-direction. Confinement occurs if the de Broglie wavelength $\lambda = h/p$ of the electron, or the spatial extent of the wavepacket describing the electron is on the order of the separation between the two interfaces, say $L_z$. That is, if the spatial dimensions are large, $L_z << L_x, L_y$, then the allowed energies form a continuum (for the $x$ and $y$ directions) and a discrete distribution for the $z$-direction.

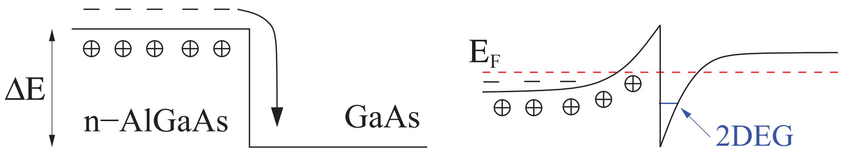

Figure 2.14: Formation of a 2DEG for a GaAs/AlGaAs heterojunction. The conduction band is shown on the left, just after the two materials are brought into contact with one another. AlGaAs has a wider bandgap than GaAs and the conduction band edges are offset by an amount $\Delta E$. Electrons from the donors in the n-doped AlGaAs move across the junction to lower energy states in GaAs, leaving charged donor ions behind. The combination of the band edge offset with the potential due to donor ions produces the band edge shown on the right. A narrow *triangular well* is formed at the interface and it is here that the 2DEG is located.

The assumption that $L_z << L_x, L_y$ (for the QW heterostructures presently considered) means that, to a first approximation the separation $H_{total} = H_{xy} + H_z$ can be made, where $H_{xy}$ is the single-particle Hamiltonian for the 2DEG, and $H_z$ is the Hamiltonian for the one-dimensional finite QW. This separation essentially means that the potential can be written as a sum of independent functions $V = V(x) + V(y) + V(z)$, where $V(x) = V(y) = 0$, and the eigenfunction of the system to be written as a product $\psi(x, y, z) = \psi_x(x)\psi_y(y)\psi_z(z)$. Formally, the electronic structure is represented by the one-dimensional Schrodinger equation

$$-\frac{\hbar^2}{2m^*}\frac{\partial^2}{\partial z^2}\psi(z) + V(z)\psi(z) = E\psi(z) \tag{2.36}$$

where a constant effective mass $m^*$ is assumed across the heterojunctions. Two important points must be made. The effective mass approximation is a valid description of bulk materials, and the heterojunctions between different materials can be described by a material potential derived from the difference in the bandgaps. Considering the first point, a realistic account of the electronic properties of heterostructures would be the variation of the effective mass across a heterojunction. This is achieved with the original Schrodinger equation, Eq. (2.36), applied to each region, with the boundary conditions for matching solutions at the heterojunctions between the regions of different effective mass [24]. The following expression then replaces Eq. (2.36) as,

$$-\frac{\hbar^2}{2}\frac{\partial}{\partial z}\frac{1}{m^*(z)}\frac{\partial}{\partial z}\psi(z) + V(z)\psi(z) = E\psi(z) \tag{2.37}$$

This is the form of the Schrodinger equation which accounts for the effective mass mismatch across the heterojunctions. The order in which the $1/m^*(z)$ term appears arises from the order in which the (Hermitian) kinetic energy operators act upon the eigenvectors [24]. Since the confining potential $V(z)$ is only in the $z$-direction, it only appears in one of the equations, with solutions which are discrete states of energy $E_z = E_n$, $n$ labeling the states. For the other two directions, the solutions are traveling waves of the form $\exp(ik_x x)$, $\exp(ik_y y)$, with a continuous range of allowed energies. The total energy of an electron of mass $m^*$, with an in-plane momentum $k_{x,y}$ is given by

$$E(k_x, k_y, n) = (\hbar^2 k_{x,y}^2)/(2m^*) + E_n \tag{2.38}$$

where $n$ indexes a set of subbands. New electron energy states $\psi(z)$ are now located in these quantum wells, confined in the growth direction $z$ but still free in the plane of the well, with the result that

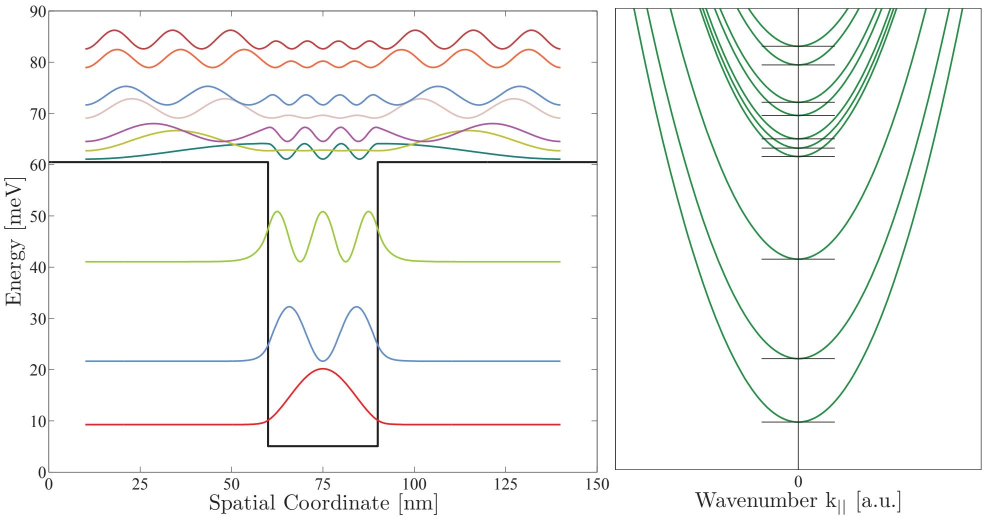

Figure 2.15: An arbitrary finite square quantum well, showing the relative placement of the subbands, and the corresponding parabolic dispersion $E(k)$ curves discussed in Sec. 2.2. The levels above the quantum well barriers are quasibound states.

the conduction band is quantized into *subbands*. The subbands are parabolic as the electrons are not confined in the plane of the well. The particle has one less degree of freedom, as the momentum is restricted to two dimensions, thus the term 2DEG. The utility of the preceding analysis is that a rather complex system has been reduced to two relatively simple problems: the 1D finite QW problem, and that of the band structure (of GaAs for example), for which information is readily available [13]. With the total energy defined, the next step is to consider particular 1D potentials $V(z)$. However, before this is done, the important concept of doping and it's consequence is outlined.

### 2.2.2 The Hartree Potential

---

QW heterostructures rely on the conduction of electrons (and holes), in which to carry a current and lead to dynamic, device-like behavior. *Remote* or *modulation doping* introduces free charges at a large distance from the "active" QW region(s) of the device in order to fulfill this requirement, but also to reduce the scattering from impurities. Heterostructures with remote doping have attracted much attention because of their advantages, such as high electron mobility and electron drift velocity due to reduced scattering on ionized impurities, intense photoluminescence, low noise, etc. [25]. With these dopants present, the heterostructure will "equilibrate" itself, redistributing the charge in the system in order to balance the charges (creating dipolar charge distributions), leading to internal electric fields. Figure 2.16 illustrates this situation, in which carriers have migrated to another region, creating a much different potential profile than the undoped heterostructure. The modification of the band structure is often referred to as 'band bending' and this feature is often used as a qualitative explanation for localization of charge. Everything so far has been discussed in terms of single charge carriers. However, realistically (especially for devices) large numbers of electrons can be present in the conduction band, and the effect of this additional carrier density must be taken into account. The electrostatics of the system are then analyzed to determine if there is a significant additional potential on top of the usual band-edge potential.

#### 2.2.2.1 Self-Consistent Schrodinger-Poisson Solution

Once the band-edge potential profile is known, as well as the particular parameters for a given material, the Schrodinger equation can be solved for the energies and wavefunctions. Modulation-doped heterostructures introduce extra charge into the system, and must be considered in the eigenvalue

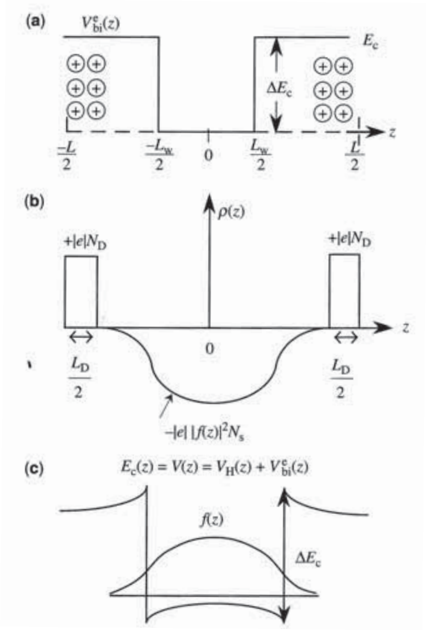

Figure 2.16: (a) The built-in potential of a modulation doped quantum well, (b) the charge density, and (c) the screened electron potential energy profile. $V_{bi}$ is the built-in potential, $E_c$ is the conduction band discontinuity, $L_w$ is the width of the well, and $V_H$ is the Hatree potential.

determination. The fixed and free charges (ionized impurities and free electrons, respectively) that make up a charge distribution $\rho$ add a perturbation to the potential profile. Every electron moves in an effective potential known as the *Hartree* potential [26], due to the average electron density distribution. The total potential is $V(z) = V_H(z) + V_c(z)$, where $V_c(z)$ and the Schrodinger equation,

$$\left[-\frac{\hbar^2}{2m^*}\frac{d^2}{dz^2} + V(z)\right]\psi_i(z) = E_i\psi_i(z) \tag{2.39}$$

where $E_i$ is the energy of the $i$-th subband, and $\psi_i(z)$ is the wavefunction. The Hartree potential satifies the Poisson equation,

$$\frac{d^2}{dz^2}V_H = -\frac{4\pi e^2}{\epsilon}[n(z) - N_d] \tag{2.40}$$

where $n(z)$ is the electron charge density and $N_d$ is the ionized donor density. As the electrons interact with the ionized donors, the Schrdinger and Poisson equations have to be solved self-consistently. In the first step, the Schrdinger equation is solved for an unperturbed potential, then the population in each state is calculated which enables a calculation of a new potential profile from the Poisson equation. This new potential is then used in the next iteration continuing until the energy levels has converged to a steady (predetermined) value. The *self-consistent* result is achieved by numerical solution of the Schrodinger-Poisson system of equations [8].

### 2.2.3 Quantum Well Variations

---

Thus far the discussion of quantum well physics has been on the general conditions under which confinement may occur. One goal of this work is to provide a thorough analytical description of some of the basic 'units' that make up real heterostructures and possible devices. Furthermore, with these analytical expressions, the response of system can be calculated, possibly providing a comprehensive analytical approach to not only the bound state problem, but to the transport and response characteristics. In this section the focus is on establishing the fact that most, if not all heterostructures can be viewed as composites of simpler units, such as the finite symmetric and asymmetric QW's, the triangular QW, and the double QW. These examples do not make up an exhaustive list, but provide the impetus for an analytical study of some of the more common bound state problems.

#### 2.2.3.1 The H656 Heterostructure

To motivate the analytical work that makes up Part I of this thesis, an example of a QW heterostructure studied in this thesis is shown in Fig. 2.17. This is a 3D schematic of the H656 structure in which different colors are assigned to different layers, which represent the distinct regions such as the drift region, quantum well active region, and the resonant tunneling filter. Figure 2.18 contains a 'flat-band' potential profile view (left-hand side), and the self-consistent potential profile (right-hand side). The self-consistent band profile was addressed in the previous subsection, and serves the purpose of illustrating how the potetnial of the structure changes due to doping (see Fig. 2.16). This has a profound effect as there now exists a substantial *triangular barrier/well* in the structure. This particular structure is based on the GaAs/Al$_x$Ga$_{1-x}$As and In$_{1-y}$Ga$_y$As system, where $x$ is the

Aluminum concentration, and $y$ is the Indium concentration. The barrier heights are determined by $x$, and the depth of the well region by $y$. Note that this structure contains an RTD, a quantum well, a trinagular barrier, and a triangular potential well. In the chapters 3-6, each of these units is studied independently.

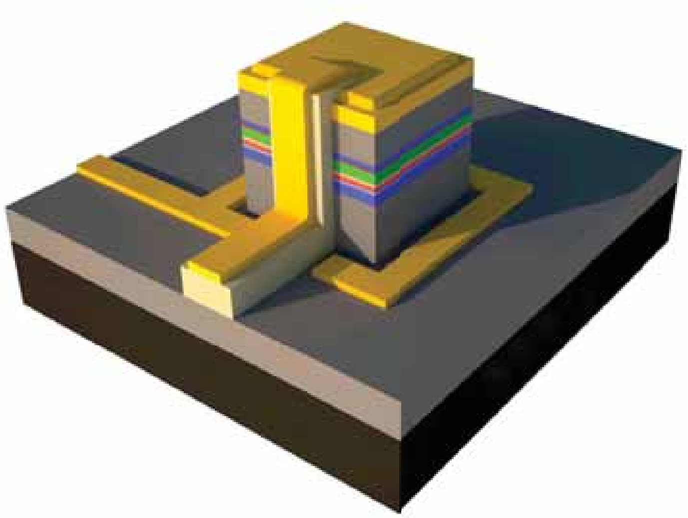

Figure 2.17: Schematic of the H656 heterostructure. The QW active region is contained in the center if the stack-like structure (colored orange). The drift regions, barriers, and RTD are also colored. The dark grey regions bordering the colored center area are the heavily doped contact layers. Note that the relative size of the different colored regions is not to scale, e.g., the height of the tower.

### 2.2.3.2 The Triangular Quantum Well

The triangular quantum well problem is commonly encountered in semiconductor physics, arising from charges that accumulate at the heterojunction between two different semiconductors. The 'wedge' potential profile was observed early on in the development of the metal-oxide-semiconductor (MOS) transistors, for example, when the heterojunction was first established. Likewise, as mentioned above for the case of the H656 structure, triangular-shaped well-regions can also exist. Figures 2.19 and 2.18 illustrate some of these scenarios in which the triangular potential well can occur.

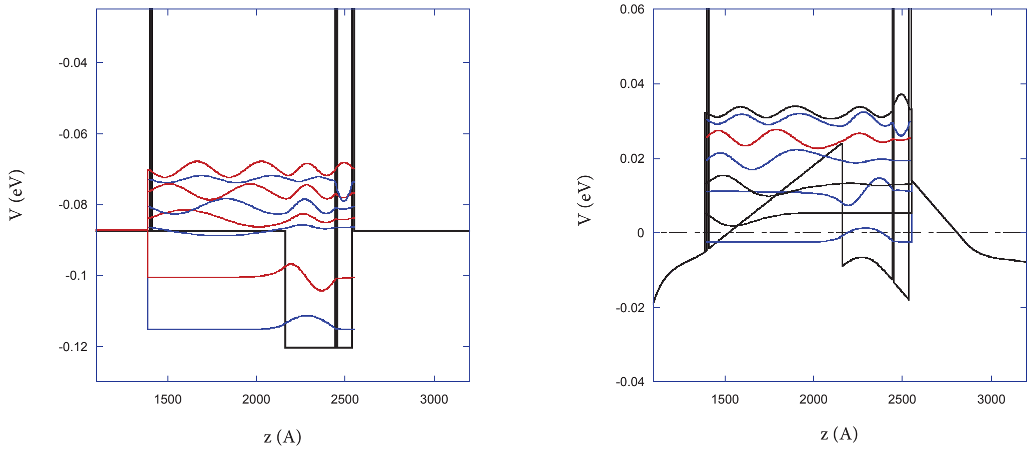

Figure 2.18: The potential profile $V(z)$ of a structure studied in this thesis, showing the 'individual' components. These include an RTD, a deep QW, a triangular barrier, and a triangular well. Additionally, the left-hand side figure shows the initial 'flat-band' potential profile, and the resulting self-consistent profile. The self-consistent wavefunctions obtained numerically (for both examples) are shown also.

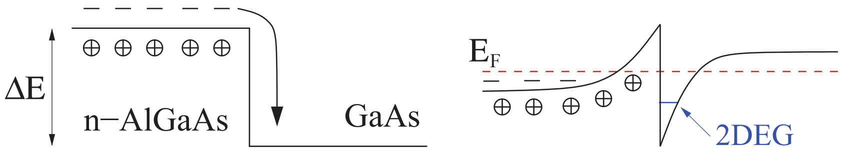

Figure 2.19: Example of a two-dimensional electron gas formed at a modulation-doped heterojunction, which takes on a triangular well shape. The band bending is caused by charge transfer across the interface when the materials are joined to produce a uniform Fermi level.

# Bibliography

[1] N.W. Ashcroft, and N.D. Mermin, *Solid State Physics* (Holt, Rinehart, Winston, New York 1976).

[2] J.D. Davies, *The Physics of Low-Dimensional Semiconductors* (Cambridge University Press, 1998).

[3] M.J. Kelly, *Low-Dimensional Semiconductors: Materials, Physics, Technology, Devices* (Oxford University Press, 1995).

[4] M. A. Morrison, *Understanding Quantum Physics* (Prentice-Hall, Englewood Cliffs, NJ, 1990).

[5] R. Gilmore, *Elementary Quantum Mechanics In One Dimension* (Johns Hopkins University Press, Baltimore, MD, 2004).

[6] J. Singh, *Physics of Semiconductors and Their Heterostructures* pp. 179-211 (McGraw-Hill, 1993).

[7] C. Kittel, *Introduction to Solid State Physics (6th Ed.)* (Wiley, New York 1986).

[8] G. Feng "Transport and Response Properties of Non-Equilibrium Steady State Semiconductor Quantum Well Structures", PhD dissertation (Boston College, 2002).

[9] "GaAs, AlAs, and $\mathrm{Ga}_x\mathrm{Al}_{1-x}\mathrm{As}$: material parameters for use in research and device applications" J. Appl. Phys. **85** (1985).

[10] P. Bhattacharya, "Properties of lattice-matched and strained Indium Gallium Arsenide", INSPEC, (1993).

[11] M. Grundmann, O. Stier, and D. Bimberg, "InAs/GaAs pyramidal quantum dots: Strain distribution, optical phonon's, and electronic structure", Phys. Rev. B **52**, 11969-11981, (1995).

[12] M.A. Shahid, S. Mahajan, D.E. Laughlin, H.M. Cox, "Atomic Ordering in $\mathrm{Ga}_{0.47}\mathrm{In}_{0.53}\mathrm{As}$ and $\mathrm{Ga}_x\mathrm{In}_{1-x}\mathrm{As}_y\mathrm{P}_y$ Alloy Semiconductors" Phys. Rev. Lett. **58** (24), 2567 (1987).

[13] J. Singh, *Semiconductor Devices: An Introduction* (McGraw-Hill, 1993).

[14] A. Pfinier, "Current Transport in InGaAs Quantum Wells", M.S. dissertation (Technical University Vienna, 2011).

[15] I. Vurgaftman, J.R. Meyer, L.R. Ram-Mohan, "Band parameters for III-V compound semiconductors and their alloys," J. Appl. Phys. **89** (11), 5815-5875 (2001).

[16] M. Levinstein, S. Rumyantsev, M. Shur, *Handbook Series an Semiconductor Parameters Vol.1* (World Scientific, 1996).

[17] X. Aymerich-Humet, F. Serra-Mestres, and J. Millan, "An analytical approximation for the Fermi-Dirac integral $\mathcal{F}_{3/2}$", Solid State Elect. **24**, pp. 981-982 (1981).

[18] W.D. Kraeft, D. Kremp, W. Ebeling, G. Röpke, *Quantum Statistics of Charged Particle Systems* (Akademie-Verlag Berlin, 1986).

[19] W. Pauli, Z. Physik. **41** 81 (1927).

[20] A. Sommerfeld, Z. Physik. **47** 1 (1928).

[21] D. Bednarczyk, and J. Bednarczyk, "The approximation of the Fermi-Dirac integral $\mathcal{F}_{1/2}(\eta)$," Phys. Lett. **64A**, 409 (1978).

[22] M. Coquelin, "Resonant plasmon and subband excitation in heterostructures", PhD dissertation (Technical University Vienna, 2008).

[23] C. Weisbuch, and B. Vinter, *Quantum Semiconductor Structures* (Academic Press, Boston, 1991).

[24] P. Harrison, *Quantum Wells, Wires, and Dots* (Wiley, 2009)

[25] Z.I. Alferov, "The history and future of semiconductor heterostructures", Semiconductors, vol. 32, no. 1, pp. 1-14, (1998).

[26] D.R. Hartree, Proc. Cambridge Philos. Soc. **24**, 89 (1928).

[27] R. Tsu, *Superlattice to Nanoeletronics* (Elsevier, 2011).

[28] A.F. Iivinsh, N.A. Goryunova, J.V. Ozolinsh, G.K. Averkieva, Sov. Phys. Cryst. **7** 691 (1963).

[29] R.T. Weidner, R.L. Sells, *Elementary Modern Physics* (Allyn and Bacon, Boston, 1980)

## Chapter 3

# Quantum Wells

---

This chapter contains the analysis of four bound state systems: the finite symmetric quantum well (SQW), the finite asymmetric QW (ASQW), the triangular/wedge well (TQW), and the finite symmetric double QW (DSQW). First, the infinite square well (ISW) is presented as it is an idealized exactly solvable model in which to begin the study of QW systems. More importantly however, the ISW result will be used in the sections that follow, where for the finite symmetric QW, a mapping to an equivalent, wider corresponding ISW is obtained. This result is then extended to the case of the finite asymmetric QW. The problem of the triangular well, or wedge well is then studied, including the infinite triangular well (ITW), and its finite height variations. After the QW systems are presented, the problem of tunneling transmission and barrier physics is studied in Chapters 4 and 5. Gaining a working knowledge and strategies to deal with the finite well problem is important as the quantum well can be viewed as a basic unit through which more complex structures can be "built". In general, the underlying philosophy here, is in establishing thorough and reasonably accurate *analytic* results for many of the so-called building blocks of more complicated quantum well heterostructures.

## 3.1 Infinite Square Well (ISW)

---

The infinitely deep one-dimensional potential well represents a simple, artificial, yet important system in quantum well physics. As shown in Appendix A for Quantum Wells, Section A.1, for a particle in an infinitely confining potential well (see Fig. 3.1),

$$V(z) = \begin{cases} 0, & \text{if } 0 \leq z \leq L; \\ \infty, & \text{otherwise.} \end{cases}$$

the energies are

$$E_{n,\infty} = \frac{(n\pi\hbar)^2}{2m^* L^2}, \qquad n = 1, 2, .. \tag{3.1}$$

and normalized eigenfunctions are given by

$$\psi_n(z) = \sqrt{\frac{2}{L}} \sin\left(\frac{n\pi z}{L}\right) \qquad n = 1, 2, .. \tag{3.2}$$

## 3.2 Finite Symmetric Quantum Well (SQW)

---

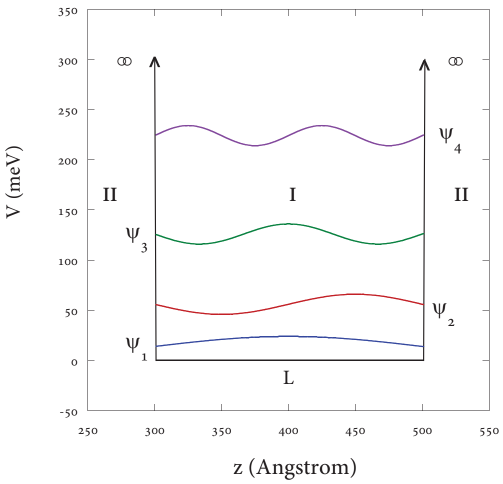

Figure 3.1: The infinite square well for well width $L = 200$ Å, showing the first four wavefunctions.

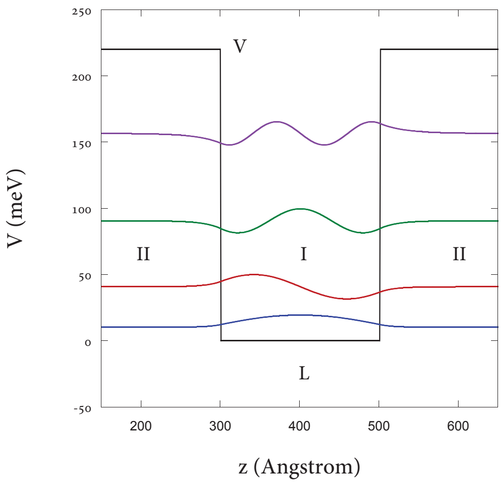

Figure 3.2: The finite symmetric well for well width $L = 200$ Å, showing the first four wavefunctions.

In contrast to the ISW, finite symmetric quantum well (SQW) represents a more realistic situation, but is also part of the standard introduction to bound states in elementary quantum mechanics. Thorough details on the subject of the "particle in the box" are given in many texts [1-5]. An important, as well as interesting feature of this problem that one can experience is the number of different approaches and approximations that are employed [6-20]. In this section an exact, simple closed-form algebraic expression for the bound-state energy levels of the SQW, in terms of an effective length is provided. The *effective length* is used to express each finite well energy in terms of a corresponding wider ISW. Methods to obtain a very good closed-form approximation for the effective length in terms of the given physical parameters of any finite quantum well are given. Next, an error analysis is presented, which illustrates the advantage of our approach compared with previous work. The wave functions are then discussed, and finally a mapping for the semi-infinite well is shown.

### 3.2.1 Energy Quantization

A particle of mass $m$ in a well of width $L$ bounded by a finite potential of height $V_0$, symmetrically placed about the origin, is given by

$$V(z) = \begin{cases} 0, & |z| \leq L/2, \\ V_0, & |z| > L/2. \end{cases} \tag{3.3}$$

Solving the time-independent Schrödinger equation in each region, and matching boundary conditions, yields the bound-state energies, $0 < E_n \leq V_0$. The energy eigenvalue is expressed through the wavenumber $k = \sqrt{2mE/\hbar^2}$, and decay constant $\kappa = \sqrt{2m(V_0 - E)/\hbar^2}$. More convenient dimensionless forms for these quantities are given by

$$\alpha = kL/2 = \sqrt{\frac{2mE}{\hbar^2}}\frac{L}{2} \qquad \beta = \kappa L/2 = \sqrt{\frac{2m(V_0 - E)}{\hbar^2}}\frac{L}{2} = \sqrt{P^2 - \alpha^2} \tag{3.4}$$

where $P = \sqrt{2mV_0/\hbar^2}(L/2)$, is the *well-strength parameter*. This parameter has been variously designated as "$K$" [13], "$S$" [15], and $P$ [14, 19] in the literature. With the continuity requirement and the imposed boundary conditions, one arrives at two transcendental equations, for solutions of even and odd parity, as shown in the appendix,

$$\begin{aligned} \alpha \tan \alpha = \beta \qquad &\text{(even parity)}, \\ -\alpha \cot \alpha = \beta \qquad &\text{(odd parity)}. \end{aligned} \tag{3.5}$$

A simpler, single eigenvalue equation incorporating solutions for both parities can be obtained [26, 13, 15, 19] (Appendix A) in the form

$$\alpha_n + \sin^{-1}\left(\frac{\alpha_n}{P}\right) = \frac{n\pi}{2}, \qquad n = 1, 2, ... \tag{3.6}$$

or

$$P \sin \theta_n + \theta_n = \frac{n\pi}{2}, \qquad n = 1, 2, ... \tag{3.7}$$

where $\alpha_n = P \sin \theta_n$, and the phase angle $\theta_n$ is bounded by 0 and $\pi/2$. The ground state is at $n = 1$. It is interesting to note that Eq. (3.6) had been derived earlier by Landau [27], directly, without distinguishing the parity of the solutions.

The maximum number of states in the well for a given $P$, can be inferred immediately from the fact that the left hand side of Equation (3.7) cannot exceed $P + \pi/2$, and thus $n > 1 + (2P/\pi)$ cannot be a solution. This shows that the marginally bound state ($E_n = V_0$) occurs for $n = n_{max} = 1 + N$, if $N = 2P/\pi$ is an integer. When $N$ exceeds an integer, the marginally bound state is lost, and the total number of bound states is given by $n_{max} = 1 + [N]$, where $[N]$ denotes the integral part of $N$. Thus, by expressing the well strength through $N$ rather than $P$, one can immediately infer the total number of bound states of that well.

The roots of Eq. (3.7) (through $\alpha_n = P \sin\theta_n$) *directly* determine the energies of the finite well as a function of the bound-state index $n$ and the well-strength parameter $P$. We show how the roots of this equation can also be used to construct an *effective length*, which provides an *alternate path* for obtaining the energies.

The *complement* of $\theta_n$, $\phi_n = \pi/2 - \theta_n$, gives an equivalent, alternate version of Eq. (3.7),

$$P\cos\phi_n - \phi_n = (n-1)\frac{\pi}{2}, \tag{3.8}$$

with $0 \leq \phi_n \leq \pi/2$. Both Eqs. (3.7) and (3.8) are transcendental equations, and would require a 'root-finding' procedure to get exact results, as is the case for the more commonly used transcendental equations like Eq. (3.5), or other equivalent procedures. We will show that both Eqs. (3.7) and (3.8) are on the other hand amenable to simple approximations which reduce them to algebraic equations: a cubic equation for (3.7), and a quadratic for (3.8). The roots can then be expressed in closed-form in terms of $n$ and $P$. Employing these explicit approximate roots in the exact formal expression for the effective length is the essential idea of this section, leading to a global, highly accurate, closed-form expression for the effective length, and thus the energies. Our approach is a departure from previous work, in that it is easy to implement, and uniformly covers any combination of (potential) height and width of the quantum well, for all bound states.

### 3.2.2 Effective Length

To introduce the effective length idea, the quantization equation can be put into a more "transparent" form. Recalling that $k_nL/2 = \alpha_n = P\sin\theta_n$, Eq. (3.7) can be rewritten as

$$\frac{k_nL}{2}\left(1+\frac{\theta_n}{P\sin\theta_n}\right)=\frac{n\pi}{2}. \tag{3.9}$$

Now we recognize that

$$L_n \equiv L\left(1+\frac{\theta_n}{P\sin\theta_n}\right) \tag{3.10}$$

represents the *effective length* for the equivalent infinite well, since Eq. (3.9) reduces to $k_nL_n = n\pi$, or $k_n = n\pi/L_n$. Eq. (3.10) can be written as

$$L_n \equiv L\left(1+\frac{a_n}{P}\right), \tag{3.11}$$

where the function $a_n$ is given by

$$a_n \equiv \frac{\theta_n}{\sin\theta_n} \equiv \frac{\pi/2-\phi_n}{\cos\phi_n}, \tag{3.12}$$

with $1 \le a_n \le \pi/2$, and $\theta_n = \theta_n(P) = \theta(n,P)$ and $\phi_n = \phi_n(P) = \phi(n,P)$ are functions of $n$ and $P$. Having derived the effective length form, an expression for the bound-state energies of the finite well in terms of $a_n$ and $P$ can be given exactly. The effective length for each level of the finite well is mapped to the corresponding level of a wider infinite well. As the infinite square well energies are given by

$$\epsilon_n^\infty = \frac{\hbar^2}{2m}\left(\frac{n\pi}{L}\right)^2, \tag{3.13}$$

an analogous way of expressing the finite well energies is

$$E_n = \frac{\hbar^2}{2m}\left(\frac{n\pi}{L_n}\right)^2, \tag{3.14}$$

where $L_n$ is given by Eq. (3.11). This result shows that *the $n$-th energy of a finite well of length $L$ is identical to the $n$-th energy of an infinite well of effective length $L_n$.* This is an *exact* relation, with $L_n$ given directly in terms of the (exact) roots of the transcendental equation, Eq. (3.7) or Eq. (3.8). A salient feature of the infinite well, the basic $n^2$-scaling for the energy levels, is preserved with

Eq. (3.14). Additionally, this expression shows the level by level departure from this simple scaling through the (weak) $n$-dependence of the effective length.

One can also view this result in terms of an infinite well of length $L$ (same as the given finite well), and consider the effect of reducing the confining potential from infinity to the given well value $V_0$ by expressing $E_n$ as

$$E_n = \epsilon_n^{\infty} f(n, P), \tag{3.15}$$

where

$$f(n, P) = (L/L_n)^2 = (1 + \frac{a_n}{P})^{-2}. \tag{3.16}$$

The factor $f$ represents the fractional change (reduction) in the energies from those of the infinite well of the same width $L$, and it depends primarily on $P$, and only weakly on $n$. Note, that as $P$ gets smaller (smaller $V_0$), $f$ also gets smaller and the energies are monotonically decreasing functions of the well-strength parameter. The next step in our analysis is to find practical approximations for the roots $\theta_n$ or $\phi_n$, leading to approximate $L_n$, $f$, and $E_n$ for the finite symmetric quantum well. However, one can draw some immediate inferences from the exact structure of $a_n$, and the ensuing characteristics of $L_n$. The main part of Figure 3.3 shows the monotonic behavior of $a_n$ for the first three levels for *any* quantum well as a function of the well-strength *number parameter* $N = 2P/\pi$. Note also, that for higher $n$ (which are not shown), this trend of $a_n$ continues, with the vertical asymptotes of $a_n \to \pi/2$, signifying the weakly-bound states, and occurring at integer values of $N = n - 1$. The limiting values of $a_n$ also give the bounds for the effective length, in terms of the original well width $L$. That is, $L(1 + 1/P) \leq L_n \leq L(1 + 1/N)$. The inset in Figure 3.3 shows the variation of $L_n$ with $n$, for a fixed $N$. For large $N$, and small $n$ (i.e. deeply-bound states), $a_n \to 1$, $L_n \to L(1 + 1/P)$, and the $n^2$-scaling is restored, as this scenario corresponds to that of the ISW. It should be noted that our effective length, and mapping to the ISW, are exact constructs, defined for all $n$ and $N$, and clearly differ from earlier usage of various effective lengths[10, 14, 28, 18]. The precise connections to the earlier literature are discussed at the end of the section.

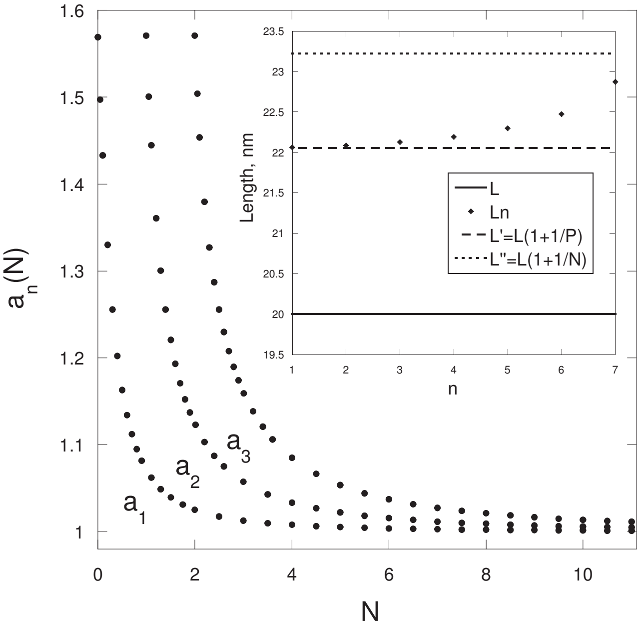

Figure 3.3: The $a_n(N)$ curves as a function of the well-strength number parameter $N = 2P/\pi$, for the levels $n = 1, 2$ and 3. The inset details the behavior of the quantity $L_n/L$ as a function of $n$, for $N = 6.2$. The bounds of the effective length are given as $L'$ and $L''$. Note the weak $n$-dependence of $L_n$.

### 3.2.3 Approximations

Two distinct approaches are employed based on Eq. (3.7) or Eq. (3.8), to obtain approximate solutions. Each of these approaches has its own domain in parameter space where it is better than the other, i.e., small $\theta_n$ will describe the deeply-bound states better, while small $\phi_n$ will be much better for the weakly-bound states. As will be shown later, the approach based on approximating $\phi_n$ has the (fortuitous) advantage that it can be applied globally for any level of any quantum well, without incurring a significant error.

#### 3.2.3.1 $\phi$-approximation

Starting with Eq. (3.8), the simplest approximation in the small $\phi_n$ domain is obtained with $\cos\phi_n \approx 1$ in Eq. (3.8), which has a solution

$$\phi_n^{(1)} = \frac{\pi}{2}(N+1-n), \tag{3.17}$$

where the superscript refers to the first approximation. This is a good approximation only for the top most weakly-bound state, where $n \lesssim N+1$. This condition makes $\phi_n^{(1)}$ a good approximation for the fast descending part of the $a_n(N)$ curves in Fig. 3.3.

The next approximation is obtained by expanding the cosine to two terms, that is, $\cos\phi_n \approx 1 - (\phi_n^2)/2$, and rewriting Eq. (3.8) as

$$\phi_n^2 + \frac{4}{N\pi}\phi_n - \frac{2}{N}(N+1-n) = 0. \tag{3.18}$$

Solving this quadratic equation for $\phi_n$ gives

$$\phi_n^{(2)} = \frac{2}{N\pi}\left(-1+\sqrt{1+\frac{N\pi^2}{2}(N+1-n)}\right), \tag{3.19}$$

where the positive root has been taken, as $\phi_n$ can't be negative, and the superscript denotes the second approximation. The resulting $L_n$ found from Eqs. (3.12) and (3.11), and the corresponding $E_n$, (3.14), are remarkably accurate even for larger $\phi_n$, thus making this approach globally applicable (i.e. for all n-levels and all strength parameters $N$).

One can generate higher approximations by more terms in the cosine expansion, and treating these terms as perturbations, or by using an iterative procedure. For example, expanding the cosine to three terms results in a quartic equation, with no cubic term,

$$\phi_n^4 - 12\phi_n^2 - \frac{48}{N\pi}\phi_n + \frac{24}{N}(N+1-n) = 0. \tag{3.20}$$

This is easily approximated by using the known $\phi_n^{(2)}$ in the fourth-order term, to obtain a new quadratic equation for $\phi_n$

$$\phi_n^2 + \frac{4}{N\pi}\phi_n - \frac{2}{N}(N+1-n) - \frac{1}{12}(\phi_n^{(2)})^4 = 0, \tag{3.21}$$

which has the explicit solution

$$\phi_n^{(3)} = \frac{2}{N\pi}\left(-1 + \sqrt{1 + N\pi[\phi_n^{(1)} + \frac{N\pi}{48}(\phi_n^{(2)})^4]}\right), \tag{3.22}$$

where $\phi_n^{(3)}$ refers to our third approximation. $\phi_n^{(2)}$ is given by Eq. (3.19), and $\phi_n^{(1)}$ is given by Eq. (3.17).

Figure 3.4 shows $|\Delta a_n(N)|$, the absolute value of the difference between the exact $a_n$, and the second and third approximations $a_n^{(2)}$, and $a_n^{(3)}$ respectively, obtained by employing Eqs. (3.19) and (3.22) in Eq. (3.12). The errors $\Delta a_n(N)$ are remarkably small for all $n$ and $N$. Also, using $\phi_n^{(3)}$ instead of $\phi_n^{(2)}$ reduces the errors by an order of magnitude. As will be shown in the error analysis, both of these approximations provide effective lengths and energies to a very high degree of accuracy, for *all* the states, for *all* $N$.

#### 3.2.3.2 $\theta$-approximation

The simplest approximation of Eq. (3.7) is obtained by taking $\sin\theta_n \approx \theta_n$, and leads to the solution

$$\theta_n^{(1)} = \frac{n\pi/2}{P+1} = \frac{n}{N + 2/\pi}. \tag{3.23}$$

This is a good approximation for the large $N$ tail region in Fig. 3.3. For small $\theta_n$, $a_n(N) \approx 1 + (1/6)(\theta_n^{(1)})^2$ is a good representation in this domain. The ratio $L_n/L$, is then seen to have the

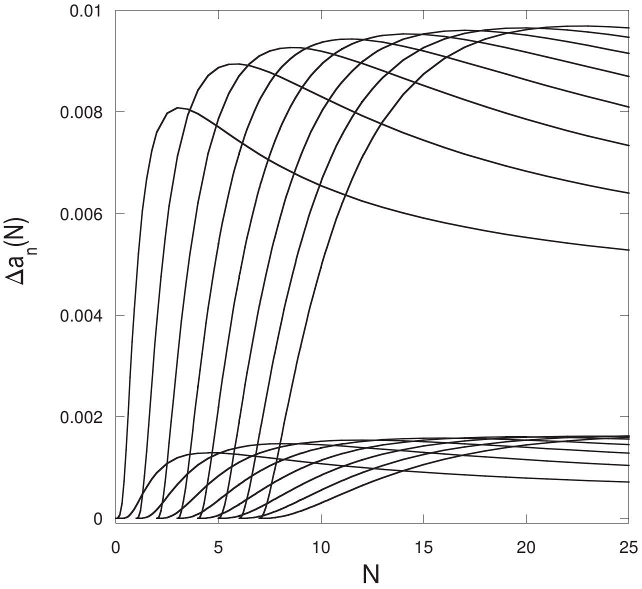

Figure 3.4: The $|\Delta a_n(N)|$ curves for the $n = 1$ through $n = 8$ levels. The top curve is the absolute value of the difference between the second approximation and exact $a_n$, $|\Delta a_n| = |a_n(\phi_n^{(2)}) - a_n|$. The bottom curve is $|\Delta a_n| = |a_n(\phi_n^{(3)}) - a_n|$, the absolute value of the difference between the third approximation and the exact $a_n$. Note the bounded nature of these approximations for all $N$.

minimum value $L'/L = (1 + 1/P)$ when $\theta_n^{(1)}$ is very small and has a parabolic rise with $n$ (for *small* $n$ and fixed $N$) as seen in the inset of Fig. 3.3.

The next approximation for $\theta_n$ is found by including the second term in the sine expansion, resulting in a "reduced" cubic equation with no quadratic term,

$$\theta_n^3 - 6\left(1 + \frac{2}{N\pi}\right)\theta_n + \frac{6n}{N} = 0, \tag{3.24}$$

which can be solved by well known methods [29-31]. There are three roots, out of which

$$\theta_n^{(2)} = 2\sqrt{2 + \frac{4}{N\pi}}\sin\left(\frac{\pi}{6} - \frac{1}{3}\tan^{-1}\delta_n\right), \tag{3.25}$$

where $\delta_n \equiv [\sqrt{(2 + (4/N\pi))^3 - (3n/N)^2}]/(3n/N)$, is the relevant root in the range 0 to $\pi/2$. A necessary condition for the validity of this solution is that the discriminant (the terms under the square root) remain positive. Rearranging these terms gives a more transparent relation between $n$ and $N$ for this to remain so,

$$n \leq \frac{2\sqrt{2}}{3}N\left(1 + \frac{2}{N\pi}\right)^{3/2}. \tag{3.26}$$

The roots of Eq. (3.24) are then all real, with Eq. (3.25) being the acceptable solution. Two points must be made concerning the use of the cubic equation in determining the approximate roots in the domain of $N$ near $n - 1$. First, the approximation will become increasingly worse as this is a poor approximation in this domain. Secondly, aside from the special case of $n = 1$, there are values of $N$ and $n$ where the discriminant becomes negative, and the root Eq. (3.25) now becomes complex. Thus it no longer provides an acceptable solution. However the solution $\theta_n^{(2)}$ can be used for a very high degree of accuracy for the deeply-bound states of moderate-to-large $N$ wells. This corresponds to the range of $a_n$ from 1 (large $N$) to 1.1 or 1.15 (moderate $N$) in Figure 3.3.

In summary, while the $\theta_n^{(1)}$ and $\theta_n^{(2)}$-approximations have their own range of application, the $\phi_n^{(2)}$-approximation is both simple and uniformly applicable for *all* $N$. As will be shown in the next section, the error incurred in the approximated energies, upon using the $\phi_n^{(2)}$-approximation does not exceed 0.4% for any $n$ and $N$.

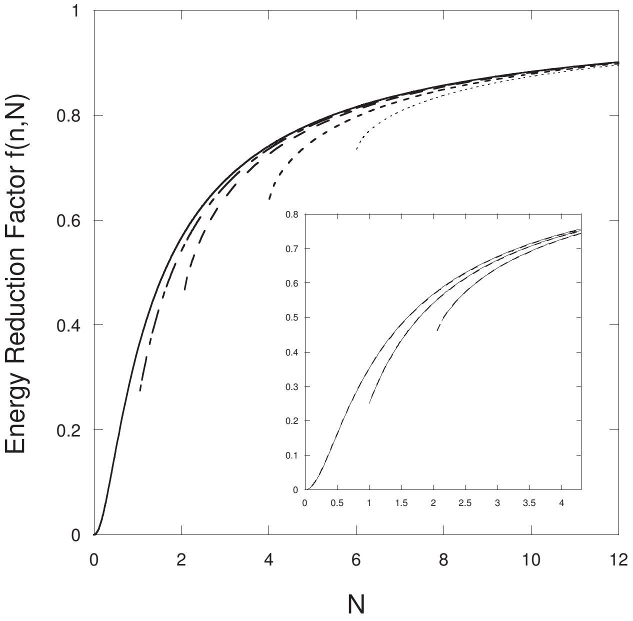

Figure 3.5: The $f^{(2)}(n,N) = E_n^{(2)}/\epsilon_n^{\infty}$ curves for the levels $n = 1, 2, 3, 5$ and 7. The $f^{(2)}(1,N)$ curve is the solid line, and each successive, shorter curve is for $n = 2, 3, 5$ and 7 respectively. $E_n^{(2)}$ is given by Eq. (3.14) and is based on the $\phi_n^{(2)}$-approximation. The inset provides a comparison of the exact $f(n,N)$ (solid lines) and approximate $f^{(2)}(n,N)$ (dashed lines) for $n = 1, 2$ and 3, showing that they are indistinguishable to the eye.

Figure 3.5 shows $f^{(2)}(n, N)$, the fractional reduction in the energies from the corresponding infinite well case of the same length $L$, using the approximate energy obtained from Eqs. (3.19), (3.12) and (3.14). For each $n$, the curves start at $N = (n-1)$, where $\phi_n^{(2)} = 0$, $a_n^{(2)} = a_n = \pi/2$ and $f^{(2)} = f = ((n-1)/n)^2$. The $f^{(2)}(1, N)$ curve forms an envelope under which the higher $n$ branches form a succession of shorter curves, each rising up and asymptotically merging with the $n = 1$ curve for large enough $N$. The exact $f$ curves (based on the exact SQW energies) are indistinguishable to the eye from the approximate $f^{(2)}$ curves, as can be seen from the inset of Figure 3.5.

To give a practical example, consider a (typical) quantum well structure [32], based on the semiconducting materials GaAs, and $\mathrm{Al_{0.3}Ga_{0.7}As}$. The subscripts refer to the relative concentration of the component materials. The GaAs region represents the potential well, and AlGaAs creates the barriers on both sides of height $\approx 240$ meV. The effective mass of an electron in GaAs is $m^* = 0.067 m_e$, where $m_e$ is the standard electron mass. For simplicity we will assume the same value for the effective mass in the barriers. Taking the value of the well width to be $L = 20$ nm, this corresponds to a well strength of $N = 4.10$. To obtain a quick calculation of $f(n, N)$ for this value of $N$, one can use the approximate form $a_n(N) \approx 1 + (1/6)(\theta_n^{(1)})^2$, where $\theta_n^{(1)} = (n)/(N + 2/\pi)$, Eq. (3.23). The $f(n, N)$ based on this approximation results in errors of $0.0037\%, 0.063\%, 0.37\%, 1.52\%$ and $7.5\%$ in the energy, for levels $n = 1$ through 5, respectively. On the other hand, the $\phi_n^{(2)}$-approximation has the corresponding resulting errors of $0.213\%, 0.227\%, 0.171\%, 0.074\%$ and $0.0006\%$.

### 3.2.4 Error Analysis

The error analysis for the $\phi_n$-approximations is as follows. The corresponding energies are remarkably accurate for *all* $N$ as seen in Figure 3.6 which shows the fractional error $\Delta E_n / E_n$ expressed as a percent error, where $\Delta E_n$ is the difference between the exact and approximate energies, $\Delta E_n = E_n - E_n^{(a)}$. The exact energy $E_n$ is obtained by solving any one of the transcendental equations, (3.6), (3.7) or (3.8). The approximate energies $E_n^{(2)}$ are obtained by using $\phi_n^{(2)}$, Eq. (3.19), to determine $L_n$, Eq. (3.11), which then provides $E_n^{(2)}$ through Eq. (3.14). The upper curves in Figure 3.6 represent the percentage errors in energy based on the $\phi_n^{(2)}$-approximation, for $n = 1$ to 8. The lower curves are based on $\phi_n^{(3)}$, Eq. (3.22), and show an order of magnitude reduction in the percent error. The maximum percent error overall, for the $\phi_n^{(2)}$-approximation, occurs in the $n = 1$ state, and occurs near $N = 1.4$. The largest percent error for any $n$ decreases with increasing $n$, and occurs at proportionately higher $N$ values. It is clear that the $\phi_n^{(2)}$-approximation provides an *explicit practical* approach for obtaining energies with an accuracy better than 1 part in 250 for all $n$ and $N$, and in fact better than 1 part in 1000 for most cases. The $\phi_n^{(3)}$-approximation improves these to 1 in 2000 for all $n$ and $N$, and 1 in $10,000$ for most $n$ and $N$.

It is not surprising that the $\phi_n$-approximations work very well in the domain of small $\phi_n$, where the expansion of $\cos\phi_n$ to a few terms is quite justified. On the other hand, the remarkable success of this method for accurate determination of energies for the domain where the $\cos\phi_n$ expansion is not justified is a surprise, and requires an explanation. It turns out that the *route* taken to find the energies (and how the error propagates for that method) is crucial to minimizing the error. Introduction of an approximation in solving an equation like Eq. (3.8) implies that the approximate value of $\phi_n^{(a)}$ differs from the exact value $\phi_n$ by a non vanishing amount $\Delta\phi_n = \phi_n - \phi_n^{(a)}$. For a given $\phi_n^{(a)}$, the corresponding $\alpha_n^{(a)}$ can be calculated in at least three different ways, and the three results will be different since the internal consistency of the original exact relations is compromised by the approximations. (1) The "direct route" to calculating the energies, via $\alpha_n = P\sin\theta_n = P\cos\phi_n$, leads to a large error rather quickly because the error in $\alpha_n$ is $\Delta\alpha_n = -P\sin\phi_n\Delta\phi_n$, and the fractional error $\Delta E_n/E_n = 2\Delta\alpha_n/\alpha_n = -2\tan\phi_n\Delta\phi_n$. It is therefore directly proportional to the error $\Delta\phi_n$, and is amplified by $\tan\phi_n$ where $\phi_n$ exceeds $\pi/4$, and becomes very large as $\phi_n$ approaches $\pi/2$. (2) Another route is through the relation $\alpha_n = n\pi/2 - \theta_n$. Here, the error is $\Delta\alpha_n = -\Delta\theta_n = \Delta\phi_n$, $\Delta E_n/E_n = 2\Delta\phi_n/[(n-1)\pi/2 + \phi_n]$, and the error remains of order $\Delta\phi_n$.

(3) Our preferred method, of first calculating the effective length in terms of the quantity $a_n/P$, produces errors that are quite small since the error in the quantity $a_n$ is consistently small as shown

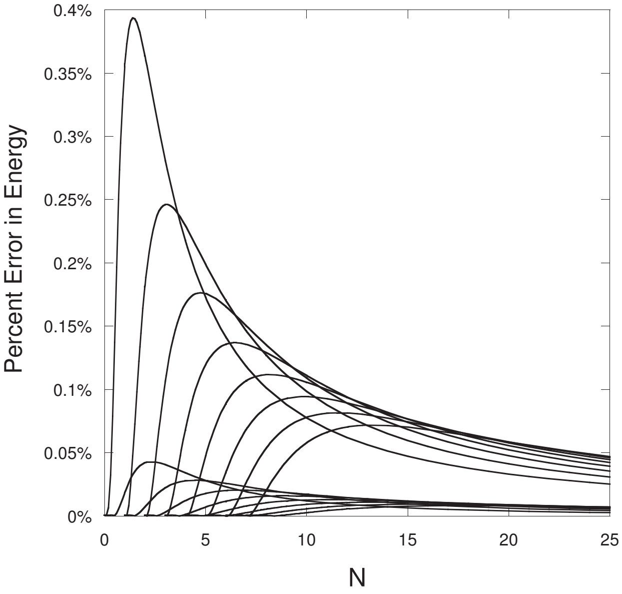

Figure 3.6: The percentage error in energies, $(\Delta E_n/E_n) \times 10^2$, for the $\phi_n^{(2)}$ (top curve), and $\phi_n^{(3)}$ (bottom curve) approximations, versus $N$, for the $n = 1$ through 8 states. Note the order of magnitude reduction for the $\phi_n^{(3)}$-approximation.

in Figure 3.4. The error in the length is given as $\Delta L_n = (L/P)\Delta a_n$, and by expressing $\Delta a_n$ in terms of $\Delta\phi_n$, it can be shown that the resulting fractional error in the energies is given by

$$\frac{\Delta E_n}{E_n} = -2\frac{\Delta\phi_n\left((\frac{\pi}{2} - \phi_n)\tan\phi_n - 1\right)}{P\cos\phi_n + \frac{\pi}{2} - \phi_n}. \tag{3.27}$$

The error in the energies is still proportional to $\Delta\phi_n$, but unlike method (1), is not amplified for the deeply-bound states as $\phi_n \to \pi/2$. In fact it is reduced by the factor $(\pi/2 - \phi_n)$, as can be seen from Eq. (3.27), by taking the appropriate limit. It is further reduced by $P$ in the denominator. If we use the quadratic approximation, the limiting values of the approximate $\phi_n^{(2)}$ and $\Delta\phi_n^{(2)}$ for the $\phi_n \to \pi/2$ domain (accessed by $N \to \infty$) are $\phi_n^{(2)} \to \sqrt{2} < \pi/2$ and

$$\lim_{N\to\infty} \Delta\phi_n^{(2)} = \frac{\pi}{2} - \sqrt{2} \approx 0.1565. \tag{3.28}$$

In spite of $\Delta\phi_n^{(2)}$ not being too small, the above mentioned factors keep the energy error small as shown in Figure 3.6. For the larger $N$, the expected $1/N$ dependence is already realized in Figure 3.6.

### 3.2.5 Wave Functions

The exact wave functions for the symmetric well are, for odd $n$

$$\psi_n(z) = \begin{cases} [C\cos(k_nL/2)\,e^{\kappa_nL/2}]e^{\kappa_nz}, & z \le -L/2, \\ C\cos(k_nz), & -L/2 \le z \le L/2, \\ [C\cos(k_nL/2)\,e^{\kappa_nL/2}]e^{-\kappa_nz}, & z \ge L/2, \end{cases} \tag{3.29}$$

and for even $n$,

$$\psi_n(z) = \begin{cases} [-C\sin(k_nL/2)\,e^{\kappa_nL/2}]e^{\kappa_nz}, & z \le -L/2, \\ C\sin(k_nz), & -L/2 \le z \le L/2, \\ [C\sin(k_nL/2)\,e^{\kappa_nL/2}]e^{-\kappa_nz}, & z \ge L/2. \end{cases} \tag{3.30}$$

The normalization constant $C = C(k_n, \kappa_n)$ is given by

$$C^{-2} = \frac{L}{2} + \frac{1}{\kappa_n}\cos^2(k_nL/2) + \frac{1}{2k_n}\sin(k_nL). \tag{3.31}$$

A further simplification can be made for this expression using Eq. (3.5), to obtain

$$C^{-2} = \frac{L}{2} + \frac{1}{\kappa_n}. \tag{3.32}$$

The wavenumber $k_n$ and the decay constant $\kappa_n$ can be given in terms of the (exact) effective length $L_n$ by $k_n = n\pi/L_n$, and $\kappa_n = \pi\sqrt{(N/L)^2 - (n/L_n)^2}$. With these substitutions the wave functions, Eqs. (3.29)-(3.32), are completely expressed in terms of the single entity $L_n$, the exact effective length.

A physical interpretation for the angle $\theta_n$ can be obtained as follows. The eigenvalue condition, Eq. (3.7), gives the relation between the effective length, the actual well width and the phase angle $\theta_n$, as $(k_n/2)(L_n - L) \equiv \theta_n$. If the sinusoidal portion of the wave function inside the well (Eqs. (3.29) or (3.30)) were to be extended outside the well the distance $l_n \equiv (L_n/2) - (L/2)$, it would accumulate the extra phase $k_n l_n = \theta_n$, making $\theta_n$ the phase to be added to the phase at the boundary $(k_n L/2)$ to make it reach $k_n L_n/2 = n\pi/2$, where the wave function vanishes. Another way to view this is to say that $\theta_n$ is the phase reduction that occurs when the barrier height is brought down from infinity to the given value $V_0$. Also, using Eq. (3.11) we see that $l_n \equiv (a_n/2P)L$, and thus $a_n$ is seen to be a measure of the length extension on each side of the well. That is, the overall effective length is given by $L_n = l_n + L + l_n$.

Explicit wave functions are obtained by introducing the approximated effective length $L_n$ in the expressions for $k_n$ and $\kappa_n$ in Eqs. (3.29) and (3.30). Note that the two expressions for the normalization constant, Eqs. (3.31) and (3.32), will not be identical when we use the approximated $L_n$. The inaccuracy of Eq. (3.32), although quite small, is a result of using (the now inaccurate) Eq. (3.5) to obtain the simpler form. Figure 3.7 compares the exact $\psi_n$ (solid lines), with these approximated $\psi_n$ (heavy dashed lines), based on the $\phi_n^{(2)}$-approximations, and they are virtually indistinguishable. Figure 3.7 is based on the GaAs quantum well example discussed earlier.

A simpler approximate form is obtained if we use the equivalent infinite well mapping for finding the wave functions as well. This approximation requires the (approximate) $\psi_n$ to vanish at and beyond the boundaries of the equivalent infinite well, $\pm L_n/2$, and so ignores the exponential decay outside the actual well. The approximate wave functions for odd $n$ are given by

$$\psi_n(z) = \begin{cases} 0 & |z| \geq L_n/2, \\ \sqrt{\frac{2}{L_n}} \cos[(n\pi z)/L_n], & |z| \leq L_n/2, \end{cases} \tag{3.33}$$

and for even $n$, the cosine term is replaced with the sine function, with the same argument. The approximate ISW $\psi_n$ for $n = 1, 3$ and 5 are shown in Fig. 3.7 by thin dashed lines. For the deeply-bound $n = 1$ state, this approximation is quite good. For the $n = 3$ state this is still rather good, however, for the topmost, nearly marginal state ($n = 5$), this method now gives an incorrect amplitude in the interior of the well. This is a quick and easy method of approximation if one is interested primarily in the deeply-bound states and the interior of the well. The approximate ISW $\psi_n$ has been given by Barker et al[14](their Eq. (19)), but their effective length is the lowest approximation compared to our effective length, and is valid only for large $P$.

### 3.2.6 The Semi-Infinite Well

The problem of the semi-infinite well (SIW),

$$V(z) = \begin{cases} \infty, & z \leq 0, \\ 0, & |z| \leq L, \\ V_0, & |z| > L. \end{cases} \tag{3.34}$$

This problem is directly related to the SQW of width $2L$ and potential $V_0$, as shown in Figure 3.8. Since all the odd wave functions of the SQW (given by even $n = 2, 4, ..$) vanish at the origin, they also constitute the correct solutions for the domain $z > 0$ for the SIW. For the SIW, the wave functions vanish for all negative $z$. Thus,

$$\psi_n^{SIW}(z) = \psi_{2n}^{SQW}(z), \qquad z > 0. \tag{3.35}$$

Each level (any $n$) of the semi-infinite well of width $L$ is therefore mapped onto the odd symmetry

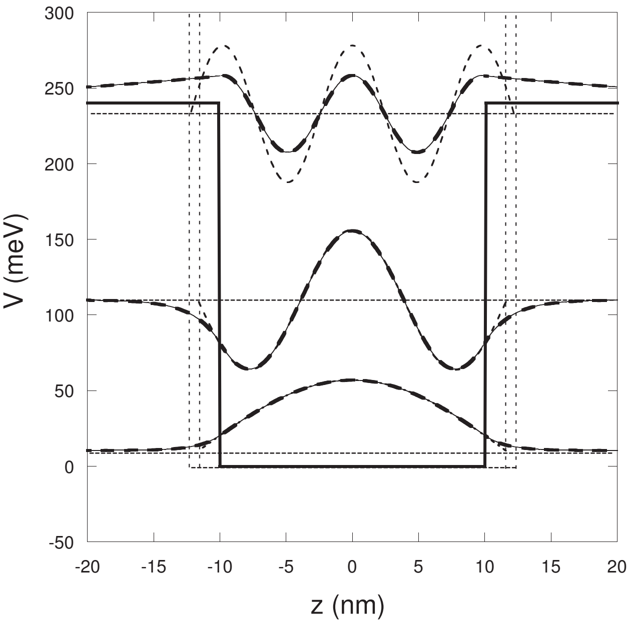

Figure 3.7: Comparison of the two methods of approximating $\psi_n$, for $n = 1, 3$ and 5. The solid line is the exact SQW wave function, the first approximate method is the heavy dashed line, and the second ISW mapping is the thin dashed line. The vertical dashes, which are at $\pm L_n/2$, mark the boundaries of the wider equivalent infinite well for each level. Due to the weak variation of $L_n$ with $n$, the boundaries for $n = 1$ and 3 are indistinguishable ($L_3 \approx L_1$), while for $n = 5$, they are visibly distinct ($L_5 > L_1$).

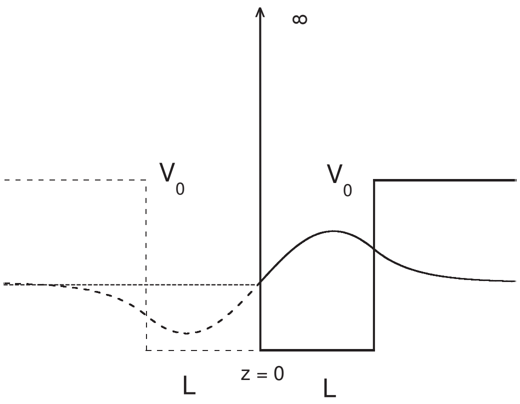

Figure 3.8: Schematic of the SQW-semi-infinite well mapping. The SQW has width $2L$, and height $V_0$ and is indicated by both the solid and dashed lines. The SIW is represented by the solid lines only. The wave function of the SIW vanishes at the infinite barrier in the middle, so that only the odd-parity states of the SQW are "selected."

states (index $2n$) of the SQW of width $2L$, with energies

$$E_n^{SIW} = E_{2n}^{SQW}. \tag{3.36}$$

This mapping also implies that the properties of the SIW are represented by the analogous eigenvalue equation,

$$P \sin \theta_n + \frac{\theta_n}{2} = \frac{n\pi}{2}. \tag{3.37}$$

which can be formally obtained from Eq. (3.7) by $P \to 2P$ and $n \to 2n$, and recognizing that $\theta_n^{SIW} \equiv \theta_{2n}^{SQW}$. Eq (3.37) can also be derived as a limiting case of the eigenvalue equation for the finite asymmetric well.

From this equation, the maximum number of states in the SIW can be found. Since the left hand side cannot exceed $P + \pi/4$, solutions exist only for $n < N + 1/2$. This shows that the marginally bound state ($E_n = V_0$) occurs for $n = n_{max} = N + 1/2$, when $N$ is half-integral. There are no bound states for $N < 1/2$. A marginal bound-state appears at $N = 1/2$, and the second state appears at $N = 3/2$.

A method has been developed which provides the energy levels and wave functions of a finite symmetric quantum well with high accuracy. The approach is global, as it is uniformly applicable to all levels $n$ for all strength parameters $P$ (or $N$), and is easy to use. An exact expression has been given for the effective length in terms of the phase angle $\theta_n$, through Eqs. (3.11) and (3.12). Explicit solution is provided for the complementary angle $\phi_n$ through Eqs. (3.19) or (3.22), and the effective length thus obtained provides energies where the worst error is less than 0.4% and 0.04% respectively. In our approach, the effective length is emphasized to be the fundamental quantity to be determined, in terms of which the energies as well as wave functions are expressed exactly through Eqs. (3.14) and (3.29)-(3.32).

Many aspects of the finite single quantum well have been explored in the past in a variety of ways by many authors. In the vast literature that spans over five decades [6-20], there are only a few papers that mention an effective length. We find Garrett[10] introduced an effective length heuristically, defined as the original length plus twice the characteristic decay length of barrier penetration for each level. This way of defining an effective length is too simplistic, and will always give a result which is an overestimate compared to the true effective length. Furthermore it becomes very large for the weakly-bound states, reaching infinity for the marginal states, thus giving completely erroneous results if applied in this domain. Barker et al[14], in their Eq. (13), also obtained an effective length, indirectly, which was the same for all levels. In terms of our exact expression for $L_n$, we see the Barker et al result as the lowest order approximation in $1/P$, obtained by simply setting $a_n = 1$ in our Eq. (3.12). Since $a_n \geq 1$, their effective length will always be an underestimate. It also misses the variation with $n$ (see Figure 3.3), and this omission becomes quite significant for the weakly-bound states where $a_n$ approaches $\pi/2$. Rokhsar[18], by considering the phase shift at the wall of a deep well, also derived an effective length, which is the same as Barker et al.

Concerning the issue of accuracy, global applicability, and simplicity of an approximation, our approach can be compared and contrasted to earlier papers. Aronstein and Stroud [19] provided a general series solution for the eigenenergies in terms of $P$, and a height ratio parameter $r$. Desired accuracy can be achieved by retaining more terms in the series. The specific choice of $r = n/(N+1)$ allows for a global approximation. As regards accuracy, their worst-case error for the second-order result ($> 1.5\%$) exceeds our worst-case error (0.4%) for the $\phi_n^{(2)}$-approximation, and similarily, our $\phi_n^{(3)}$-approximation has smaller errors (0.04%) than their third-order results (0.11%). In addition, our closed-form result is easier to evaluate than their series solution. Bonfim and Griffiths [20] gave simple, closed-form expressions for the energy eigenvalues by replacing the cosine function in their transcendental equations by various algebraic expressions. We have evaluated the resulting errors in their energies, for all parameter values, and find that for the ground state ($n = 1$), their worst-case error is almost the same as our $\phi_n^{(2)}$-approximation-based result. For higher $n$, their errors are an order of magnitude larger than our $\phi_n^{(2)}$-approximation results.

The approach put forth in this section is extended to the study of the finite asymmetric quantum well, with similar results of comparable accuracy. Further extensions (with appropriate modifications of method) to more complex systems are envisaged, and are examined in the following sections of this chapter. Examples of such systems are the symmetric and asymmetric double quantum wells [21], multiple quantum wells, all with or without applied electric fields, and with or without charge carriers that produce screening effects [22], and other systems representing (more) realistic quantum well devices.

## 3.3 Finite Asymmetric Quantum Well (ASQW)

---

While the SQW is a standard illustrative bound-state problem in elementary quantum mechanics, the finite asymmetric quantum well (ASQW) is a rarely encountered one. Due to the unequal potential barrier heights, the ASQW [27, 33, 34, 26, 3, 4, 35, 36] is inherently more complex, but also more interesting than the SQW. At a practical level the ASQW is a prominent component in real quantum well devices such as quantum well sub-millimeter wave detectors [37], resonant tunneling diodes (RTD'S) [38], and electron waveguides [39, 40]. Based on Section 3.2 on the simpler SQW system, the question can be asked whether it is possible to extend that approach and approximations to the study of the ASQW.

In this section a practical and novel method of expressing and approximating the bound-state energies and eigenfunctions of the ASQW is given, based on the effective length idea presented in the previous section for the finite SQW. For the SQW, appropriately defined *effective lengths* were used to express the SQW energies in terms of corresponding wider infinite square wells. In a similar manner, we obtain appropriate definitions of the effective lengths for the ASQW energies. In addition, we develop approximations that provide explicit and accurate expressions for the energies and wave functions, in terms of the given physical parameters of the problem. The eigenvalue condition for the asymmetric well is derived, and the bound-state condition is studied, along with its consequences. After the effective length for the ASQW is defined, the method of approximation is given along with the error analysis.

### 3.3.1 Energy quantization condition

A particle of mass $m$ in a well of width $L$, bounded by finite potentials of heights $V_l$, and $V_r$, is given by

$$V(z) = \begin{cases} V_l, & z \leq 0, \\ 0, & 0 \leq z \leq L, \\ V_r, & z \geq L, \end{cases} \tag{3.38}$$

where the subscripts $l$ and $r$ refer to left and right, respectively. The time-independent Schrödinger equation is solved in each region, and bound-state energies, $0 < E_n < V_r$ are sought. We choose without loss of generality, $V_l \geq V_r$. The wave functions for the three separate regions are

$$\psi_n(z) = \begin{cases} Ae^{\kappa_l z}, & z \leq 0, \\ C\sin(kz+\delta), & 0 \leq z \leq L, \\ Be^{-\kappa_r z}, & z \geq L, \end{cases} \tag{3.39}$$

where $\kappa_l = \sqrt{2m(V_l - E)}/\hbar$, $k = \sqrt{2mE}/\hbar$, and $\kappa_r = \sqrt{2m(V_r - E)}/\hbar$. Matching logarithmic derivatives at the barrier edges $z = 0$ and $z = L$ eliminates the constants $A$, $C$, and $B$, giving the two following conditions [27, 34]

$$\begin{aligned} \kappa_l &= k\cot(\delta), \\ \kappa_r &= -k\cot(kL+\delta). \end{aligned} \tag{3.40}$$

Since the cotangent is periodic with period $\pi$, we can write

$$\begin{aligned} \delta &= \sin^{-1}\left(\frac{k}{\sqrt{k^2+\kappa_l^2}}\right) + n_1\pi, \\ \delta + kL &= -\sin^{-1}\left(\frac{k}{\sqrt{k^2+\kappa_r^2}}\right) + n_2\pi, \end{aligned} \tag{3.41}$$

where $n_1$ and $n_2$ are integers and the value of the inverse sine lies between 0 and $\pi/2$. Thus, eliminating $\delta$, we have

$$kL = n\pi - \sin^{-1}\left(\frac{\hbar k}{\sqrt{2mV_r}}\right) - \sin^{-1}\left(\frac{\hbar k}{\sqrt{2mV_l}}\right), \tag{3.42}$$

with $n = n_2 - n_1$ (see Appendix A). Since $k > 0$, $n = 1, 2, 3, ..,$ provide the allowed roots $k = k_n$, and the eigenenergies of the ASQW are $E_n = (\hbar k_n)^2/(2m)$. Equation (3.42) can be recast in terms of the dimensionless energy parameter $\alpha = kL/2$, and *two* well-strength parameters, $P_l = \sqrt{2mV_l/\hbar^2}L/2$ and $P_r = \sqrt{2mV_r/\hbar^2}L/2$, as

$$\alpha + \frac{1}{2}\sin^{-1}\left(\frac{\alpha}{P_r}\right) + \frac{1}{2}\sin^{-1}\left(\frac{\alpha}{P_l}\right) = \frac{n\pi}{2}. \tag{3.43}$$

An alternate form is obtained by introducing phase angles $\theta_l = \sin^{-1}(\alpha/P_l)$ and $\theta_r = \sin^{-1}(\alpha/P_r)$, with $0 \le \theta_l \le \pi/2$ and $0 \le \theta_r \le \pi/2$. Since

$$\alpha = P_l \sin\theta_l = P_r \sin\theta_r, \tag{3.44}$$

we can also write the eigenvalue equation as

$$P_r \sin\theta_r + \frac{1}{2}\theta_l + \frac{1}{2}\theta_r = \frac{n\pi}{2}, \tag{3.45}$$

where the two angles are related by "Snell's Law", $\sin\theta_l = (P_r/P_l)\sin\theta_r$. Using this to eliminate $\theta_l$, $\theta_r$ becomes the eigenvalue parameter with solutions $\theta_{r,n} = \theta_{r,n}(P_l, P_r)$. Corresponding equations could also be written in terms of $\theta_l$, with roots $\theta_{l,n} = \theta_{l,n}(P_l, P_r)$. The advantage of choosing to express the eigenvalue condition in terms of $\theta_r$ will be made clear in the section on approximations. The connection to the SQW can be seen immediately by setting $P_l = P_r = P$ in Eq. (3.43), which leads to the Eq. (3) in Section 3.2.

Unlike an SQW which always has at least one bound state even for the smallest strength $P$, there can be ASQW's which have *no bound states.* An ASQW is defined by two parameters $P_r$ and $P_l$, or alternately (with $P_l \ge P_r$) by $P_r$ and $\xi \equiv P_r/P_l$. $\xi$ is the *asymmetry parameter.* Clearly $0 \le \xi \le 1$, with $\xi = 1$ the SQW limit, and $\xi = 0$ the semi-infinite well limit, which are both discussed in the SQW section. Consider the case where a SQW ($P_r = P_l = P$ or $\xi = 1$) has $N_r = 2P_r/\pi$ only slightly greater than an integer $m$. Then as shown in Sec. 3.2, the top-most bound state has $n = m + 1$, and it is just below $V_r$, ($E_n \lesssim V_r$). For an ASQW with the same $V_r$, even a small increase in $V_l$ (i.e. a small decrease in $\xi$) will raise that state to $E_n = V_r$ and any further decrease in $\xi$ pushes that bound state out of the ASQW. Eq. (3.44) shows that $\theta_l < \theta_r$ and Eq. (3.45) then provides a larger $\theta_r$ for the same $P_r$. Thus $\theta_r$ increases as $\xi$ is reduced, and when it reaches $\pi/2$, $\alpha = P_r$, and the bound state energy is at $V_r$. The critical value of $\xi$ where this occurs is given by letting $\theta_r = \pi/2$ in Eq. (3.45), leading to

$$N_r = n - \frac{1}{2} - \frac{1}{\pi}\sin^{-1}(\xi_c), \tag{3.46}$$

or

$$\xi_c = \sin[(n - (1/2) - N_r)\pi]. \tag{3.47}$$

As an illustration, consider a SQW with $N_r = 0.1$. Then $m = 0$, and $n = 1$ is the only bound state. For an ASQW with the same $N_r$, if we reduce $\xi$ from 1 to $\xi_c \approx 0.951$, given by Eq. (3.47), the bound state $E_1$ reaches $V_r$, and any further decrease in $\xi$ produces ASQW's with no bound states. Thus all ASQW's with $N_r = 0.1$ and the left barrier $V_l$ exceeding the right barrier $V_r$ by as little as $\approx 11.1\%$ have no bound states.

It is clear from Eq. (3.47), with $n = 1$, that this phenomenon will occur for $0 \leq N_r \leq 1/2$. $\xi_c$ reaches 0 (i.e. $V_l \to \infty$) when $N_r = 1/2$. If the original $N_r > 1/2$, the bound state cannot be pushed out of the well, even if $V_l$ is made infinite. For any $n$, the range of strengths $0 \leq N_r - (n-1) \leq 1/2$ leads to ASQW's where increasing the asymmetry pushes out the topmost bound state at the critical ratio $\xi_c$. For $N_r = 1.1$, the SQW has two bound states and the corresponding ASQW will lose the second state when $\xi = \xi_c \approx 0.951$.

On the other hand, if $1/2 \leq N_r - (n - 1) \leq 1$, the number of bound states in an ASQW remains the same as that for a SQW with the same $N_r$, even when the strength ratio $\xi$ varies over the full range from 1 to 0. For this range of $N_r$, even the topmost state of the SQW is too far below the barrier $V_r$ to be pushed up above $V_r$ in the corresponding ASQW by increasing $V_l$. This is easily seen from Eqs. (3.44) and (3.45); to reach $E = V_r$ requires $\theta_r = \pi/2$ by Eq. (3.44), but Eq. (3.45) then becomes Eq. (3.46), which cannot be satisfied since the fractional part of the LHS is above 1/2, and the fractional part of the RHS is below 1/2. Thus $\theta_r$ can never reach $\pi/2$ for this case, and none of the bound states can escape even by taking $V_l \to \infty$.

### 3.3.2 The Effective Length

The *exact* effective length $L_n$ for the asymmetric well can be determined by rewriting the eigenvalue condition, Eq. (3.45), using the relations $k_n L/2 = \alpha_n = P_r \sin\theta_r$, as

$$\frac{k_n L}{2}\left(1 + \frac{\theta_l}{2P_r \sin\theta_r} + \frac{\theta_r}{2P_r \sin\theta_r}\right) = \frac{n\pi}{2}. \tag{3.48}$$

Now invoking the relation $P_l \sin\theta_l = P_r \sin\theta_r$ in the denominator of the second term, the following identification can be made

$$L_n \equiv L\left(1 + \frac{\theta_l}{2P_l \sin\theta_l} + \frac{\theta_r}{2P_r \sin\theta_r}\right). \tag{3.49}$$

This is the *effective length* for the equivalent infinite well, as Eq. (3.48) reduces to $k_n L_n = n\pi$ or $k_n = n\pi/L_n$. $L_n$ can be expressed more compactly as

$$L_n \equiv L\left(1 + \frac{c_{l,n}}{2P_l} + \frac{c_{r,n}}{2P_r}\right), \tag{3.50}$$

where

$$c_{r,n} \equiv \frac{\theta_{r,n}}{\sin\theta_{r,n}} \equiv \frac{\pi/2 - \phi_{r,n}}{\cos\phi_{r,n}}, \tag{3.51}$$

and the expression for $c_{l,n}$, is identical to that above with $r$ (right) replaced with $l$ (left). We note that $\theta_{l,n}$, $\theta_{r,n}$, $\phi_{l,n}$, and $\phi_{r,n}$ are all functions of *both* $P_l$ and $P_r$. Also, from Eq. (3.51) we have $1 \leq c_{r,n} \leq \pi/2$, $1 \leq c_{l,n} \leq \pi/2$. If $P_r = P_l$, we have a SQW and $c_{r,n} = c_{l,n} = a_n$ in the notation of Sec. 3.2. Now, the energies of the ASQW can be expressed in a form analogous to that of an ISW as

$$E_n = \frac{\hbar^2 k_n^2}{2m} = \frac{\hbar^2}{2m}\left(\frac{n\pi}{L_n}\right)^2. \tag{3.52}$$

where the effective length $L_n$ is given *exactly* by Eq. (3.49) in terms of the (exact) roots of the transcendental equation, Eq. (3.45). Eq. (3.52) shows that the primary $n^2$-scaling of the infinite well is preserved, but is slightly modified by the small variation of $L_n$ with $n$. In terms of an infinite well of length $L$, with energies $\epsilon_n^\infty = (n\pi\hbar)^2/(2mL^2)$, the ASQW energies can be written

$$E_n = \epsilon_n^\infty f_n, \tag{3.53}$$

where

$$f_n = (L/L_n)^2 = \left(1 + \frac{c_{r,n}}{2P_r} + \frac{c_{l,n}}{2P_l}\right)^{-2}. \tag{3.54}$$

The factor $f_n$ represents the fractional reduction in the energies from those of the infinite well of the same width $L$, and it depends primarily on $P_r$, $P_l$ and only weakly on $n$.

In the next subsection it is shown how to obtain practical approximations of the roots of the transcendental equations, leading to approximate $L_n$ and $E_n$. Before discussing the approximations, a few immediate points can be made concerning the exact $c_n$ functions and their dependence on $N_r$ and $\xi$.

Figure 3.9 shows $c_{r,n}$ and $c_{l,n}$ as functions of $N_r$ for various strength ratios $\xi$, for the states $n = 1$ and $n = 2$. $\xi = 1$ represents the SQW limit and the solid circles are the corresponding $a_n$. Smaller values of $\xi$ represent increasing asymmetry, and $c_{r,n}$ and $c_{l,n}$ diverge away from $a_n$ in opposite directions, $c_{r,n}$ being the upper curves.

The highest value $a_n = \pi/2$ is reached at $N_r = n - 1$ for any $n$. As $\xi$ is decreased, the right branches $c_{r,n}$ also attain the maximum value $\pi/2$, but at an increasingly larger value $N_r(\xi) = n - 1 + (1/\pi)\cos^{-1}\xi$, a relation analogous to Eq. (3.46). The left branches also begin at this $N_r$ and have the value at that point, $c_{l,n} = (1/\xi)\sin^{-1}\xi$. If we eliminate $\xi$ from these two equations, we get the envelope function of the starting points of $c_{l,n}$'s, $c_{l,n}^{envelope} = (n-1/2-N_r)\pi/\sin[(n-1/2-N_r)\pi]$. This is represented by the dashed lines in Figure 3.9, for $n = 1$ and $n = 2$. All these results are easily derived from Eqs. (3.44) and (3.45) by noting that $c_{r,n} = \pi/2$ also implies $\theta_{r,n} = \pi/2$. We note that for any given $\xi < 1$, there is a blank range of $N_r$ from $N_r = n-1$ to $N_r = N_r(\xi)$, for which

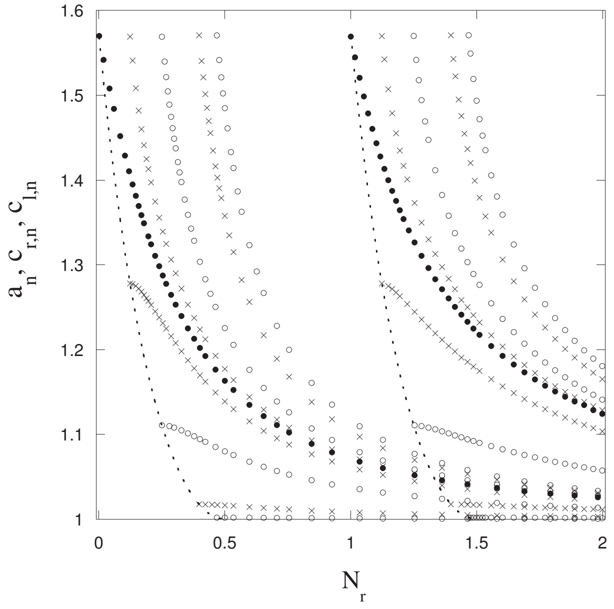

Figure 3.9: The (exact) functions $a_n$, $c_{r,n}(\xi)$ and $c_{l,n}(\xi)$ vs. $N_r$, for the $n = 1$ and $n = 2$ states, for various values of $\xi \equiv P_r/P_l$. The solid circles are $a_n$ ($\xi = 1$). The $c_{r,n}$ and $c_{l,n}$ deviate away from $a_n$ in opposite directions with decreasing $\xi$. Shown here are $\xi = 0.925, 0.816, 0.707, 0.316$ and $0.1$. The $c_{r,n}$ are the upper curves.

there are no eigen-solutions, indicating that for a given $\xi$, there is no bound state with that $n$ in that range of $N_r$. In contrast, the corresponding symmetric well always has a bound state in that range. For any $\xi$, and any $n$, as $N_r$ is increased, the $c_{r,n}$ and $c_{l,n}$ decrease monotonically and eventually asymptotically approach the limiting value 1. These are the main characteristics of the coefficients $c_{r,n}$ and $c_{l,n}$ which we need to obtain the effective length $L_n$, Eq. (3.50). The higher $n$ curves, while not shown exhibit the same 'fanning' characteristic. Incidentally, as $\xi \to 0$, the ASQW becomes the semi-infinite well. In this limit, $c_{l,n} \to 1$, $c_{r,n} \to a_{2n}(2L)$, which was made explicit in the section for the SQW. In the next subsection we develop approximations to obtain explicit representations of the $c_n$'s and $L_n$.

### 3.3.3 Approximations

Based on the remarkable and surprising success of the study of the SQW, a similar procedure is adopted for approximating the energies of the finite ASQW. It is shown that this can be done easily for the semi-infinite well (SIW). Next, this will be generalized to include small values of the asymmetry parameter $\xi \equiv P_r/P_l$, and finally for all $\xi$. We begin by noting that the defining equation for the SIW is given by

$$P_r \sin\theta_r + \frac{1}{2}\theta_r = \frac{n\pi}{2}, \tag{3.55}$$

which can be seen from Eqs. (3.44) and (3.45) as a result of $P_l \to \infty$. This is also given as Eq. (3.37) in Section 3.2, obtained through symmetry considerations. Multiplying Eq. (3.55) by 2 converts it to the SQW eigenvalue equation (Eq.(3.7) in Section 3.2), with strength parameter $2P_r$ and energy level index $2n$. Therefore $\theta^{si}_{r,n}(P_r) \equiv \theta^{SQW}_{2n}(2P_r)$. To solve this approximately, the above equation is rewritten in terms of the complement $\phi_r = \pi/2 - \theta_r$ as

$$P_r \cos\phi_r - \frac{1}{2}\phi_r = (n - 1/2)\frac{\pi}{2}. \tag{3.56}$$

In analogy with our approximations for the SQW, replacing the cosine with the first two terms of its expansion results in a quadratic equation for $\phi_r$, with the following solution

$$\phi^{si}_{r,n} = \frac{1}{N_r \pi} \left( -1 + \sqrt{1 + N_r \pi^2 (2N_r + 1 - 2n)} \right). \tag{3.57}$$

Using this in Eq. (3.51), the effective length for the SIW $L_n = L(1 + c_{r,n}/2P_r)$, is obtained, and then using Eq. (3.52) results in the approximate eigenenergies. In the error analysis section we will show the percentage errors in the energies of the SIW in this approximation, and these are seen to be even smaller than those for the SQW.

Next we raise the question of how to solve Eq. (3.45) or its equivalent form in terms of the asymmetry parameter $\xi$,

$$P_r \sin\theta_r + \frac{1}{2}\theta_r + \frac{1}{2}\sin^{-1}(\xi \sin\theta_r) = \frac{n\pi}{2}. \tag{3.58}$$

We observe that for $\xi \sin\theta_r << 1$, Eq. (3.58) reduces to the following form

$$P^{'}_r \sin\theta_r + \frac{1}{2}\theta_r = \frac{n\pi}{2}, \tag{3.59}$$

which is identical in form to Eq. (3.55) for the SIW, with $P^{'}_r \equiv P_r + \xi/2$ representing a shift in the well-strength parameter due to $\xi$. As discussed above for the solution of Eqs. (3.55) and (3.56), the solution for Eq. (3.59) is obtained in the form of Eq. (3.57) with $N_r$ replaced by $N^{'}_r = N_r + \xi/\pi$. The effective length and the energy is then found in the same manner used for the SIW.

To generalize this approach to all $\xi$, we write Eq. (3.58) as

$$P^{''}_r \sin\theta_r + \frac{1}{2}\theta_r = \frac{n\pi}{2}, \tag{3.60}$$

where now $P^{''}_r \equiv P_r + s/2$, and

$$s = \left[ \frac{\sin^{-1}(\xi \sin\theta_r)}{\sin\theta_r} \right]. \tag{3.61}$$

While Eq. (3.60) has the solution in the form of Eq. (3.57), with $N_r$ replaced by $N^{''}_r = N_r + s/\pi$, this is still an implicit solution since $s$ depends on $\theta_r$, which itself varies with $\xi$. The simplest approach to make this explicit is to approximate $\theta_r$ in $s$ through interpolation between the known limiting values at $\xi = 0$ (SIW) and $\xi = 1$ (SQW). This is expressed as

$$\theta_r = \theta_r^{si} - \xi(\theta_r^{si} - \theta_r^{sym}), \quad 1/2 \le N_r - (n-1). \tag{3.62}$$

For the range $0 \le N_r - (n-1) \le 1/2$, the $\theta_r$ fit will be different since $\theta_r$ attains the maximum value $\pi/2$ at $\xi = \xi_c$, before the asymmetric well becomes a semi-infinite well. At this value of $\xi$, the marginal state leaves the quantum well, and thus $\xi_c$ (and not 0) is the minimum value of $\xi$ for this range of $N_r$. The fit now becomes

$$\theta_r = \frac{\pi}{2} - \frac{(\xi - \xi_c)}{(1-\xi_c)}(\frac{\pi}{2} - \theta_r^{sym}), \quad 0 \le N_r - (n-1) \le 1/2, \tag{3.63}$$

where $\xi_c$ is given by Eq. (3.47). Using these fits for the appropriate range of $N_r$ in the alternate form of Eq. (3.60),

$$P_r^{''} \cos\phi_r - \frac{1}{2}\phi_r = (n - 1/2)\frac{\pi}{2}, \tag{3.64}$$

and expanding the cosine to two terms results in a quadratic equation for $\phi_r$, with the explicit solution

$$\phi_{r,n} = \frac{1}{N_r^{''}\pi}\left(-1 + \sqrt{1 + N_r^{''}\pi^2(2N_r^{''} + 1 - 2n)}\right), \tag{3.65}$$

where $N_r^{''} = N_r + s/\pi$. The alternate form of Eq. (3.44), $P_r \cos\phi_r = P_l \cos\phi_l$ is then used to find the corresponding $\phi_{l,n}$. An explicit expression for the energy is then found through Eqs. (3.51), (3.50) and (3.52). The *process* of obtaining the approximate ASQW energies by inserting the quadratic expression for $\phi_{r,n}$ in the effective length expression, is the key to achieving high accuracy, just as was the case for the SQW.

The function $f_n = f(n, N_r, \xi)$ that was given in Eq. (3.54) represents the fractional reduction in the ASQW energies from the corresponding infinite well of length $L$. The approximate $f(n, N_r, \xi)$ curves for the levels $n = 1, 3, 5$ and 7 are shown in Figure 3.10 as a function of $N_r$, for three values of $\xi$, $\xi = 0$, $\xi = 0.707$, and $\xi = 1$. The $f(1, N_r, \xi)$ curve for each $\xi$ forms an envelope about the successively shorter $n = 3, 5$ and 7 curves. For each $\xi$ the curves also asymptotically merge with the $n = 1$ curve. For each $n$, the curves $f(n, N_r, \xi = 1)$ start at the value of $f = ((n-1)/n)^2$, at $N_r = (n-1)$, with $c_l = c_r = \pi/2$. For $0 < \xi < 1$ however, the $f(n, N_r, \xi)$ curves start with the

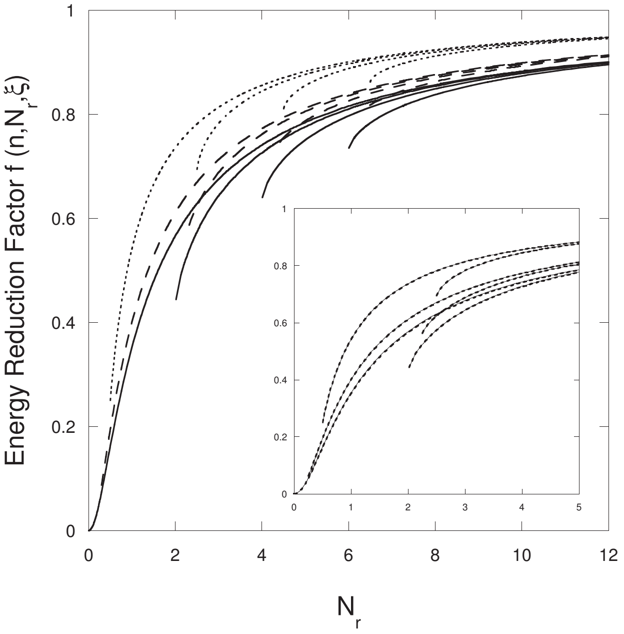

Figure 3.10: The $f(n, N_r, \xi) = E_n/\epsilon_n^\infty$ curves for the levels $n = 1, 3, 5$ and 7. The solid lines represent the $\xi = 1$ limit of the approximations based on Eq. (3.65), while the dotted lines represent the $\xi = 0$ limit. The dashed curve in between the two is for $\xi = 0.707$, or $V_l = 2V_r$. The inset provides a comparison between the exact $f$ curves (solid lines) and the approximate $f$ curves (dashed lines) for the case of $n = 1$ and $n = 3$, for the same $\xi$ values as in the main figure.

value $f = (N_r/n)^2$, at $N_r = n - 1/2 - (1/\pi)\sin^{-1}(\xi)$. This can be seen in Figure 3.10 for each $n$, for the range $0 \leq N_r - (n-1) \leq 1/2$. The inset shows the comparison of the exact $f$ curves with the approximate $f$ curves based on Eq. (3.65) for $n = 1$ and $n = 3$. The two sets of curves are essentially indistinguishable to the eye. The inset also shows clearly that the $0 < \xi < 1$ curves do not reach $N_r = n - 1$ but $N_r = n - 1/2 - (1/\pi)\sin^{-1}(\xi)$.

### 3.3.4 Error analysis

The errors made in approximating the ASQW energies are shown in Figure 3.11 for the levels $n = 1, 3, 5$ and 7 (dashed lines). The figure gives the percentage error $(\Delta E_n/E_n) \times 10^2$, where $\Delta E_n = E_n - E_n^{(a)}$, is defined as the difference between the exact energy $E_n$, and the approximated energy $E_n^{(a)}$. The exact $E_n$ is obtained by use of any one of the transcendental equations, (3.43), (3.44) or (3.45). The approximate $E_n^{(a)}$, Eq. (3.52), is found by use of (3.65) in Eqs. (3.51) and (3.50). So as not to clutter the plot, only three values $\xi = 1 (V_l = V_r)$, $\xi = 0 (V_l = \infty)$ and $\xi = 0.707 (V_l = 2V_r)$ were chosen. The maximum, or peak error for the family of $\xi$ curves for each $n$ occurs around $N_r \lesssim 2n$. The largest error made is $< 0.5\%$ (for $n = 1, \xi = 1$), the errors diminish with increasing $n$, and for $n \geq 7$ the error for all cases is $< 0.1\%$. Note that for any $n$ and any given $\xi$, the error curves start with zero error at $N_r = n - 1/2 - (1/\pi)\sin^{-1}(\xi)$.

The errors in approximated ASQW energies are comparable to those in the approximated SQW energies. Figure 3.11 also includes the approximated SQW energies (solid lines, from the SQW study) for the levels $n = 1, 3, 5$ and 7. The curves based on both the SQW and ASQW approximations share the same uniform behavior for all $n$. The limiting case of the ASQW approximation for $\xi = 1$ also represents the SQW, but solved through the "shift method." The two methods for getting the SQW energies do not give identical results (that is not unexpected since an additional approximation is made in the ASQW method) but it is reassuring that the two sets of error curves (the solid lines and the top ($\xi = 1$) ASQW curve) have the same shape and only slightly different numerical values.

Additionally, for higher $n$, the difference between these two curves becomes indistinguishable. The SIW percentage errors are also given in the figure as dotted lines. For any $n$, the progression from the SIW ($\xi = 0$) case to the SQW ($\xi = 1$) case can be followed by moving upward on the figure.

There are two approximations made in this analysis of the ASQW. The first is approximating $\cos\phi_r$ by a two-term expansion in Eq. (3.64). Second is the modeling of $\theta_r$ in the shift $s$ through linear interpolation. These two approximations lead to an error $\Delta\phi_r = \phi_r^{exact} - \phi_r^{(a)}$. In principle, the energies could have been calculated via $\alpha = P_r \cos\phi_r$, once an explicit expression for $\phi_r$ was obtained. The resulting error in $\alpha$ is $\Delta\alpha = -P_r \sin\phi_r \Delta\phi_r$. But the resulting fractional error in $\alpha$, $\Delta\alpha/\alpha = -\tan\phi_r\Delta\phi_r$, becomes quite large due to the $\tan\phi_r$ factor when $\phi_r$ exceeds $\pi/4$ and approaches $\pi/2$. On the other hand when we obtain the energy through the concept of the effective length (Eqs. (3.50) and (3.52)), the errors become small, just as was the case for the SQW study.

### 3.3.5 Wave Functions

The exact wave function of the ASQW is given by

$$\psi_n(z) = C \begin{cases} e^{\kappa_l z} \sin\delta, & z \leq 0, \\ \sin(k_n z + \delta), & 0 \leq z \leq L, \\ e^{-\kappa_r (z-L)} \sin(k_n L + \delta), & z \geq L, \end{cases} \tag{3.66}$$

where the constants $A$ and $B$ in Eq. (3.39) have been re-expressed in terms of $C$ by applying the continuity condition at the boundaries of the well. The normalization constant $C$ is given by

$$C^{-2} = \frac{L}{2} - \frac{1}{4k_n}[\sin(2k_n L + 2\delta) + \sin(2\delta)] + \frac{1}{\kappa_l}\sin^2\delta + \frac{1}{\kappa_r}\sin^2(k_n L + \delta). \tag{3.67}$$

A simpler expression can be obtained by using Eq. (3.40),

$$C^{-2} = \frac{L}{2} + \frac{1}{2\kappa_l} + \frac{1}{2\kappa_r}. \tag{3.68}$$

The wavenumber, the decay constants, and the phase angle can be expressed in terms of the exact effective length, as $k_n = n\pi/L_n$, $\kappa_{l,n} = \pi\sqrt{(N_l/L)^2 - (n/L_n)^2}$, $\kappa_{r,n} = \pi\sqrt{(N_r/L)^2 - (n/L_n)^2}$,

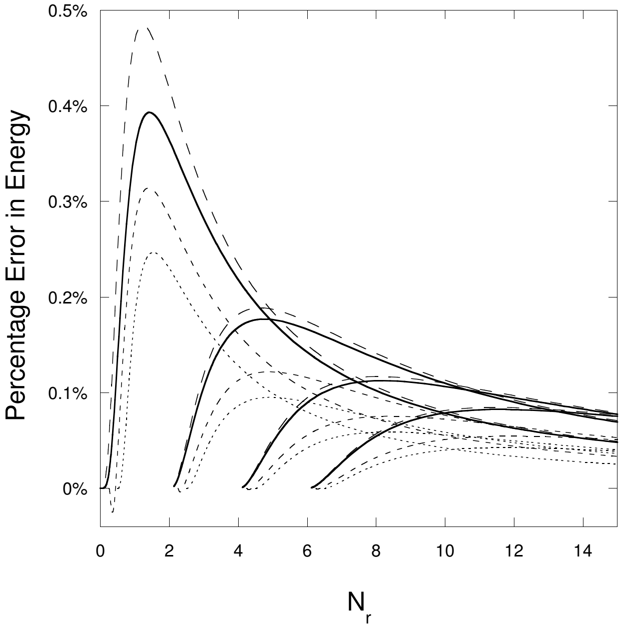

Figure 3.11: The percentage error in $\Delta E_n/E_n \times 10^2$ vs. $N_r$, for $n = 1, 3, 5$ and 7, based on the quadratic-$\phi_r$ approximation. The dashed curves are the ASQW approximation, which for each $n$, start at $\xi = 0$ (the bottom curve) and move higher for increasing $\xi$. The topmost dashed curve for each $n$ represents the $\xi = 1$ case from the ASQW approximations, while the solid curve is the SQW approximation of Sec. 3.2. The dashed line in between the $\xi = 0$ and $\xi = 1$ case is for $\xi = 0.707$.

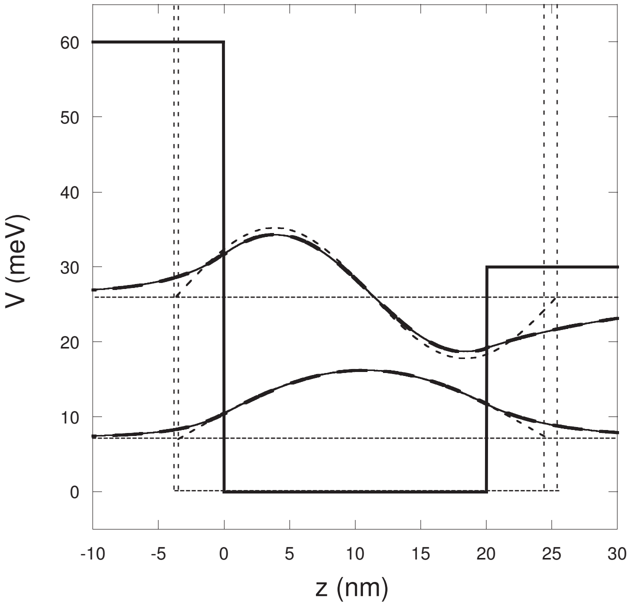

Figure 3.12: Comparison of the exact and the approximated $\psi_n$, for $n = 1$ and $n = 2$. For each $n$, the solid line is the exact ASQW wave function, the heavy dashed line represents use of the approximated $L_n$ in Eq. (3.66), and the thin dashed line represents Eq. (3.71). Note that the approximate $\psi_n$ based on Eq. (3.66) are indistinguishable from the exact $\psi_n$. The vertical dashes displaced by $l_{l,n}$ and $l_{r,n}$ from the boundaries of the actual well mark the boundaries of the equivalent wider infinite wells for the levels shown. Since $L_n$ depends weakly on $n$, the shifts for $n = 1$ and $n = 2$ do not differ much.

$\delta = \sin^{-1}(nL/N_l L_n)$. The wave functions are then completely expressed in terms of the effective length.

A physical interpretation can now be made regarding the phase angles $\theta_r$ and $\theta_l$, derived in conjunction with the eigenvalue equation, and the effective length $L_n$. Eq. (3.45) can be recast as $(\theta_r/2) + (\theta_l/2) \equiv (k_n/2)(L_n - L)$. If the sinusoidal portion of the wave function inside the well (Eq. (3.66)) were to be extended outside the well the distance $l_{l,n} \equiv (L_n)$(on the left side of the well), it would reduce the phase by $k_n l_{l,n} = \theta_{l,n}$, making $\theta_{l,n}$ the phase to be subtracted from the phase at the boundary ($z = 0$) to make it reach zero, where the wave function vanishes. For the right-hand side of the well, if the wave function were to be extended the distance $l_{r,n} \equiv (L + L_n)$, it would accumulate the extra phase $k_n l_{r,n} = \theta_{r,n}$, making $\theta_{r,n}$ the phase to be added to the phase at the boundary ($z = L$) to make it reach $k_n L_n/2 = n\pi/2$, where the wave function vanishes. The phase change that occurs when the barrier height is brought down from infinite to the given value $V_l$, and $V_r$, is precisely $\theta_{l,n}$ for the left side, and $(-\theta_{r,n})$ for the right side. Using Eq. (3.51), $l_{r,n} \equiv (c_{r,n}/2P_r)L$. Identical arguments for the left side lead to $l_{l,n} \equiv (c_{l,n}/2P_l)L$, and the overall effective length is therefore given by $L_n = l_{l,n} + L + l_{r,n}$.

Another consequence of the asymmetry is the shift in the center of symmetry for the wave function. As $P_l > P_r$ (by choice), the auxiliary relation $P_l \sin\theta_l = P_r \sin\theta_r$ implies $\theta_l < \theta_r$, and therefore the extension of the wave function will be greater on the lower barrier side and smaller on the higher barrier side. The shift is obtained (exactly) based on the effective length expression, Eq. (3.50), as

$$z_{center,n} = \frac{L}{2} + l_n, \tag{3.69}$$

where

$$l_n = \left(\frac{l_{r,n}}{2} - \frac{l_{l,n}}{2}\right), \tag{3.70}$$

is the magnitude of the shift, and $L/2$ is the geometric center of the asymmetric well. Note that $l_n$ being a function of $n$, is different for each level. In studies of realistic quantum well structures, knowledge of where the wave function center of symmetry is located (in asymmetric wells) allows one to determine where the charge density is most likely to reside [44], for example. Furthermore, additional (analytical) insight may be possible when studying more complicated structures, such as a coupled, or double asymmetric quantum well, in which two ASQW's are separated by a barrier of varying thickness.

Employing the approximation (3.65) in the effective length expression, Eq. (3.50), explicit approximate wave functions are obtained. Note that the normalization constants, Eqs. (3.67) and (3.68), will now no longer be identical. The inaccuracy of Eq. (3.68), although quite small, is a result of using (the now inaccurate) Eq. (3.40) to obtain the simpler form. Figure 3.12 compares these approximated $\psi_n$ (heavy dashed lines), with the exact $\psi_n$ (solid lines), and shows that they are indistinguishable to the eye. The parameter values chosen for the figure are based on a (typical) quantum well structure composed of the semiconducting materials gallium arsenide GaAs, and aluminum gallium arsenide, $\mathrm{Al}_{0.3}\mathrm{Ga}_{0.7}\mathrm{As}$, where the subscripts refer to the relative concentration of the component materials[2]. The parameter values are $N_r = 1.46$ ($V_r = 30$ meV) and $N_l = 2.07$ ($V_l = 60$ meV), and $L = 20$ nm. Figure 3.12 also illustrates the shift $l_1$ in the location of the center of the ground state ($n = 1$) wave functions due to the unequal barrier heights. The $n = 2$ wave function has a shift $l_2$ in the location of the node.

A simpler approximation, though of limited applicability, can be obtained by a mapping to the wider infinite well. The wave functions are given by the ISW form

$$\psi_n(z) = \begin{cases} \sqrt{2/L_n}\sin[(n\pi/L_n)(z + l_{l,n})], & -l_{l,n} \le z \le L + l_{r,n}, \\ 0, & \text{otherwise.} \end{cases} \tag{3.71}$$

where $l_{l,n} = (c_{l,n}/2P_l)L$. The shift $l_n$, Eq. (3.70), in the position of the central node (even $n$) or of the central maximum (odd $n$) is accounted for by Eq. (3.71). This simple approximation for $\psi_n$ is represented in Figure 3.12 as the thin dashed line. The vertical dashed lines in the figure represent the boundaries $\pm L_n/2$ of the equivalent wider infinite well for each level $n = 1$ and $n = 2$. While for both $n = 1$ and $n = 2$, the wave functions are well-approximated in the interior region of the well by this simpler form, the latter obviously fails to describe the exponential decay. Additionally, the amplitudes for this ISW form are slight overstatements in the interior of the well. This effect will increase with $n$, becoming especially large for $n$ levels which can become marginal, or near-marginal. Despite these limitations, the ISW mapping offers a quick and simple approximation of the deeper-bound finite ASQW states.

Accurate approximate energies and wave functions of the finite asymmetric quantum well based on the effective length approach have been obtained. The approach employed is globally applicable to all cases (for all $n$, strength parameter $P_r$ and asymmetry parameter $\xi = P_r/P_l$). The resulting worst-case error in energy is less than 0.5%. That the errors remain uniformly small and bounded, is due to the algebraic structure of the effective length, through which the energies are found. As in the SQW analysis, the emphasis here also is on the effective length, which serves as the fundamental quantity.

As the approximate energies are inversely proportional to the square of the effective length $L_n$, the percentage errors of $L_n$ are only half the percentage errors of the corresponding $E_n$. Thus the accuracy of our wave functions (which directly depend on $L_n$) is very good. This fact will be crucial in establishing analytic descriptions of more complex quantum well systems which can be compounded from the basic units, ASQW and SQW, described in this and the preceding section. In the next section, the problem of the triangular, or wedge-well potential is presented.

## 3.4 **The Triangular Quantum Well**

This section contains the triangular quantum well results, studied separately in the following four subsections: the infinite triangular well (ITW), in which there are infinitely confining potentials on either side Fig. 3.13 (a), the half-infinite triangular well, Fig. 3.13 (b), for which the vertical wall has a finite potential height, but with an infinitely extended slope, the second variation of the half-infinite triangular well, Fig. 3.14 (a), which has a truncated slope, but with an infinitely high vertical wall, and lastly, the fully finite triangular well (FTW), in which both sides of the potential are finite valued, Fig. 3.14 (b).

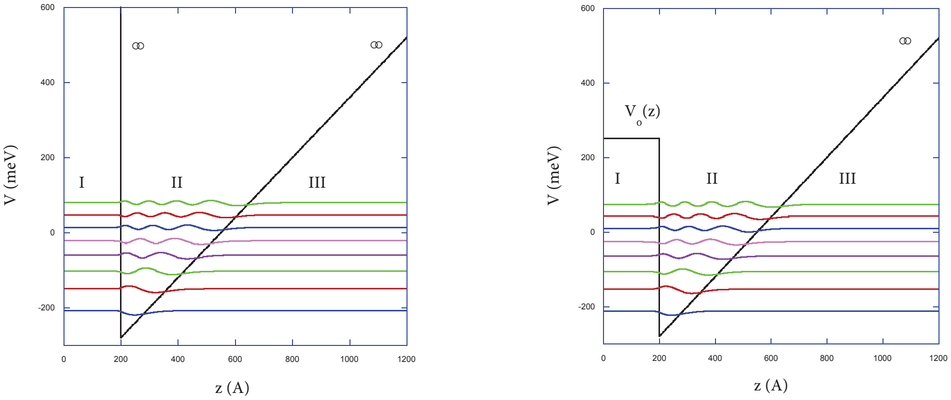

(a) (b)

Figure 3.13: A schematic of the infinite triangular well (ITW), and the half-infinite well, in which the slope is of infinite extent, but finite vertical wall.

### 3.4.1 The Infinite Triangular Well (ITW)

Just as in the ISW case, the inifinte triangular well (ITW) is the simplest of the wedge-shaped potentials to study (Fig. 3.13 (a)). The potential is defined as

$$V(z) = \begin{cases} \infty, z \leq 0 \\ Fz, z > 0 \end{cases}$$

where $F$ is the strength of the applied electric field. The Schr$\ddot{o}$dinger equation

$$\frac{d^2\psi(z)}{dz^2} + \frac{2m^*}{\hbar^2}(E - Fz)\psi(z) = 0 \tag{3.72}$$

can be put into dimensionless form, by taking

$$y = \alpha z - \gamma, \qquad \alpha = \left(\frac{2m^* F}{\hbar^2}\right)^{1/3}, \qquad \gamma = \frac{\alpha E}{F} \tag{3.73}$$

giving the Airy differential equation

$$\phi''(y) - y\phi(y) = 0 \tag{3.74}$$

with the general solutions

$$\phi(y) = C \cdot Ai(y) + D \cdot Bi(y) \tag{3.75}$$

Taking the vertical wall to be at $z = 0$, the boundary conditions require that $\phi(y)$ go to zero at $z = 0$ and also at $z \to \infty$. From the properties of the $Bi(y)$ function in the Airy solution, this requires $B = 0$, with the solution now given by

$$\phi(z = 0) = C \cdot Ai(-\gamma) = 0 \tag{3.76}$$

where the zeroes of the Airy function $Ai(-\gamma)$ are well-known and tabulated. The eigenvalues of the triangular potential well are related to the zeroes of the $Ai(-\gamma)$, and are given by

$$E_n = \frac{\gamma_n F}{\alpha} = \gamma_n \left( \frac{\hbar^2 F^2}{2m^*} \right)^{1/3} \tag{3.77}$$

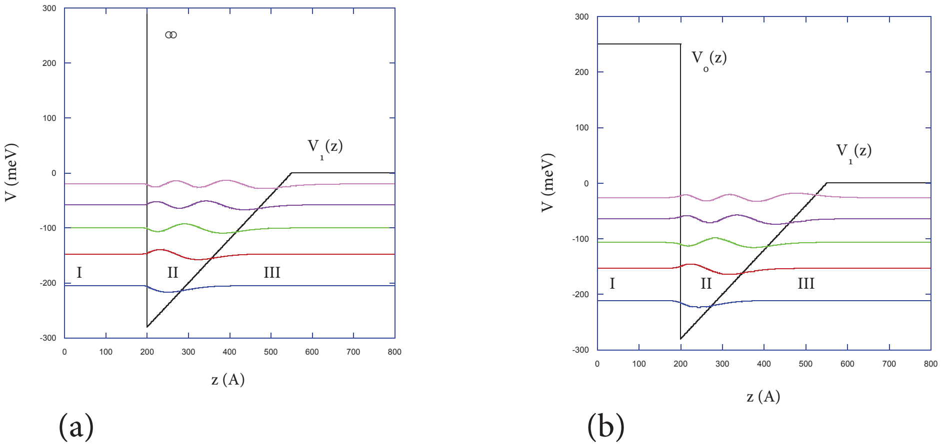

(a) (b)

Figure 3.14: A schematic of the half-infinite triangular well, in which there is an infinite vertical wall, but finite-extent slope, and the finite triangular well (FTW), where both slope and wall are finite.

### 3.4.2 The Finite Barrier Height Wedge Potential

The next variation for the infinite triangular well is one in which left-side infinite barrier is lowered to a finite value $V_0$ as shown in Figure 3.13(b). Here the wavefunctions are given by

$$\psi(z) = \begin{cases} Ce^{\rho z}, & z < 0 \\ \\ D \cdot Ai(\alpha z - \gamma_n + \epsilon), & z > 0 \end{cases} \tag{3.78}$$

where $\rho = \sqrt{2m^*(V_0 - E)/\hbar^2}$, $\alpha = (2m^* F/\hbar^2)^{1/3}$. Matching boundary conditions at $z = 0$ gives

$$C = Ai(\epsilon - \gamma_n), \qquad \rho C = \alpha D \cdot Ai'(\epsilon - \gamma_n) \tag{3.79}$$

and divding these two equations eliminates $C$, giving

$$\frac{\rho}{\alpha} = \frac{Ai'(\epsilon - \gamma_n)}{Ai(\epsilon - \gamma_n)} \tag{3.80}$$

Expanding the Airy function about its zeroes,

$$Ai(\epsilon - \gamma_n) \approx \epsilon Ai'(-\gamma_n) \tag{3.81}$$

and inserting this into Eq. (3.80) gives a simple approximation for $\epsilon$:

$$\epsilon \approx \frac{\alpha}{\rho} \tag{3.82}$$

For large potentials $V_0$, and low energies, this is approximately

$$\epsilon \approx \frac{\alpha}{\kappa}, \qquad \kappa = \sqrt{\frac{2m^* V_0}{\hbar^2}} \tag{3.83}$$

and the corresponding wavefunctions are

$$\psi_{II}(z) \approx A_2 Ai(\alpha(z + \kappa^{-1}) - \gamma_n) \tag{3.84}$$

Now the eigenvalues for an Airy function in an infinite wedge potential are obtained through the relation between the phase and the 'slope':

$$C_n Ai(gz + f) \quad \Leftrightarrow \quad -Ff/g \tag{3.85}$$

and therefore the approximate eigenvalues are

$$E_n \approx \frac{F}{\alpha}\left(\gamma_n - \frac{\alpha}{\kappa}\right) = E_\infty^n - \frac{F}{\kappa} \tag{3.86}$$

Note that this result can be derived geometrically when looking for an appropriate effective wedge.

### 3.4.3 Truncated Wedge with Infinite Barrier Height

---

The second variation on the infinite triangular well is that of the half-infinite TW in which the slanted side is of finite extent $V_0$, and with an infinitely high vertical barrier, as shown in Figure 3.14 (a). For the truncated wedge, the wavefunctions are given by

$$\psi_I = Ai(y) + R \cdot Bi(y), \qquad y < \frac{\alpha}{F}(V_0 - E) \tag{3.87}$$

$$\psi_{II} = Ce^{\rho y/\alpha}, \qquad y > \frac{\alpha}{F}(V_0 - E) \tag{3.88}$$

noting that where the wedge stops is $y_0 = (\alpha/F)(V_0 - E)$. The boundary condition at the infinite barrier, $z = 0$, are

$$\psi_I\left(y = -\frac{\alpha E}{F}\right) = Ai\left(-\frac{\alpha E}{F}\right) + R \cdot Bi\left(-\frac{\alpha E}{F}\right) = 0 \tag{3.89}$$

Now approximating the eigenvalues as $E \approx E^\infty - \epsilon$, and inserting above gives

$$Ai\left(-|\gamma_n| + \frac{\alpha\epsilon}{F}\right) + R \cdot Bi\left(-|\gamma_n| + \frac{\alpha\epsilon}{F}\right) = 0 \tag{3.90}$$

Taking $\epsilon$ to be a small correction to the energies, the $Ai$ term can be expanded to obtain an expression for the coefficient $R$:

$$R = \frac{Ai'(-|\gamma_n|)}{Bi(-|\gamma_n|)} \cdot \frac{\alpha\epsilon}{F} \tag{3.91}$$

The next boundary condition at $y_1 = (\alpha/F)(V_0 - E)$, where the wedge becomes constant, results in

$$\frac{\psi_I'(y_1)}{\psi_I(y_1)} = \frac{Ai'(y_1) + R \cdot Bi'(y_1)}{Ai(y_1) + R \cdot Bi(y_1)} \tag{3.92}$$

and

$$\frac{\psi_{II}'(y_1)}{\psi_{II}(y_1)} = \frac{-\rho}{\alpha} = -\sqrt{y_1} \tag{3.93}$$

Since $y_1 > 1$ especially for small $E$, the derivatives of the Airy function can be approximated by their asymptotic expansions:

$$Ai'(y_1) \approx -\sqrt{y_1} Ai(y_1) \tag{3.94}$$

$$Bi'(y_1) \approx \sqrt{y_1} Bi(y_1) \tag{3.95}$$

and

$$Bi(y_1) \approx 2e^{\frac{4}{3}y^{3/2}} Ai(y_1) \tag{3.96}$$

With these three relations, Eq. (3.92) becomes:

$$\frac{Ai'(y_1) + R \cdot Bi'(y_1)}{Ai(y_1) + R \cdot Bi(y_1)} = -\frac{1}{4y_1} + \sqrt{y_1}\left[1 - \frac{2}{1 + 2Re^{\frac{4}{3}y^{3/2}}}\right] \tag{3.97}$$

Now setting this equation equal to Eq. (3.93), a second expression for $R$ is obtained:

$$R \approx -\frac{Ai(y_1)}{Bi(y_1)} \cdot \frac{1}{1 + 8y_1^{3/2}} \tag{3.98}$$

Taking the two espressions for $R$, Eq. (3.91) and Eq. (3.98), an expression for the perturbation to the eigenvalues, $\epsilon$, is found:

$$\epsilon \approx -\frac{Ai(y_1)Bi(-|\gamma_n|)F}{Bi(y_1)Ai'(-|\gamma_n|)\alpha}(1 + 8y_1^{3/2})^{-1} \tag{3.99}$$

Note that $\epsilon$ is always greater than zero because the signs of the Airy functions for all possible values.

### 3.4.4 The Finite Triangular Well (FTW)

---

The situation for which both barriers are finite is presented here as shown in Fig. 3.14 (b). By the construction of reducing each barrier height, the left-side vertical wall, and the right-side slant, the previous results can be applied independently, as a first approximation, so that the overall energies may be written as

$$E \approx E^{\infty} - \epsilon_1 - \epsilon_2 \tag{3.100}$$

This approximation can be made conceptually based on the previous two half-infinite cases. First, consider the left vertical barrier being lowered to a finite value $V_0$. This leads to an effective infinite wedge potential with a reduction given by:

$$\epsilon_1 = \frac{F\hbar}{\sqrt{2m^* V_0}} \tag{3.101}$$

as derived earlier, Eq. (3.86). Secondly, consider the truncation of the wedge at $y_1$. Though the effective position of $y_1$ with respect to $y_0$ has been changed, the effect of truncating the wedge remains the same. This leads to a lowering of the energies given by:

$$\epsilon_2 \approx \frac{-Ai(y_1 - \alpha\kappa_1^{-1})Bi(-|\gamma_n| - \alpha\kappa_1^{-1})F}{Bi(y_1 - \alpha\kappa_1^{-1})Ai'(-|\gamma_n| - \alpha\kappa_1^{-1})\alpha}\left(1 + 8(y_1 - \alpha\kappa_1^{-1})^{3/2}\right)^{-1} \tag{3.102}$$

where the extra $\kappa$ term in comparison with equation Eq. (3.99) comes from the lowering of the left barrier. Thus, while there is a change in this reduction due to the first reduction, the manner in which the energy is reduced is unchanged. To summarize, the eigenenergies for this now finite barrier and wedge system are given by the equation:

$$E \approx E^{\infty} - \frac{F}{\kappa} - \frac{-Ai(y_1 - \alpha\kappa_1^{-1})Bi(-|\gamma_n| - \alpha\kappa_1^{-1})F}{Bi(y_1 - \alpha\kappa_1^{-1})Ai'(-|\gamma_n| - \alpha\kappa_1^{-1})\alpha}\left(1 + 8(y_1 - \alpha\kappa_1^{-1})^{3/2}\right)^{-1} \tag{3.103}$$

## 3.5 Double Symmetric Quantum Well (DSQW)

The finite double quantum well (DSQW), or coupled-well problem is a very interesting and important one in that this model system describes many semiconductor heterostructure devices. This scenario allows a coupling to exist between the neighboring wells, leading to the possibility of many new and interesting transport phenomena. Figures 3.15 and 3.16 shows four possiblilities of the finite DQW system. In this section an exact transcendental equation for the eigenvalues of the DSQW is given (with details on the derivation given in Appendix A), upon which analytical approximations are made that allow explicit forms for the energies to be obtained.

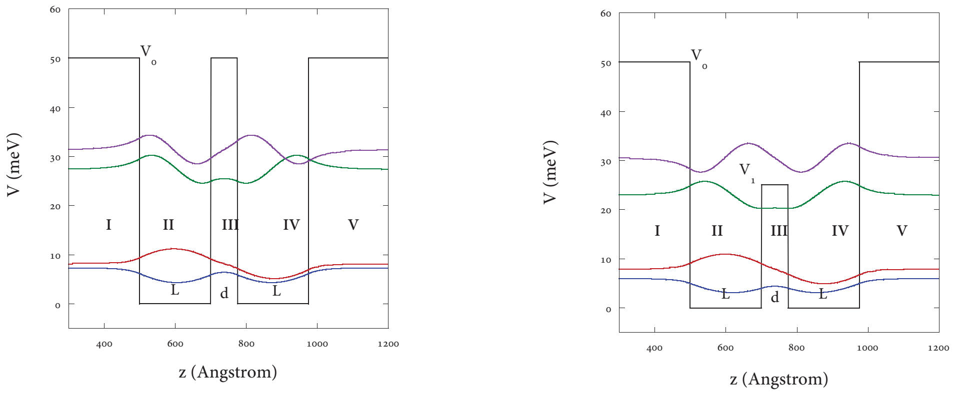

(a)

(b)

Figure 3.15: Examples of possible finite 1D double well systems, including the (a) the (fully) symmetric double quantum well (DSQW), and (b) the asymmetric double quantum well (ADSQW).

Figure 3.15 (a) shows the potential energy of the DSQW, with equal well widths $L$ and barrier width $d$, and with all barrier heights equal to $V_0$. Also shown is Fig. 3.15 (b) the case of the finite double quantum well for which the middle barrier height $V_1$ is $V_1 < V_0$. The finite DQW with variable middle barrier height, but with unequal well widths (Fig. 3.16 (a)), and the DQW with unequal barrier heights and unequal well and barrier widths (Fig. 3.16 (b)), are also possible. The value $z = 0$ is taken at the center of the middle barrier. In this section only the fully symmetric DQW is studied.

$$V(z) = \begin{cases} V_0, & -\infty < z < -L,\ -d/2 < zd/2,\ L < z < \infty; \\ \\ 0, & -L < z < -d/2,\ d/2 < z < L \end{cases} \tag{3.104}$$

The range of the potential is split up and denoted by the roman numerals I through V, and the TISE is given by the following forms

$$\frac{-\hbar^2}{2m^*}\frac{d^2\psi(z)}{dz^2} = E\psi(z) \qquad \text{(II,IV)} \tag{3.105}$$

$$\frac{-\hbar^2}{2m^*}\frac{d^2\psi(z)}{dz^2} = (V_0 - E)\psi(z) \qquad \text{(I,III,V)} \tag{3.106}$$

or in terms of the quantities $k$ and $\kappa$ as

$$\frac{d^2\psi(z)}{dz^2} = k^2\psi(z) \qquad \text{(II,IV)} \tag{3.107}$$

$$\frac{d^2\psi(z)}{dz^2} = \kappa^2\psi(z) \qquad \text{(I,III,V)} \tag{3.108}$$

where

$$k = \sqrt{\frac{2m^*E}{\hbar^2}} \qquad \kappa = \sqrt{\frac{2m^*(V_0 - E)}{\hbar^2}} \tag{3.109}$$

The wavefunctions of the SDQW in regions I,III,V are denoted by

$$\psi_I(z) = Ae^{\kappa z} + Be^{-\kappa z} \tag{3.110}$$

$$\psi_{III}(z) = Ce^{\kappa z} + De^{-\kappa z} \tag{3.111}$$

$$\psi_V(z) = Fe^{\kappa z} + Ge^{-\kappa z} \tag{3.112}$$

and in regions II,IV

$$\psi_{II}(z) = H\cos\left\{k\left[z + \left(\frac{L}{2} + \frac{d}{2}\right)\right]\right\} + I\sin\left\{k\left[z + \left(\frac{L}{2} + \frac{d}{2}\right)\right]\right\} \tag{3.113}$$

$$\psi_{IV}(z) = J\cos\left\{k\left[z-\left(\frac{L}{2}+\frac{d}{2}\right)\right]\right\} + K\sin\left\{k\left[z-\left(\frac{L}{2}+\frac{d}{2}\right)\right]\right\} \tag{3.114}$$

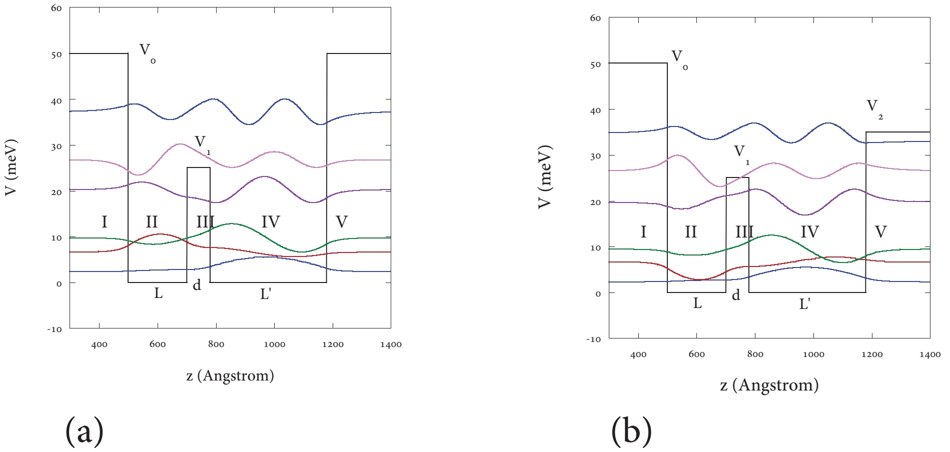

Figure 3.16: Examples of possible finite 1D double well systems, including the (a) the (fully) symmetric double quantum well (DSQW), and (b) the asymmetric double quantum well (ADSQW).

As detailed in the appendix, the solution for the energie of the DSQW are given by

$$(\kappa + k\cot(kL/2)(\kappa - k\tan(kL/2) = \pm(k^2+\kappa^2)e^{-\kappa d} \tag{3.115}$$

Multiplying through by $L/2$ and rearranging gives

$$\beta - \alpha\tan\alpha = \pm\frac{(\alpha^2+\beta^2)}{(\beta+\alpha\cot\alpha)}\gamma, \qquad \gamma \equiv e^{-\kappa d} \tag{3.116}$$

where $\alpha = \sqrt{(2m^*E)/\hbar^2}(L/2)$ and $\beta = \sqrt{(2m^*(V_0-E))/\hbar^2}(L/2)$ (see Eq. (3.4)). Considering the 'zeroth' order, $\gamma \to 0$, Eq. (3.116) is then

$$\beta - \alpha\tan\alpha = 0 \qquad \Longrightarrow \qquad \frac{\beta}{\alpha} = \tan\alpha \tag{3.117}$$

and this resulting zeroth-order solution is just Eq. (3.5), that of the single SQW for the *even* wavefunctions. Next, to first-order in $\gamma$, Eq. (3.116) gives

$$\beta - \alpha \tan\alpha = \pm \frac{(\alpha^2+\beta^2)}{(\beta + \alpha\cot\alpha)}\gamma, \tag{3.118}$$

and using the zeroth-order expression for $\beta/\alpha$ above,

$$\beta - \alpha \tan\alpha = \pm \frac{(\alpha^2+\beta^2)}{(\beta + \frac{\alpha}{\beta/\alpha})}\gamma, \tag{3.119}$$

$$\beta - \alpha \tan\alpha = \pm \frac{(\alpha^2+\beta^2)}{\frac{1}{\beta}(\alpha^2+\beta^2)}\gamma,$$

or

$$\beta - \alpha\tan\alpha = \pm\beta\gamma, \qquad \Longrightarrow \qquad \alpha\tan\alpha = \beta\lambda, \qquad \lambda \equiv (1 \mp \gamma) \tag{3.120}$$

Note this has the same form as that of Eq. (3.5). A solution to this equation for the eigenvalues of the DSQW can be found by the graphical method outlined in detail in the Appendix A as follows.

$$\tan\alpha = \frac{\beta\lambda}{\alpha}, \qquad \Longrightarrow \qquad \tan^2\alpha = \frac{P^2 - \alpha^2\lambda^2}{\alpha^2} \qquad \Longrightarrow \qquad \sec^2\alpha - 1 = \frac{P^2\lambda^2 - \alpha^2\lambda^2}{\alpha^2}$$

$$\approx \sec^2\alpha = \frac{P^2\lambda^2}{\alpha^2} \qquad \Longrightarrow \qquad |\cos\alpha| = \frac{\alpha}{P\lambda} \tag{3.121}$$

where the assumption $\lambda \approx 1$ has been made. This is a reasonable one as this implies that $V_0$ be large and/or $d$ be large which is the case for many realistic situations. The error incurred from this will be shown below. Now, from the graphical method (see Appendix A), $|\cos\alpha|$ can be approximately written as

$$|\cos\alpha| = \frac{\alpha}{P\lambda} \qquad \Longrightarrow \qquad \frac{n\pi}{2} - \alpha_n = \frac{\alpha_n}{P\lambda} \qquad \Longrightarrow \qquad \frac{n\pi}{2} = \alpha_n\left(1 + \frac{1}{P\lambda}\right) \tag{3.122}$$

Now invoking the idea of the effective length (which was similarly introduced for the SQW), this can be recast as

$$n\pi = kL', \qquad L' \equiv L\left(1 + \frac{1}{p\lambda}\right) \tag{3.123}$$

and expressing $k$ in terms of $E$, this is written

$$k = \frac{n\pi}{L'} \qquad \Longrightarrow \qquad \sqrt{\frac{2m^*E}{\hbar^2}} = \frac{n\pi}{L'} \qquad \Longrightarrow \qquad E_n = \frac{(n\pi\hbar)^2}{2m^*L'^2} \tag{3.124}$$

This expression for $E_n$ is identical in form to that of the ISW, Eq. (3.1). The approximated eigenenergies of the SDQW for the *even states* (+) can therefore be written as

$$E_n^+ = E_{n,\infty}\left(\frac{1}{1+\frac{1}{P(1\mp\gamma)}}\right)^2, \qquad \gamma \equiv e^{-\kappa d} \tag{3.125}$$

where $\lambda$ has been rewritten in terms of the well-strength $P$, and the energies depend explicilty in terms of the middle barrier width $d$.

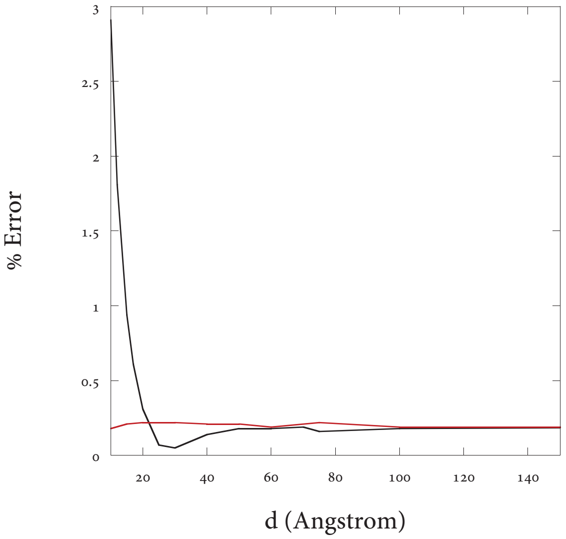

Figure 3.17: The percentage error in using Eqs. (3.125) and (3.128) to calculate the even and odd state energies of the DSQW, as a function of the middle barrier width $d$, for the case of $L$=200 Å and barrier height $V_0$=250 meV.

Similarly, for the *odd states*, starting with Eq. (3.116), and performing the same iteration, gives

$$\cot\alpha = -\frac{\beta\lambda}{\alpha}, \qquad \Longrightarrow \qquad \cot^2\alpha = \frac{P^2 - \alpha^2\lambda^2}{\alpha^2} \qquad \Longrightarrow \qquad \csc^2\alpha - 1 = \frac{P^2\lambda^2 - \alpha^2\lambda^2}{\alpha^2}$$

$$\approx \csc^2\alpha = \frac{P^2\lambda^2}{\alpha^2} \qquad \Longrightarrow \qquad |\sin\alpha| = \frac{\alpha}{P\lambda} \tag{3.126}$$

and

$$|\sin\alpha| = \frac{\alpha}{P\lambda} \qquad \Longrightarrow \qquad n\pi - \alpha_n = \frac{\alpha_n}{P\lambda} \qquad \Longrightarrow \qquad n\pi = \alpha_n\left(1 + \frac{1}{P\lambda}\right) \tag{3.127}$$

and the approximated eigenenergies for the *odd states* (-) are

$$E_n^- = 4E_{n,\infty}\left(\frac{1}{1+\frac{1}{P(1\mp\gamma)}}\right)^2, \qquad \gamma \equiv e^{-\kappa d} \tag{3.128}$$

Using Eqs. (3.125) and (3.128), approximate energies for the even and odd states $E_1^+$, $E_1^-$ of the DSQW system are found. Fig (3.17) shows the % error compared with the exact values found from the transcendental equation, (3.115). The case used was for a DSQW of well width $L$=200 Å and height $V_0$=250 meV,

### 3.5.1 Resonant Coupling in Double Quantum Wells

---

When two (or more) quantum wells, with discrete energy levels, are close to each other, there is a non-zero coupling that exists, and leads to very interesting physics. Fig. (3.18) shows a schematic of a situation in which there is a coupling in a DQW system, with $E_0$ denoting the energy of the corresponding isolated QW, and $E_1$ and $E_2$ denoting the energies of the coupled system.

In Figure (3.18) the states presented between cases a) and b), and between c) and d) are the *time-independent* eigenstates of the DQW, and represent equal probabilities to be in each well. This can be seen from the $|\psi_1(z)|^2$ and $|\psi_2(z)|^2$ of each state, which have a maximum probability in the center

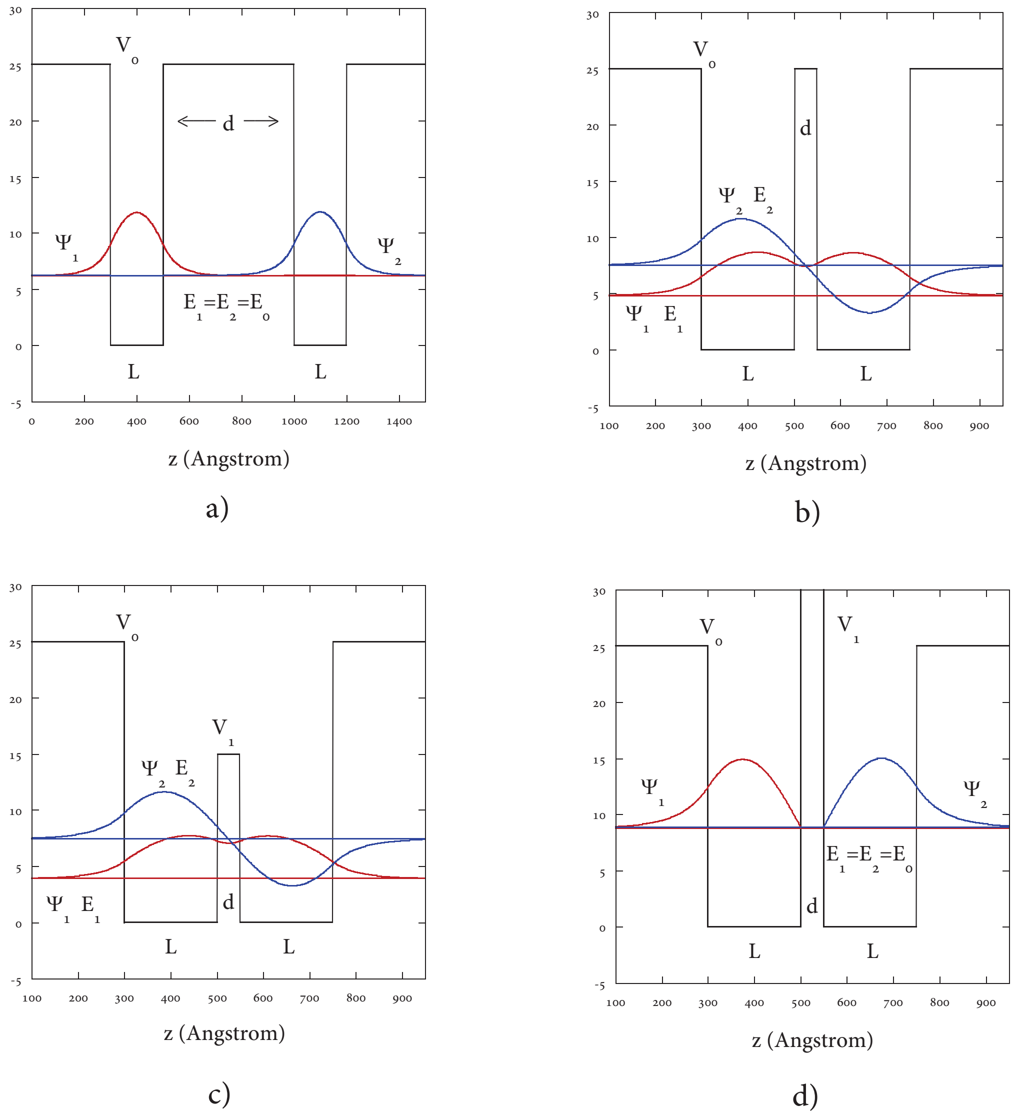

a)

b)

c)

d)

Figure 3.18: Schematic of the coupling between energy levels in a DQW system. a), b) When the middle barrier width is much larger than the individual well widths, $d >> L$, (with the barrier heights equal) the coupling $\approx 0$ and the energies of the DQW, $E_1 \approx E_2 \approx E_0$, where $E_0$ is the energy of the uncoupled, isolated well. As $d$ is made smaller, the initially doubly degenerate levels split into two levels, with the symmetric wave function having a lower energy than the antisymmetric wave function. c), d) For the case in which $d$ is fixed, and the middle barrier height $V_1 >> V_0$, a similar situation arises. Note that in the cases a) and b), the degenerate level $E_0$ is more or less the average of the energies $E_1$ and $E_2$. However in the cases c) and d), the level $E_0$ has risen substantially, comparitively. d) shows the limit in which the single ASQW is achieved, while in a) the limit of two single SQW's is obtained. The levels for the cases a) and b) are *not* equal to those in cases c) and d).

of each respective well. However, realistically, a particle (or wavepacket description of one) will be in *either* one of wells at any given time. That is, there is an oscillation of the probability $|\psi(z,t)|^2$ between the two wells with some frequency $\omega$. To gain an understanding of this time-dependence, consider the sum of the symmetric and antisymmetric states at $t = 0$. If we start with the example given in Fig. (3.18 b), arbitrarily, then

$$\Psi(z,t) = \frac{1}{\sqrt{2}}\left(\psi_s(z)e^{iE_1t/\hbar} + \psi_a(z)e^{iE_2t/\hbar}\right) \tag{3.129}$$

and for $t = 0$

$$\Psi(z,0) = \frac{1}{\sqrt{2}}\left(\psi_s(z) + \psi_a(z)\right) \tag{3.130}$$

and due to the parity, on the right side of the DQW, a cancellation occurs, and in the left well a 'build-up' of the wavefunction occurs, representing a localization of the particle in the left side at $t = 0$. Taking the square of the absolute value of $\Psi(z,t)$,

$$|\Psi(z,t)|^2 = \frac{1}{2}\left[\psi_s(z)e^{iE_1t/\hbar} + \psi_a(z)e^{iE_2t/\hbar}\right]\left[\psi_s^*(z)e^{-iE_1t/\hbar} + \psi_a^*(z)e^{-iE_2t/\hbar}\right]$$

$$|\Psi(z,t)|^2 = \frac{1}{2}\left[|\psi_s(z)|^2 + |\psi_a(z)|^2 + \psi_a(z)\psi_s^*(z)e^{i(E_2-E_1)t/\hbar} + \psi_s\psi_a^*(z)e^{i(E_2-E_1)t/\hbar}\right]$$

$$|\Psi(z,t)|^2 = \frac{1}{2}\left[|\psi_s(z)|^2 + |\psi_a(z)|^2 + \psi_s\psi_a^*(z)\cos(\frac{\Delta Et}{\hbar})\right]$$

or

$$|\Psi(z,t)|^2 = \frac{1}{2}\left[|\psi_s(z)|^2 + |\psi_a(z)|^2 + \psi_s\psi_a^*(z)\cos(\omega t)\right] \tag{3.131}$$

where $\Delta E = E_2 - E_1$ and $\omega = \Delta E/\hbar$ is the frequency of the oscillation of the probability. Fig. (3.19)

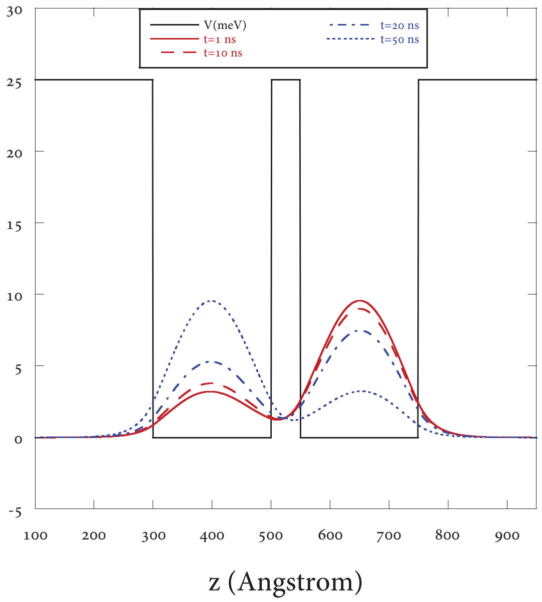

Figure 3.19: Example showing the oscillation of the probability in the DSQW.

## 3.6 The Finite Symmetric Quantum Well with Particles

---

The Poisson eq. for the three-dimensional charge density $n(z)$ is

$$\frac{d^2V_H}{dz^2} = -\frac{4\pi e^2}{\epsilon}n(z) = -\frac{4\pi e^2}{\epsilon}\left(n_s|\psi(z)|^2\right) \tag{3.132}$$

where $V_H$ is the Hartree potential, $\epsilon$ is the permittivity of the material (for GaAs, $\epsilon = 13.1$), and $n_s$ is the areal density of the QW, which can be determined explicity. For the SQW, it has been empirically determined that for moderately doping ($n_d\ 1x10^{-6}A$) the ground-state wavefunction $\psi$ (in the presence of charge) could be reasonably modeled by

$$\psi(z) = A - Bz^2 - Cz^4 \tag{3.133}$$

Using this in the Poisson eq. (3.132),

$$\frac{d^2V_H}{dz^2} = -\frac{4\pi e^2}{\epsilon}\left(n_s(A - Bz^2 - Cz^4)^2\right) \tag{3.134}$$

$$\frac{d^2V_H}{dz^2} = -\frac{4\pi e^2}{\epsilon}\left(n_s(A - Bz^2 - Cz^4)^2\right)$$

and

$$\frac{d^2V_H}{dz^2} = -\frac{4\pi e^2}{\epsilon}\left(n_s(A - Bz^2 - Cz^4)^2\right)$$

and keeping only three terms,

$$\frac{d^2V_H}{dz^2} = -\frac{4\pi e^2}{\epsilon}\left(n_s(A - Bz^2 - Cz^4)^2\right) \tag{3.135}$$

The results here show that for a (symmetrically) doped SQW, the bottom of the potential well is very well described as a cosine function of the position.

# Bibliography

[1] C. Cohen-Tannoudji, B. Diu, and F. Laloe, *Quantum Mechanics* (Wiley-Interscience, New York, 1977) vol 1, pp. 74-78.

[2] R. Eisberg, R. Resnick, *Quantum Physics of Atoms, Molecules, Solids, Nuclei, and Particles* (Wiley, New York, 1987), pp. G1-G6.

[3] M. A. Morrison, *Understanding Quantum Physics* (Prentice-Hall, Englewood Cliffs, NJ, 1990), pp. 319-340.

[4] R. Gilmore, *Elementary Quantum Mechanics In One Dimension* (Johns Hopkins University Press, Baltimore, MD, 2004), pp. 91-104.

[5] D. J. Griffiths, *Introduction to Quantum Mechanics* (Prentice-Hall, Englewood Cliffs, NJ, 1995), pp. 60-62.

[6] P. H. Pitkanen, "Rectangular potential well problem in quantum mechanics," Am. J. Phys., **23**, 111-113 (1955).

[7] C. D. Cantrell, "Bound-state energies of a particle in a finite square well: an improved graphical solution," Am. J. Phys., **39**, 107-110 (1971).

[8] P. G. Guest, "Graphical solutions for the square well," Am. J. Phys., **40**, 1175-1176 (1972).

[9] R. D. Murphy, J. M. Phillips, "Bound-state eigenvalues of the square-well potential," Am. J. Phys., **44** (6), 574-576 (1976).

[10] S. Garrett, "Bound state energies of a particle in a finite-square well: a simple approximation," Am. J. Phys., **47** (2), 195-196 (1978).

[11] C. E. Siewert, "Explicit results for the quantum-mechanical energy states basic to a finite square-well potential," J. Math. Phys., **19** (2), 434-435 (1978).

[12] E. J. Burge, “Improved simple graphical solution for the eigenvalues of the finite square well potential,” Eur. J. Phys., **6**, 154-164 (1985).

[13] B. C. Reed, “A single equation for finite rectangular well energy eigenvalues,” Am. J. Phys., **58** (5), 503-504 (1990).

[14] B. I. Barker, G. H. Rayborn, J. W. Ioup, and G. E. Ioup, “Approximating the finite square well with an infinite well: energies and eigenfunctions,” Am. J. Phys., **59** (11), 1038-1041 (1991).

[15] D. W. L. Sprung, H. Wu, J. Martorell, “A new look at the square well potential,” Eur. J. Phys., **13**, 21-25 (1992).

[16] D. W. L. Sprung, H. Wu, J. Martorell, “Poles, bound states, and resonances illustrated by the square well potential,” Am. J. Phys., **64** (2), 136-144 (1996).

[17] J. V. Mallow, “Simple graphical solution for the finite square well with no change of variables,” Am. J. Phys., **64** (8), 1072-1073 (1996).

[18] D. S. Rokhsar, “Ehrenfest’s theorem and the particle-in-a-box,” Am. J. Phys., **64** (11), 1416-1418 (1996).

[19] D. L. Aronstein, C. R. Stroud, Jr., “General series solutions for finite square-well energy levels for use in wave-packet studies,” Am. J. Phys., **68** (10), 943-949 (2000).

[20] O. F. de Alcantara Bonfim, D.J. Griffiths, “Exact and approximate energy spectrum for the finite square well and related potentials,” Am. J. Phys., **74** (1), 43-48 (2006).

[21] A. Yariv, C. Lindsey, U. Sivan, “Approximate analytic solution of electronic wave functions and energies in coupled quantum wells,” J. Appl. Phys., **58** (9), 3669-3672 (1985).

[22] K. A. Bulashevich, S. Yu. Karpov, R. A. Suris, “Analytical model for the quantum-confied Stark effect including electric field screening by non-equilibrium carriers,” Phys. stat. sol. (b), **243** (7), 1625-1629 (2006).

[23] L. L. Chang, L. Esaki, R. Tsu, "Resonant tunneling in semiconductor barriers," Appl. Phys. Lett., **24** (10), 593-595 (1974).

[24] J. Faist, F. Capasso, D. L. Sivco, A. L. Hutchinson, C. Sirtori, S. N. G. Chu, A. Y. Cho, "Quantum cascade laser: Temperature dependence of the performance characteristics and high $T_0$ operation," Appl. Phys. Lett., **65** (23), 2901-2903 (1994).

[25] H. C. Liu, *Quantum well infrared photodetector physics and novel devices, Intersubband Transition in Quantum Wells: Physics and Device Applications I.* In: H.C. Liu and F. Capasso, Editors, *Semiconductors and Semimetals* vol. 62, (Academic Press, San Diego, 2000).

[26] A. S. Davydov, *Quantum Mechanics* (Pergamon Press, Oxford, 1965), pp. 88-90.

[27] L. D. Landau, L. Lifshitz, *Quantum Mechanics* (Pergamon Press, Oxford 1958), pp. 61-64.

[28] T. Yamaguchi, M. Kato, K. Tada, "A new variational method for calculating eigen energy in various quantum wells on the basis of effective well width," IEEE Conference Proceedings, Lasers and Electro-Optics Society Annual Meeting (LEOS '94), (2), 293-294 (1994).

[29] W. Squire, "Landen's solution of the cubic," Am. J. Phys., **55** (4), 374-375 (1987).

[30] V. Namias, "Simple derivation of the roots of a cubic equation," Am. J. Phys., **53** (8), 775 (1985).

[31] J. P. McKelvey, "Simple transcendental expressions for the roots of cubic equations," Am. J. Phys., **52** (3), 269-270 (1984).

[32] J. H. Davies, *The Physics of Low-Dimensional Semiconductors: An Introduction* (Cambridge University Press, Cambridge, UK, 1998), pp. 142-146.

[33] A. Messiah, *Quantum Mechanics* (John Wiley and Sons, 1958), pp. 88-91.

[34] D. Ter Harr, *Selected Problems in Quantum Mechanics* (Academic, New York, 1964), pp. 47-49.

[35] J. F. Bloch, V. Ignatovich, "A new approach to bound states in potential wells," Am. J. Phys., **69** (11), 1177-1181 (2001).

[36] A. Ganguly, S. Kuru, J. Negro, L.M. Nieto, “A study of the bound states for square potential wells with position-dependent mass,” Phys. Lett. A., **360**, 228-233 (2006).

[37] D. D. Coon, R. P. G. Karunasiri, “New mode of IR detection using quantum wells,” Appl. Phys. Lett., **45**, 649-651 (1984).

[38] K. Araki, “Analysis of barrier transmission in resonant tunneling diodes,” J. Appl. Phys., **62**, 1059-1069 (1987).

[39] T. K. Gaylord, K.F. Brennan, “Electron wave optics in semiconductors,” J. Appl. Phys., **65** (2), 814-820 (1989).

[40] T. K. Gaylord, E.N. Glytsis, K.F. Brennan, “Semiconductor quantum wells as electron wave slab waveguides,” J. Appl. Phys., **66** (4), 1842-1848 (1989).

[41] R. Q. Yang, J. M. Xu, “Energy-dependent electron wave coupling between two asymmetric quantum well waveguides,” J. Appl. Phys., **59**, 315-317 (1991).

[42] S. L. Chuang, B. Do, “Electron states in two coupled wells-A strong coupling-of-modes approach,” J. Appl. Phys., **62**, 1290-1297 (1987).

[43] J. J. Butler, T. Pierce, P. Bakshi, “Practical approximations for wave functions and energies of the single quantum wells: I. The symmetric quantum well,” to be published.

[44] C. Lien, Y. Huang, H. Chien, W. Wang, “Charge control model of the double delta-doped quantum-well field-effect transistor,” IEEE Trans. Electron Devices, **41** (8), 1351-1356 (1994).

[45] H. Morkoc, J. Chen, U.K. Reddy, S. Luryi, “,” Appl. Phys. Letters, **49** (70), (1986).

[46] E.E. Mendez, E. Calleja, C.E.T. Goncalves da Silva, L.L. Chang and W.I. Wang, “,” Phys. Rev. B, **33** 7368 (1986).

[47] M. Heiblum, M.V. Fischetti, W.P. Dumke, D.J. Frank, I.M. Anderson, C.M. Knoedler, and L. Osterling, “Electron interference effects in quantum wells: Observation of bound and resonant states,” Phys. Rev. Let., 58 **8** 7368 (1987).

## Chapter 4

# Tunneling Transmission

---

The concept of tunneling through a potential barrier illustrates a fundamental principle of quantum theory, the wave-like property of matter. Tunneling was introduced into solid state physics in 1928 by Fowler and Nordheim [1], and by Oppenheimer [2] in an attempt to describe field emission from metals. Zener [3], in 1934 described the internal field emission in semiconductors, and tunneling between the valence and conduction bands of a semiconductor p-n junction diode was reported by Esaki in 1958 [4]. The examples cited here essentially involved a triangular-shaped barrier. The first observation of *resonant tunneling* through double-barrier resonant tunneling structures (DBRTS) by Tsu, Esaki and Chang [5, 6] in the early 1970's attracted much interest due to their potential applications [7, 8, 9] and the potential opportunities they offer for both theoretical and experimental study of quantum effects and tunneling processes [10, 11].

A theoretical treatment of tunneling was done by Bohm [12] in 1951 using the WKB approximation. A thorough review of the tunneling phenomena in solids was given by Duke [13], and a more recent review of tunneling in semiconductors done by Price [14]. After the advent of molecular beam epitaxy for compound semiconductor crystal growth techniques, electron tunneling was predicted for an AlGaAs/GaAs/AlGaAs double barrier heterostructure based on the electron wave resonance [5]. A “particle” picture in which an electron is constrained inside the GaAs quantum well, can describe the dwell time (before escaping into the anode region), with a bias-dependent tunneling current through the structure, showing a negative differential resistance as a result of the resonant tunneling. This process is quantitatively described by the transmission and reflection of electron waves through the structure [15].

In this chapter, the transmission probability of *single barriers* is studied: the single symmetric rectangular barrier, the triangular barrier, and the single asymmetric rectangular barrier. An important and *new* result is an exact mapping from the rectangular barrier result to that of the triangular barrier. Through this mapping an effective barrier width and barrier strength is found, for the triangular barrier. As in the previous chapter, the Appendix B gives the full details of the derivations, while only the most relevant details are given here.

## 4.1 The Symmetric Single Rectangular Barrier

---

In this section the matrix elements for the transmission through a single symmetric rectangular barrier are derived. The single rectangular barrier is a well-known one, and is important in illustrating the use of the transfer matrices. The results obtained here can then be used for the case of the symmetric double barrier, the triple barrier and the superlattice, in which there are many similar barriers in succession. Particles encountering barriers and other obstacles must be handled appropriately through the *transfer matrix* [16], in which the potential of interest is divided into piece-wise constant regions, as shown in Fig. 4.1.

Fig. 4.2 gives the picture of the single barrier studied here. The potential only exists between $z = -d$ and $z = d$,

$$V(z) = \begin{cases} 0, & z < -d, \\ V_0, & -d < z < d, \\ 0, & z > d, \end{cases} \tag{4.1}$$

with both incoming and outgoing waves on either side of the barrier described by propagating waves $k^2 = (2m^*E)/\hbar^2$, while in the barrier the waves are attenuated, with $\kappa^2 = (2m^*(V_0 - E))/\hbar^2$. The wavefunction is given in general by

$$\psi(z) = \begin{cases} A_1 e^{ikz} + B_1 e^{-ikz}, & z < -d, \\ A_2 e^{\kappa z} + B_2 e^{-\kappa z}, & -d < z < d, \\ A_3 e^{ikz} + B_3 e^{-ikz}, & z > d, \end{cases} \tag{4.2}$$

where $A_i$'s and $B_i$'s are the amplitudes of the waves. Applying the boundary and continuity equations results in a matrix expression for the transmission and reflection coefficients (see Appendix B for details), the relevant matrix elements $M_{11}^{sb}$ and $M_{21}^{sb}$ are given as

$$M_{11}^{sb} = \left[\cosh(2\kappa d) - \frac{i}{2}\frac{k^2 - \kappa^2}{k\kappa}\sinh(2\kappa d)\right] e^{2ikd}, \quad \text{single symmetric barrier} \tag{4.3}$$

and

$$M_{21}^{sb} = -\frac{i}{2}\frac{k^2 - \kappa^2}{k\kappa}\sinh(2\kappa d), \quad \text{single symmetric barrier} \tag{4.4}$$

The tunneling transmission probability $T(E)$ is given by

$$T = \frac{1}{|M_{11}|^2} \quad \Longrightarrow \quad = \left[\cosh^2(2\kappa d) + \left(\frac{k^2 - \kappa^2}{2k\kappa}\right)^2 \sinh^2(2\kappa d)\right]^{-1} \tag{4.5}$$

or

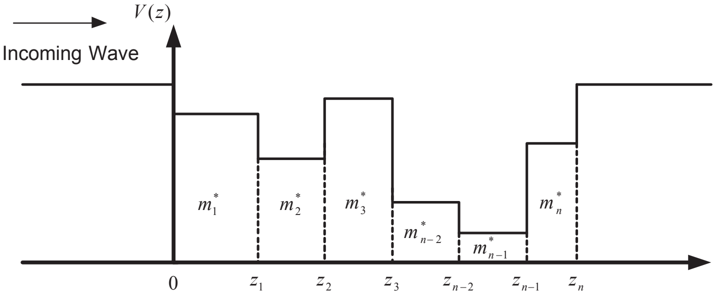

Figure 4.1: Illustration of the transfer matrix method by dividing up the potential into segemnts.

$$T = \frac{1}{1 + \left(\frac{k^2+\kappa^2}{2k\kappa}\right)^2 \sinh^2(2\kappa d)} \qquad (E < V_0) \tag{4.6}$$

$$T = \frac{1}{1 + \left(\frac{k^2-k'^2}{2kk'}\right)^2 \sin^2(2k'd)} \qquad (E > V_0) \tag{4.7}$$

where the second equation accounts for above the barrier transmission, with $\kappa \to ik'$, and $k'^2 = 2m^*(E - V_0)/\hbar^2$. The overall behavior of the tunneling coefficient is shown in Fig. 4.2. Eqns. (4.6) and (4.7) can be expressed in terms of the energy variables, as

$$T^{-1} = 1 + \frac{V_0^2}{4E(V_0 - E)} \sinh^2(2\kappa d) \qquad (E < V_0) \tag{4.8}$$

$$T^{-1} = 1 + \frac{V_0^2}{4E(E - V_0)} \sin^2(2k'd) \qquad (E > V_0) \tag{4.9}$$

By introducing the scaled energy $\epsilon$ and barrier strength parameter $Q$, defined by

$$\epsilon = (E/V_0) \qquad\qquad Q = 2dk_0 = 2d\sqrt{2m^*V_0/\hbar^2} \tag{4.10}$$

the transmission coefficient is seen to be a function of only two variables, $\epsilon$ and $Q$,

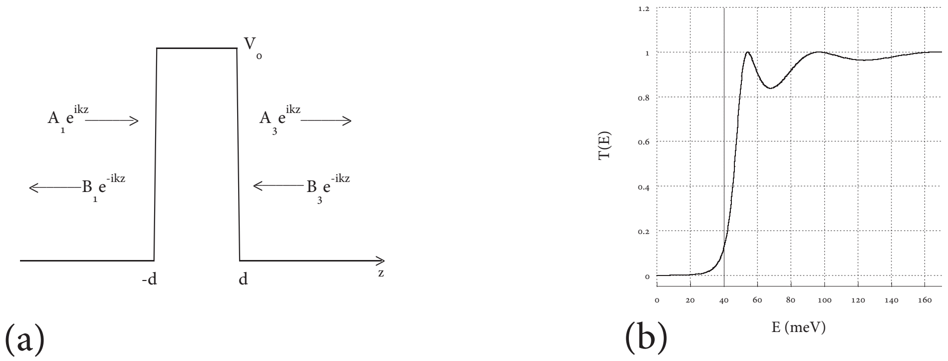

Figure 4.2: The single rectangular barrier of total width $2d$, and height $V_0$. The tunneling transmission probability $T(E)$ as a function of the energy, in meV. $T(E)$ pictured at right for a barrier of $V_0$=40 meV, and width 100 Å.

$$T^{-1}(\epsilon, Q) = 1 + [4\epsilon(1-\epsilon)]^{-1}\sinh^2(Q\sqrt{1-\epsilon}) \qquad \epsilon < 1 \tag{4.11}$$

$$T^{-1}(\epsilon, Q) = 1 + [4\epsilon(\epsilon-1)]^{-1}\sin^2(Q\sqrt{\epsilon-1}) \qquad \epsilon > 1 \tag{4.12}$$

Thus all rectangular barriers of equal strengths $Q$ have the same transmission coefficient at the same scaled energy. This is a mapping from a barrier of potential height $V_0$ and width $2d$ (strength $Q$) to a barrier of height $V_0'$ and width $2d'$ such that $Q'$=$Q$, for corresponding energies $E = \epsilon V_0$ and $E' = \epsilon V_0'$. The particular functional form of $T$ is characteristic of the *shape* of the potential, i.e., it is the same for *all* rectangular barriers. We will show in the section this universality property, $T = T(\epsilon, Q)$, is valid for any barrier shape. The Schrӧdinger equation can be cast into a dimensionless form in terms of $\epsilon$ and $Q$, $V_0$ being the maximum value of the potential and $2d$ the spatial extent of the potential. The particular functional form of $T(\epsilon, Q)$ depends on the shape of the potential, and for example will differ from Eq. (4.11) for a triangular barrier, $\mathrm{T}_{triangle}(\epsilon, Q) \neq \mathrm{T}_{rectangle}(\epsilon, Q)$. This raises the interesting question: Is it possible to find a mapping from one shape to another by defining an 'equivalent' strength parameter for the other shape? Can we have $\mathrm{T}_{triangle}(\epsilon, Q) = \mathrm{T}_{rectangle}(\epsilon, Q')$

for some suitably defined $Q'$?

## 4.2 The Triangular Barrier

---

Consider a triangular barrier defined by

$$V(z) = \begin{cases} 0, \quad z < 0, \\ V_0(z/L), \quad 0 < z < L, \\ 0, \quad z > L, \end{cases} \tag{4.13}$$

The Schrö̈dinger equation for energy $E$ is given by

$$-\frac{\hbar^2}{2m}\frac{d^2}{dz^2}\psi(z) + V_0(z/L)\psi(z) = E\psi(z), \qquad 0 < z < L, \tag{4.14}$$

Let $E = (\hbar^2/2m)k^2$, $V_0 = (\hbar^2/2m)K_0^2$, $y = z/L$, $\epsilon = E/V_0$, and $Q = K_0 L = L\sqrt{2mV_0/\hbar^2}$ and Eq. (4.14) reduces to

$$\frac{d^2}{dy^2}\psi(y) = \begin{cases} Q^2(y-\epsilon)\psi(y), & 0 < y < 1, \\ -\epsilon Q^2\psi(y), & \text{outside} \end{cases} \tag{4.15}$$

Note $\epsilon Q^2 = k^2L^2$ and the outside solutions are $exp(\pm ikLy) = exp(\pm ikz)$. It is clear from Eq. (4.15) $\psi(y) = \psi(y;\epsilon, Q)$ and the transmission coefficient obtained from solving this equation with appropriate boundary conditions can only be a function of $\epsilon$ and $Q$. All triangular barriers with different

$V_0$ and $L$, but with the same strength parameter $Q$ will lead to identical transmission coefficients at the same scaled energy $\epsilon$.

A further change of variables

$$\xi = (y - \epsilon)Q^{2/3} \tag{4.16}$$

converts Eq. (4.15) to the standard Airy equation in the interval $y = (0, 1)$ or $z = (0, L)$,

$$\frac{d^2}{d\xi^2}\psi = \xi\psi \tag{4.17}$$

and outside this interval we have

$$\frac{d^2}{d\xi^2}\psi = -\epsilon Q^{2/3}\psi \tag{4.18}$$

The solutions in terms of Airy functions of argument $\xi$ are discussed in the next subsection. An arbitrarily-shaped potential $V(z)$ of limited extent (0 to $L$) can also be treated similarly, by defining $V_0 = [V(z)]_{max}$, $y = z/L$, $Q = K_0 L$, and the dimensionless potential $v(y) = V(z)/V_0$. Then the Schr$\ddot{o}$dinger equation is

$$\frac{d^2}{dy^2}\psi(y) = \begin{cases} Q^2(v(y) - \epsilon)\psi(y), & 0 < y < 1, \\ -\epsilon Q^2\psi(y), & \text{outside} \end{cases} \tag{4.19}$$

and the resulting transmission coefficients will also have the form $T = T(\epsilon, Q)$. All similar potentials obtained by scaling $V(z) \to \lambda V(z)$ and $L \to L/\sqrt{\lambda}$ will preserve $Q$ and thus lead to the same $T(\epsilon, Q)$.

### 4.2.1 The Triangular-Rectangular Barrier Mapping

---

Figure 4.3 shows the triangular potential $(V_0, L)$ and a particle of energy $E$. It is clear that the higher the energy, the lesser the obstruction due to the barrier will be. The effective distance traversed through the barrier is only $L(1-(E/V_0)) = L(1-\epsilon)$. We can relate this situation to a rectangular barrier of width $L_{eff} = L(1-\epsilon)$. The triangular potential has a maximum of $V_0$ only at the tip of $L$, and its value above $E$ diminishes to 0 at $z = L\epsilon$. So a rectangle of height $V_0$ and width $L_{eff}$ will still be a stronger obstruction than this triangle. A further reduction of $L_{eff}$ is required to get the correct effective $V_0$. One way to estimate this is to use the WKB picture, where the relevant measure is $\int \kappa(z)dz$ over the distance inside the triangular barrier:

$$\int_{L\epsilon}^{L} dz\sqrt{\frac{2m}{\hbar^2}}\sqrt{V_0(\frac{z}{L}) - E} \tag{4.20}$$

$$= \frac{2}{3}L(1-\epsilon)\sqrt{\frac{2m}{\hbar^2}(V_0 - E)} \tag{4.21}$$

$$\equiv L_{eff}^{rect.}\sqrt{\frac{2m}{\hbar^2}(V_0 - E)} \tag{4.22}$$

This shows that the equivalent length for the rectangle is further reduced by the factor 2/3. So we can expect a rectangular barrier of height $V_0$ and width $L_{eff}^{rect.} = (2/3)L(1-\epsilon)$ to have a transmission coefficient similar to the triangle under consideration. The corresponding strength parameter for the rectangle will be $Q' = K_0 L_{eff}^{rect.} = Q(2/3)(1-\epsilon) = Qr$. Based on this, we can expect $T_{triangle}(\epsilon, Q) = T_{rectangle}(\epsilon, Q')$, where $Q' = Qr(\epsilon, Q)$, and the strength reduction factor, $r$, could, in general depend on $Q$ also. Since WKB is a good approximation for strong barriers, (i.e. $Q >> 1$), we can expect that for $Q >> 1$, the rectangle $T$ formula, Eq. (4.11) with strength $Q' = rQ$, with $r = (2/3)(1-\epsilon)$ will provide the transmission coefficient for the triangular barrier.

This conjecture can be tested by computer evaluation of the exact transmission coefficient for a triangular barrier of strength $Q$ and determining the effective length or effective strength $Q'$ of

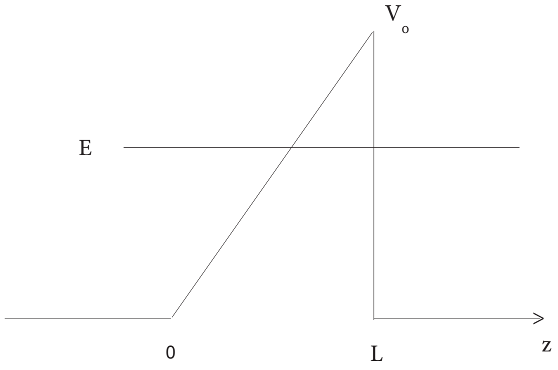

Figure 4.3: The triangular barrier of height $V_0$ and length $L$.

a rectangular barrier that will match that transmission coefficient. This comparison is shown in Fig. 4.4 for several triangular barriers with different $Q$'s. The ratio $r = Q'/Q$ is plotted vs. $\epsilon$, and it shows that indeed $r = (2/3)(1-\epsilon)$ for the case of the largest $Q$. Even for decreasing $Q$, the $r$ curves remain straight lines and the intercept moves from 2/3 to 1/2 and the slope moves from -2/3 to 0 as $Q$ is decreased. A full analysis of Eq. 4.15 in terms of Airy functions is given below.

Consider the triangular barrier, with the wavefunctions defined as

$$\psi(z) = \begin{cases} A_1 e^{ikz} + B_1 e^{-ikz}, \quad z < 0, \\ A_2 Ai(\xi(z)) + B_2 Bi(\xi(z)), \quad 0 < z < L, \\ A_3 e^{ikz}, \quad z > L, \end{cases} \tag{4.23}$$

where $\xi$ is given by Eq. (4.16), and $Ai(\xi)$ and $Bi(\xi)$ are the Airy functions the arise due to the slanted barrier. From the continuity conditions of the wavefunction and its derivative (denoted by primes) at the boundary $z = 0$ we have

$$A_1 + B_1 = A_2 Ai(0) + B_2 Bi(0), \qquad ik(A_1 - B_1) = A_2 Ai'(0) + B_2 Bi'(0) \tag{4.24}$$

and at $z = L$,

$$A_3e^{ikL} = A_2Ai(L) + B_2Bi(L), \qquad ikA_3e^{ikL} = A_2Ai'(L) + B_2Bi'(L) \tag{4.25}$$

Here $Ai(0)$ means $Ai(\xi(0))$ etc. Now taking $A_1 = 1$, and rewriting $A_2$ as $a_2$, $B_1$ as $b_1$, etc. these equations can be written as

$$1 + b_1 = a_2Ai(0) + b_2Bi(0), \qquad ik(1 - b_1) = a_2Ai'(0) + b_2Bi'(0) \tag{4.26}$$

and at $z = L$,

$$a_3e^{ikL} = a_2Ai(L) + b_2Bi(L), \qquad ika_3e^{ikL} = a_2Ai'(L) + b_2Bi'(L) \tag{4.27}$$

From (4.27) we have

$$ik = \frac{a_2Ai'(L) + b_2Bi'(L)}{a_2Ai(L) + b_2Bi(L)} = \left.\frac{Ai' + \rho_2Bi'}{Ai + \rho_2Bi}\right|_L \tag{4.28}$$

where $\rho_2 = b_2/a_2$. Rewriting Eq. (4.28) as

$$ik(Ai + \rho_2Bi) = Ai' + \rho_2Bi' \quad \Longrightarrow \quad (ikAi - Ai') = \rho_2(Bi' - ikBi) \tag{4.29}$$

or

$$\rho_2 = \left.\frac{ikAi - Ai'}{Bi' - ikBi}\right|_L \tag{4.30}$$

For Eq. (4.26),

$$ik\frac{1-b_1}{1+b_1} = \left.\frac{a_2 Ai' + b_2 Bi'}{a_2 Ai + b_2 Ai'}\right|_0 \qquad \Longrightarrow \qquad \left.\frac{Ai' + \rho_2 Bi'}{Ai + \rho_2 Bi}\right|_0$$

or

$$\frac{1-b_1}{1+b_1} = \left.\frac{Ai' + \rho_2 Bi'}{ik(Ai + \rho_2 Bi)}\right|_0 \tag{4.31}$$

and

$$b_1 = \left.\frac{(ikAi - Ai') + \rho_2(ikBi - Bi')}{(ikAi + Ai') + \rho_2(ikBi + Bi')}\right|_0 \tag{4.32}$$

$$= -\left.\frac{(Ai' - ikAi) + \rho_2(Bi' - ikBi)}{(Ai' + ikAi) + \rho_2(Bi' + ikBi)}\right|_0$$

$$b_1 = -\left.\frac{a^* + \rho_2 b^*}{a + \rho_2 b}\right|_0, \qquad a = Ai' + ikAi\Big|_0, \qquad b = Bi' + ikBi\Big|_0 \tag{4.33}$$

Taking the absolute value sqaured,

$$|b_1|^2 = \left.\frac{(a^* + \rho_2 b^*)(a + \rho_2^* b)}{(a + \rho_2 b)(a^* + \rho_2^* b^*)}\right|_0 \tag{4.34}$$

$$|b_1|^2 = \frac{aa^* + \rho_2\rho_2^* bb^* + \rho_2 ab^* + \rho_2^* a^* b}{aa^* + \rho_2\rho_2^* bb^* + \rho_2^* ab^* + \rho_2 a^* b} \tag{4.35}$$

and for the transmission coefficient,

$$T = 1 - |b_1|^2 = \frac{\rho_2^* ab^* + \rho_2 a^* b - (\rho_2 ab^* + \rho_2^* a^* b)}{aa^* + \rho_2\rho_2^* bb^* + \rho_2^* ab^* + \rho_2 a^* b} \tag{4.36}$$

$$T = \frac{ab^*(\rho_2^* - \rho_2) + (\rho_2 - \rho_2^*)a^* b}{aa^* + \rho_2\rho_2^* bb^* + \rho_2^* ab^* + \rho_2 a^* b} \tag{4.37}$$

$$T = \frac{(\rho_2 - \rho_2^*)(a^* b - ab^*)}{aa^* + \rho_2\rho_2^* bb^* + \rho_2^* ab^* + \rho_2 a^* b} \tag{4.38}$$

The numerator can be simplified as follows. The first factor is

$$\rho_2 - \rho_2^* = \frac{ikAi - Ai'}{Bi' - ikBi} - \frac{-ikAi - Ai'}{Bi' + ikBi} \tag{4.39}$$

$$= \frac{ikAi - Ai'}{Bi' - ikBi} + \frac{ikAi + Ai'}{Bi' + ikBi}$$

$$= \frac{(ikAi - Ai')(ikBi + Bi') + (Bi' - ikBi)(Ai' + ikAi)}{(Bi')^2 + k^2(Bi)^2}$$

$$= \left.\frac{2ik(AiBi' - Ai'Bi)}{(Bi')^2 + k^2(Bi)^2}\right|_L$$

Identifying the Wronskian $W(Ai, Bi) \equiv AiBi' - Ai'Bi$, the expression above becomes

$$\rho_2 - \rho_2^* = \frac{2ikW}{(Bi')^2 + k^2(Bi)^2} \tag{4.40}$$

where $W$ the Wronskian is a constant for the Schrodinger equation.

For the second term in the numerator, ($a^*b - ab^* = 2iIm(a^*b)$), and since

$$a^*b = (Ai' - ikAi)(Bi' + ikBi)\Big|_0 \tag{4.41}$$

we have

$$iIm(a^*b) = -ik(AiBi' - Ai'Bi) = -ikW \tag{4.42}$$

or

$$a^*b - ab^* = -2ikW \tag{4.43}$$

Finally, the expression for $T$ above, Eq. (4.38), can be written as

$$T = \frac{2ikW}{(Bi')^2 + k^2(Bi)^2}\;\frac{-2ikW}{aa^* + \rho_2\rho_2^*bb^* + \rho_2^*ab^* + \rho_2a^*b}$$

$$= \frac{4(kW)^2}{(Bi')^2 + k^2(Bi)^2}\;\frac{1}{aa^* + \rho_2\rho_2^*bb^* + \rho_2^*ab^* + \rho_2a^*b} \tag{4.44}$$

For strong barriers ($Q >> 1$), $\rho_2$ and $\rho_2^*$ become very small and only $aa^*$ remains in the second denominator in Eq. (4.34). Also $Bi$ and $Bi'$, which are evaluated at $z = L$ become very large and the asymptotic forms for the $Bi$ and $Bi'$ functions are valid. Then we find

$$T_{triangle}(\epsilon, Q) \Longrightarrow \sqrt{16\epsilon(1-\epsilon)}e^{-2Q\sqrt{1-\epsilon}\ r_0} \tag{4.45}$$

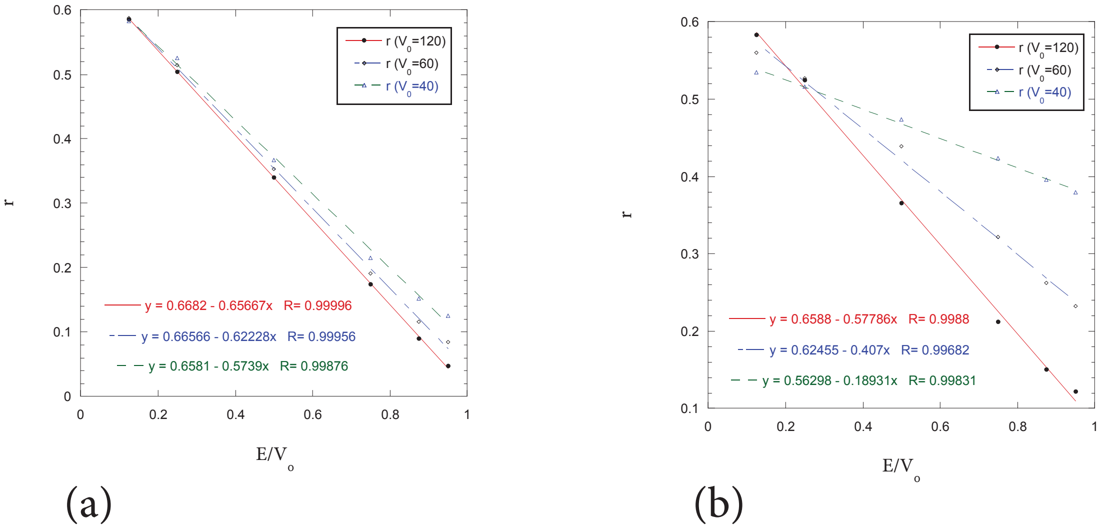

Figure 4.4: Mapping factor $r = r(\epsilon, Q)$ vs. $\epsilon$ for various $Q$ values.

where $r_0 = (2/3)(1-\epsilon)$. In this limit ($Q >> 1$),

$$T_{rect}(\epsilon, Q') \Longrightarrow 16\epsilon(1-\epsilon)e^{-2Q'\sqrt{1-\epsilon}} \tag{4.46}$$

and so the mapping is $Q' = r_0 Q$. This proves that the WKB-based mapping is valid in the lowest order in $1/Q$. For any $Q$ the mapping is given by $Q' = Qr(\epsilon, Q)$ where the $r$-factor is displayed in Fig. 4.4. The analytical form of $r(\epsilon, Q)$ can be determined from detailed analysis of (4.44) in terms of the properties of the Airy functions.

# Bibliography

[1] R.H. Fowler and L.W. Nordheim, "Electron emission in intense electric fields", Proc. Royal Soc. (London) **A119**, pp. 173-181 (1928).

[2] J.R. Oppenheimer, Phys. Rev. **31**, 914 (1928).

[3] C. Zener, Proc. Royal Soc. **A145**, 523 (1934).

[4] L. Esaki, Phys. Rev. **109**, 603 (1958).

[5] R. Tsu, L. Esaki, Appl. Phys. Lett. **22**, 562 (1973).

[6] L.L. Chang, L. Esaki, and R. Tsu, Appl. Phys. Lett. **24** (12), 593 (1974).

[7] E.R. Brown, T.C.L.G. Sollner, W.D. Goodhue, and C.D. Parker, Appl. Phys. Lett. **50**, 83 (1987).

[8] N. Yokohama, K. Imamura, S. Muto, S. Hiyamizu, and H. Nishi, Jpn. J. Appl. Phys. Lett. **24**, L853, (1985).

[9] R.C. Potter, A.A. Lakhani, and H. Hier, J. Appl. Phys. **64**, 3735 (1988).

[10] M. Tsuchiya, T. Matsusue, and H. Sakaki, Phys. Rev. Lett. **59**, 2536 (1987).

[11] C. Weisbuch, and B. Vinter, *Quantum Semiconductor Structures: Fundamentals and Applications* Academic Press, New York (1991).

[12] D. Bohm, *Quantum Theory* Prentice Hall, p. 283 (1951).

[13] C.B. Duke, *Tunneling in Solids: Solid State Physics Supplement 10* (1969).

[14] P.J. Price, *Electron Tunneling in Semiconductors in "Basic Propereties of Semiconductors"* Vol. 1, P.T. Landsberg editor, North Holland, (1992).

[15] H. Mizuta and T. Tonoue, *The Physics and Applications of Resonant Tunneling Diodes* Cambridge Univ. Press, (1995).

[16] R. Gilmore, *Elementary Quantum Mechanics in One Dimension* The Johns Hopkins University Press, (2004).

Chapter 5

# Finite Barrier Width Structures

---

Resonant tunneling-based devices, which utilize electron-wave resonance in potential barriers, have emerged as one of the most important testing grounds for transport physics. Resonant tunneling in semiconductor double barriers was first demonstrated by Chang, Esaki and Tsu in 1974 [1, 2], and since then has become a topic of great interest, investigated both from the standpoints of quantum physics and of its application in functional quantum devices [3]. Over the past three decades, resonant tunneling structures have received a great deal of attention. Despite its simple structure, the resonant tunneling diode (RTD) can reveal various manifestations of quantum transport in semiconductor nanostructures, such as single electron tunneling [4], and enable the study of more complex and advanced quantum mechanical systems [5]. RTDs have two distinct features when compared with other semiconductor devices, from an applications point of view: their potential for very high speed operation and their negative differential conductance (NDC) [4].

The finite barrier width structure represents a novel device concept based on the quantum mechanical nature of electrons. As discussed in Chapter 3, the electronic states in a quantum well with very thick barriers are bound states, and an electron cannot leave the well without an external excitation, because there are no equivalent energy states outside the well to where the electron can move. A far more realistic and equally important situation is that of the quantum well with *finite* barriers, both in height and thickness, as this naturally gives rise to the concept of a *decaying state*, which in turn implies that a current can exist. From the point of view of 'device-physics', this is a fundamental requirement, in order that there be device-like behavior. The electron states are now *quasibound* or *resonant* states, rather than true bound states; as a consequence of the finite barriers, the energy of a resonant state is spread into a range $\hbar/\tau$, where $\tau$ is the lifetime of the carriers in that state. These quasibound states can become resonant with the energy of an incoming electron (or stream of electrons), thereby acting as an energy filter.

The distinctive feature of the tunneling process in the double barrier structure is that the transmission rises to much higher values than the product of the two individual barrier transmissions at energies around the values corresponding to the resonant levels. This is the resonant tunneling phenomena. In a structure with identical barriers there is perfect transmission at the resonance energy, however small the transmission through the individual barriers. Knowledge of the transmission coefficient is necessary in order to calculate the current-voltage characteristic of the double barrier structure, or any device containing such a structure.

In this chapter the transmission probability of a symmetric finite-width double barrier structure is studied, with a resulting *new transcendental* equation for the energy levels. To our knowledge this has not been given previously. Two methods are employed to study this problem: the first in which the transmission of particles incident on the double barrier is considered, and the second, in which particles leak out of the double barrier, thereby giving the complex energies. It is then shown that the eigenvalue equation for the finite SQW becomes modified by an additional factor due to the finite barrier thickness $d$ and in the limit of large $d$, the SQW eigenvalue equation is obtained.

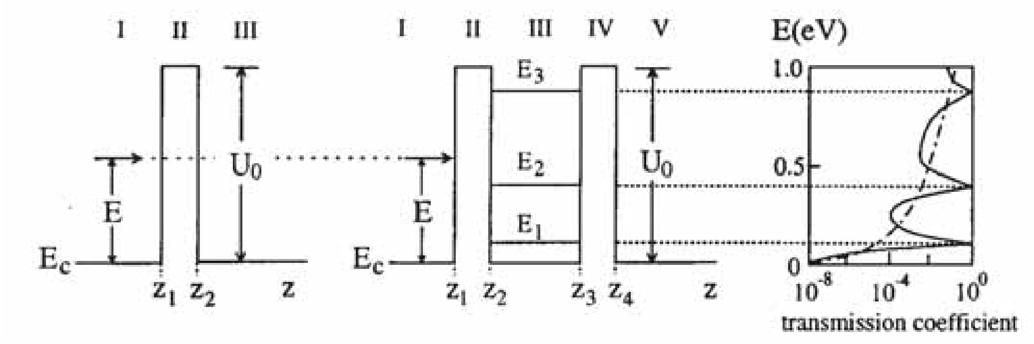

Figure 5.1: An illustration of the relation between the single and double rectangular barrier transmission characteristics. A particle of energy $E$ incident on a barrier of height $U_0$ and the resulting transmission coefficient $T(E)$. The double barrier contains resonant energy levels.

## 5.1 The Double Symmetric Rectangular Barrier

---

In this section the first method is presented, in which the usual transfer matrix approach is used, for waves incident on the barriers. Figure 5.2 depicts a schematic for the double barrier structure, propagation constants are denoted. We begin by calculating the transfer matrix $\mathcal{M}_{i,j}$ for each interface (as as done in Chapter 4 for the single rectangular barrier problem). The potential of the double barrier structure is given by

$$V(z) = \begin{cases} 0, \;\; z < -d - a/2, \\ V_0, \;\; -d - a/2 < z < -a/2, \\ 0, \;\; -a/2 < z < a/2, \\ V_0, \;\; a/2 < z < d + a/2, \\ 0, \;\; z > d + a/2, \end{cases} \tag{5.1}$$

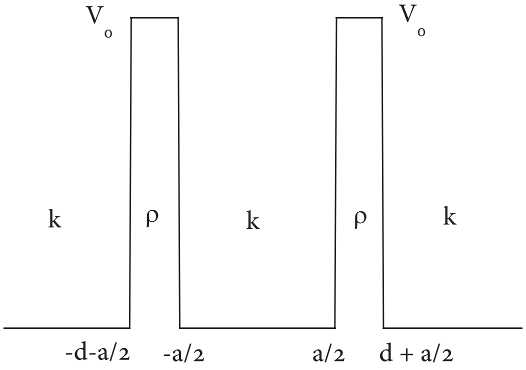

Figure 5.2: The symmetric double rectangular barrier with height $V_0$, barrier widths $d$, and (total) well width $a$. The propagation constants for the appropriate region are labled.

and the wavefunctions in each region are given by

$$\psi(z) = \begin{cases} A_1 e^{ikz} + B_1 e^{-ikz}, & z < -d - a/2, \\ A_2 e^{\rho z} + B_2 e^{-\rho z}, & -d - a/2 < z < -a/2, \\ A_3 e^{ikz} + B_3 e^{-ikz}, & -a/2 < z < a/2, \\ A_4 e^{\rho z} + B_4 e^{-\rho z}, & a/2 < z < d + a/2, \\ A_5 e^{ikz} + B_5 e^{-ikz}, & z > d + a/2, \end{cases} \tag{5.2}$$

where the propagation constants $k^2 = (2m^*E)/\hbar^2$ and $\rho^2 = (2m^*(V_0 - E))/\hbar^2$. Note that in Chapter 4 (and in the Appendix B, Section B.1 for the details of the single rectangular barrier) the propagation constant for the single barrier was taken as $\kappa$ and the barrier width was $2d$. In this chapter $\rho$ is used, and the (single) barrier width is $d$. Figure 5.2 shows the double barrier structure and the relevant wavenumbers. As there are four interfaces, there will be four matrix multiplications. Listed here are the matrices (see Appendix B, Section B.2 for details),

$$\begin{bmatrix} A_1 \\ B_1 \end{bmatrix} = \begin{bmatrix} \left(\frac{ik+\rho}{2ik}\right) e^{(ik-\rho)(d+a/2)} & \left(\frac{ik-\rho}{2ik}\right) e^{(ik+\rho)(d+a/2)} \\ \left(\frac{ik-\rho}{2ik}\right) e^{-(ik-\rho)(d+a/2)} & \left(\frac{ik+\rho}{2ik}\right) e^{-(ik-\rho)(d+a/2)} \end{bmatrix} \begin{bmatrix} A_2 \\ B_2 \end{bmatrix}$$

$$\begin{bmatrix} A_2 \\ B_2 \end{bmatrix} = \begin{bmatrix} \left(\frac{ik+\rho}{2\rho}\right) e^{-(ik-\rho)(a/2)} & -\left(\frac{ik-\rho}{2\rho}\right) e^{(ik+\rho)(a/2)} \\ -\left(\frac{ik-\rho}{2\rho}\right) e^{-(ik+\rho)(a/2)} & \left(\frac{ik+\rho}{2\rho}\right) e^{(ik-\rho)(a/2)} \end{bmatrix} \begin{bmatrix} A_3 \\ B_3 \end{bmatrix}$$

Before doing the next two matrices, the matrix elements for the *single* barrier transmission can be found and are identical to the results derived in Section 4.1 of Chapter 4. Writing

$$\begin{bmatrix} A_1 \\ B_1 \end{bmatrix} = \begin{bmatrix} \mathcal{M}_{11}^{sb} & \mathcal{M}_{12}^{sb} \\ \mathcal{M}_{21}^{sb} & \mathcal{M}_{22}^{sb} \end{bmatrix} \begin{bmatrix} A_3 \\ B_3 \end{bmatrix}$$

where the individual elements are given by (*sb* denoting single barrier)

$$\mathcal{M}_{11}^{sb} = \left[\cosh(\rho d) - \frac{i}{2}\frac{k^2-\rho^2}{k\rho}\sinh(\rho d)\right] e^{ikd}, \tag{5.3}$$

$$\mathcal{M}_{21}^{sb} = -\frac{i}{2}\frac{k^2+\rho^2}{k\rho}\sinh(\rho d) e^{-ik(d+a)} \tag{5.4}$$

$$\mathcal{M}_{22}^{sb} = \left[\cosh(\rho d) + \frac{i}{2}\frac{k^2-\rho^2}{k\rho}\sinh(\rho d)\right] e^{-ikd}, \tag{5.5}$$

$$\mathcal{M}_{12}^{sb} = +\frac{i}{2}\frac{k^2+\rho^2}{k\rho}\sinh(\rho d) e^{ik(d+a)} \tag{5.6}$$

which gives the following relations,

$$\mathcal{M}^{sb}_{22} = \mathcal{M}^{sb*}_{11} \qquad \mathcal{M}^{sb}_{12} = \mathcal{M}^{sb*}_{21} \tag{5.7}$$

For the next two interfaces

$$\begin{bmatrix} A_3 \\ B_3 \end{bmatrix} = \begin{bmatrix} \left(\frac{ik+\rho}{2\rho}\right) e^{-(ik-\rho)(a/2)} & \left(\frac{ik-\rho}{2\rho}\right) e^{-(ik+\rho)(a/2)} \\ \left(\frac{ik-\rho}{2\rho}\right) e^{(ik+\rho)(a/2)} & \left(\frac{ik+\rho}{2\rho}\right) e^{(ik-\rho)(a/2)} \end{bmatrix} \begin{bmatrix} A_4 \\ B_4 \end{bmatrix}$$

$$\begin{bmatrix} A_4 \\ B_4 \end{bmatrix} = \begin{bmatrix} \left(\frac{ik+\rho}{2ik}\right) e^{(ik-\rho)(d+a/2)} & -\left(\frac{ik-\rho}{2ik}\right) e^{-(ik+\rho)(d+a/2)} \\ -\left(\frac{ik-\rho}{2ik}\right) e^{(ik+\rho)(d+a/2)} & \left(\frac{ik+\rho}{2ik}\right) e^{-(ik-\rho)(d+a/2)} \end{bmatrix} \begin{bmatrix} A_5 \\ B_5 \end{bmatrix}$$

and as expected the product of these matrices results in identical expressions for $\mathcal{M}^{sb}_{11}$, $\mathcal{M}^{sb}_{12}$, $\mathcal{M}^{sb}_{21}$, and $\mathcal{M}^{sb}_{22}$ for the *second* barrier. To obtain an expression for the total transmission

$$\begin{bmatrix} A_1 \\ B_1 \end{bmatrix} = \begin{bmatrix} \mathcal{M}^{12}_{11} & \mathcal{M}^{12}_{12} \\ \mathcal{M}^{12}_{21} & \mathcal{M}^{12}_{22} \end{bmatrix} \begin{bmatrix} \mathcal{M}^{23}_{11} & \mathcal{M}^{23}_{12} \\ \mathcal{M}^{23}_{21} & \mathcal{M}^{23}_{22} \end{bmatrix} \begin{bmatrix} \mathcal{M}^{34}_{11} & \mathcal{M}^{34}_{12} \\ \mathcal{M}^{34}_{21} & \mathcal{M}^{34}_{22} \end{bmatrix} \begin{bmatrix} \mathcal{M}^{45}_{11} & \mathcal{M}^{45}_{12} \\ \mathcal{M}^{45}_{21} & \mathcal{M}^{45}_{22} \end{bmatrix} \begin{bmatrix} A_5 \\ B_5 \end{bmatrix}$$

Multiplying out the first two matrices gives

$$\begin{bmatrix} A_1 \\ B_1 \end{bmatrix} = \begin{bmatrix} \mathcal{M}^{12}_{11}\mathcal{M}^{23}_{11} + \mathcal{M}^{12}_{11}\mathcal{M}^{23}_{11} & \mathcal{M}^{12}_{11}\mathcal{M}^{23}_{12} + \mathcal{M}^{12}_{12}\mathcal{M}^{23}_{22} \\ \mathcal{M}^{12}_{21}\mathcal{M}^{23}_{11} + \mathcal{M}^{12}_{22}\mathcal{M}^{23}_{21} & \mathcal{M}^{12}_{21}\mathcal{M}^{23}_{12} + \mathcal{M}^{12}_{22}\mathcal{M}^{12}_{22} \end{bmatrix} \times$$

$$\begin{bmatrix} \mathcal{M}^{34}_{11}\mathcal{M}^{45}_{11}+\mathcal{M}^{34}_{12}\mathcal{M}^{45}_{21} & \mathcal{M}^{34}_{11}\mathcal{M}^{45}_{12}+\mathcal{M}^{34}_{12}\mathcal{M}^{45}_{22} \\ \mathcal{M}^{34}_{21}\mathcal{M}^{45}_{11}+\mathcal{M}^{34}_{22}\mathcal{M}^{45}_{21} & \mathcal{M}^{34}_{21}\mathcal{M}^{45}_{12}+\mathcal{M}^{34}_{22}\mathcal{M}^{45}_{22} \end{bmatrix} \begin{bmatrix} A_5 \\ B_5 \end{bmatrix}$$

Now the first element of the first matrix, $(\mathcal{M}^{12}_{11}\mathcal{M}^{23}_{11}+\mathcal{M}^{12}_{11}\mathcal{M}^{23}_{11}) = \mathcal{M}^{sb}_{11}$ and the first element of the second matrix $(\mathcal{M}^{34}_{11}\mathcal{M}^{45}_{11}+\mathcal{M}^{34}_{12}\mathcal{M}^{45}_{21}) = \mathcal{M}^{sb}_{11}$ are just that of the single rectangular barrier,

$$\mathcal{M}^{sb}_{11} = \left[\cosh(\rho d) - \frac{i}{2}\frac{k^2-\rho^2}{k\rho}\sinh(\rho d)\right]e^{ikd} \tag{5.8}$$

The second, upper entry in the first matrix, as well as the first, lower entry in the second matrix $(\mathcal{M}^{12}_{11}\mathcal{M}^{23}_{12}+\mathcal{M}^{12}_{12}\mathcal{M}^{23}_{22}) = \mathcal{M}^{sb}_{21}$ and $(\mathcal{M}^{34}_{21}\mathcal{M}^{45}_{11}+\mathcal{M}^{34}_{22}\mathcal{M}^{45}_{21}) = \mathcal{M}^{sb}_{21}$ respectively, are the $\mathcal{M}^{sb}_{21}$ for the single barrier:

$$\mathcal{M}^{sb}_{21} = -\frac{i}{2}\frac{k^2+\rho^2}{k\rho}\sinh(\rho d)e^{-ik(d+a)} \tag{5.9}$$

Now the product of these gives the transmission probability through the double barrier system, that is

$$(\mathcal{M}^{12}_{11}\mathcal{M}^{23}_{11}+\mathcal{M}^{12}_{11}\mathcal{M}^{23}_{11}) \times (\mathcal{M}^{34}_{11}\mathcal{M}^{45}_{11}+\mathcal{M}^{34}_{12}\mathcal{M}^{45}_{21}) \tag{5.10}$$

$$\Longrightarrow (\mathcal{M}^{sb}_{11})^2 \tag{5.11}$$

and

$$(\mathcal{M}^{12}_{11}\mathcal{M}^{23}_{12}+\mathcal{M}^{12}_{12}\mathcal{M}^{23}_{22}) \times (\mathcal{M}^{34}_{21}\mathcal{M}^{45}_{11}+\mathcal{M}^{34}_{22}\mathcal{M}^{45}_{21}) \tag{5.12}$$

$$\Longrightarrow (\mathcal{M}^{sb}_{21})^2 \tag{5.13}$$

or

$$\mathcal{M}_{T11} = (\mathcal{M}_{11}^{sb})^2 + (\mathcal{M}_{21}^{sb})^2 \tag{5.14}$$

$$= \left\{\left[\cosh(\rho d) - \frac{i}{2}\frac{k^2-\rho^2}{k\rho}\sinh(\rho d)\right]e^{ikd}\right\}^2 + \left\{-\frac{i}{2}\frac{k^2+\rho^2}{k\rho}\sinh(\rho d)e^{-ik(d+a)}\right\}^2 \tag{5.15}$$

$$= -\frac{(k^2+\rho^2)^2}{(2ik\rho)^2}\sinh^2(\rho d)e^{2ik(d+a)} + \frac{1}{4ik^2\rho^2}\left[2ik\rho\cosh(\rho d) + (k^2-\rho^2)\sinh(\rho d)\right]^2 e^{2ikd} \tag{5.16}$$

$$= -\frac{(k^2+\rho^2)^2}{(2ik\rho)^2}\left(\frac{e^{2\rho d}-1}{2e^{\rho d}}\right)^2 e^{2ik(d+a)} + \frac{1}{4ik^2\rho^2}\left[2ik\rho\cosh(\rho d) + (k^2-\rho^2)\sinh(\rho d)\right]^2 e^{2ikd} \tag{5.17}$$

where the $\sinh(\rho d)$ was re-expressed in terms of exponentials, and

$$= \frac{1}{(16k^2\rho)^2}\left((k^2+\rho^2)^2 e^{-2\rho d}(e^{2\rho d}-1)^2 e^{2ik(d+a)} - 4\left[2ik\rho\cosh(\rho d) + (k^2-\rho^2)\sinh(\rho d)\right]^2 e^{2ikd}\right) \tag{5.18}$$

$$= \frac{1}{(16k^2\rho)^2}\left((k^2+\rho^2)^2 e^{-2\rho d}(e^{2\rho d}-1)^2 e^{2ik(d+a)} - 4\left[2ik\rho\cosh(\rho d) + (k^2-\rho^2)\sinh(\rho d)\right]^2 e^{2ikd}\right) \tag{5.19}$$

$$= \frac{1}{(16k^2\rho)^2}e^{-2\rho d}e^{2ikd}\left((k^2+\rho^2)^2(e^{2\rho d}-1)^2 e^{2ika} - 4e^{2\rho d}\left[2ik\rho\cosh(\rho d) + (k^2-\rho^2)\sinh(\rho d)\right]^2\right) \tag{5.20}$$

Now letting $\kappa^2 = (k^2 + \rho^2)$, we have

$$= \frac{1}{(16k^2\rho)^2} e^{2d(ik-\rho)} \left( \kappa^4 e^{2ika} (e^{2\rho d} - 1)^2 - 4e^{2\rho d} \left[ 2ik\rho \cosh(\rho d) + (k^2 - \rho^2) \sinh(\rho d) \right]^2 \right) \qquad (5.21)$$

This is identical to the result in [6], p. 17.

### 5.1.1 Quasibound State Determination

---

$$\begin{bmatrix} A_1 \\ B_1 \end{bmatrix} = \begin{bmatrix} \mathcal{M}_{11}\mathcal{M}_{12} \\ \mathcal{M}_{21}\mathcal{M}_{22} \end{bmatrix} \begin{bmatrix} A_5 \\ B_5 \end{bmatrix}$$

In this expression, $B_5 = 0$ (no incoming waves from the right), $A_1 = 1$, $A_5 = t$, $B_1 = r$, and the transmission and reflection coefficients are given by

$$T = |t^2|, \qquad R = |r^2| \qquad \Longrightarrow \qquad T + R = 1 \qquad (5.22)$$

For the case of full transmission,

$$A_1 = \mathcal{M}_{11} A_5 \qquad \Longrightarrow \qquad 1 = \mathcal{M}_{11} \qquad (5.23)$$

and

$$T = |t^2| = \frac{1}{|\mathcal{M}_{11}|^2} \qquad \Longrightarrow \qquad |\mathcal{M}_{11}|^2 = 1 \qquad (5.24)$$

Eq. (5.24) is the condition required, and when this occurs, $R = 0$ and $B_1 = 0$. With this,

$$B_1 = \mathcal{M}_{21} A_5 + \mathcal{M}_{22} B_5 \qquad \Longrightarrow \qquad \mathcal{M}_{21} = 0 \tag{5.25}$$

as $B_5 = 0$ and $A_5 \neq 0$. Eqs. (5.24) and (5.25) are equivalent conditions for full transmission in the symmetric double barrier structure. Alternately, the quasibound state energies (transmission energies) are then given by either

$$|\mathcal{M}_{11}|^2(E_j) = 1 \qquad \mathcal{M}_{21}(E_j) = 0, \qquad j = 1, 2... \tag{5.26}$$

While both of these equations are different, they give equivalent transcendental equations for the $E_j$'s. For the case of full transmission it can be shown that Eq. (5.21) can be expressed as

$$16\epsilon^2 \sin^4(2\phi) = \left[e^{-ika}(1-\epsilon) + (e^{2i\phi} - \epsilon e^{-2i\phi})\right] \cdot \left[e^{-ika}(1-\epsilon) - (e^{2i\phi} - \epsilon e^{-2i\phi})\right] \cdot [cc] \tag{5.27}$$

where $\epsilon = e^{-2\rho d}$, $\phi = \tan^{-1}(k/\rho)$ and $[cc]$ is the product of the complex conjugates of the first two brackets. We expect that this transcendental equation will produce an energy condition of the form

$$ka = n\pi - 2\phi - g(\epsilon, \phi) \tag{5.28}$$

This is expected because, in the case of the infinite square well, the energy eigenvalue condition was given by

$$ka = n\pi \tag{5.29}$$

while that of the finite square well (SQW) with *infinitely* thick barriers, was given by

$$ka = n\pi - 2\phi \tag{5.30}$$

For the SQW, the effect of the finite potential height is contained in the $\phi$-parameter. Thus it is expected that in the case of the finite width and finite height double barrier that there will be an additional function $g$ which depends on the finite barrier width, which is characterized by the $\epsilon$-parameter and the height, again given by the $\phi$-parameter.

### 5.1.2 Complex Energy Roots

---

The second method employed for obtaining the quasibound state energies and their intrinsic linewidth, is to consider the scenario in which particles only leak out (in contrast to the waves incident on the barriers). The population decay of $N$ particles is described by $N(t) = N_0 e^{-\Gamma t}$. This can be seen from the following. An electron in a state with $E_j$ is given by $\psi(z,t) = e^{-i\omega t}\psi(z)$, with $|\psi(z)|^2$ is constant in time. The time-development is given by $|\psi(t)|^2 \; e^{-\Gamma t}$, where $\omega = E/\hbar$, so that $e^{-i\omega t} = e^{-i(\omega_R - i(\Gamma/2))t} = e^{-i\omega_R t} e^{-(\Gamma/2)t}$. Thus

$$E_c = \hbar(\omega_R - i\frac{\Gamma}{2}), \qquad E_{Im} = -i\frac{\hbar\Gamma}{2} \tag{5.31}$$

where $\hbar\Gamma$ is the 'energy width'. Now considering $A_1 = B_5 = 0$, that is, with outgoing particles only, so that $B_1 \neq 0$ and $A_5 \neq 0$. Then the matrix equation becomes

$$\begin{bmatrix} 0 \\ \\ B_1 \end{bmatrix} = \begin{bmatrix} \mathcal{M}_{11}\mathcal{M}_{12} \\ \\ \mathcal{M}_{21}\mathcal{M}_{22} \end{bmatrix} \begin{bmatrix} A_5 \\ \\ 0 \end{bmatrix}$$

and

$$0 = \mathcal{M}_{11} A_5, \qquad \Longrightarrow \qquad \mathcal{M}_{11} = 0 \tag{5.32}$$

This condition provides the complex energy roots $E_j^c$, with $Re(E_j^c) \approx E_j$ from the first method, and $Im(E_j^c) = -\hbar\Gamma_j/2$ gives the linewidths. From $B_1 = \mathcal{M}_{21} A_5$, the relative fluxes are in the ratio $|B_1|^2$ to $|A_5|^2$. That is,

$$\text{Flux to left} = |\mathcal{M}_{21}|^2 \times \text{Flux to right} \tag{5.33}$$

or

$$\frac{J_L}{J_R} = |\mathcal{M}_{21}|^2 \tag{5.34}$$

For flat potentials, $J_L \propto T_L \propto \alpha$ and $J_R \propto T_R \propto \beta$. $T_L$ and $T_R$ are the tunneling transmission probabilities for the left and right barrier, respectively, and $\alpha$ and $\beta$ are the *injection* and *extraction* rates, or escape rates. For the symmetric DB, the incoming and outgoing rates are the same, $\alpha = \beta$ and $\Gamma = \alpha + \beta = 2\beta$, and $\beta = \Gamma/2 = \alpha$. In summary, use of conditions $|\mathcal{M}_{11}|^2 = 1$ or $\mathcal{M}_{21} = 0$ will determine the real $E_j$, and from $\mathcal{M}_{11} = 0$, the complex energies $E_j^c = E_j^R - i(\hbar\Gamma/2)$ are found. Note $E_j^c$ will be $E_j^R \approx E_j$ of the first methods.

Now taking the expression for $\mathcal{M}_{11}$ of the symmetric double barrier and now with the condition $\mathcal{M}_{11} = 0$, we have, with $\epsilon = exp(2\rho d)$,

$$e^{2ika} - \left(\frac{\rho - ik}{\rho + ik}\right)^2 = 2\epsilon\left(e^{2ika} - 1\right) + \epsilon^2\left(\left(\frac{\rho + ik}{\rho - ik}\right)^2 - e^{2ika}\right) \tag{5.35}$$

which can be further simplified as

$$e^{2ika}(1-\epsilon)^2 = \left(\frac{\rho - ik}{\rho + ik} - \epsilon\frac{\rho + ik}{\rho - ik}\right)^2 \tag{5.36}$$

with the definitions $k = K\sin\theta$, $\rho = K\cos\theta$, and $P = Ka/2$, this reduces to

$$\mp e^{ika}(1-\epsilon) = e^{2i\theta} - \epsilon e^{2i\theta}, \qquad \mp = e^{-in\pi}, \qquad n = 1, 3, 5, ..or\ 2, 4, 6 \tag{5.37}$$

where the terms $\rho - ik \to K\cos\theta - K\sin\theta \to Ke^{-i\theta}$, and $\rho + ik \to K\cos\theta + K\sin\theta \to Ke^{i\theta}$. Now we have

$$e^{ika - in\pi}(1-\epsilon) = e^{-2i\theta} - \epsilon e^{2i\theta}, \Longrightarrow e^{i(ka - n\pi + 2\theta)}(1-\epsilon) = 1 - \epsilon e^{4i\theta},$$

$$\Longrightarrow e^{i(ka-n\pi+2\theta)} = \frac{1-\epsilon e^{4i\theta}}{(1-\epsilon)} \equiv Z,$$

so $Z = Re^{i\phi}$. Then

$$e^{i(ka-n\pi+2\theta)} = e^{\ln Z} = e^{\ln Re^{i\phi}},$$

or

$$e^{i(ka-n\pi+2\theta)} = e^{\ln R}e^{i\phi}, \tag{5.38}$$

where $R$ is given by

$$R^2 = a^2 + b^2, \qquad a = \frac{1}{1-\epsilon}(1 - \epsilon\cos(4\theta)), \qquad b = \frac{-\epsilon\sin(4\theta)}{1-\epsilon}$$

and $\tan\phi = b/a$ can be written

$$\tan\phi = \frac{-\epsilon\sin(4\theta)}{1-\epsilon\cos(4\theta)}$$

Note that $\epsilon$ and $\theta$ can be complex, in general. However, for real values of $\theta$, $\phi$ is real. On the real axis in the $\theta$-plane, one can define $\phi$ as

$$\phi = -\tan^{-1}\left(\frac{\epsilon\sin(4\theta)}{1-\epsilon\cos(4\theta)}\right) \tag{5.39}$$

and from Eq. (5.38),

$$e^{i(ka-n\pi+2\theta)} = e^{\ln R}e^{i\phi}, \tag{5.40}$$

$$e^{i(ka-n\pi+2\theta)} + \tan^{-1}\left(\frac{\epsilon\sin(4\theta)}{1-\epsilon\cos(4\theta)}\right) = e^{\ln R} \tag{5.41}$$

Now taking the log and multiplying by $-i$:

$$ka - n\pi + 2\theta + \tan^{-1}\left(\frac{\epsilon\sin(4\theta)}{1-\epsilon\cos(4\theta)}\right) = -i\ln R \tag{5.42}$$

Taking $R$ from Eq. (5.1.2) and expressing as

$$R^2 = a^2 + b^2 \qquad \Longrightarrow \qquad \frac{1}{(1-\epsilon)^2}\left[(1-\epsilon\cos^2(4\theta))^2 + \epsilon^2\sin^2(4\theta)\right] \tag{5.43}$$

$$\Longrightarrow \qquad \frac{1}{(1-\epsilon)^2}\left[(1+\epsilon^2 - 2\epsilon\cos(4\theta))\right] \tag{5.44}$$

$$\Longrightarrow \qquad \frac{1}{(1-\epsilon)^2}\left[(1-\epsilon)^2 - 2\epsilon(1-\cos(4\theta))\right]$$

or

$$R^2 = 1 + \frac{2\epsilon}{(1-\epsilon)^2}2\sin^2(2\theta)$$

$$= 1 + \frac{4\epsilon}{(1-\epsilon)^2} \sin^2(2\theta) \tag{5.45}$$

so that

$$ka - n\pi + 2\theta + \tan^{-1}\left(\frac{\epsilon \sin(4\theta)}{1 - \epsilon\cos(4\theta)}\right) = -\frac{i}{2} \ln\left[1 + \frac{4\epsilon}{(1-\epsilon)^2} \sin^2(2\theta)\right] \tag{5.46}$$

This is the basic equation arising from the condition $\mathcal{M}_{11} = 0$. On the real $\theta$-axis, the LHS side of Eq. (5.46) defines solutions $\theta_n^R$, since then, $ka = 2P \sin\theta$, and the RHS alters this expression. This is to be compared to the expression for both the infinite square well result, $ka = n\pi$, and the finite SQW, $ka = n\pi - 2\theta$.

The complex roots can be analyzed by rewriting Eq. (5.46) as

$$2P\sin\theta + 2\theta + \tan^{-1}\left(\frac{\epsilon \sin(4\theta)}{1 - \epsilon\cos(4\theta)}\right) = n\pi - \frac{i}{2} \ln\left[1 + \frac{4\epsilon}{(1-\epsilon)^2} \sin^2(2\theta)\right] \tag{5.47}$$

and rewriting further as

$$f(\theta) = n\pi - \frac{i}{2} \ln\left[1 + \frac{4\epsilon}{(1-\epsilon)^2} \sin^2(2\theta)\right]. \tag{5.48}$$

The effective parameter for the 'imaginary' term is $4\epsilon/((1-\epsilon)^2)$. Therefore this can be expressed as

$$f(\theta_{n,0}) = n\pi, \qquad \text{for real solutions.} \tag{5.49}$$

$$f(\theta_{n,0} + \theta_{n,1}) = n\pi - \frac{i}{2} \ln\left[1 + \frac{4\epsilon}{(1-\epsilon)^2} \sin^2(2\theta)\right], \qquad \text{for 'altered' solutions.} \tag{5.50}$$

For small $\theta_{n,1}$,

$$f(\theta_{n,0} + \theta_{n,1}) = f(\theta_{n,0}) + \theta_{n,1} f'(\theta_{n,0}) \tag{5.51}$$

and since $f(\theta_{n,0}) = n\pi$,

$$\theta_{n,1} f'(\theta_{n,0}) = -\frac{i}{2} \ln\left[1 + \frac{4\epsilon}{(1-\epsilon)^2} \sin^2(2\theta_{n,0})\right] + \theta_{n,1}\left(\frac{-i}{2}\frac{a'}{b}\right) \tag{5.52}$$

# Bibliography

[1] R. Tsui, L. Esaki, "Tunneling in a finite superlattice", Appl. Phys. Lett. **22**, 562 (1973).

[2] L.L. Chang, L. Esaki, and R. Tsui, "Resonant tunneling in semiconductor barriers", Appl. Phys. Lett. **24**, 593 (1974).

[3] S. Datta, *Electronic transport in mesoscopic systems* (Cambridge University Press, Cambridge 1995).

[4] H. Mizuta and T. Tanoue, *The physics and applications of resonant tunneling diodes* (Cambridge University Press, Cambridge 1995).

[5] S. M. Sze, *High-speed semiconductor devices* (John Wiley ic Sons Inc., New York 1990).

[6] S.J. O'Mullane, "Basic Quantum Mechanics of One-Dimensional Quantum Well and Barrier Structures", (Senior Honor Thesis, Boston College, 2012).

[7] Zhao, H.Yamamoto, Taniguchi, "Theoretical study of resonant tunneling and confining with mass variation in unsymmetrical rectangular doublebarrier structures". Appl. Phys. A 60, 369-376 (1995).

Chapter 6

# Current in QW Structures

---

## 6.1 Tunneling Current

---

The analysis of the tunneling current through a semiconductor layer as a function of the applied voltage begins by considering the electron fluxes incident at the interfaces and the quantum mechanical transmission coefficient. The current density through the two interfaces depends on the perpendicular component of the wave vector $k_z$, the transmission coefficient $T(E_z)$, the perpendicular velocity $v_z$, the density of states and the distribution function at both sides of the barrier:

$$J_z = \left( \frac{2e\hbar}{(2\pi)^3 m^*} \right) \int_0^\infty k_z dk_z T(E_z) \int d\mathbf{k}_\perp f_{FD}(E). \tag{6.1}$$

$f(E) = (1 + exp(E - \mu)/kT)^{-1}$ is the Fermi-Dirac distribution function. Note that when calculating the $J_z$ in from the left side, the lower limit will change to $E_F - E_F^0$ to reflect the limited range of incoming particles. The change to $E_z$ can be done by starting with $E_z = (\hbar k_z)^2/2m^*$,

$$E_z = \frac{(\hbar k_z)^2}{2m^*} \quad \Longrightarrow \quad k_z = \sqrt{2m^* E_z/\hbar^2} \quad \Longrightarrow \quad dk_z = \sqrt{\frac{2m^*}{\hbar^2}} \frac{1}{2} \frac{dE_z}{\sqrt{E_z}},$$

$$\Longrightarrow k_z dk_z = \frac{m^*}{\hbar^2} dE_z.$$

Inserting above, gives

$$J_z = \frac{2e\hbar}{(2\pi)^3 m^*} \int_0^\infty \left(\frac{m^*}{\hbar^2}\right) dE_z T(E_z) \int d\mathbf{k}_\perp f_{FD}(E),$$

and so

$$J_z = \frac{2e}{(2\pi)^3 \hbar} \int_0^\infty dE_z T(E_z) \int d\mathbf{k}_\perp f_{FD}(E).$$

Since the $T(E_z)$ is a function only of the $z$-direction, the $\mathbf{k}_\perp$-integration can be done. Rewriting this integral in terms the magnitude $k_\perp$ and the angle $\phi$,

$$J_z = \frac{2e}{(2\pi)^3 \hbar} \int_0^\infty dE_z T(E_z) \int_0^\infty \int_0^{2\pi} k_\perp dk_\perp d\phi f_{FD}(E),$$

and with $k_\perp dk_\perp = (m^*/\hbar^2) dE_\perp$,

$$J_z = \frac{2e}{(2\pi)^3 \hbar} \int_0^\infty dE_z T(E_z) \int_0^\infty \int_0^{2\pi} \frac{m^*}{\hbar^2} dE_\perp d\phi f_{FD}(E),$$

$$J_z = \frac{2e * 2\pi * m^*}{(2\pi)^3 \hbar^3} \int_0^\infty dE_z T(E_z) \int_0^\infty dE_\perp f_{FD}(E),$$

$$J_z = \frac{em^*}{2\pi^2 \hbar^3} \int_0^\infty dE_z T(E_z) \int_0^\infty dE_\perp f_{FD}(E).$$

Inserting the Fermi-Dirac distribution into the above expression,

$$J_z = \frac{em^*}{2\pi^2 \hbar^3} \int_0^\infty dE_z T(E_z) \int_0^\infty \frac{dE_\perp}{1 + e^{-\beta(\mu - E_z - E_\perp)}}, \tag{6.2}$$

$$J_z = \frac{em^*}{2\pi^2 \hbar^3} \int_0^\infty dE_z T(E_z) \left\{ (1/\beta) \ln\left(\frac{1}{1+e^{-x}}\right) \Big|_0^\infty \right\},$$

where a substitution on the $E_\perp$-integral has been performed, and is of the form

$$\int \frac{dx}{1+e^x} = \ln\left(\frac{1}{1+e^{-x}}\right) + C, \quad x \equiv -\beta(\mu - E_z - E_\perp) \tag{6.3}$$

and $C$ is an integration constant. The result is

$$J_z = \frac{em^*}{2\pi^2 \hbar^3 \beta} \int_0^\infty T(E_z) dE_z \ln(1 + e^{\beta(\mu - E_z)}), \tag{6.4}$$

for the (particle) current flux. This expression for the current flux contains the $n_{2D}$ factor, which can be resolved into a $T = 0$ term, and a $T \neq 0$ term, as

$$n_{2D} = kT \ln(1 + e^{\beta(\mu - E_z)}) \qquad \Longrightarrow \qquad kT \ln[e^{\beta(\mu - E_z)}(e^{-\beta|\mu - E_z|} + 1)],$$

$$\Longrightarrow kT[\ln e^{\beta(\mu-E_z)}+\ln(1+e^{-\beta|\mu-E_z|})] \quad \Longrightarrow \quad kT[\beta(\mu-E_z)+\ln(1+e^{-\beta|\mu-E_z|})],$$

or with $kT = 1/\beta$

$$n_{2D}=(\mu-E_z)\Theta(\mu-E_z)+\frac{1}{\beta}\ln(1+e^{-\beta|\mu-E_z|}),$$

or

$$n_{2D}=(\mu-E_z)\Theta(\mu-E_z)+\hat{n}_{2D}, \tag{6.5}$$

with

$$\hat{n}_{2D}=\frac{1}{\beta}\ln(1+e^{-\beta|\mu-E_z|}). \tag{6.6}$$

Inserting the into the $J_z$ integral above gives

$$J_z=\frac{em^*}{2\pi^2\hbar^3}\int_0^\infty T(E_z)\left[(\mu-E_z)\Theta(\mu-E_z)+\hat{n}_{2D}\right]dE_z, \tag{6.7}$$

or

$$J_z=J_z(T=0)+J_z(T\neq 0), \tag{6.8}$$

where

$$J_z(T=0)=\frac{em^*}{2\pi^2\hbar^3}\int_0^\infty T(E_z)(\mu-E_z)\Theta(\mu-E_z)dE_z \tag{6.9}$$

$$J_z(T\neq 0)=J_z(T=0)+\frac{em^*}{2\pi^2\hbar^3}\int_0^\infty T(E_z)n_{2D}dE_z. \tag{6.10}$$

Next the energy flux associated with the current into and out of the structure will be found. The energy flux, and the average energy flux associated with the $z$-directed incoming current is readily found, as it is only dependent upon the $z$-component, $E_z$, of the total energy. The perpendicular component, $E_\perp$, must be dealt with separately as the resulting expression is not easily evaluated.

## 6.2 Energy flux

---

The energy flux associated with the current flux in the $z$-direction is $J^{\epsilon} = J^{E_z} + J^{E_\perp}$, where the charge $e$ has been omitted, and the total energy is $\epsilon = E_z + E_\perp$. In the following expressions, the $J^{E_z}$ does not contain $E_\perp$ as it has been integrated out, and the $J^{E_\perp}$-integral must be analyzed further as it contains both $E_z$ and $E_\perp$. The goal here is to obtain the average incoming and outgoing energy flux associated with the current entering and leaving the structure, which will be detailed below.

$$J^{E_z} = \frac{m^*}{2\pi^2\hbar^3\beta}\int_0^\infty T(E_z)E_z dE_z \ln(1 + e^{\beta(\mu - E_z)}), \tag{6.11}$$

$$J^{E_\perp} = \frac{m^*}{2\pi^2\hbar^3}\int_0^\infty dE_z T(E_z)\int_0^\infty \frac{E_\perp dE_\perp}{1 + e^{-\beta(\mu - E_z - E_\perp)}}. \tag{6.12}$$

### 6.2.1 Energy Flux: $T = 0$ Limit

---

The $T = 0$ contribution to $J^{E_z}$ can immediately be seen, using Eq. (6.5), as

$$J^{E_z}(T = 0) = \frac{m^*}{2\pi^2\hbar^3\beta}\int_0^\infty T(E_z)E_z(\mu - E_z)\Theta(\mu - E_z)dE_z. \tag{6.13}$$

The $J^{E_\perp}$ expression can also be written as

$$J^{E_\perp} = \frac{m^*}{2\pi^2\hbar^3}\int_0^\infty dE_z T(E_z)\int_0^\infty \frac{E_\perp dE_\perp}{1 + Ce^{\beta E_\perp}},$$

with $C = e^{-\beta(\mu - E_z)}$. Factoring out the $e^{\beta E_\perp}$ term in the denominator

$$\begin{aligned} J^{E_\perp} &= \frac{m^*}{2\pi^2\hbar^3}\int_0^\infty dE_z T(E_z)\int \frac{E_\perp dE_\perp}{e^{\beta E_\perp}(e^{-\beta E_\perp} + C)} \\ &\rightarrow \frac{m^*}{2\pi^2\hbar^3}\int_0^\infty dE_z T(E_z)\int \frac{E_\perp e^{-\beta E_\perp} dE_\perp}{(e^{-\beta E_\perp} + C)}, \end{aligned}$$

and letting $x = e^{-\beta E_\perp}$ (and $e^{-\beta E_\perp}dE_\perp = -(1/\beta)dx$), then

$$J^{E_\perp} = \frac{m^*}{2\pi^2\hbar^3}\int_0^\infty dE_z T(E_z)\int \frac{(-1/\beta)E_\perp dx}{(x + C)},$$

and finally replacing $E_\perp = -(1/\beta)\ln x$, the expression becomes

$$J^{E_\perp} = \frac{m^*}{2\pi^2\hbar^3}\int_0^\infty dE_z T(E_z)\int\frac{(1/\beta)^2\ln x dx}{(x+C)},$$

or

$$J^{E_\perp} = \frac{m^*}{2\pi^2\hbar^3\beta^2}\int_0^\infty dE_z T(E_z)\int\frac{\ln x dx}{(x+C)}. \tag{6.14}$$

In the $T = 0K$ limit, the $f_{FD}$ distribution is the Heaviside step function $\Theta(x)$, and $\Theta(x) = 0$ if $x < 0$. Starting with Eq. (6.12),

$$J^{E_\perp}(T=0) = \frac{m^*}{2\pi^2\hbar^3}\int_0^\infty T(E_z)dE_z\int_0^\infty E_\perp\Theta(-\beta(\mu - E_z - E_\perp))dE_\perp, \tag{6.15}$$

$$= \frac{m^*}{2\pi^2\hbar^3}\int_0^\infty T(E_z)dE_z\int_0^{\mu-E_z} E_\perp dE_\perp,$$

$$= \frac{m^*}{2\pi^2\hbar^3}\int_0^\infty T(E_z)dE_z\left(\frac{1}{2}E_\perp^2\right)\Big|_0^{\mu-E_z},$$

$$J^{E_\perp}(T=0) = \frac{m^*}{2\pi^2\hbar^3}\int_0^\infty T(E_z)dE_z\left(\frac{1}{2}(\mu - E_z)^2\right). \tag{6.16}$$

### 6.2.2 Average Energy Flux: $T = 0$ Limit

---

As noted above, the average energy into the structure depends only on $z$, while that of the outgoing energy has a component associated with the perpendicular direction, which will be integrated out, leaving it in terms of $E_z$. The average $\langle Q\rangle$ of a physical quantity $Q(E_z)$ is defined as (in terms of $E_z$)

$$\langle Q\rangle = \frac{\int g(E_z)QdE_z}{\int g(E_z)dE_z}. \tag{6.17}$$

The average energy flux is then defined as

$$\langle E\rangle = \langle E_z\rangle + \langle E_\perp\rangle, \tag{6.18}$$

where

$$\langle E_\perp \rangle = \frac{J^{E_\perp}}{J_{flux}} \tag{6.19}$$

$$\langle E_z \rangle = \frac{J^{E_z}}{J_{flux}}. \tag{6.20}$$

For $\langle E_\perp \rangle$ in the $T = 0$ limit

$$\langle E_\perp \rangle_{T=0} = \frac{J^{E_\perp}(T=0)}{J_{flux}(T=0)}, \tag{6.21}$$

or

$$\langle E_\perp \rangle_{T=0} = \frac{\frac{m^*}{2\pi^2\hbar^3}\int_0^\infty T(E_z)dE_z\left(\frac{1}{2}(\mu - E_z)^2\right)\Theta(\mu - E_z)}{\frac{m^*e}{2\pi^2\hbar^3}\int_0^\infty T(E_z)dE_z kT\ln(1 + e^{\beta(\mu - E_z)})},$$

or

$$\langle E_\perp \rangle_{T=0} = \frac{\frac{m^*}{2\pi^2\hbar^3}\int_0^\infty T(E_z)dE_z\left(\frac{1}{2}(\mu - E_z)^2\right)\Theta(\mu - E_z)}{\frac{m^*e}{2\pi^2\hbar^3}\int_0^\infty T(E_z)dE_z(\mu - E_z)\Theta(\mu - E_z)}. \tag{6.22}$$

In terms of the statistical average defined above, this can be written

$$\langle E_\perp \rangle_{T=0} = \frac{\int_0^\infty \frac{1}{2}(\mu - E_z)g(E_z)dE_z}{\int_0^\infty g(E_z)dE_z}, \tag{6.23}$$

where the weight factor $g(E_z)$ is defined here as

$$g(E_z) \equiv T(E_z)(\mu - E_z)\Theta(\mu - E_z). \tag{6.24}$$

By Eq. (6.17) this gives

$$\langle E_\perp \rangle_{T=0} = \frac{1}{2}\langle \mu - E_z \rangle = \frac{1}{2}\mu - \frac{1}{2}\langle E_z \rangle. \tag{6.25}$$

In the $T = 0$ limit, for $\langle E_z \rangle$,

$$\langle E_z \rangle_{T=0} = \frac{J^{E_z}(T=0)}{J_{flux}(T=0)} = \frac{\frac{m^*}{2\pi^2\hbar^3}\int_0^\infty T(E_z)dE_z E_z(\mu - E_z)\Theta(\mu - E_z)}{\frac{m^*}{2\pi^2\hbar^3}\int_0^\infty T(E_z)dE_z kT\ln(1 + e^{\beta(\mu - E_z)})}, \tag{6.26}$$

or

$$\langle E_z \rangle_{T=0} = \frac{\frac{m^*}{2\pi^2\hbar^3}\int_0^\infty T(E_z)dE_z E_z(\mu - E_z)\Theta(\mu - E_z)}{\frac{m^*}{2\pi^2\hbar^3}\int_0^\infty T(E_z)dE_z(\mu - E_z)\Theta(\mu - E_z)}.$$

Again, as in Eq. (6.17), this is written

$$\langle E_z \rangle_{T=0} = \frac{\int_0^\infty E_z g(E_z)dE_z}{\int_0^\infty g(E_z)dE_z}, \tag{6.27}$$

where the weight factor $g(E_z)$ is given by Eq. (6.24), and is evaluated as

$$\langle E_z\rangle_{T=0} = \langle E_z\rangle\,. \tag{6.28}$$

Now the total average energy flux at $T = 0$, is

$$\langle E\rangle_{T=0} = \langle E_z\rangle_{T=0} + \langle E_\perp\rangle_{T=0}\,,$$

or

$$\langle E\rangle_{T=0} = \langle E_z\rangle + \frac{1}{2}\mu - \frac{1}{2}\langle E_z\rangle\,,$$

or

$$\langle E\rangle_{T=0} = \frac{1}{2}\mu + \frac{1}{2}\langle E_z\rangle\,. \tag{6.29}$$

### 6.2.3 Energy Flux: Full T dependence

---

Starting with the current flux

$$J_{flux} = \frac{2}{(2\pi^2)^3\hbar}\int_0^\infty T(E_z)f(\epsilon)dE_z dE_\perp, \qquad f(\epsilon) = \frac{1}{1+e^{-\beta(\mu-\epsilon)}} \tag{6.30}$$

and taking the $\partial/\partial\beta$-derivative,

$$\frac{\partial J_{flux}}{\partial\beta} = \frac{2}{(2\pi^2)^3\hbar}\int_0^\infty\int_0^\infty T(E_z)\frac{\partial f(\epsilon)}{\partial\beta}dE_z dE_\perp, \tag{6.31}$$

$$\frac{\partial J_{flux}}{\partial\beta} = \frac{2}{(2\pi^2)^3\hbar}\int_0^\infty\int_0^\infty T(E_z)\left\{\frac{|\mu-\epsilon|e^{-\beta(\mu-\epsilon)}}{(1+e^{-\beta(\mu-\epsilon)})^2}\right\}dE_z dE_\perp,$$

$$\frac{\partial J_{flux}}{\partial\beta} = \frac{2}{(2\pi^2)^3\hbar}\int_0^\infty\int_0^\infty T(E_z)\left\{\frac{|\mu-\epsilon|(e^{-\beta(\mu-\epsilon)}+1-1)}{(1+e^{-\beta(\mu-\epsilon)})^2}\right\}dE_z dE_\perp,$$

$$\frac{\partial J_{flux}}{\partial \beta} = \frac{2}{(2\pi^2)^3\hbar}\int_0^\infty\int_0^\infty T(E_z)\left\{\frac{(|\mu-\epsilon|)(e^{-\beta(\mu-\epsilon)}+1)-(|\mu-\epsilon|)}{(1+e^{-\beta(\mu-\epsilon)})^2}\right\}dE_z dE_\perp,$$

$$\frac{\partial J_{flux}}{\partial \beta} = \frac{2}{(2\pi^2)^3\hbar}\int_0^\infty\int_0^\infty T(E_z)\left\{\frac{(|\mu-\epsilon|)}{(1+e^{-\beta(\mu-\epsilon)})}-\frac{(|\mu-\epsilon|)}{(1+e^{-\beta(\mu-\epsilon)})^2}\right\}dE_z dE_\perp,$$

$$= \frac{2}{(2\pi^2)^3\hbar}\mu\int_0^\infty\int_0^\infty T(E_z)\frac{1}{(1+e^{-\beta(\mu-\epsilon)})}dE_z dE_\perp - \frac{2}{(2\pi^2)^3\hbar}\int_0^\infty\int_0^\infty T(E_z)\epsilon\frac{1}{(1+e^{-\beta(\mu-\epsilon)})}dE_z dE_\perp$$
$$-\frac{2}{(2\pi^2)^3\hbar}\int_0^\infty\int_0^\infty T(E_z)\frac{|\mu-\epsilon|}{(1+e^{-\beta(\mu-\epsilon)})^2}dE_z dE_\perp,$$

$$= \frac{2}{(2\pi^2)^3\hbar}\mu\int_0^\infty\int_0^\infty T(E_z)f(\epsilon)dE_z dE_\perp - \frac{2}{(2\pi^2)^3\hbar}\int_0^\infty\int_0^\infty T(E_z)\epsilon f(\epsilon)dE_z dE_\perp$$
$$-\frac{2}{(2\pi^2)^3\hbar}\int_0^\infty\int_0^\infty T(E_z)\frac{|\mu-\epsilon|}{(1+e^{-\beta(\mu-\epsilon)})^2}dE_z dE_\perp,$$

$$\frac{\partial J_{flux}}{\partial \beta} = \mu J_{flux} - J^{\epsilon}_{flux} - I(\beta),$$

where $J_{flux}$ is the current flux integral (which is to be integrated over the perpendicular energies giving $J_z$), and $J^{\epsilon}_{flux}$ is the (total) energy flux integral, and $I(\beta)$ is given by,

$$I(\beta) = \frac{2}{(2\pi^2)^3\hbar}\int_0^\infty\int_0^\infty T(E_z)\frac{|\mu-\epsilon|}{(1+e^{-\beta(\mu-\epsilon)})^2}dE_z dE_\perp,$$

which is intractable.

A new integral $L$, can be defined such that the derivative $-\partial L/\partial\beta$ gives terms that can be evaluated. $L$ is given by

$$L = \int_0^\infty dE_z T(E_z) \int_0^\infty dE_\perp \ln(1 + e^{-\beta(\epsilon-\mu)}), \tag{6.32}$$

where $\epsilon = E_z + E_\perp$ is the total energy. A property of this integral is such that the $J^E_{flux}$ can be evaluated by noting that

$$-\frac{\partial L}{\partial\beta} = \int_0^\infty dE_z T(E_z) \int_0^\infty dE_\perp \frac{(\epsilon-\mu)e^{-\beta(\epsilon-\mu)}}{1 + e^{-\beta(\epsilon-\mu)}}, \tag{6.33}$$

$$= \int_0^\infty dE_z T(E_z) \int_0^\infty dE_\perp \frac{\epsilon-\mu}{1 + e^{\beta(\epsilon-\mu)}}, \tag{6.34}$$

$$= -\int_0^\infty dE_z T(E_z) \int_0^\infty dE_\perp \frac{\mu}{1 + e^{\beta(\epsilon-\mu)}} + \int_0^\infty dE_z T(E_z) \int_0^\infty \frac{\epsilon dE_\perp}{1 + e^{\beta(\epsilon-\mu)}}, \tag{6.35}$$

$$= -\mu \int_0^\infty dE_z T(E_z) \int_0^\infty \frac{dE_\perp}{1 + e^{\beta(\epsilon-\mu)}} + \int_0^\infty dE_z T(E_z) \int_0^\infty \frac{\epsilon dE_\perp}{1 + e^{\beta(\epsilon-\mu)}}, \tag{6.36}$$

or

$$-\frac{\partial L}{\partial\beta} = -\mu J_{flux} + J^E_{flux}, \tag{6.37}$$

and rearranging, the following expression is then evaluated,

$$J^E_{flux} = \mu J_{flux} - \frac{\partial L}{\partial\beta}. \tag{6.38}$$

Recalling from the defining equation for the average energy flux, Eq. (6.19)

$$\langle E\rangle = \mu - \frac{1}{J_{flux}}\frac{\partial L}{\partial\beta}. \tag{6.39}$$

If the $\partial L/\partial\beta$ term can be evaluated then the average energy can be found. Taking Eq. (6.32) and first making the substitution $y = e^{-\beta(\epsilon-\mu)}$, $dy = -\beta e^{-\beta(\epsilon-\mu)} dE_\perp = -\beta y dE_\perp$, or $dE_\perp = -dy/(\beta y)$, and the limits change from $E_\perp = 0 \to y = y_1$, where $y_1 = e^{\beta(\mu-E_z)}$, $E_\perp = \infty \to y = 0$,

$$L = \int_0^\infty dE_z T(E_z) \int_0^{e^{\beta(\mu-E_z)}} \left(\frac{1}{\beta}\frac{dy}{y}\right) \ln(1+y),$$

$$L = \int_0^\infty dE_z T(E_z) \int_0^{e^{\beta(\mu-E_z)}} \left(\frac{1}{\beta}\frac{\ln(1+y)dy}{y}\right). \tag{6.40}$$

Then

$$-\frac{\partial L}{\partial\beta} = \int_0^\infty dE_z T(E_z) \left\{ \left(\frac{1}{\beta^2}\int_0^{e^{\beta(\mu-E_z)}} \frac{\ln(1+y)dy}{y}\right) - \left(\frac{1}{\beta}\frac{\ln(1+y_1)}{y_1}(\mu - E_z)e^{\beta(\mu-E_z)}\right)\right\},$$

$$-\frac{\partial L}{\partial\beta} = \int_0^\infty dE_z T(E_z) \left\{ \left(\frac{1}{\beta^2}\int_0^{e^{\beta(\mu-E_z)}} \frac{\ln(1+y)dy}{y}\right) - \left(\frac{1}{\beta}(\mu - E_z)\ln(1+y_1)\right)\right\},$$

or

$$-\frac{\partial L}{\partial\beta} = \int_0^\infty dE_z T(E_z) \left\{ \left(\frac{1}{\beta^2}\int_0^{y_1} \frac{\ln(1+y)dy}{y}\right) - D_1\right\}, \tag{6.41}$$

where $D_1$ is (and the upper limit has been written as $y_1 = e^{\beta(\mu-E_z)}$)

$$D_1 = \frac{1}{\beta}(\mu - E_z)\ln(1+y_1), \tag{6.42}$$

and can be positive or negative depending on whether $E_z < \mu$ or $E_z > \mu$. At this point Eq. (6.41) must be analyzed separately for $y_1 < 1$ or $E_z > \mu$ and $y_1 > 1$ or $E_z < \mu$.

### 6.2.4 L-integral: $y_1 > 1$

---

For the case $y_1 > 1$ or $E_z < \mu$ the $y$-integral, Eq. (6.41), must be split between 0 and 1, and 1 and $y_1$,

$$-\frac{\partial L}{\partial\beta} = \int_0^\infty dE_z T(E_z) \left\{ \frac{1}{\beta^2}\left[\int_0^1 \left(\frac{\ln(1+y)dy}{y}\right) + \int_1^{y_1}\left(\frac{\ln(1+y)dy}{y}\right)\right] - D_1\right\}.$$

Now the first integral can be evaluated, and in the second integral, the identity $\ln(1+y) \equiv \ln y + \ln(1+1/y)$ is inserted, that is

$$C_1 = \int_0^1 \left(\frac{\ln(1+y)dy}{y}\right) = \frac{\pi^2}{12}, \tag{6.43}$$

$$\int_1^{y_1}\left(\frac{\ln(1+y)dy}{y}\right)\to\int_1^{y_1}\frac{\ln y}{y}dy+\int_1^{y_1}\frac{\ln(1+1/y)}{y}dy\to Q_1+Q_2. \tag{6.44}$$

The $Q_1$-integral can now be evaluated as

$$Q_1=\int_1^{y_1}\frac{\ln y}{y}dy=\frac{1}{2}\beta^2(\mu-E_z)^2\Theta(\mu-E_z), \tag{6.45}$$

where the theta function represents the $T=0$ limit term. The $\partial L/\partial\beta$ now reads

$$-\frac{\partial L}{\partial\beta}=\int_0^\infty dE_zT(E_z)\left\{\frac{1}{\beta^2}\left[C_1+Q_1+Q_2\right]-D_1\right\}, \tag{6.46}$$

and the $Q_2$-integral remains to be evaluated, which can be done by another substitution $t=1/y$, $dt=-(1/y^2)dy$, which gives,

$$Q_2=\int_1^{y_1}\frac{\ln(1+1/y)}{y}dy\qquad\to\int_{1/y_1}^{1}\frac{\ln(1+t)}{t}dt, \tag{6.47}$$

where the limits have changed from $y=1\to t=1$ and $y=y_1\to t=1/y_1$. Expanding the ln term in a power series

$$Q_2=\int_{1/y_1}^{1}\frac{\ln(1+t)}{t}dt\to\int_{1/y_1}^{1}\frac{1}{t}(t-\frac{1}{2}t^2+\frac{1}{3}t^3-\frac{1}{4}t^4+\frac{1}{5}t^5-\frac{1}{6}t^6+\cdots)dt, \tag{6.48}$$

$$Q_2=\int_{1/y_1}^{1}(1-\frac{1}{2}t+\frac{1}{3}t^2-\frac{1}{4}t^3+\frac{1}{5}t^4-\frac{1}{6}t^5+\cdots)dt, \tag{6.49}$$

and integrating,

$$Q_2=(t-\frac{1}{4}t^2+\frac{1}{9}t^3-\frac{1}{16}t^4+\frac{1}{25}t^5-\frac{1}{36}t^6+\cdots)\Big|_{1/y_1}^{1}, \tag{6.50}$$

$$Q_2=\left\{1-\frac{1}{4}+\frac{1}{9}-\frac{1}{16}+\frac{1}{25}-\frac{1}{36}+\cdots\right\}$$
$$-\left\{\frac{1}{y_1}-\frac{1}{4}\frac{1}{(y_1)^2}+\frac{1}{9}\frac{1}{(y_1)^3}-\frac{1}{16}\frac{1}{(y_1)^4}+\frac{1}{25}\frac{1}{(y_1)^5}-\frac{1}{36}\frac{1}{(y_1)^6}+\cdots\right\},$$

or with $y_1=e^{\beta(\mu-E_z)}$

$$Q_2=\frac{\pi^2}{12}-\left\{e^{-\beta(\mu-E_z)}-\frac{1}{4}e^{-2\beta(\mu-E_z)}+\frac{1}{9}e^{-3\beta(\mu-E_z)}-\frac{1}{16}e^{-4\beta(\mu-E_z)}+\frac{1}{25}e^{-5\beta(\mu-E_z)}-\cdots\right\}. \tag{6.51}$$

### 6.2.5 L-integral: $y_1 < 1$, $E_z > \mu$ case

---

For the case of $y_1 < 1$ or $E_z > \mu$, the log term in Eq. (6.41) can be expanded as

$$\int_0^{y_1} \frac{\ln(1+y)}{y} dy = \int_0^{y_1} \frac{1}{y}(y - \frac{y^2}{2} + \frac{y^3}{3} - \frac{y^4}{4} + \cdots)dy, \tag{6.52}$$

$$= \int_0^{y_1} (1 - \frac{y}{2} + \frac{y^2}{3} - \frac{y^3}{4} + \cdots)dy, \tag{6.53}$$

$$= (y - \frac{y^2}{4} + \frac{y^3}{9} - \frac{y^4}{16} + \cdots)\Big|_0^{y_1}, \tag{6.54}$$

$$= (y_1 - \frac{y_1^2}{4} + \frac{y_1^3}{9} - \frac{y_1^4}{16} + \cdots). \tag{6.55}$$

The portion of the $\partial L/\partial\beta$ expression which contains this term can be called $Y_1$,

$$Y_1 = \int_\mu^\infty dE_z T(E_z)(kT)^2 \left[ e^{(\mu-E_z)/kT} - \frac{1}{4}e^{2(\mu-E_z)/kT} + \frac{1}{9}e^{3(\mu-E_z)/kT} - \frac{1}{16}e^{4(\mu-E_z)/kT} + \cdots \right], \tag{6.56}$$

and is valid for $E_z$ beyond the chemical potential.

#### 6.2.5.1 L-Integral: $T = 0$ Limit

The average energy flux for $T = 0$ can be found based on the $L$-integration, as the $J^E_{flux}$ is given by

$$J^E_{flux} = \mu J_{flux} - \frac{\partial L}{\partial \beta} \tag{6.57}$$

and

$$\langle E \rangle \Big|_{T=0} = \mu - \frac{1}{J_{flux}} \frac{\partial L}{\partial \beta}\Big|_{T=0}. \tag{6.58}$$

The $\partial L/\partial\beta$ form is, with the upper integration limit now $\mu$,

$$-\frac{\partial L}{\partial\beta}\bigg|_{T=0} = \int_0^\mu dE_zT(E_z)\left\{\frac{1}{\beta^2}\left[C_1+Q_1+Q_2\right]-D_1\right\}, \tag{6.59}$$

$$= \int_0^\mu dE_zT(E_z)\left\{\left[\frac{C_1}{\beta^2}+\frac{Q_1}{\beta^2}+\frac{Q_2}{\beta^2}\right]-D_1\right\},$$

$$= \int_0^\mu dE_zT(E_z)\left\{\left(\frac{\pi^2}{12}(kT)^2+\frac{1}{2}(\mu-E_z)^2+(kT)^2Q_2\right)-D_1\right\}.$$

with $\beta = 1/kT$. The $D_1$-term can be factored to separate the $T=0$ and $T\neq 0$ terms, as follows:

$$D_1 = kT(\mu-E_z)\ln(1+y_1)\rightarrow kT(\mu-E_z)\ln(1+e^{\beta(\mu-E_z)}), \tag{6.60}$$

$$= kT(\mu-E_z)\ln\left[e^{\beta(\mu-E_z)}(e^{-\beta(\mu-E_z)}+1)\right],$$

$$= kT(\mu-E_z)\left\{\frac{1}{kT}(\mu-E_z)+\ln(1+e^{-\beta(\mu-E_z)})\right\},$$

or

$$D_1 = (\mu-E_z)^2\Theta(\mu-E_z)+(\mu-E_z)kT\ln(1+e^{-\beta|\mu-E_z|}), \tag{6.61}$$

where the first term above represents the $T=0$ term.

With these factorizations, the $\partial L/\partial\beta$ expression reads,

$$-\frac{\partial L}{\partial\beta}\bigg|_{T=0} = \int_0^\mu dE_zT(E_z)\left\{\left(\frac{\pi^2}{12}(kT)^2+\frac{1}{2}(\mu-E_z)^2+(kT)^2Q_2\right)-(\mu-E_z)^2-kT\ln(1+e^{-\beta|\mu-E_z|})\right\}, \tag{6.62}$$

and in the $T=0$ limit,

$$-\frac{\partial L}{\partial\beta}\bigg|_{T=0} = \int_0^\mu dE_zT(E_z)\left\{\left(\frac{1}{2}(\mu-E_z)^2\right)\right\}-(\mu-E_z)^2,$$

or

$$-\frac{\partial L}{\partial\beta}\bigg|_{T=0} = -\int_0^\mu dE_zT(E_z)\left(\frac{1}{2}(\mu-E_z)^2\right), \tag{6.63}$$

and with

$$\langle E\rangle_{T=0} = \mu-\frac{1}{J_{flux}}\frac{\partial L}{\partial\beta}\bigg|_{T=0}, \tag{6.64}$$

this becomes

$$\langle E\rangle_{T=0} = \mu-\frac{1}{J_{flux}}\int_0^\mu dE_zT(E_z)\left(\frac{1}{2}(\mu-E_z)^2\right).$$

The $J_{flux}$ here is the $T = 0$ limit and is given by Eq. (6.9), as

$$J_z(T=0) = \frac{em^*}{2\pi^2\hbar^3}\int_0^\infty T(E_z)(\mu - E_z)\Theta(\mu - E_z)dE_z,$$

,

and the average energy at $T = 0$ is written

$$\langle E\rangle_{T=0} = \mu - \frac{\frac{m^*}{2\pi^2\hbar^3}\int_0^\infty dE_z T(E_z)\left(\frac{1}{2}(\mu - E_z)^2\right)\Theta(\mu - E_z)}{\frac{m^*}{2\pi^2\hbar^3}\int_0^\infty dE_z T(E_z)(\mu - E_z)\Theta(\mu - E_z)}, \tag{6.65}$$

or, by Eq. (6.17)

$$\langle E\rangle_{T=0} = \mu - \frac{\int_0^\infty dE_z g(E_z)\frac{1}{2}(\mu - E_z)}{\int_0^\infty dE_z g(E_z)},$$

with $g(E_z)$ given by Eq. (6.24). This expression then reads

$$\langle E\rangle_{T=0} = \mu - \frac{1}{2}\langle \mu - E_z\rangle = \mu - \frac{1}{2}\mu + \frac{1}{2}\langle E_z\rangle, \tag{6.66}$$

and

$$\langle E\rangle_{T=0} = \frac{1}{2}\mu + \frac{1}{2}\langle E_z\rangle, \tag{6.67}$$

### 6.2.6 Summary-Average Energy Flux: Full T-dependence

---

For the full $T$ range, the average energy flux expression reads,

$$\langle E \rangle = \mu - \frac{1}{J_{flux}} \frac{\partial L}{\partial \beta}, \tag{6.68}$$

and with $\partial L / \partial \beta$ given by Eq. (6.46),

$$-\frac{\partial L}{\partial \beta} = \int_0^\infty dE_z T(E_z) \left\{ \frac{1}{\beta^2} \left[ C_1 + Q_1 + Q_2 \right] - D_1 \right\}, \tag{6.69}$$

where $C_1, Q_1, Q_2$ and $D_1$ given by Eq's (6.43,6.45,6.51,6.60), and $J_{flux}$ (the particle flux) by,

$$J_{flux} = \frac{em^*}{2\pi^2\hbar^3} \int_0^\infty dE_z T(E_z) kT \ln(1 + e^{(\mu - E_z)/kT}) \tag{6.70}$$

this can be written as

$$\langle E \rangle = \mu + A + B + C - D, \tag{6.71}$$

where

$$A = \frac{\frac{m^*}{2\pi^2\hbar^3} \int_0^\infty dE_z T(E_z) \frac{\pi^2}{12} (kT)^2}{\frac{em^*}{2\pi^2\hbar^3} \int_0^\infty dE_z T(E_z) kT \ln(1 + e^{(\mu - E_z)/kT})} \tag{6.72}$$

$$B = \frac{\frac{m^*}{2\pi^2\hbar^3} \int_0^\infty dE_z T(E_z) \frac{1}{2} (\mu - E_z)^2 \Theta(\mu - E_z)}{\frac{em^*}{2\pi^2\hbar^3} \int_0^\infty dE_z T(E_z) kT \ln(1 + e^{(\mu - E_z)/kT})} \tag{6.73}$$

$$C = \frac{\frac{m^*}{2\pi^2\hbar^3} \int_0^\infty dE_z T(E_z) (kT)^2 \left\{ \frac{\pi^2}{12} - \left[ e^{-(\mu - E_z)/kT} - \frac{1}{4} e^{-2(\mu - E_z)/kT} + \frac{1}{9} e^{-3(\mu - E_z)/kT} - \ldots \right] \right\}}{\frac{em^*}{2\pi^2\hbar^3} \int_0^\infty dE_z T(E_z) kT \ln(1 + e^{(\mu - E_z)/kT})} \tag{6.74}$$

$$D = \frac{\frac{m^*}{2\pi^2\hbar^3} \int_0^\infty dE_z T(E_z) (\mu - E_z) kT \ln(1 + e^{(\mu - E_z)/kT})}{\frac{em^*}{2\pi^2\hbar^3} \int_0^\infty dE_z T(E_z) kT \ln(1 + e^{(\mu - E_z)/kT})} \tag{6.75}$$

## Chapter 7

# Transport Models

## 7.1 The H656 Structure

This chapter discusses the comparison of the theoretical transport modeling with the current-voltage (IV) measurements of the H656 structure. The sample H656 was designed to investigate the behavior of a single period structure. Figure 7.1 gives the conduction band diagram at zero bias as a function of the growth direction, showing the wavefunctions at the corresponding energy levels. The energies, wavefunctions, and resulting potential of the structure were calculated self-consistently using a Schrodinger-Poisson solver [1]. H656 consists of a 1.2 nm wide AlAs barrier, followed by 75 nm wide GaAs drift region and a 28.2 nm wide $In_{0.5}Ga_{0.95}As$ quantum well region. Directly adjacent to the quantum well is the resonant tunneling diode (RTD), which consists of an 8.4 nm $In_{0.5}Ga_{0.95}As$ quantum well between two 1.2 nm AlAs barriers. After the RTD, there is a 100 nm GaAs spacer region, and a 70 nm n-doped region. A doping region, with $n_d = 5\ x\ 10^{16}$ cm$^{-2}$ surrounds both sides, which act as electron reservoirs. The redistribution of electrons throughout the structure and the GaAs/InGaAs band offset results in a deep pocket (quantum well) region.

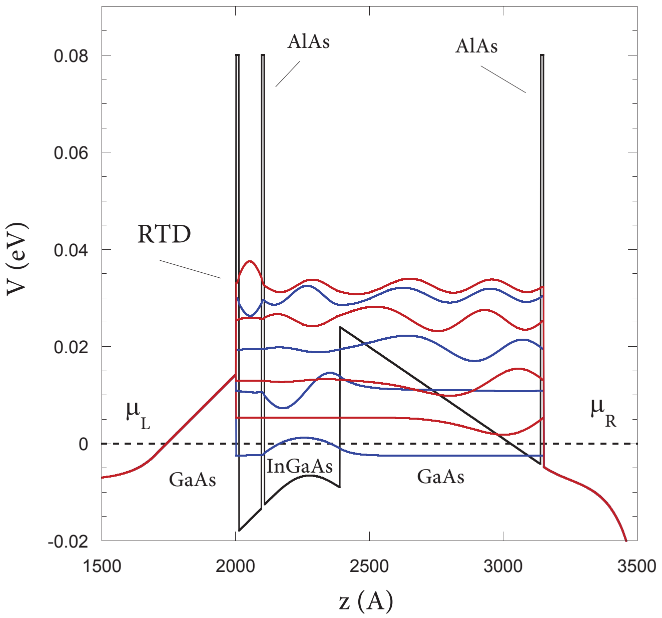

Figure 7.1: Conduction band diagram vs. growth axis, showing the relative placement of the wavefunctions (at their corresponding energies), at zero bias ($V_b = 0, \mu_L = \mu_R$). $\mu_L$ and $\mu_R$ are the left and right chemical potentials respectively. Dotted line represents the quasi-Fermi level.). Note that the height of the AlAs barriers is much higher than depicted on the plot.

In order to characterize the properties of the investigated samples with respect to their proper behavior, both *spectral* and *transport* measurements were performed. As there is a significant serial resistance in addition to the device resistance, small samples are ideal for current voltage measurements. In contrast, device geometries with longer and larger surface areas (long fingers, or comb-like structure) are assumed to optimize the efficiency of the emission behavior. Therefore two devices with different lateral shape are processed for each different utilization [2-5]. Samples were produced and current-voltage measurements were performed on this sample by the Vienna group [3], as shown in Fig. 7.2. This depicts the current vs. bias on a log scale, for both bias directions (negative bias ≡ forward bias, positive bias ≡ reverse bias). In the next chapter, the observed radiation and the comparison with theoretical work is discussed. In the following subsections, the analysis is divided between the low bias and mid-to-high bias ranges, as there are different physical mechanisms which occur in these ranges.

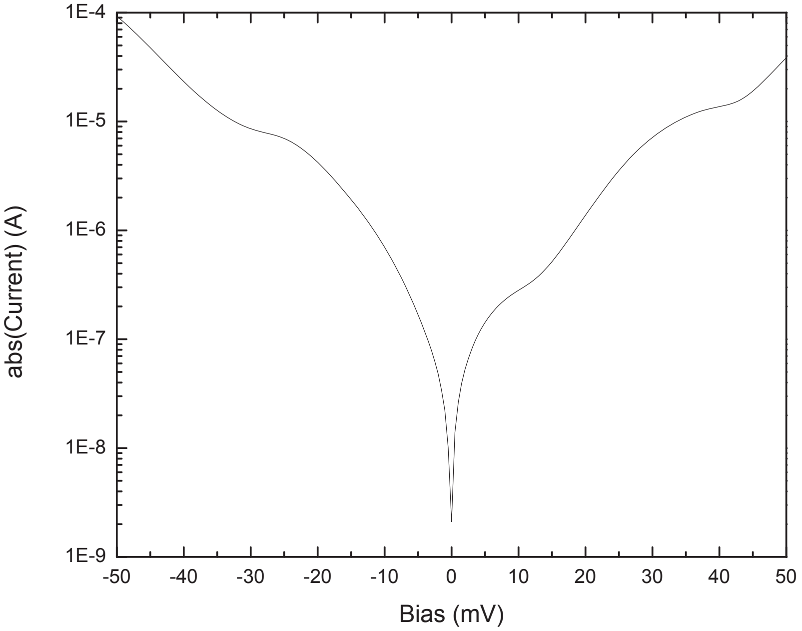

Figure 7.2: Experimental current $I$ vs. bias $V_b$ for the one-period H656 structure, for both *forward* (negative) and *reverse* (positive) bias. Current is plotted on a log scale. There are three main features, one at $V_b$=-25 meV, and two on the reverse side, at roughly $V_b$=10 meV and $V_b$=40 meV.

The structure as a whole can be broadly considered as two adjacent resonant tunneling structures, one portion of the structure containing the region of the RTD + deep well, and the other distinct part of the structure containing the triangular wedge/barrier region. This is easily seen by referring to Fig. 7.1. This *asymmetrical* aspect of H656, in which there is a 'wedge-well' RT structure, alongside the deep-well RT structure explains the difference between the relative magnitude of the features (at low bias) for each bias range.

When the system is in the reverse bias direction, the entry into the structure is through the (outside) triangular barrier, plus the RTD, and the exit is through the wedge-levels of the latter portion of the structure. On the forward bias side, the entry/exit is reversed and so electrons will encounter the wedge-well region first, and then exit through the deep well levels, and RTD (at sufficiently high biases). Below it is shown that these particular features in the IV's are due to the passage of the wedge-levels past the injection region (for reverse bias), and for the forward bias, the triangular well level allowing an additional channel for the current to enter the structure.

The goal of this chapter is to quantitatively described the features of the low-bias IV's for the H656 structure, for both forward and reverse bias. This is not intended as a comprehensive description of the entire IV curves. The reasons for focusing on the low-bias range, is that at these biases there is a minimum number of processes occurring, such as effects due to scattering. The LO phonon process can only come in to the picture when there is an energy spacing of at least 36 meV. Based on self-consistent calculations of the NESS consistent with the IV's, LO phonons must be taken into account around $V_b$ 120 meV and higher. In the modeling presented here, the electron-electron interaction is implicitly considered through the assumption that there is a quasi-thermal equilibrium established through the fast collision times. For the acoustic phonon process, the average energy flux was considered in Chapter 6. This new consideration of this macro-constraint into our modeling through the average energy inequality, places bounds on the available NESS's possible. For a truly quantitative description of all relevant internal processes, the full phase-space calculation must be made, and is not considered here.

### 7.1.1 Low Bias Range

---

For the low bias ranges, for *both* forward and reverse biases, the model is based on three parameters: the bound state chemical potential $\mu_1$ assumed to hold for both the first and second well levels, the chemical potential of the continuum distribution $\mu_c$, and a common temperature $T$ for all particles in the structure. These three parameters are subject to three constraints: $J_{in} = J_{out} = J_{observed}$, and $E_{in}^{avg} \leq E_{out}^{avg}$. The existence of a continuum population inside the deep well must be considered in order to account for the observed current. In particular, on the reverse bias side, the first feature/bump of the experimentally observed IV's, as seen in Fig. 7.3, can only be explained by allowing a continuum population to coexist with the bound-state population. In Fig. 7.1 the bound-state wavefunctions are represented for the case of $V_b$=0. Just as in the case of a simple RTD, there exists a continuum process bringing particles into the structure which have an imprint of that distribution. In the deep well-region, the assumption of a common $T$ accounts for the electron-electron collisions to produce a quasi-thermal equilibrium. Even though the numerical electron-electron scattering rates have not been calculated for this structure (for any bias), the assumption of a common $T$ implicitly takes this into consideration.

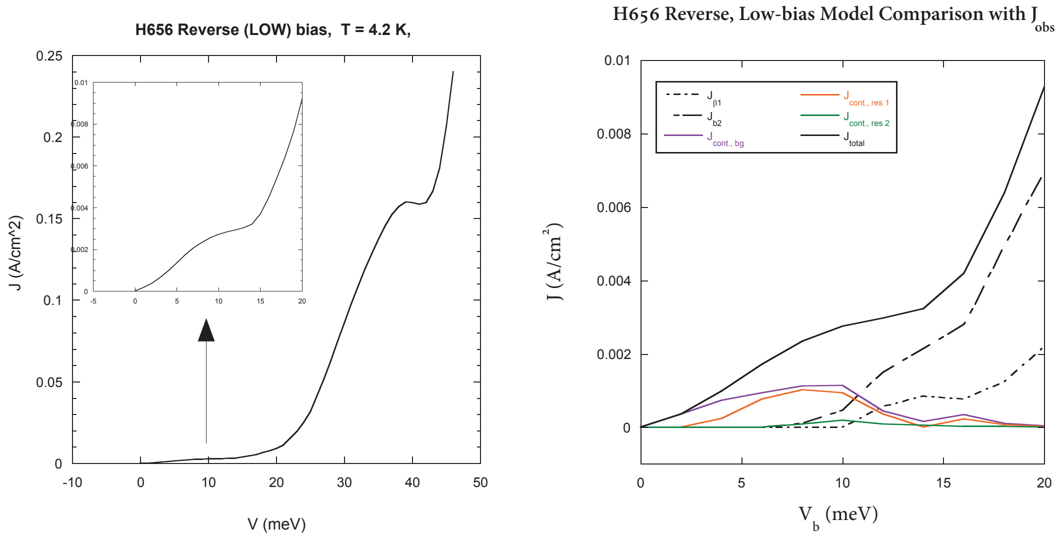

Figure 7.3: Comparison of the low-bias transport model self-consistent calculated NESS, with the experimental JV (solid line) for the one-period H656 structure, *reverse* bias (right). The various contributions are labeled, and the sum of the calculated currents matches the observed current. On the left is the experimental JV showing a detail of the very low bias bump.

The self-consistent calculation of the nonequilibrium steady state (NESS) was compared to the observed JV's as a function of the applied bias by applying the conservation conditions discussed above. In Figure 7.3 the results of these calculations for the *reverse* bias range up to $V_b$=17 meV are shown. The solid line represents both the observed current and the total of the calculated currents based on the model outlined above. The broad humped feature which begins around $V_b$=3 meV and extends to around $V_b$=14 meV, is due to effectively three processes that involve the continuum distribution in the deep well. In the Fig. 7.3 the currents are designated as follows: $J_{\beta 1}(\mu_1, T)$ is the $E_1$ bound state-associated current, $J_{\beta 2}(\mu_1, T)$ is the current from the $E_2$ bound state. Due to the transmission characteristics of the side of the structure which contains the wedge-well, there are the following contributions: $J_{cont}^{bg}(\mu_{cont}, T)$ is the 'background' continuum current, $J_{cont1}^{res}(\mu_{cont}, T)$ is the first wedge-resonance, and $J_{cont2}^{res}(\mu_{cont}, T)$ is the second wedge-resonance. All three of these (continuum) processes extract carriers from the continuum population, as those of the bound-state cannot contribute. That is, the $E_1$ and $E_2$ levels have very narrow Lorentz-distributions (especially at the very low biases), and contribute a small amount to the observed outgoing current in this range. As the bias increases, the continuum population is depleted because the first wedge-resonant level passes through the injection band, no longer taking particles out, while that of the second bound state begins to pick up.

For the forward bias, low-bias range, the entry into the structure is *through* the triangular well, and out through one of the deep well levels. For the very low-bias ranges, this entry assists particles into the well region across the (large) triangular barrier. The feature at $V_b$=25 meV is due to the passage of the second wedge level through the injection band. This can be seen from Fig. 7.5, where the self-consistent NESS's (consistent with the observed current condition) for two bias values, $V_b$ =16 meV and $V_b$ =22 meV show the tail portion of the second well level passing through and out of the triangular well region. As the bias is increased, the $E_2$ level falls out of range, and it is this process which is observed as a dip on the JV curve. This is basically an NDR phenomena, which is routinely observed in simple RTD's.

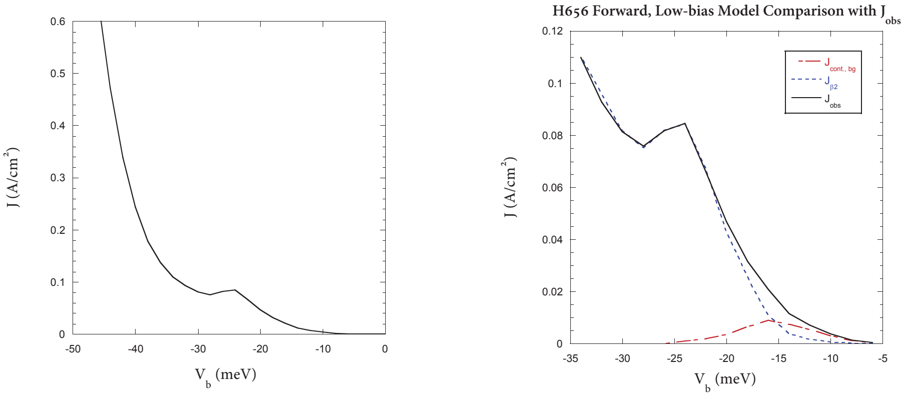

Figure 7.4: Experimental current density $J$ vs. bias $V_b$ for the one-period H656 structure, for *forward* bias (left) and model comparison (right).

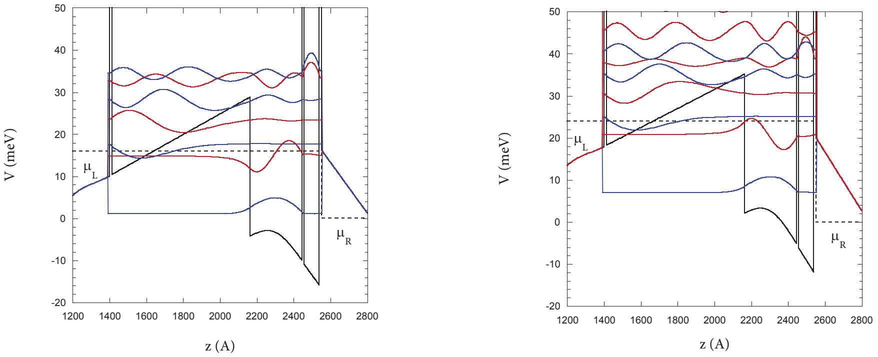

Figure 7.5: NESS for $V_b$=16 meV and 22 meV, forward bias, indicating the placement of the second deep well level within range of the injection band.

### 7.1.2 Mid-High Bias Range

---

For the mid-high bias range, on both bias directions, the resulting current is essentially that of a pass-through current. On the forward side, the drift region (which is the triangular barrier region) will begin to disappear, and the current coming into the structure will be less obstructed, and more importantly there is no longer a entry-well region, which means the electrons can traverse the

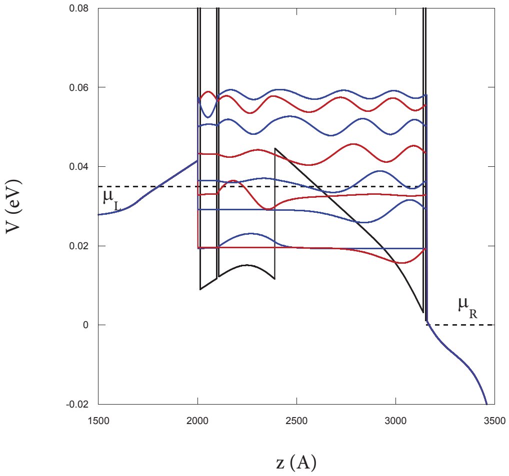

Figure 7.6: Calculated NESS for the $V_b$=35 meV, reverse bias, corresponding to the second bump on the IV. This clearly shows the resonant interaction of the second deep well level with the third wedge level. As the bias is increased the wedge level will cross enhancing the current, then passing through the injection region, which accounts for the observed dip in the IV around 40 meV.

structure, either tunneling out of the structure, or transitioning down to lower levels through LO phonon, and electron-electron interactions. Then they exit the structure through those lower levels.

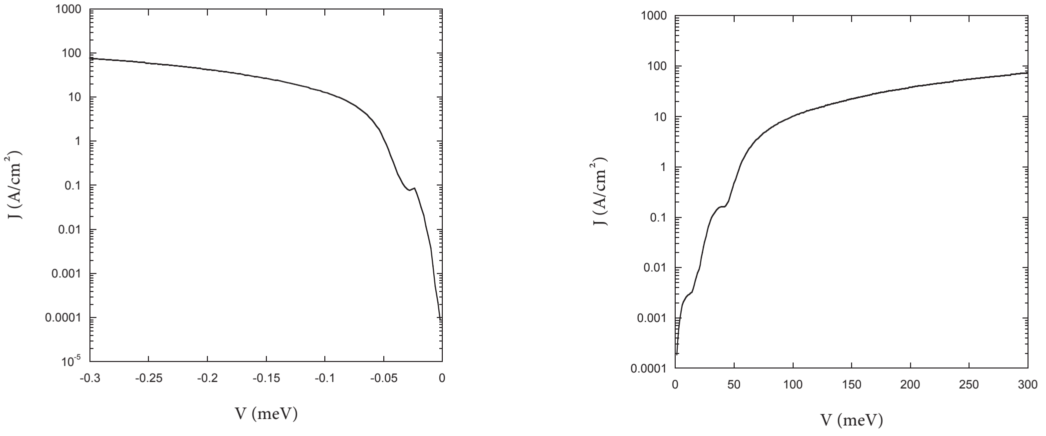

Figure 7.7: Measured JV curve (semi-log scale) for the forward (left) and reverse (right) bias, showing that for biases $V_b \sim 100$ meV there are no discernible features.

## 7.2 Summary

The transport modeling for the low-bias range of both the forward and reverse bias directions, based on three parameters $\mu_b$, $\mu_c$, and $T$, subject to the three conditions $J_{in} = J_{out}$, $J_{in} = J_{obs}$, and $E_{in}^{avg} \leq E_{out}^{avg}$ has decisively shown that there must exist a continuum population, in addition to the usual bound-state population in the structure. As the bias increases, the bound-state levels begin to send out more current as these levels will enter into the region of the incoming injection band, allowing for fast entry of particles into those levels of the structure. Various intersubband transport processes can redistribute them to other levels, from which they exit the structure. When the bias is high enough, LO phonon processes start if $V_b - E_1 > 36$ meV. The full interlevel dynamics involving LO-phonon, electron-electron, electron-surface interactions would be required to arrive at the NESS in these bias domains. However, the scattering processes, such as the LO phonon and electron-electron scattering must be handled numerically through a detailed balance to correctly account for the transport into the structure and the subsequent transitions to lower levels through which the particles exit.

# Bibliography

[1] G. Feng, “Transport and Response Properties of Non-Equilibrium Steady State Semiconductor Quantum Well Structures”, PhD dissertation (Boston College, 2002).

[2] M. Coquelin, “Resonant plasmon and subband excitation in heterostructures”, PhD dissertation (Technical University at Vienna, 2008).

[3] A. Pfinier, “Current Transport in InGaAs Quantum Wells”, M.S. dissertation (Technical University Vienna, 2011).

## Chapter 8

# Radiation and Response

---

This chapter discusses the response theory needed to describe the radiation emitted from quantum well heterostructures. As introduced at the beginning of the thesis, the H656 structure was specially designed to produce THz radiation, based on the plasma instability concept. This plasma instability-based concept offers distinct advantages as it relies on a collective phenomenon, which is less susceptible to disruption due to higher temperatures and various scattering effects. Based on previous investigations of plasma instabilities in various other systems, it was determined that quantum well structures operating under bias in a nonequilibrium steady state (NESS), with appropriate carrier injection and extraction rates were the best candidates for a realization of this idea [1]. The simplest scenario for the generation of plasma instabilities requires [3] a three-subband system, with the first and third subband well populated and the second nearly empty (or vice-versa). The essential instability mechanism is the resonant interaction of two plasma modes, due to the up and down depolarization shifted intersubband plasmons, in such a structure [1].

The response program was developed by Dr. Kempa and Dr. Bakshi long before I joined this research effort. The modeling done, and presented in Chapter 7 determined the appropriate NESS at a given bias, consistent with the observed IV measurements. With a particular NESS determined, the energies and wavefunctions are then entered into the response program to obtain the lineshape of radiation. It is shown that for the H656 structure at a bias of $V_b$ =150 meV

## 8.1 Plasma Instability

---

A plasma is a system of charged particles interacting through the long-range Coulomb force. In a quantum well heterostructure the active region is considered to be a slab of plasma in which the charged particles are electrons and ions. While the electrons are highly mobile, the ions remain essentially fixed to the lattice sites, providing a uniform neutralizing background, and participating in lattice vibrations which scatter electrons (and holes). Through the Coloumb interaction, and their response to external electric and magnetic fields, a collective oscillation arises, known as a *plasmon*.

If a nonequilibrium carrier distribution is created, the relaxation to equilibrium can occur through phonon, photon, and plasmon processes. Under certain, special conditions plasmon generation can be the dominant channel for relaxation to equilibrium, with the plasmons arising from a population inversion in the carrier distribution function. Therefore a substantial energy transfer in to a growing plasma mode may become possible under suitable conditions, resulting in a plasma instability. This energy relaxation mode will be the dominant mechanism for energy loss of the carriers. This plasmon energy can then be transformed into electromagnetic radiation at the frequency of the plasma mode, leading to potential device scenarios. The frequency of the radiation is in the THz and meV range.

## 8.2 **Intersubband Plasmon**

The excited intersubband (ISB) excitation is known to be a collective mode of the 2D electron gas (2DEG), the *intersubband plasmon.* The ISB plasmon can be thought of as a coherent superposition of single-particle intersubband excitations, with an energy renormalized from the bare intersubband spacing by Coulomb and exchange effects [4, 5]. In the case of the intersubband resonance (ISR) plasmon the Coulomb interactions of two electron subbands are described as a virtual exchange of plasmons, i.e., when averaged over time some parts of the electron subband energies are stored in a quasiparticle. The ISR plasmon can therefore likewise be considered as a coherent superposition of two subband wavefunctions weighted with their respective subband electron sheet densities that undergo Rabi type oscillations under the action of their mutual Coulomb interaction [7]. Physically the depolarization effect arises because in the case of high carrier densities each electron in a subband resides in a field which is different from the external field by the mean Hartree field of the other electrons polarized by the external field.

### 8.2.1 Two-Level Case-Depolarization Shift

A one-band model is insufficient to describe an intersubband excitation, and taking multiple subbands into consideration complicates an analytical solution because the Fourier component of the nonequilibrium correction to the density becomes a (complicated) function in space. Therefore the Random Phase Approximation (RPA) approach is used which works on the principle that inter-

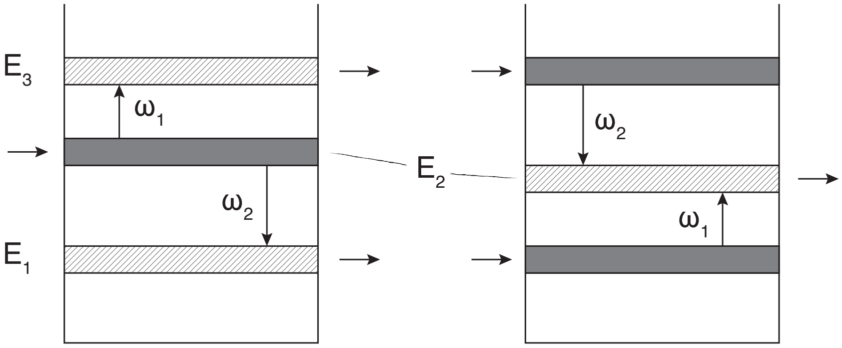

Figure 8.1: A schematic of the three level system, with subbands $E_1$, $E_2$, and $E_3$. The single-particle (bare) frequencies are labeled

actions between density fluctuations can be neglected if the phase of the interactions is randomly varying [7]. Using the RPA one can derive the plasmon frequency of a two-band 2D system:

$$\tilde{\omega}_{21} = \frac{1}{\hbar}\sqrt{\Delta E_{21}^2 + W_P^2} \tag{8.1}$$

where

$$W_P^2 = -4\Delta f_{21}\Delta E_{21}G_{2121} \tag{8.2}$$

is the depolarization shift which depends on the single particle transition energy $\Delta E_{21}$, the difference in population density $\Delta f_{21}$, and the Coulomb matrix element

$$G_{2121}(\omega) = \frac{e^2}{\epsilon\epsilon_r}\int \psi_1(\mathbf{r})\psi_2(\mathbf{r})\frac{1}{|\mathbf{r}-\mathbf{r}'|}\psi_1(\mathbf{r}')\psi_2(\mathbf{r}')d\mathbf{r}d\mathbf{r}' \tag{8.3}$$

with $z$ the direction perpendicular to the layers of the sample. In the case of a 'normal' distribution $f_2 < f_1$, the depolarization is a blueshift of the bare frequency. However, in the case of population inversion, i.e., when $f_2 > f_1$, the depolarization is a redshift of the bare frequency $(E_2 - E_1)/\hbar$ to the plasmon frequency $\omega_{21}$.

### 8.2.2 Three-Level Case-Intersubband Resonance

It can be shown that for an electron plasma with a strong enough population inversion (basically a two-humped velocity distribution function) the plasmon frequency becomes complex and the imaginary part $\gamma = Im(\omega)$ can become positive, leading to an exponential growth in time of the plasmon mode. That defines the plasma instability. Figure 8.1 shows such a system in two different inversion situations. In each case an absorption $\omega_1$ and an emission process $\omega_2$ from one or two "source" levels into a relatively empty band (drain levels) are both possible. The corresponding plasmonic modes of the two processes may become resonant if, after the depolarization shifts, their frequencies match, $\omega_2$=$\omega_1$. According to the expressions above, and due to the inversion situation $\omega_2$ will be redshifted while $\omega_1$ will be blueshifted.

### 8.2.3 Criteria for Plasma Instabilities in a Three-Level System

The signatures of the plasma instability are summarized as follows [2]. In the range of the instability a mode-merging is expected to result, which is essentially an attractive crossing of the emission and absorption modes. For most bias ranges the emission and absorption modes are distinct, but in the range of interaction the merging of these modes results in a *mode locking.* The second signature of the instability is a maximum value for the growth rate of the instability in the range of the mode locking. The growth rate reduces to zero where the emission and absorption modes separate. If the instability can overcome losses due to collisions, then the linewidth vanishes, and an extremely sharp line of high intensity is produced. This is the onset of the plasma instability, which results in the (stimulated) generation of plasmons. In the range of biases where the (calculated) growth rate is not strong enough to overcome losses, line-narrowing, and an increased line intensity will sill occur. Thus a comparison of the linewidths both outside and in the range of mode merging provides the third criteria for the plasma instability. The fourth condition for the PI arises from the fact that the mode frequency becomes complex in the range of the plasma instability. The mixing of the original emission and absorption modes modifies the typical Lorentzian shape by the form $(1 + ax)/(1 + x^2)$ rather than the standard $1/(1 + x^2)$, where $a$ is a constant depending on the amount of mixing of the two original modes. The resulting new feature is a sharp maximum followed by a sharp minimum, or vice versa.

## 8.3 **Observed Radiation/Comparison**

---

In this section a calculated lineshape corresponding to a self-consistent NESS is compared with the observed radiation lineshape. Measurements were made [7] for the single period H656 structure corresponding to currents 100 mA and 300 mA, displayed in Figs. 8.2 and 8.3. A calculated lineshape based on an assumed NESS is given in Fig. 8.4, and has the main features of the observed lineshape.

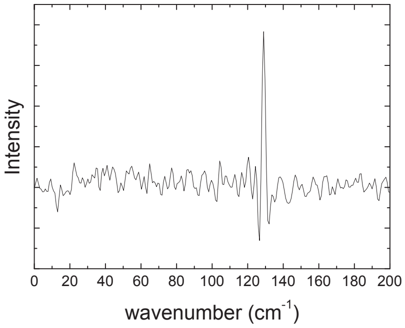

Figure 8.2: FTIR measurements of the radiation for the forward bias direction of sample H656, for the measured current of $I$ =100 mA. The characteristic feature of this lineshape is that of a modified Lorentzian.

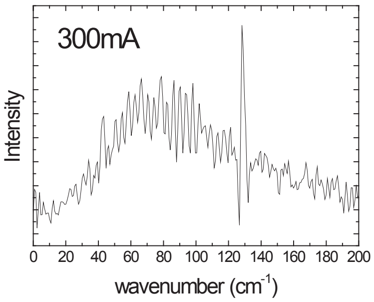

Figure 8.3: FTIR measurements of the radiation for forward bias of H656 for a current of 300 mA. Note the appearance of the broadband background radiation.

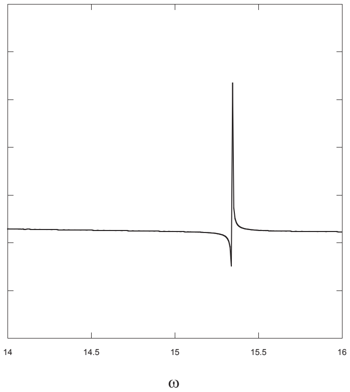

Figure 8.4: Theoretical lineshape showing the modified Lorentzian form.

## Bibliography

[1] P. Bakshi, K. Kempa, "Inter-subband plasmon-emission-based THz lasers", Physica E 7, pp. 63-68 (2000)

[2] P. Bakshi, K. Kempa, *Plasma Instabilities in Quantum Well Structures, in Condensed Matter Theories, Vol. 20*, Edited by J.W. Clark, R.M. Panoff, and H. Li, pp. 45-53 (2006)

[3] P. Bakshi and K. Kempa "Mathematical Signatures of Plasma Instabilities in Low- Dimensional Solid State Systems" in *Condensed Matter Theories*, J. Clark and P. Panat (eds.), NOVA Science Publishers, Vol. 12, 399 (1997)

[4] J.B. Williams, M.S. Sherwin, K.D. Maranowski, and A.C. Gossard, "Dissipation of Intersubband Plasmons in Wide Quantum Wells", Phys. Rev. Lett., 87, 3, 037401.

[5] M. Helm, in *Intersubband Transitions in Quantum Wells: Physics and Device Applications I*, edited by H. C. Liu and F. Capasso, Semiconductors and Semimetals Vol. 62 (Academic Press, San Diego, 2000), pp. 199.

[6] J. Singh *Quantum Mechanics. Fundamentals and Applications to Technology*, (McGraw-Hill, 1971)

[7] M. Coquelin, "Resonant plasmon and subband excitation in heterostructures", PhD dissertation (Technical University at Vienna, 2008).

[8] A.L. Fetter, and J.D. Walecka *Quantum Theory for Many-Particle Physics*, edited by H. C. Liu and F. Capasso, Semiconductors and Semimetals Vol. 62 (Academic Press, San Diego, 2000), pp. 199.

[9] G. Mahan *Many-Particle Physics*, (Plenum, 1981)

Chapter 9

# Conclusions and Outlook

In Part I globally accurate algebraic expressions were obtained for the finite SQW, ASQW, and the triangular well. Concerning the transmission properties of the triangular barrier, an exact mapping of the triangular barrier problem into the rectangular barrier has been established. Finally a new transcendental equation has been given describing the energy levels of the finite-width double barrier structure. Extensions of these methods are topics for further study: the finite SQW with particles in the well, with and without bias, the asymmetric double quantum well, with and without particles, and the analysis of composite structures.

In Part II the transport modeling revealed the underlying processes responsible for the main features of the experimental IV's for the low bias range, for both forward and reverse bias. Further tranport studies with various intersubband processes included are envisioned allowing for the NESS for the mid- to higher biases to be calculated, and the resulting radiation profiles for this sample, and other samples can be determined.

## Appendix A

# Quantum Wells

---

In this appendix the details regarding the derivation of the energies and wavefunctions of the systems presented in Chapter 3 are given. This includes: the infinte square well (ISW), the finite symmetric quantum well (SQW), the finite asymmetric quantum well (ASQW), and the finite symmetric double quantum well (SDQW) (both well widths equal and all barrier heights equal). Any standard quantum mechanics text [1-8] gives plenty of details on the ISW, and the SQW. However, for the case of the ASQW, and the double square well, both symmetric and asymmetric, little widespread information exists [2, 9, 12, 13].

## A.1 The Infinite Square Well (ISW)

For a particle in an infinite potential well (see Fig. A.1),

$$V(z) = \begin{cases} 0, & \text{if } -L/2 \leq z \leq L/2; \\ \infty, & \text{otherwise.} \end{cases} \tag{A.1}$$

As the potential is infinite, the boundary conditions at $z = +L/2$ and $z = -L/2$ are required to be

$$\psi(z = +L/2) = 0, \qquad \psi(z = -L/2) = 0, \tag{A.2}$$

and as $V = 0$ inside the well region (between $-L/2$ and $L/2$), and the time-independent Schrodinger equation (TISE) is,

$$-\frac{\hbar^2}{2m^*}\frac{d^2\psi(z)}{dz^2} = E\psi(z), \qquad -L/2 \leq z \geq +L/2 \tag{A.3}$$

which can also be expressed as

$$\frac{d^2\psi(z)}{dz^2} + k^2\psi(z) = 0, \qquad k^2 = \frac{2m^*E}{\hbar^2} \tag{A.4}$$

where $m*$ is the effective mass value for the particular semiconductor material (e.g. for GaAs $m^* = 0.067m_e$. Between $-L/2$ and $L/2$ the general solution which satisfies Eq. (A.3) is

$$\psi(z) = A\sin(kz) + B\cos(kz), \tag{A.5}$$

and with the boundary conditions $\psi(-L/2) = \psi(L/2) = 0$,

$$\psi(L/2) = A\sin(kL/2) + B\cos(kL/2) = 0 \quad \Longrightarrow \quad A = 0 \quad \Longrightarrow \quad \psi(z) = B\cos(kz).$$

The wavenumber $k$ can be found from the condition $\psi(L/2) = A\cos(kL/2) = 0 \rightarrow kL/2 = n\pi/2$ or $k = n\pi/L$. To fix the constant $B$, the normalization condition is used:

$$\int_{-\infty}^{\infty} |\psi(z)|^2 dz = |B|^2 \int_{-L/2}^{L/2} \cos^2(n\pi z/L) dz = |B|^2\frac{L}{2} = 1, \tag{A.6}$$

$$\Longrightarrow B = \sqrt{\frac{2}{L}}, \tag{A.7}$$

so that the normalized stationary states of the infinite potential well of width $L$ are given by

$$\boxed{\psi_n(z) = \sqrt{\frac{2}{L}}\cos\left(\frac{n\pi z}{L}\right), \qquad n = 1, 2, ..} \tag{A.8}$$

It is noted that the above wavefunctions form a complete set, are alternately even and odd functions about the center of the well and with increasing $n$, each successive state has one more node in the wavefunction. This can be seen from Fig. (A.1). The eigenvalues are obtained from the relation in Eq. (A.4)

$$k = \sqrt{\frac{2mE}{\hbar^2}} \quad \Longrightarrow \quad E = \frac{(\hbar k)^2}{2m^*} \quad \Longrightarrow \boxed{E_{n,\infty} = \frac{(n\pi\hbar)^2}{2m^* L^2}, \qquad n = 1, 2, ..} \tag{A.9}$$

where the relation $k = n\pi/L$ was used.

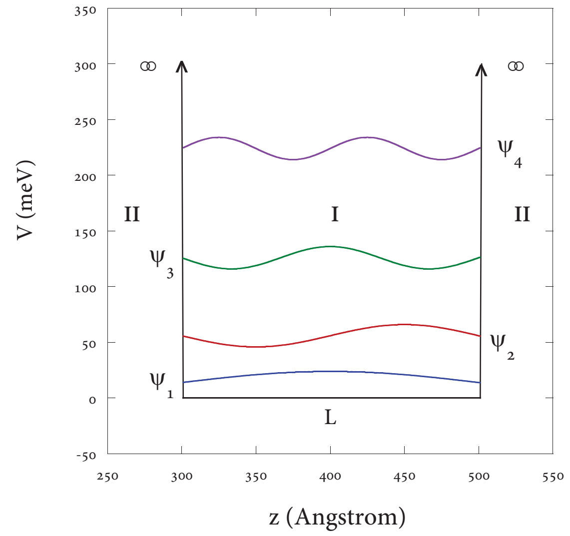

Figure A.1: The infinite square well for well width $L = 200$ Å, showing the first four wavefunctions.

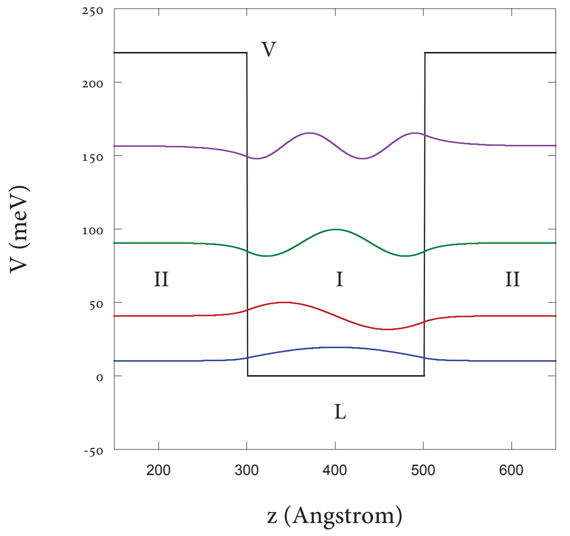

Figure A.2: The finite symmetric well for well width $L = 200$ Å, showing four wavefunctions.

## A.2 The Finite Symmetric Quantum Well (SQW)

In contrast to the case of a particle in an infinite potential well, the finite symmetric quantum well has barriers of finite height. For a particle in finite potential well of width $L$ and barrier height $V$ (Fig. A.2), the TISE reads

$$-\frac{\hbar^2}{2m^*}\frac{d^2\psi(z)}{dz^2} + V(z)\psi(z) = E\psi(z) \tag{A.10}$$

where the potential $V(z)$ is constant in the three regions, denoted $I$ and $II$ and given by

$$V(z) = \begin{cases} 0, & \text{if } -L/2 \leq z \leq L/2; \\ \\ V, & \text{otherwise.} \end{cases} \tag{A.11}$$

The general solution of the TISE in the region between $-L/2$ and $L/2$ is

$$\psi(z) = A \sin k_I z + B \cos k_I \qquad - L/2 \leq z \geq +L/2 \tag{A.12}$$

where $k_I = \sqrt{2m^* E}/\hbar$, and in the regions of the barriers, the general solutions are

$$\psi(z) = Ce^{k_{II} z} + De^{-k_{II} z} \qquad z < -L/2 \tag{A.13}$$

$$\psi(z) = Fe^{k_{II} z} + Ge^{-k_{II} z} \qquad z > L/2 \tag{A.14}$$

where $k_{II} = \sqrt{2m^*(V - E)}/\hbar$. To determine the constants, first note that in the limit $z \rightarrow +\infty, -\infty$, it is required that $D = F = 0$. Next impose the boundary conditions that the wavefunctions and the derivatives be continuous at the boundary $z = -L/2$ and $z = +L/2$. This results in four equations:

$$-A \sin(k_I L/2) + B \cos(k_I L/2) = Ce^{-k_{II} L/2} \tag{A.15}$$

$$Ak_I \cos(k_I L/2) + Bk_I \sin(k_I L/2) = Ck_{II} e^{-k_{II} L/2} \tag{A.16}$$

$$A \sin(k_I L/2) + B \cos(k_I L/2) = Ge^{-k_{II} L/2} \tag{A.17}$$

$$Ak_I \cos(k_I L/2) - Bk_I \sin(k_I L/2) = -Gk_{II} e^{-k_{II} L/2} \tag{A.18}$$

Subtracting Eq. (A.15) from Eq. (A.17) gives

$$2A \sin(k_I L/2) = (G - C)e^{-k_{II} L/2}, \tag{A.19}$$

Adding Eq. (A.15) to Eq. (A.17) gives

$$2B\cos(k_I L/2) = (G+C)e^{-k_{II}L/2}, \tag{A.20}$$

Subtracting Eq. (A.18) from Eq. (A.16) gives

$$2Bk_I \sin(k_I L/2) = (G+C)k_{II}e^{-k_{II}L/2} \tag{A.21}$$

And finally adding Eq. (A.18) to Eq. (A.16) gives

$$2Ak_I \cos(k_I L/2) = -(G-C)k_{II}e^{-k_{II}L/2} \tag{A.22}$$

The equations (A.19)-(A.22) can be reduced to two equations, one for each *parity.* Dividing Eq. (A.21) by Eq. (A.20) yields

$$k_I \tan(k_I L/2) = k_{II}, \qquad \text{even parity} \tag{A.23}$$

and dividing Eq. (A.22) by Eq. (A.19) yields

$$k_I \cot(k_I L/2) = -k_{II}, \qquad \text{odd parity} \tag{A.24}$$

Multiplying through by $L/2$, and letting $\alpha = k_I L/2$ and $P = k_{II}L/2 = \sqrt{2m^* V/\hbar^2}L/2$, these can be written

$$\boxed{\alpha \tan\alpha = \sqrt{P^2-\alpha^2}, \quad \text{(even parity)} \quad -\alpha\cot\alpha = \sqrt{P^2-\alpha^2} \quad \text{(odd parity)}} \tag{A.25}$$

where

$$\boxed{\alpha = \sqrt{\frac{2m^* E}{\hbar^2}}\frac{L}{2} \qquad P = \sqrt{\frac{2m^* V}{\hbar^2}}\frac{L}{2}} \tag{A.26}$$

and $\alpha$ represents the energy eigenvalue, and $P$ represents the *well-strength parameter.* The two Eqs. (A.25) can be further reduced as

$$\alpha\tan\alpha = \sqrt{P^2-\alpha^2} \quad \Longrightarrow \tan\alpha = \frac{\sqrt{(P^2-\alpha^2)}}{\alpha} \quad \Longrightarrow \tan^2\alpha = \frac{P^2-\alpha^2}{\alpha^2} \tag{A.27}$$

$$\Longrightarrow \sec^2\alpha = \frac{P^2-\alpha^2+\alpha^2}{\alpha^2} \qquad \Longrightarrow \cos^2\alpha = \frac{\alpha^2}{P^2} \qquad \Longrightarrow \boxed{\,|\cos\alpha| = \frac{\alpha}{P}\,} \tag{A.28}$$

and similarly for the odd parity solution:

$$-\alpha\cot\alpha = \sqrt{P^2-\alpha^2} \qquad \Longrightarrow \boxed{\,|\sin\alpha| = \frac{\alpha}{P}\,} \tag{A.29}$$

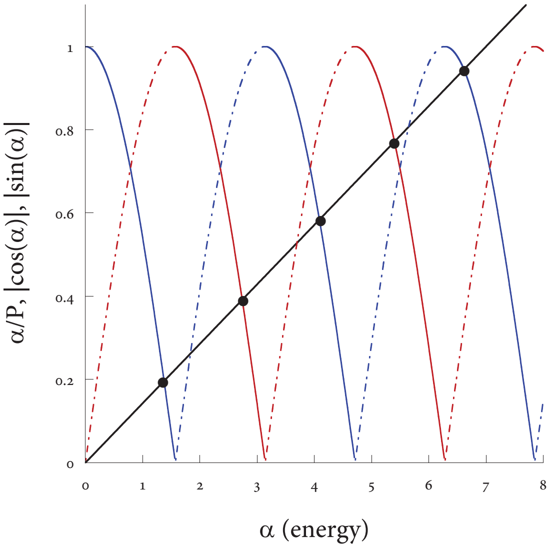

Figure A.3: Graphical solution of Eqs. (A.28) and (A.29) giving the energies of the finite symmetric square well for (an arbitrarily chosen) well-strength $P = 7$, showing five solutions (bound states), determined by the intersection of the descending portion of the $|\cos\alpha|$ and $|\sin\alpha|$ with the $\alpha/P$ curve.

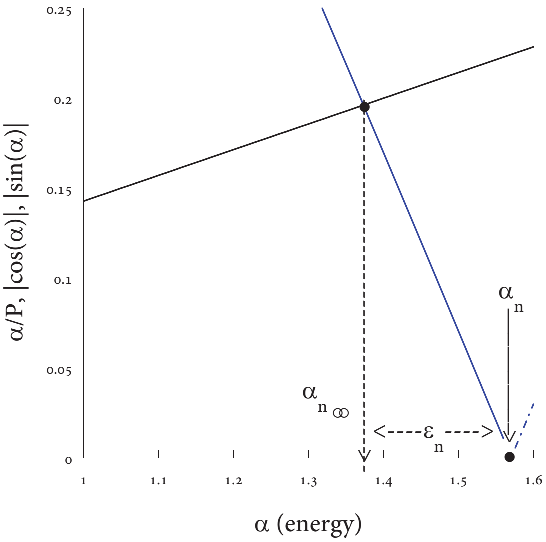

Figure A.4: Detail of the graphical method for the SQW energies. Plot is close-up of the $n = 1$ solution for the $P = 7$ case presented in the text, showing the 'smallness' parameter $\epsilon_n = \alpha_n - \alpha_{n,\infty}$, where $\alpha_{n,\infty} = n\pi/2$ and $\alpha_n$ is the approximate energy eigenvalue.

The standard approach to solving these *transcendental* equations is to take the Eqs. (A.28),(A.29) and find a solution by graphical means [4], or numerically. Fig. (A.3) shows a plot of Eq. (A.28) and (A.28); the conventional method of solution is by finding the intersection (the roots) of $\alpha/P$ with the descending branch of both $|\cos\alpha|$ and $|\sin\alpha|$. The method will be presented here as it is used in approximating the energies of the DQW system (see below). From the graph of $|\cos\alpha|$ and $|\sin\alpha|$ vs. $\alpha/P$, it is seen that the actual solutions (intersections) are 'close' to the value $\alpha_{n,\infty} = n\pi/2$. Therefore an approximation of the cosine and sine can be made, by defining the 'small' departure $\epsilon_n$ from the value $n\pi/2$, as

$$\epsilon_n = \alpha_{n,\infty} - \alpha_n \Longrightarrow \qquad \cos\alpha_n = \cos(\frac{n\pi}{2} - \epsilon_n) = \sin\epsilon_n = \epsilon_n - \frac{\epsilon_n^3}{3!} + \frac{\epsilon_n^5}{5!} - \cdots \tag{A.30}$$

where $\alpha_n$ represents the approximate energy eigenvalue, and the sine expansion is used as $\epsilon$ is small. Taking the first term in the sine expansion gives

$$\cos\alpha_n = \epsilon_n \qquad \Longrightarrow \qquad \frac{\alpha_n}{P} = \alpha_{n,\infty} - \alpha_n \qquad \Longrightarrow \qquad \alpha_n = \frac{P}{P+1}\alpha_{n,\infty} \tag{A.31}$$

$$\Longrightarrow \qquad E_n = E_{n,\infty}\left(\frac{P}{P+1}\right)^2 \tag{A.32}$$

where $a\alpha_n = \sqrt{2m^* E_n/hbar^2}$ was used. For the next higher approximation, taking the two terms in the sine expansion gives

$$\cos\alpha_n = \epsilon_n - \frac{\epsilon_n^3}{3!} \qquad \Longrightarrow \qquad \frac{\alpha_n}{P} = (\alpha_{n,\infty} - \alpha_n) - \frac{(\alpha_{n,\infty} - \alpha_n)^3}{6} \tag{A.33}$$

$$\Longrightarrow \qquad \frac{\alpha_n}{P} = (\alpha_{n,\infty} - \alpha_n) - \frac{1}{6}\left(\alpha_{n,\infty} - \left(\alpha_{n,\infty}\frac{P}{P+1}\right)\right)^3 \tag{A.34}$$

where the result $\alpha_n = \alpha_{n,\infty}(P/(P+1))$ from the first approximation was used,

$$\Longrightarrow \qquad \alpha_n = \alpha_{n,\infty}\left(\frac{P}{P+1}\right)\left[1 - \frac{1}{6}\frac{\alpha_{n,\infty}^2}{(P+1)^3}\right] \tag{A.35}$$

or in terms of $E_{n,\infty}$

$$E_n = E_{n,\infty}\left(\frac{P}{P+1}\right)^2\left[1 - \frac{1}{6}\frac{(n\pi/2)^2}{(P+1)^3}\right] \tag{A.36}$$

and up to three terms,

$$\begin{aligned}
\cos\alpha_n = \epsilon_n - \frac{\epsilon_n^3}{3!} + \frac{\epsilon_n^5}{5!} \qquad &\Longrightarrow \qquad \frac{\alpha_n}{P} = (\alpha_{n,\infty} - \alpha_n) - \frac{(\alpha_{n,\infty} - \alpha_n)^3}{6} + \frac{(\alpha_{n,\infty} - \alpha_n)^5}{120} \\
&\Longrightarrow \qquad \frac{\alpha_n}{P} = (\alpha_{n,\infty} - \alpha_n) - \frac{1}{6}\left(\alpha_{n,\infty} - \left(\alpha_{n,\infty}\frac{P}{P+1}\right)\right)^3 + \cdots \\
&\qquad + \frac{1}{120}\left(\alpha_{n,\infty} - \left(\alpha_{n,\infty}\frac{P}{P+1}\right) - \frac{P\alpha_{n,\infty}^3}{6(P+1)^4}\right)^5
\end{aligned} \tag{A.37}$$

$$\alpha_n = \left(\frac{P}{P+1}\right)\alpha_{n,\infty}\left[1 - \frac{1}{6}\frac{\alpha_{n,\infty}^2}{(P+1)^3} + \frac{\alpha_{n,\infty}^4}{120}\left(1 - \frac{6(P(P+1)^3) - P\alpha_{n,\infty}^2}{6(P+1)^4}\right)^5\right]$$

or

$$E_n = E_{n,\infty}\left(\frac{P}{P+1}\right)\left[1-\frac{1}{6}\frac{(n\pi/2)^2}{(P+1)^3}+\frac{(n\pi/2)^4}{120}\left(1-\frac{6(P(P+1)^3)-P(n\pi/2)^2}{6(P+1)^4}\right)^5\right]^2 \tag{A.38}$$

### A.2.1 SQW Wavefunctions

The wavefunctions are determined as follows. Recalling the general solution for the regions $I$ and $II$, for the odd parity solutions, it is required that $A = D = F = 0$, and $C = G$, that is

$$\psi(z) = Ce^{k_{II}z} \qquad z < -L/2 \tag{A.39}$$

$$\psi(z) = B\cos k_I \qquad -L/2 \leq z \geq +L/2 \tag{A.40}$$

$$\psi(z) = Ge^{-k_{II}z} \qquad z > L/2 \tag{A.41}$$

and $C$ and $G$ are found from Eqs. (A.17) as

$$B\cos(k_I L/2) = Ge^{-k_{II}L/2}, \qquad G = B\cos(k_I L/2)e^{k_{II}L/2} = C, \tag{A.42}$$

and so the odd eigenfunctions are

$$\psi_n(z) = \begin{cases} [B\cos(k_I L/2)\,e^{k_{II}L/2}]e^{k_{II}z}, & z \leq -L/2, \\ B\cos(k_I z), & -L/2 \leq z \leq L/2, \\ [B\cos(k_I L/2)\,e^{k_{II}L/2}]e^{-k_{II}z}, & z \geq L/2, \end{cases} \tag{A.43}$$

and similarly for the even solutions, the eigenfunctions are

$$\psi_n(z) = \begin{cases} [-B\sin(k_I L/2)\,e^{k_{II}L/2}]e^{k_{II}z}, & z \leq -L/2, \\ B\sin(k_I z), & -L/2 \leq z \leq L/2, \\ [B\sin(k_I L/2)\,e^{k_{II}L/2}]e^{-k_{II}z}, & z \geq L/2. \end{cases} \tag{A.44}$$

The final constants $B$ are determined by the normalization condition,

$$1 = \int_{-\infty}^{\infty} |\psi(z)|^2 dz = |B|^2 (\int_{-\infty}^{-L/2} \cos^2(k_I L/2) e^{2k_{II}L/2} e^{2k_{II}z} dz + \int_{-L/2}^{L/2} \cos^2(k_I z) dz + \cdots$$

$$+ \int_{L/2}^{+\infty} \cos^2(k_I L/2) e^{2k_{II}L/2} e^{-2k_{II}z} dz) \tag{A.45}$$

or

$$1 = |B|^2 (\cos^2(k_I L/2) e^{2k_{II}L/2} \frac{1}{2k_{II}} e^{2k_{II}z} \Big|_{-\infty}^{-L/2} + \frac{1}{2} z + \frac{1}{4k_I} \sin(2k_I z) \Big|_{-L/2}^{L/2} + \cdots$$

$$+ \cos^2(k_I L/2) e^{2k_{II}L/2} \frac{-1}{2k_{II}} e^{-2k_{II}z} \Big|_{L/2}^{\infty}) \tag{A.46}$$

and

$$1 = |B|^2 (\cos^2(k_I L/2) e^{2k_{II}L/2} \frac{1}{2k_{II}} e^{-k_{II}L} + \frac{L}{2} + \frac{1}{4k_I} (\sin(k_I L) - \sin(-k_I L)) + \cdots$$

$$- \cos^2(k_I L/2) e^{2k_{II}L/2} \frac{-1}{2k_{II}} e^{-k_{II}L}) \tag{A.47}$$

and then

$$1 = |B|^2 (\frac{L}{2} + \frac{1}{2k_{II}} \cos^2(k_I L/2) \frac{1}{2k_{II}} + \frac{1}{2k_I} \sin(k_I L)) \tag{A.48}$$

so that the normalization constant is given by

$$\boxed{B = \left( \frac{L}{2} + \frac{1}{2k_{II}} \cos^2(k_I L/2) \frac{1}{2k_{II}} + \frac{1}{2k_I} \sin(k_I L) \right)^{-1}} \tag{A.49}$$

Putting the TISE in the form

$$\frac{d^2\psi(z)}{dz^2} = \frac{2m^*(V(z) - E)}{\hbar^2} \psi(z) \tag{A.50}$$

allows one to examine the curvature of the wavefunctions. This can be interpreted by saying that the left-hand side, the rate of change of the slope, is the *curvature*, i.e., the curvature of the function is equal to (essentially) $(V(z) - E)\psi(z)$. This means that if $E > V(z)$, for $\psi(z)$ positive, then $\psi(z)$ is curving negatively, and for $\psi(z)$ negative, then $\psi(z)$ is curving positively. In both cases, $\psi(z)$ is always curving towards the axis. This means that for $E > V(z)$, $\psi(z)$ has a kind of stability: its curvature is always bringing it back towards the axis, so it has oscillatory character. On the other hand, for $V(z) > E$, the curvature is always away from the axis. This means that $\psi(z)$ tends to diverge to infinity. Only under exactly the right conditions will this curvature be just enough to bring the wave function to zero as $z$ goes to infinity, and as $\psi(z)$ tends to zero, the curvature tends to zero, too.

### A.2.2 Single Eigenvalue Equation for the SQW

For the purposes of analytical approximations, it desirable to have a single eigenvalue equation instead of the individual parity solutions. Taking Eqs. (A.15) and (A.16)[10, 11] and expressing $A$ and $B$ in terms of $C$ and $D$, then using this to eliminate $A$ and $B$ in Eqs. (A.17) and (A.18), gives the result

$$D = C[\sin(2\alpha)((\sqrt{P^2-\alpha^2})/\alpha + \cot\alpha) - 1] \tag{A.51}$$

and

$$D = -C[\cos(2\alpha) - (\alpha/(\sqrt{P^2-\alpha^2}))\sin(2\alpha)] \tag{A.52}$$

respectively, and equating these two gives

$$\sin(2\alpha)((\sqrt{P^2-\alpha^2}/\alpha) - (\sqrt{P^2-\alpha^2}) + \cot\alpha) + \cos(2\alpha) = 1 \tag{A.53}$$

Next, from the definition of $\alpha$ and $P$, the following form is obtained

$$\left(1 - 2\frac{\alpha^2}{P^2}\right)\sin(2\alpha) + \left(2\frac{\alpha}{P}\sqrt{1-\frac{\alpha^2}{P^2}}\right)\cos(2\alpha) = 0 \tag{A.54}$$

This has been shown to be an identity for the sine of the sum of two angles,

$$\sin[2(\alpha+\Phi)], \qquad \text{where} \qquad \Phi = \sin^{-1}\left(\frac{\alpha}{P}\right) \tag{A.55}$$

and from these two equations can then be combined to give

$$\boxed{\alpha + \sin^{-1}\left(\frac{\alpha}{P}\right) = \frac{n\pi}{2}} \tag{A.56}$$

This particular will prove useful for the approximations made for the SQW.

## A.3 The Finite Asymmetric Square Well (ASQW)

For a finite potential well with barrier heights $V_1 > V_2$ (see Fig. A.5),

$$V(z) = \begin{cases} V_1, & \text{if } z < 0; \\ 0, & \text{if } 0 < z < L \\ V_2, & \text{if } z > L \end{cases} \tag{A.57}$$

the Schrodinger equation is

$$\frac{-\hbar^2}{2m^*}\frac{d^2\psi(z)}{dz^2} = (V_1 - E)\psi(z) \qquad \Longrightarrow \qquad \frac{d^2\psi(z)}{dz^2} = \kappa_I^2\psi(z) \qquad \text{(I)} \tag{A.58}$$

$$\frac{-\hbar^2}{2m^*}\frac{d^2\psi(z)}{dz^2} = E\psi(z) \qquad \Longrightarrow \qquad \frac{d^2\psi(z)}{dz^2} = k^2\psi(z) \qquad \text{(II)} \tag{A.59}$$

$$\frac{-\hbar^2}{2m^*}\frac{d^2\psi(z)}{dz^2} = (V_2 - E)\psi(z) \qquad \Longrightarrow \qquad \frac{d^2\psi(z)}{dz^2} = \kappa_{III}^2\psi(z) \qquad \text{(III)} \tag{A.60}$$

where

$$k = \sqrt{\frac{2m^*E}{\hbar^2}} \qquad \kappa_I = \sqrt{\frac{2m^*(V_1 - E)}{\hbar^2}} \qquad \kappa_{III} = \sqrt{\frac{2m^*(V_2 - E)}{\hbar^2}} \tag{A.61}$$

The wavefunctions are given by

$$\psi_I(z) = A_I e^{\kappa_I z} \qquad z \le 0 \tag{A.62}$$

$$\psi_{II}(z) = A\sin(kz + \delta) \qquad 0 \le z \le L \tag{A.63}$$

$$\psi_{III}(z) = A_{III} e^{-\kappa_{III} z} \qquad z \ge L \tag{A.64}$$

and matching the logarithmic derivatives at $z = 0$ and $z = L$,

$$\frac{1}{\psi_I(z)}\frac{d\psi_I(z)}{dz}\bigg|_{z=0} = \frac{1}{\psi_{II}(z)}\frac{d\psi_{II}(z)}{dz}\bigg|_{z=0} \tag{A.65}$$

$$\Longrightarrow \frac{1}{A_I}A_I\kappa_I = \frac{1}{A_I\sin\delta}A_I k\cos\delta \qquad \Longrightarrow \qquad \kappa_I = k\cot\delta \tag{A.66}$$

and similarly,

$$\frac{1}{\psi_{II}(z)}\frac{d\psi_{II}(z)}{dz}\bigg|_{z=L} = \frac{1}{\psi_{III}(z)}\frac{d\psi_{III}(z)}{dz}\bigg|_{z=L} \tag{A.67}$$

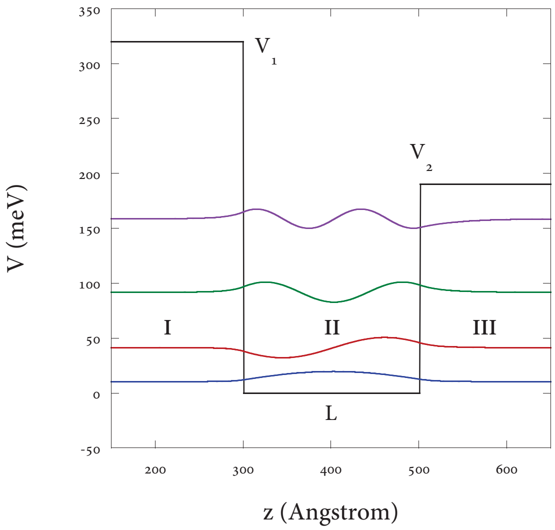

Figure A.5: The ASQW for well width $L = 200$ Å, showing the first four wavefunctions.

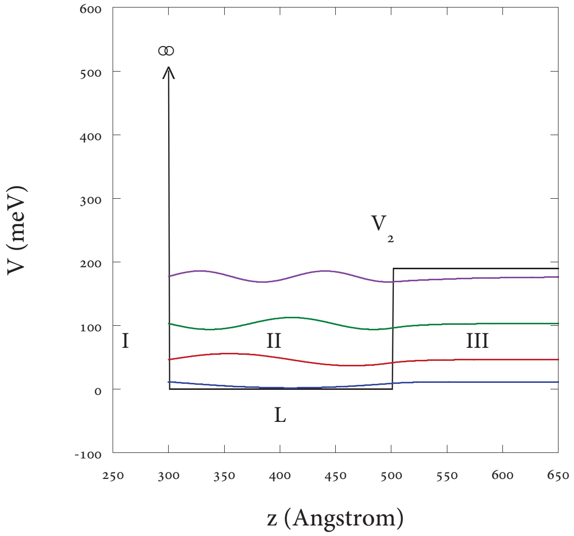

Figure A.6: The half-inifinte well, in which $V_1 \to \infty$ for well width $L = 200$ Å, showing the first four wavefunctions.

$$\implies \frac{1}{A\sin(kL+\delta)}Ak\cos(kL+\delta) = \frac{1}{A_{III}e^{-\kappa_{III}L}} - \kappa_{III}A_{III}e^{-\kappa_{III}L} \tag{A.68}$$

$$\implies \qquad \kappa_{III} = -k\cot(kL+\delta) \tag{A.69}$$

The above two equations can be rewritten as

$$\cot\delta = \frac{\kappa_I}{k} \implies \delta = \cot^{-1}(\frac{\kappa_I}{k}) \implies n\pi - \sin^{-1}(\frac{\kappa_I}{k}) \tag{A.70}$$

where the identity $\cot^{-1}(x) = n\pi - \sin^{-1}(1/\sqrt{1+x^2})$ was used, and similarly for the second condition,

$$\cot(kL+\delta) = -\frac{\kappa_{III}}{k} \implies kL+\delta = \cot^{-1}(\frac{\kappa_{III}}{k}) \implies n\pi - \sin^{-1}(\frac{\kappa_{III}}{k}) \tag{A.71}$$

Eliminating $\delta$ gives

$$kL = n\pi - \sin^{-1}\left(\frac{k\hbar}{2m^*V_1}\right) - \sin^{-1}\left(\frac{k\hbar}{2m^*V_2}\right) \tag{A.72}$$

This is the eigenvalue equation for the finite asymmetric quantum well. In chapter 3 this is equation is used to approximate the energies. The wavefunctions are given by

$$\psi_n(z) = C \begin{cases} e^{\kappa_l z} \sin \delta, & z \leq 0, \\ \sin(k_n z + \delta), & 0 \leq z \leq L, \\ e^{-\kappa_r (z-L)} \sin(k_n L + \delta), & z \geq L, \end{cases} \tag{A.73}$$

## A.4 The Finite Symmetric Double Quantum Well (DSQW)

This section details the work of the finite symmetric double quantum well (DSQW), with equal well widths $L$, barrier width $d$, and with all barrier heights equal to $V_0$ (refer to Fig. 3.14 (a)). The value $z = 0$ is taken at the center of the middle barrier, and the potential is given by

$$V(z) = \begin{cases} V_0, & -\infty < z < -L,\ -d/2 < zd/2,\ L < z < \infty; \\ 0, & -L < z < -d/2,\ d/2 < z < L \end{cases} \tag{A.74}$$

The range of the potential is split up and denoted by the roman numerals I through V, and the TISE is given by the following forms

$$\frac{-\hbar^2}{2m^*} \frac{d^2\psi(z)}{dz^2} = E\psi(z) \qquad \text{(II,IV)} \tag{A.75}$$

$$\frac{-\hbar^2}{2m^*} \frac{d^2\psi(z)}{dz^2} = (V_0 - E)\psi(z) \qquad \text{(I,III,V)} \tag{A.76}$$

or in terms of the quantities $k$ and $\kappa$ as

$$\frac{d^2\psi(z)}{dz^2} = k^2\psi(z) \qquad \text{(II,IV)} \tag{A.77}$$

$$\frac{d^2\psi(z)}{dz^2} = \kappa^2\psi(z) \qquad \text{(I,III,V)} \tag{A.78}$$

where

$$k = \sqrt{\frac{2m^*E}{\hbar^2}} \qquad \kappa = \sqrt{\frac{2m^*(V_0 - E)}{\hbar^2}} \tag{A.79}$$

The wavefunctions of the SDQW in regions I,III,V are denoted by

$$\psi_I(z) = Ae^{\kappa z} + Be^{-\kappa z} \tag{A.80}$$

$$\psi_{III}(z) = Ce^{\kappa z} + De^{-\kappa z} \tag{A.81}$$

$$\psi_V(z) = Fe^{\kappa z} + Ge^{-\kappa z} \tag{A.82}$$

and in regions II,IV

$$\psi_{II}(z) = H\cos\left\{k\left[z + \left(\frac{L}{2} + \frac{d}{2}\right)\right]\right\} + I\sin\left\{k\left[z + \left(\frac{L}{2} + \frac{d}{2}\right)\right]\right\} \tag{A.83}$$

$$\psi_{IV}(z) = J\cos\left\{k\left[z - \left(\frac{L}{2} + \frac{d}{2}\right)\right]\right\} + K\sin\left\{k\left[z - \left(\frac{L}{2} + \frac{d}{2}\right)\right]\right\} \tag{A.84}$$

To begin with this problem, first note that the requirement that $\psi(z)$ be finite at all $z$ implies that $\psi(z) \to 0$ as $|z| \to \infty$, and since $e^{\kappa z} \to \infty$ as $z \to \infty$ and $e^{-\kappa z} \to \infty$ as $z \to -\infty$, we get $B = F = 0$. Next, due to the symmetry of this system, that is, $V(z) = V(-z)$, there are even and odd functions, and this requirement gives

$$\psi_I(z) = \pm\psi_I(-z) \Longrightarrow A = \pm G \tag{A.85}$$

$$\psi_{III}(z) = \pm\psi_{III}(-z) \Longrightarrow C = \pm D \tag{A.86}$$

$$\psi_{II}(z) = \pm\psi_{IV}(-z) \Longrightarrow \begin{cases} H = \pm J \\ \\ I = \pm K \end{cases} \tag{A.87}$$

where the upper sign corresponds to the even state and the lower sign to the odd state. The updated wavefunctions now are,

$$\psi_I(z) = \pm G e^{\kappa z} \tag{A.88}$$

$$\psi_{III}(z) = \pm D e^{\kappa z} + D e^{-\kappa z} \tag{A.89}$$

$$\psi_V(z) = G e^{-\kappa z} \tag{A.90}$$

and in region II,IV

$$\psi_{II}(z) = H\cos\left\{k\left[z + \left(\frac{L}{2} + \frac{d}{2}\right)\right]\right\} + I\sin\left\{k\left[z + \left(\frac{L}{2} + \frac{d}{2}\right)\right]\right\} \tag{A.91}$$

$$\psi_{IV}(z) = J\cos\left\{k\left[z - \left(\frac{L}{2} + \frac{d}{2}\right)\right]\right\} + K\sin\left\{k\left[z - \left(\frac{L}{2} + \frac{d}{2}\right)\right]\right\} \tag{A.92}$$

Now matching the logarithmic derivatives, $(1/\psi)d\psi/dz$, at the boundaries $z = -L - d/2$ and $z = -d/2$, that is in the region of the left well,

$$\frac{1}{\psi_I(z)}\frac{d\psi_I(z)}{dz}\bigg|_{z=-L-d/2} = \frac{1}{\psi_{II}(z)}\frac{d\psi_{II}(z)}{dz}\bigg|_{z=-L-d/2} \tag{A.93}$$

$$\frac{1}{\psi_{II}(z)}\frac{d\psi_{II}(z)}{dz}\bigg|_{z=-d/2} = \frac{1}{\psi_{III}(z)}\frac{d\psi_{III}(z)}{dz}\bigg|_{z=-d/2} \tag{A.94}$$

Starting with Eq. (A.93), the expression becomes

$$\frac{1}{Ge^{-\kappa(L+d/2)}}G\kappa e^{-\kappa(L+d/2)} = \frac{-Hk\sin(-kL/2)+Ik\cos(-kL/2)}{H\cos(-kL/2)+I\sin(-kL/2)}$$

and factoring out the ratio $H/I$, and using the even/odd property of the sine and cosine functions,

$$\kappa = \frac{(H/I)k\sin(kL/2)+k\cos(kL/2)}{(H/I)\cos(kL/2)-\sin(kL/2)} \tag{A.95}$$

Now taking the second condition Eq. (A.94), we get

$$\frac{-Hk\sin(kL/2)+Ik\cos(kL/2)}{H\cos(kL/2)+I\sin(kL/2)} = \frac{\pm D\kappa e^{-\kappa d/2}\mp D\kappa e^{\kappa d/2}}{\pm De^{-\kappa d/2}+De^{\kappa d/2}}$$

or

$$\frac{-(H/I)k\sin(kL/2)+k\cos(kL/2)}{(H/I)\cos(kL/2)+\sin(kL/2)} = \frac{\pm D\kappa e^{-\kappa d/2}(1-e^{\kappa d/2})}{De^{-\kappa d/2}(1+e^{\kappa d/2})}$$

and then

$$\frac{-(H/I)k\sin(kL/2)+k\cos(kL/2)}{(H/I)\cos(kL/2)+\sin(kL/2)} = \pm\kappa\frac{(1-e^{\kappa d/2})}{(1+e^{\kappa d/2})} \tag{A.96}$$

Next defining the ratio $\tan\delta \equiv H/I$, Eqs. (A.95) and (A.96) become

$$\kappa = \frac{\tan\delta k\sin(kL/2)+k\cos(kL/2)}{\tan\delta\cos(kL/2)-\sin(kL/2)}$$

$$\pm\kappa\frac{(1-e^{\kappa d/2})}{(1+e^{\kappa d/2})} = \frac{-\tan\delta k\sin(kL/2)+k\cos(kL/2)}{\tan\delta\cos(kL/2)+\sin(kL/2)}$$

and expressing each of these equations in terms of $\tan\delta$, respectively, gives

$$\tan\delta = \frac{\kappa\sin(kL/2) + k\cos(kL/2)}{\kappa\cos(kL/2) - k\sin(kL/2)} \tag{A.97}$$

$$\tan\delta = \frac{k\cos(kL/2) \mp \lambda\sin(kL/2)}{\pm\lambda\cos(kL/2) + k\sin(kL/2)}, \qquad \lambda \equiv \kappa\frac{(1-e^{-\kappa d})}{(1+e^{\kappa d})} \tag{A.98}$$

Now eliminating $\tan\delta$, one expression is obtained as

$$\frac{\kappa\sin(kL/2) + k\cos(kL/2)}{\kappa\cos(kL/2) - k\sin(kL/2)} = \frac{k\cos(kL/2) \mp \lambda\sin(kL/2)}{\pm\lambda\cos(kL/2) + k\sin(kL/2)} \tag{A.99}$$

which gives

$$[\kappa + k\cot(kL/2)][\pm\lambda\cot(kL/2) + k] = [k\cot(kL/2) \mp \lambda][\kappa\cot(kL/2) - k]$$

or

$$\pm k\kappa\frac{(1-e^{\kappa d})}{(1+e^{\kappa d})}\cot^2(kL/2) - k\kappa\cot^2(kL/2) \pm 2\kappa^2\frac{(1-e^{\kappa d})}{(1+e^{\kappa d})}\cot(kL/2) + 2k^2\cot(kL/2) = -k\kappa \pm k\kappa\frac{(1-e^{\kappa d})}{(1+e^{\kappa d})}$$

which then becomes

$$k\kappa\cot^2(kL/2)\left(\frac{\mp e^{\kappa d}}{(1+e^{\kappa d})}\right) \pm 2\cot(kL/2)\left[\frac{\kappa^2(1-e^{\kappa d}) + k^2(1+e^{\kappa d})}{1+e^{\kappa d}}\right] = \mp k\kappa \pm k\kappa\left(\frac{\mp e^{\kappa d}}{(1+e^{\kappa d})}\right)$$

which reduces to

$$k\kappa\cot^2(kL/2) \pm \cot(kL/2)e^{-\kappa d}\left(\kappa^2(1-e^{\kappa d}) + k^2(1+e^{\kappa d})\right) = k\kappa$$

Next factoring out the cot term:

$$k\kappa\cot^2(kL/2) \pm \cot(kL/2)\left[e^{-\kappa d}(\kappa^2 + k^2) + k^2 - \kappa^2\right] = k\kappa$$

and then factoring out the $k\kappa$ term,

$$k\kappa\left(\cot^2(kL/2)-1\right)=\cot(kL/2)\left[\pm e^{-\kappa d}(\kappa^2+k^2)+k^2-\kappa^2\right] \tag{A.100}$$

Now recognizing that the $\cot^2(kL/2)$ term can be put in terms of a single $\cot(kL/2)$, from the identity

$$\tan(\theta+\phi)=\frac{\cot\theta+\cot\phi}{\cot\theta\cot\phi-1}, \tag{A.101}$$

where for $\theta=\phi=kL/2$ this gives

$$\cot^2(kL/2)-1=\frac{2\cot(kL/2)}{\tan(kL)}, \tag{A.102}$$

and so Eq. (A.100) becomes

$$2k\kappa\cot(kL)=k^2-\kappa^2\pm(k^2+\kappa^2)e^{-\kappa d} \tag{A.103}$$

where $k$ and $\kappa$ are given by

$$k=\sqrt{\frac{2m^*E}{\hbar^2}} \qquad \kappa=\sqrt{\frac{2m^*(V_0-E)}{\hbar^2}} \tag{A.104}$$

This is the eigenvalue equation for the symmetric DQW, with well width $L$, barrier height $V_0$, and middle barrier width $d$. The $\pm$ sign accounts for the even ($+$) and odd ($-$) states of the double well system and the exponential factor 'splitting' or separation of the even and odd wavefunctions as $d$ varies. To accurately determine the energies, Eq. (A.103) must be solved numerically. However, analytical approximations will made with this equation to arrive at algebraic expressions for the energy eigenvalues, in terms of the well-strength parameter appropriate for this system (see main text, Chap.3). To get a feel for how the energies vary with the middle barrier width variation, however, Eq. (A.103) was solved numerically. Fig. (A.7) shows this behavior of the first and second energy levels as $d$ is increased.

One further useful result is a variation of Eq. (A.103) above. By using the identity $\cot\theta = (1/2)\cot(\theta/2)-(1/2)\tan(\theta/2)$,

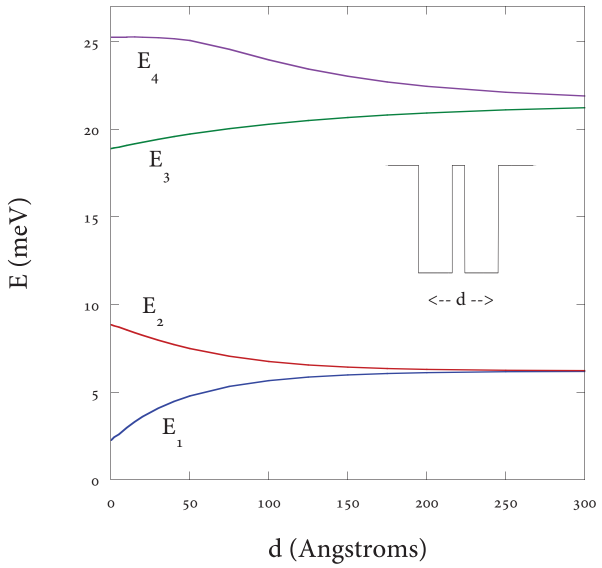

Figure A.7: The finite SDQW: variation of the $E_n^{\pm}$ with $d$, $V_0$ fixed. Well widths $L = 200$ Å, height $V_0$. The first two 'doublets' are shown.

$$2k\kappa\left[(1/2)\cot(kL/2) - (1/2)\tan(kL/2)\right] - k^2 + \kappa^2 = \pm(k^2+\kappa^2)e^{-\kappa d}$$

or

$$k\kappa\cot(kL/2) - k\kappa\tan(kL/2) - k^2 + \kappa^2 = \pm(k^2+\kappa^2)e^{-\kappa d}$$

and

$$\kappa^2 - k^2\cot(kL/2)\tan(kL/2) + k\kappa\cot(kL/2) - k\kappa\tan(kL/2) = \pm(k^2+\kappa^2)e^{-\kappa d}$$

where $\cot(kL/2)\tan(kL/2) = 1$ was inserted, and finally

$$(\kappa + k\cot(kL/2)(\kappa - k\tan(kL/2) = \pm(k^2+\kappa^2)e^{-\kappa d} \qquad \text{(A.105)}$$

### A.4.1 DSQW: Limiting Cases, $d \to \infty$, $d \to 0$ and $V_0 \to \infty$

By using this second form of the SDQW eigenvalue equation, two important limiting cases are quickly obtained. As the middle barrier width is increased, $d \to \infty$, $e^{-\kappa d} \to 0$ and we expect this equation to reduce to that of the single finite quantum well. Eq. (A.105) then becomes

$$(\kappa + k\cot(kL/2)(\kappa - k\tan(kL/2) = 0$$

and therefore

$$(\kappa + k\cot(kL/2)) = 0 \qquad \Longrightarrow -\alpha\cot\alpha = \sqrt{P^2-\alpha^2} \quad \text{(odd parity)} \tag{A.106}$$

$$(\kappa - k\tan(kL/2)) = 0 \qquad \Longrightarrow \alpha\tan\alpha = \sqrt{P^2-\alpha^2}, \quad \text{(even parity)} \tag{A.107}$$

where both expressions in Eqs. (A.108) and (A.109) were multiplied by $L/2$, and then using the identification of $\alpha = \sqrt{2m^*E}L/2$. These are just the eigenvalue equations for the separate SQW of width $L$, and height $V_0$, as expected. For the next limit, $d \to 0$, $e^{-\kappa d} \to 1$, it is more convenient to use the first SDQW eigenvalue equation, Eq. (A.103), which gives

$$2k\kappa\cot(kL) = k^2 - \kappa^2 \pm (k^2+\kappa^2)$$

and because of the ±, this becomes

$$2k\kappa\cot(kL) = -2\kappa^2 \implies k\cot(kL) = -\kappa \implies$$

$$\Longrightarrow \boxed{-\alpha\cot(2\alpha) = \sqrt{P^2-\alpha^2} \ \text{(odd parity)}} \tag{A.108}$$

$$2k\kappa\cot(kL) = 2k^2 \implies k\tan(kL) = \kappa \implies$$

$$\Longrightarrow \boxed{\alpha \tan(2\alpha) = \sqrt{P^2 - \alpha^2}, \quad \text{(even parity)}} \tag{A.109}$$

These two expressions are simply the eigenvalue equations for the SQW of width $2L$. For the intermediate $d$ values, analytical approximations were made and are detailed in the main text in Chapter 3. For the limit $V_0 \to \infty$,

# Bibliography

[1] L. D. Landau, L. Lifshitz, *Quantum Mechanics* (Pergamon Press, Oxford 1958), pp. 61-64.

[2] D. Ter Harr, *Selected Problems in Quantum Mechanics* (Academic, New York, 1964), pp. 47-49.

[3] A. S. Davydov, *Quantum Mechanics* (Pergamon Press, Oxford, 1965), pp. 88-90.

[4] C. Cohen-Tannoudji, B. Diu, and F. Laloe, *Quantum Mechanics* (Wiley-Interscience, New York, 1977) vol 1, pp. 74-78.

[5] R. Eisberg, R. Resnick, *Quantum Physics of Atoms, Molecules, Solids, Nuclei, and Particles* (Wiley, New York, 1987), pp. G1-G6.

[6] M. A. Morrison, *Understanding Quantum Physics* (Prentice-Hall, Englewood Cliffs, NJ, 1990), pp. 319-340.

[7] R. Gilmore, *Elementary Quantum Mechanics In One Dimension* (Johns Hopkins University Press, Baltimore, MD, 2004), pp. 91-104.

[8] D. J. Griffiths, *Introduction to Quantum Mechanics* (Prentice-Hall, Englewood Cliffs, NJ, 1995), pp. 60-62.

[9] M. A. Morrison, *Quantum States of Atoms, Molecules, etc* (Prentice-Hall, Englewood Cliffs, NJ, 1990), pp. 319-340.

[10] B. C. Reed, “A single equation for finite rectangular well energy eigenvalues,” Am. J. Phys., **58** (5), 503-504 (1990).

[11] D. W. L. Sprung, H. Wu, J. Martorell, “A new look at the square well potential,” Eur. J. Phys., **13**, 21-25 (1992).

[12] J. F. Bloch, V. Ignatovich, “A new approach to bound states in potential wells,” Am. J. Phys., **69** (11), 1177-1181 (2001).

[13] A. Ganguly, S. Kuru, J. Negro, L.M. Nieto, "A study of the bound states for square potential wells with position-dependent mass," Phys. Lett. A., **360**, 228-233 (2006).

# Appendix B

# Appendix: Tunneling and Transfer Matrix Calculations

---

In this appendix, the details of the derivation of the tunneling transmission probability are presented for several relevant cases: the single symmetric rectangular barrier, the asymmetric rectangular barrier, the trinagular barrier, the symmetric double barrier, and the asymmetric double barrier.

## B.1 Single Rectangular Barrier

Consider a simple, single rectangular barrier as shown in Fig. 4.2 (a) of Chapter 4, Section 4.1. The potential only exists between $z = -d$ and $z = d$,

$$V(z) = \begin{cases} 0, & z < -d, \\ V_0, & -d < z < d, \\ 0, & z > d, \end{cases} \tag{B.1}$$

with both incoming and outgoing waves on either side of the barrier described by propagating waves $k^2 = (2m^*E)/\hbar^2$, while in the barrier the waves are attenuated, with $\kappa^2 = (2m^*(V_0 - E))/\hbar^2$. The wavefunction is given in general by

$$\psi(z) = \begin{cases} A_1 e^{ikz} + B_1 e^{-ikz}, & z < -d, \\ A_2 e^{\kappa z} + B_2 e^{-\kappa z}, & -d < z < d, \\ A_3 e^{ikz} + B_3 e^{-ikz}, & z > d, \end{cases} \tag{B.2}$$

where $A_i$'s and $B_i$'s are the amplitudes of the waves. There are six unknowns to evaluate. Since the *transmission* of a wave through the barrier incident from the left is sought, the incoming wave from the right is ignored. However, when considering the double and triple barrier cases, this will not be so, as there will be reflected waves from those boundaries to be considered. Applying the conditions $\psi_1(z=-d) = \psi_2(z=-d)$ and $\psi_1'(z=-d) = \psi_2'(z=-d)$ to the first interface, $z = -d$, gives the two conditions

$$A_1 e^{-ikd} + B_1 e^{ikd} = Ce^{-\kappa d} + De^{\kappa d}, \qquad ik[A_1 e^{-ikd} - B_1 e^{ikd}] = \kappa[A_2 e^{-\kappa d} - B_2 e^{\kappa d}], \tag{B.3}$$

which can be solved for $A_1$ and $B_1$ in terms of $A_2$ and $B_2$. First, adding these two equations gives $A_1$ in terms of $A_2$ and $B_2$, then subtracting these equations gives $B_1$ in terms of $A_2$ and $B_2$:

$$A_1 = A_2 \left(\frac{ik+\kappa}{2ik}\right) e^{(ik-\kappa)d} + B_2 \left(\frac{ik-\kappa}{2ik}\right) e^{(ik+\kappa)d} \tag{B.4}$$

$$B_1 = A_2 \left(\frac{ik-\kappa}{2ik}\right) e^{-(ik+\kappa)d} + B_2 \left(\frac{ik+\kappa}{2ik}\right) e^{-(ik-\kappa)d} \tag{B.5}$$

or in terms of matrices,

$$\begin{bmatrix} A_1 \\ B_1 \end{bmatrix} = M_{[1,2]} \begin{bmatrix} A_2 \\ B_2 \end{bmatrix}$$

where $M_{[1,2]}$ is given by

$$M_{[1,2]} = \begin{bmatrix} \left(\frac{ik+\kappa}{2ik}\right) e^{(ik-\kappa)d} & \left(\frac{ik-\kappa}{2ik}\right) e^{(ik+\kappa)d} \\ \left(\frac{ik-\kappa}{2ik}\right) e^{-(ik+\kappa)d} & \left(\frac{ik+\kappa}{2ik}\right) e^{-(ik-\kappa)d} \end{bmatrix}$$

For the interface at $z = d$, the amplitudes $A_2$ and $B_2$ in terms of $A_3$ and $B_3$ are (from the $\psi$ and $\psi'$ matching)

$$A_3e^{ikd} + B_3e^{-ikd} = A_2e^{\kappa d} + A_3e^{-\kappa d}, \qquad ik[A_3e^{ikd} - B_3e^{-ikd}] = \kappa[A_2e^{\kappa d} - B_2e^{-\kappa d}], \tag{B.6}$$

where again, adding and subtracting these equations gives the $A_2$ and $B_2$ in terms of $A_3$ and $B_3$:

$$A_2 = A_3\left(\frac{ik+\kappa}{2\kappa}\right)e^{(ik-\kappa)d} - B_3\left(\frac{ik-\kappa}{2\kappa}\right)e^{-(ik+\kappa)d} \tag{B.7}$$

$$B_2 = -A_3\left(\frac{ik-\kappa}{2\kappa}\right)e^{(ik+\kappa)d} + B_3\left(\frac{ik+\kappa}{2\kappa}\right)e^{-(ik-\kappa)d} \tag{B.8}$$

or in terms of matrices,

$$\begin{bmatrix} A_2 \\ B_2 \end{bmatrix} = M_{[2,3]} \begin{bmatrix} A_3 \\ B_3 \end{bmatrix}$$

where the matrix $M_{[2,3]}$ is

$$M_{[2,3]} = \begin{bmatrix} \left(\frac{ik+\kappa}{2\kappa}\right) e^{(ik-\kappa)d} & -\left(\frac{ik-\kappa}{2\kappa}\right) e^{-(ik+\kappa)d} \\ -\left(\frac{ik-\kappa}{2\kappa}\right) e^{(ik+\kappa)d} & \left(\frac{ik+\kappa}{2\kappa}\right) e^{-(ik-\kappa)d} \end{bmatrix}$$

Now putting the $A_1, B_1$ matrix in terms of the $A_3, B_3$ matrix,

$$\begin{bmatrix} A_1 \\ \\ B_1 \end{bmatrix} = M_{[1,2]} M_{[2,3]} \begin{bmatrix} A_3 \\ \\ B_3 \end{bmatrix}$$

or

$$\begin{bmatrix} A_1 \\ \\ B_1 \end{bmatrix} = \begin{bmatrix} \left(\frac{ik+\kappa}{2ik}\right) e^{(ik-\kappa)d} & \left(\frac{ik-\kappa}{2ik}\right) e^{(ik+\kappa)d} \\ \\ \left(\frac{ik-\kappa}{2ik}\right) e^{-(ik+\kappa)d} & \left(\frac{ik+\kappa}{2ik}\right) e^{-(ik-\kappa)d} \end{bmatrix} \begin{bmatrix} \left(\frac{ik+\kappa}{2\kappa}\right) e^{(ik-\kappa)d} & -\left(\frac{ik-\kappa}{2\kappa}\right) e^{-(ik+\kappa)d} \\ \\ -\left(\frac{ik-\kappa}{2\kappa}\right) e^{(ik+\kappa)d} & \left(\frac{ik+\kappa}{2\kappa}\right) e^{-(ik-\kappa)d} \end{bmatrix} \begin{bmatrix} A_3 \\ \\ B_3 \end{bmatrix}$$

Now the $M_{11}^{sb}$ for the *single barrier* is

$$M_{11}^{sb} = \left(\frac{ik+\kappa}{2ik}\right)\left(\frac{ik+\kappa}{2\kappa}\right) e^{2(ik-\kappa)d} - \left(\frac{ik-\kappa}{2\kappa}\right)\left(\frac{ik-\kappa}{2ik}\right) e^{2(ik+\kappa)d}$$

$$= \left[\left(\frac{-k^2+2ik\kappa+\kappa^2}{4ik\kappa}\right)(\cosh(2\kappa d)-\sinh(2\kappa d)) - \left(\frac{-k^2+2ik\kappa+\kappa^2}{4ik\kappa}\right)(\cosh(2\kappa d)+\sinh(2\kappa d))\right] e^{2ikd}$$

where $e^x = \cosh x \pm \sinh x$ was used, and then

$$\boxed{M_{11}^{sb} = \left[\cosh(2\kappa d) - \frac{i}{2}\frac{k^2-\kappa^2}{k\kappa}\sinh(2\kappa d)\right] e^{2ikd}, \text{single symmetric barrier}} \qquad \text{(B.9)}$$

For the $M_{21}^{sb}$ element, multiplication gives

$$M_{21}^{sb} = \left(\frac{ik+\kappa}{2\kappa}\right)\left(\frac{ik-\kappa}{2ik}\right) e^{2-\kappa d} - \left(\frac{ik+\kappa}{2\kappa}\right)\left(\frac{ik-\kappa}{2ik}\right) e^{2\kappa d}$$

$$= \left(\frac{-k^2-\kappa^2}{4ik\kappa}\right)(\cosh(2\kappa d)-\sinh(2\kappa d)) - \left(\frac{k^2-\kappa^2}{4ik\kappa}\right)(\cosh(2\kappa d)+\sinh(2\kappa d))$$

or

$$\boxed{M_{21}^{sb} = -\frac{i}{2}\frac{k^2+\kappa^2}{k\kappa}\sinh(2\kappa d)\text{single symmetric barrier}} \tag{B.10}$$

The remaining elements $M_{21}^{sb}$ and $M_{22}^{sb}$ are similarly found to be

$$\boxed{M_{22}^{sb} = \left[\cosh(2\kappa d)+\frac{i}{2}\frac{k^2-\kappa^2}{k\kappa}\sinh(2\kappa d)\right]e^{-2ikd}, \text{single symmetric barrier}} \tag{B.11}$$

$$\boxed{M_{12}^{sb} = +\frac{i}{2}\frac{k^2+\kappa^2}{k\kappa}\sinh(2\kappa d)\text{single symmetric barrier}} \tag{B.12}$$

which gives the following relations,

$$M_{22} = M_{11}^* \qquad\qquad M_{12} = M_{21}^* \tag{B.13}$$

### B.1.1 Tunneling Probability

For the case of a particle tunneling from the left to the right of the single barrier, $G = 0$, then $A = M_{11}F$, and the transmission probability is given by

$$T = \frac{1}{|M_{11}|^2} \qquad \Longrightarrow \qquad = \left[\cosh^2(2\kappa a)+\frac{k^2-\kappa^2}{k\kappa}\sinh^2(2\kappa a)\right]^{-1} \tag{B.14}$$

or

$$\boxed{T = \frac{1}{1 + \left(\frac{k^2+\kappa^2}{2k\kappa}\right)^2 \sinh^2(2\kappa a)} \qquad (E < V)} \tag{B.15}$$

$$\boxed{T = \frac{1}{1 + \left(\frac{k^2+k'^2}{2kk'}\right)^2 \sin^2(2k'a)} \qquad (E > V)} \tag{B.16}$$

where the second equation accounts for above the barrier transmission, with $\kappa \rightarrow ik'$.

## B.2 Single Asymmetric Rectangular Barrier

The next example is the single rectangular barrier with one side of the barrier off-set by the amount $-V_1$, and lower (see Fig. (B.1)). Here the wavevector on the left side remains unchanged from the previous example, but the right side waves are characterized by different wave vectors, $k_1 = \sqrt{(2m^*/\hbar^2)(E - (-V_1))}$. Therefore the condtions at $z = -d$ remain unchanged, but the conditions at $z = d$ are now

$$A_3 e^{ik_1 d} + B_3 e^{-ik_1 d} = A_2 e^{\kappa d} + B_2 e^{-\kappa d}, \qquad ik_1[A_3 e^{ik_1 d} - B_3 e^{-ik_1 d}] = \kappa[A_2 e^{\kappa d} - B_2 e^{-\kappa d}], \tag{B.17}$$

$$A_2 = A_3 \left(\frac{ik_1 + \kappa}{2\kappa}\right) e^{(ik_1 - \kappa)d} - B_3 \left(\frac{ik_1 - \kappa}{2\kappa}\right) e^{-(ik_1+\kappa)d} \tag{B.18}$$

$$B_2 = -A_3 \left(\frac{ik_1 - \kappa}{2\kappa}\right) e^{(ik_1+\kappa)d} + B_3 \left(\frac{ik_1 + \kappa}{2\kappa}\right) e^{-(ik_1-\kappa)d} \tag{B.19}$$

and in matrix form,

$$\begin{bmatrix} A_2 \\ \\ B_2 \end{bmatrix} = \begin{bmatrix} \left(\frac{ik_1+\kappa}{2\kappa}\right) e^{(ik_1-\kappa)a} & \left(\frac{ik_1-\kappa}{2\kappa}\right) e^{-(ik_1+\kappa)a} \\ \\ \left(\frac{ik_1-\kappa}{2\kappa}\right) e^{(ik_1+\kappa)a} & \left(\frac{ik_1+\kappa}{2\kappa}\right) e^{-(ik_1-\kappa)a} \end{bmatrix} \begin{bmatrix} A_3 \\ \\ B_3 \end{bmatrix}$$

Again putting the $A_1, B_1$ matrix in terms of the $A_3, B_3$ matrix, and recasting in terms of the $M_{i,j}$

$$\begin{aligned} M_{11} &= \left(\frac{ik+\kappa}{2ik}\right)\left(\frac{ik_1+\kappa}{2\kappa}\right) e^{(ik+ik_1-2\kappa)a} - \left(\frac{ik_1-\kappa}{2\kappa}\right)\left(\frac{ik-\kappa}{2ik}\right) e^{(ik+ik_1+2\kappa)a} \\ &= \left(\left(\frac{-kk_1 + ik_1\kappa + ik\kappa + \kappa^2}{4ik_1\kappa}\right)(\cosh(2\kappa a) - \sinh(2\kappa a))\right) e^{2ik_1 a} - \end{aligned}$$

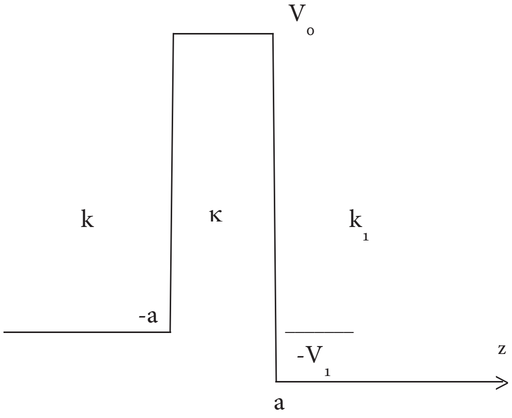

Figure B.1: Single rectangular barrier of height $V_0$, but with an offset $-V_1$.

$$\left(\left(\frac{-k_1k+ik_{III}\kappa+ik\kappa+\kappa^2}{4ik_1\kappa}\right)(\cosh(2\kappa a)+\sinh(2\kappa a))\right)e^{2ik_1a}$$

and

$$\boxed{M_{11}=\left[\frac{1}{2}\left(1+\frac{k_1}{k}\right)\cosh(2\kappa a)-\frac{i}{2}\frac{kk_1-\kappa^2}{k\kappa}\sinh(2\kappa a)\right]e^{i(k+k_1)a}} \tag{B.20}$$

For the element $M_{21}$, the same is done,

$$\begin{aligned}M_{21}&=\left(\frac{ik+\kappa}{2\kappa}\right)\left(\frac{ik-\kappa}{2ik}\right)e^{-2\kappa a-i(k-k_1)a}-\left(\frac{ik+\kappa}{2\kappa}\right)\left(\frac{ik-\kappa}{2ik}\right)e^{2\kappa a-i(k-k_1)a}\\&=\left(\frac{-k^2-\kappa^2}{4ik\kappa}\right)(\cosh(2\kappa a)-\sinh(2\kappa a))-\left(\frac{k^2-\kappa^2}{4ik\kappa}\right)(\cosh(2\kappa a)+\sinh(2\kappa a))\end{aligned}$$

$$\boxed{M_{21}=-\left[\frac{i}{2}\left(\frac{kk_1+\kappa^2}{k\kappa}\right)\sinh(2\kappa a)+\frac{1}{2}\left(\frac{k_1}{k}-1\right)\cosh(2\kappa a)\right]e^{-i(k-k_1)a}} \tag{B.21}$$

Now the momenta are different on each side of the barrier, and so the determinant of the matrix is no unity, and considering only outgoing waves on the right-hand side, $G=0$, and the transmission coefficient for the asymmetrical single rectangular barrier is given by

$$\boxed{T=\frac{k_1}{k}\frac{1}{|M_{11}|^2}=\frac{4k_1k/(k_1+k)^2}{1+\frac{(\kappa^2+k^2)(\kappa^2+k_1^2)}{\kappa^2(k_1+k)^2}\sinh^2(2\kappa a)}} \tag{B.22}$$

Two points can be made from the above expression for $T$. First, the numerator describes the asymmetry in the propagation constants on either side of the barrier, and the denominator describes the *transparency* of the barrier. Additionally, the ratio of the wavenumbers $k$ and $k_1$ in $T$ are both of

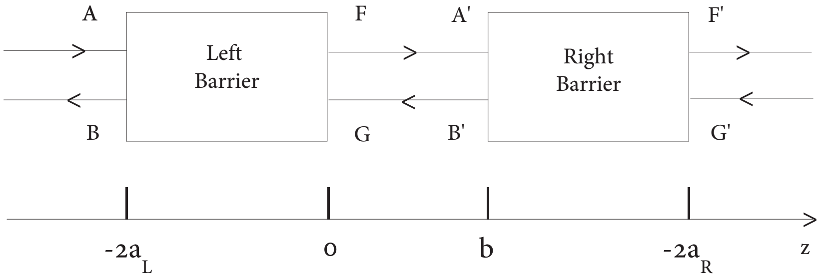

Figure B.2: The schematic for analyzing the general case of the double barrier system. The arrows indicate the incoming and outgoing waves, with the lengths labeled. For this general case, the wavenumbers are denoted for each region.

the same order, representing a symmetry of the structure (even though the barrier is asymmetric), meaning that the transmission is the same whether going left-to-right of right-to-left.

## B.3 Double Rectangular Barrier

In this section the details of the derivation of the transmission characteristics of the symmetric double barrier structure are given. In general, a wave propagating to the right and to the left, respectively, between the barriers, will be given by

$$A' = Fe^{ikb}, \qquad B' = Ge^{-ikb} \qquad \Longrightarrow \qquad \begin{bmatrix} F \\ G \end{bmatrix} = \begin{bmatrix} e^{-ikb} & 0 \\ 0 & e^{ikb} \end{bmatrix} \begin{bmatrix} A' \\ B' \end{bmatrix} \tag{B.23}$$

where $b$ is the width of the well region and $k$ is the wave vector for that region. This gives the connection between the left-hand barrier and the right-hand barrier, as (taking the results from above)

$$\begin{bmatrix} A \\ B \end{bmatrix} = [\mathbf{M}_L]\,[\mathbf{M}_W]\,[\mathbf{M}_R] \begin{bmatrix} F' \\ G' \end{bmatrix}$$

where the subscripts $L$, $W$ and $R$ refer to left, well and right respectively. In terms of the elements,

$$[\mathbf{M}_L] = \begin{bmatrix} M_{L11} & M_{L12} \\ M_{L21} & M_{L22} \end{bmatrix}, \quad [\mathbf{M}_W] = \begin{bmatrix} M_{W11} & M_{W12} \\ M_{W21} & M_{W22} \end{bmatrix}, \quad [\mathbf{M}_R] = \begin{bmatrix} M_{R11} & M_{R12} \\ M_{R21} & M_{R22} \end{bmatrix} \tag{B.24}$$

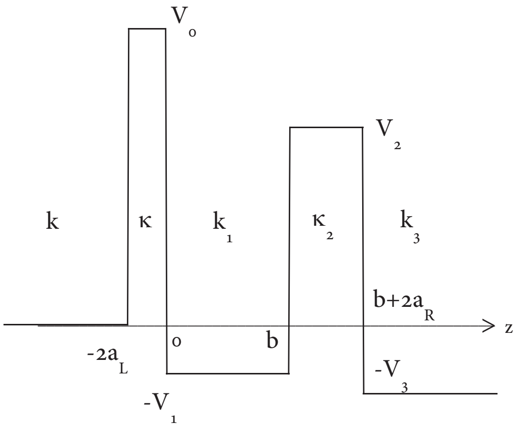

Figure B.3: The general double rectangular barrier with heights $V_0$, $V_2$ and barrier widths $2a_L$ and $2a_R$, and potential well width $b$ and depth $-V_1$.

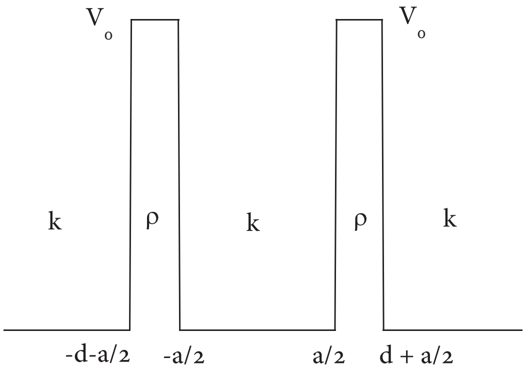

Figure B.4: The symmetric double rectangular barrier with height $V_0$, barrier widths $2a$, and well width $b$.

As the $M_i$'s are complex, it is convenient to write them in the following form

$$M_i = m_i e^{i\theta_i} \tag{B.25}$$

where $i \equiv L11, L12, R11, R21$ and

$$M_{L11} = \sqrt{\frac{1}{4}\left(1 + \frac{k_1}{k}\right)^2 \cosh^2(2\kappa a_L) + \frac{1}{4}\left(\frac{kk_1 - \kappa^2}{k\kappa}\right)^2 \sinh^2(2\kappa a_L)} \tag{B.26}$$

$$M_{L12} = \sqrt{\frac{1}{4}\left(\frac{kk_1 + \kappa^2}{k\kappa}\right)^2 \sinh^2(2\kappa a_L) + \frac{1}{4}\left(\frac{k_1}{k} - 1\right)^2 \cosh^2(2\kappa a_L)} \tag{B.27}$$

$$M_{R11} = \sqrt{\frac{1}{4}\left(1 + \frac{k_3}{k_1}\right)^2 \cosh^2(2\kappa_2 a_R) + \frac{1}{4}\left(\frac{k_1 k_3 - \kappa_2^2}{k_1 \kappa_2}\right)^2 \sinh^2(2\kappa_2 a_R)} \tag{B.28}$$

$$M_{R12} = \sqrt{\frac{1}{4}\left(\frac{k_1 k_3 + \kappa_2^2}{k_1 \kappa_2}\right)^2 \sinh^2(2\kappa_2 a_R) + \frac{1}{4}\left(\frac{k_3}{k_1} - 1\right)^2 \cosh^2(2\kappa_2 a_R)} \tag{B.29}$$

and the phases are given by

$$\theta_{L11} = -\tan^{-1}\left[\frac{kk_1-\kappa^2}{(k+k_1)\kappa}\tanh(2\kappa a_L)\right] + (k+k_1)a_L \tag{B.30}$$

$$\theta_{L12} = -\tan^{-1}\left[\frac{kk_1+\kappa^2}{(k+k_1)\kappa}\tanh(2\kappa a_L)\right] + \pi + (k-k_1)a_L \tag{B.31}$$

$$\theta_{R11} = -\tan^{-1}\left[\frac{k_1k_2-\kappa_1^2}{(k_1+k_2)\kappa_1}\tanh(2\kappa_1 a_R)\right] - (k_1+k_2)a_R \tag{B.32}$$

$$\theta_{R21} = \tan^{-1}\left[\frac{k_1k_2-\kappa_1^2}{(k_2-k_1)\kappa_1}\tanh(2\kappa_1 a_R)\right] + \pi + (k_1-k_2)a_R \tag{B.33}$$

# Appendix C

## Growth Sheet

---

| Layer | Thickness (nm) | Doping (cm$^{-3}$) |
|---|---|---|
| GaAs substrate | 350 ± 25 $\mu$m | SI |
| GaAs | 400 | 2.00·10$^{18}$ |
| GaAs | 70 | 5.00·10$^{16}$ |
| GaAs | 30 | - |
| AlAs | 1.2 | - |
| In$_{0.05}$Ga$_{0.95}$As | 8.4 | - |
| AlAs | 1.2 | - |
| In$_{0.05}$Ga$_{0.95}$As | 28.2 | - |
| GaAs | 75 | - |
| AlAs | 1.2 | - |
| GaAs | 40 | 5.00·10$^{16}$ |
| GaAs | 200 | 2.00·10$^{18}$ |

Figure C.1: Growth sheet for H656.